

Copyright
by
Jessica Lea Ziehr
2014

**The Dissertation Committee for Jessica Lea Ziehr Certifies that this is the approved
version of the following dissertation:**

**Kinetics and specificity of human mitochondrial DNA polymerase
gamma and HIV-1 reverse transcriptase**

Committee:

Kenneth Johnson, Supervisor

Alan Lambowitz

Rick Russell

Edward Marcotte

Kevin Dalby

**Kinetics and specificity of human mitochondrial DNA polymerase
gamma and HIV-1 reverse transcriptase**

by

Jessica Lea Ziehr, B.S. Bio.

Dissertation

Presented to the Faculty of the Graduate School of

The University of Texas at Austin

in Partial Fulfillment

of the Requirements

for the Degree of

Doctor of Philosophy

The University of Texas at Austin

August 2014

Dedication

To Nathan and Olivia

Acknowledgements

I would like to thank my advisor Dr. Kenneth Johnson for his support over the last five years. He has continuously provided me with expert wisdom throughout my research and showed full support and encouragement for me during this pursuit. I would also like to thank Dr. JoAnn Hunter Johnson for her unwavering commitment to making our laboratory the best it can be. She and Dr. Kenneth Johnson have played a critical role in shaping the scientist and person that I am today.

I would also like to thank the other members of my lab that I have been fortunate to work with. Dr. Dipanwita Batabyal, Dr. Matthew Kellinger and Dr. John Brandis all were excellent teachers who taught me much of what I've learned in the lab. My lab mates Virginia Nguyen, Patricia Estep, An Li, Shanzhong Gong, Jiawen Li and Dr. Yufeng Qian have all been consistently supportive and I thank them for making my time in the Johnson lab so enjoyable.

In addition, I thank my committee members Dr. Alan Lambowitz, Dr. Rick Russell, Dr. Edward Marcotte and Dr. Kevin Dalby for their guidance and expertise.

Finally, I would like to show my deepest appreciation to my family members that have shown unwavering support during my graduate career. Thank you to my husband Nathan who is always ready to take me to lab on weekends and shows a genuine interest in my work, which makes me so happy to share it with him. Thank you to my parents (Dad, Mom, Dave and Maryanne) for always believing in me and teaching me the importance of hard work and integrity. I also owe a thank you to my wonderful daughter and my siblings who consistently provided me with so much joy through the ups and downs of my graduate career.

Kinetics and specificity of human mitochondrial DNA polymerase gamma and HIV-1 reverse transcriptase

Jessica Lea Ziehr, PhD.

The University of Texas at Austin, 2014

Supervisor: Kenneth Allen Johnson

The human mitochondrial DNA (mtDNA) genome must be faithfully maintained by the mitochondrial DNA replication machinery. Deficiencies in mtDNA maintenance result in the accumulation of mutations and deletions, which have been associated with a number of neuromuscular degenerative disorders including, mtDNA depletion syndrome, Alpers syndrome, progressive external ophthalmoplegia (PEO), and sensory ataxic neuropathy, dysarthria, and ophthalmoparesis (SANDO). The mtDNA replication machinery is comprised of a nuclear-encoded DNA polymerase gamma (Pol γ), single-stranded DNA binding protein (mtSSB), and a hexameric mtDNA helicase. In this work, we employed quantitative pre-steady state kinetic techniques to establish the mechanisms responsible for the replication of the human mitochondrial DNA by Pol γ and explored the effects of point mutations that are observed in heritable diseases. With our biochemical characterization of mutants of Pol γ , we have shown unique characteristics that would lead to profound physiological consequences over time. Additionally, we have made significant progress towards reconstitution of the mitochondrial DNA replisome by monitoring DNA polymerization that is dependent on helicase unwinding of double stranded DNA. Overall, this work provides a better understanding of the mechanism of

mtDNA replication and has important implications toward understanding the role of mitochondrial DNA replication in mitochondrial disease, ageing and cancer.

In addition to the work on the mtDNA replisome, we have applied pre-steady state kinetic techniques to better understand the mechanism of RNA-dependent DNA polymerization by HIV reverse transcriptase (HIV-RT). This enzyme is responsible for the replication of the viral genome in HIV and is a common target for anti-HIV drugs. We have characterized the role of enzyme conformational changes in the kinetics of incorporation of correct nucleotide and the Nucleotide Reverse Transcriptase Inhibitor (NRTI) AZT by wild-type enzyme, as well as a mutant with clinical resistance to AZT. This work provides a better understanding of the complete mechanism of RNA-dependent DNA polymerization, the changes in the mechanism in the presence of inhibitor and the development of resistance to this nucleoside analog; and thereby this work contributes to the long-term goal of designing more effective drugs that can possibly deter resistance and be used successfully for treatment of HIV.

Table of Contents

List of Tables	xii
List of Figures	xiii
Chapter 1: Introduction	1
1.1 Project Summary	1
1.2 Mitochondrial DNA Replication.....	2
Mutagenesis of mtDNA leads to mitochondrial diseases	4
Mode of mitochondrial DNA replication.....	7
Mitochondrial DNA polymerase gamma.....	8
Point mutations of Pol γ and their relation to disease	11
Mitochondrial DNA SSB and helicase	13
1.3 HIV Reverse Transcriptase	15
Replication of the HIV single-stranded RNA genome	16
HIV reverse transcriptase structure.....	19
HIV Reverse Transcriptase Inhibitors and resistance mutations	20
Chapter 2: Characterization of Mitochondrial DNA Polymerase Gamma Disease Mutations	22
2.1 Introduction.....	22
2.2 Materials and Methods.....	26
Site directed mutagenesis of Pol γ A	26
Baculovirus expression of Pol γ A.....	28
Purification of Pol γ A	29
Cloning, expression and purification of Pol γ B	32
Preparation of substrate DNA.....	33
Correct nucleotide incorporation assays	34
Nucleotide misincorporation assays	35
Active site titration with DNA	36
Global data fitting	36

2.3 Results	38
Kinetics of correct incorporation	38
Kinetics of DNA binding	43
Kinetics of misincorporation.....	43
2.4 Discussion	53
Relating biochemical characterization to clinical phenotype	54
H932Y/A mutants	54
R943H mutant	57
R953C mutant	57
A957S mutant	58
R1096C mutant	59
Summary of all mutants	60
Chapter 3: Characterization of Mitochondrial DNA Polymerase Gamma Active Site Mutations	67
3.1 Introduction	67
Mutations of these residues are rarely seen clinically	68
3.2 Materials and Methods.....	69
Cloning expression and purification.	69
Accessory subunit Pol γ B	69
Catalytic subunit Pol γ A	70
Preparation of substrate DNA.....	72
Kinetics of correct nucleotide incorporation.....	73
Nucleotide misincorporation assays	73
Pyrophosphate Release Assay.....	74
Pyrophosphate Release Controls.....	75
Global data fitting	76
3.3 Results	78
Kinetics of correct incorporation	78
Nucleotide Misincorporation Assays	84
3.4 Discussion	88

Mutation E895A.....	90
Mutation Y951F.....	91
Mutation K947A.....	91
Relating active site mutations to disease mutations.....	92
Chapter 4: Reconstitution of the Human Mitochondrial DNA Replisome.....	95
4.1 Introduction.....	95
4.2 Materials and Methods.....	98
Cloning, expression and purification of Pol γ A.....	98
Cloning, expression and purification of Pol γ B.....	99
Cloning, expression and purification of mtDNA Helicase.....	99
Cloning of mtDNA Helicase trimer.....	104
Preparation of DNA substrates.....	110
Helicase Unwinding Assays.....	112
Replisome Assays.....	113
4.3 Results.....	114
Kinetics of helicase unwinding.....	114
Kinetics helicase unwinding in the presence of polymerase.....	116
Kinetics of mtDNA Replisome.....	116
Alternative assembly strategies.....	119
4.4 Discussion.....	121
Pol γ stimulates DNA helicase activity.....	121
Kinetics of mtDNA Replisome.....	122
Chapter 5: Characterization of HIV Reverse Transcriptase Nucleotide incorporation on a DNA/RNA substrate by WT and TAMS mutants.....	124
5.1 Introduction.....	124
5.2 Materials and Methods.....	128
Site directed mutagenesis of HIV-RT.....	128
Expression of HIV-RT p66 and p51 subunits.....	131
Purification and MDCC labeling of HIV-RT.....	133
Preparation of substrate DNA and RNA.....	137

Synthesis of 2', 3'-dideoxyterminated dd26mer.....	138
Quench flow kinetic assays.....	139
Stopped flow nucleotide incorporation assays.....	140
Stopped flow nucleotide dissociation assays	140
Global data fitting	141
5.3 Results.....	141
Kinetics of nucleotide binding and incorporation by quench flow methods	141
Kinetics of nucleotide binding and incorporation by stopped flow methods	144
Global fitting of HIV-RT wild-type TTP incorporation	145
Global fitting of HIV-RT wild-type AZTTP incorporation.....	150
Global fitting of HIV-RT TAMS TTP incorporation	152
Global fitting of HIV-RT TAMS AZTTP incorporation	154
5.4 Discussion	157
Chapter 6: HIV Reverse Transcriptase Labeling Site Mutations.....	163
6.1 Introduction.....	163
6.2 Materials and Methods.....	167
Site directed mutagenesis of HIV-RT	167
Expression, purification and MDCC-labeling of HIV-RT	170
Preparation of substrate DNA.....	170
Fluorimeter assay measuring substrate binding.....	170
Stopped flow assay measuring nucleotide incorporation.....	171
6.3 Results.....	171
6.4 Discussion	175
Appendix.....	178
References.....	179
Vita	192

List of Tables

Table 2.1. Mutagenic primers for Pol γ A Disease Mutants.....	27
Table 2.2. Sequencing primers for Pol γ A.....	27
Table 2.3 DNA primer-template sequences for Pol γ	34
Table 2.4 Pol γ Kinetic Parameters of dATP Incorporation.....	40
Table 2.5 Pol γ Kinetic Parameters of Misincorporation	50
Table 2.6 Pol γ Kinetic Parameters of Misincorporation	52
Table 3.1 Mutagenic primers for Pol γ A Active Site Mutants	70
Table 3.2 DNA primer-template sequences for Pol γ	72
Table 3.3 Pol γ Kinetic Parameters of dATP Incorporation.....	79
Table 3.4 Pol γ Kinetic Parameters of dATP Incorporation.....	80
Table 3.5 Pol γ Kinetic Parameters of Misincorporation	87
Table 3.6 Pol γ Kinetic Parameters of Misincorporation	88
Table 4.1 Oligomers for construction of mtHelicase trimer	105
Table 4.2 Substrates for replisome assays	111
Table 5.1 Mutagenic primers for HIV-RT.....	130
Table 5.2 DNA-primer/RNA-template sequences for HIV-RT.....	139
Table 5.3 HIV-RT Incorporation parameters.....	144
Table 5.4 Rate constants for TTP and AZTTP Incorporation by HIV-RT determined by global fitting.....	156
Table 5.5 Specificity, discrimination and resistance determined by global fitting	156
Table 6.1 Residues selected for cysteine mutagenesis and MDCC labeling	166
Table 6.2 Mutagenic primers for HIV-RT labeling site mutants.....	169
Table 6.3 Primer template sequences for HIV-RT labeling mutants.....	170

List of Figures

Figure 1.1 Proteins at the mtDNA replication fork.....	4
Figure 1.2 Proposed modes of mtDNA replication.	8
Figure 1.3 The crystal structure of Pol γ (PDB:3IKM, (45)).....	10
Figure 1.4 Disease-associated residues near the polymerase active site.	11
Figure 1.5 HIV Genome Replication.....	18
Figure 1.6 Structure of HIV Reverse Transcriptase.....	19
Figure 2.1 Clustering of POLG disease mutations.	23
Figure 2.2 Location of disease mutations on Pol γ A.	24
Figure 2.3 Baculovirus expression of Pol γ A in SF9 cells.....	28
Figure 2.4 Nickel-NTA column purification of Pol γ A.....	30
Figure 2.5 SP sepharose column purification of Pol γ A.....	31
Figure 2.6. Correct incorporation of dATP by wild-type and mutants of Pol γ A.....	42
Figure 2.7 Active site titration of A957S mutant.....	43
Figure 2.8 Formation of a T:T mismatch by wild-type exo^- Pol γ	46
Figure 2.9 Misincorporation of dTTP by Pol γ exo^- H932Y mutant.	47
Figure 2.10 Misincorporation by wild-type and mutant exo^- Pol γ	49
Figure 2.11. Contributions of K_d and k_{pol} to specificity displayed on a free energy scale.....	62
Figure 2.12. Comparison of wild-type and mutant Pol γ	63
Figure 2.13. Calculating a Mutation Severity Index for Pol γ mutants.	65
Figure 2.14. Relating biochemical parameters in POLG mutants to age of onset of disease.....	66
Figure 3.1 Active site residues of Pol γ	68

Figure 3.2. Crystal structure of MDCC-PBP.....	75
Figure 3.3 Kinetics of incorporation of dATP for the Y951F and E895A mutants.....	82
Figure 3.4 Stopped flow controls for pyrophosphate release assay.....	83
Figure 3.5 Kinetics of misincorporation by the E895A and Y951F mutants.	85
Figure 3.6. Contributions of K_d and k_{pol} to specificity displayed on a free energy scale.	89
Figure 3.7. Calculating a Mutation Severity Index for Pol γ mutants.	94
Figure 4.1. Reconstitution of the mtDNA Replication fork.....	97
Figure 4.2. Growth kinetics of E. coli expressing mtDNA Helicase.	100
Figure 4.3 Nickel sepharose column purification of mtDNA helicase.....	102
Figure 4.4 Tandem column purification of mtDNA helicase.	103
Figure 4.5 Cloning of mtHelicase trimer – adding gene insertion sites.....	107
Figure 4.6 Cloning of mtHelicase trimer – construction of gene 2.	108
Figure 4.7 Cloning of mtHelicase trimer – construction of gene 3.	109
Figure 4.8 Cloning of mtHelicase trimer – tripartite ligation.	110
Figure 4.9. Pol γ stimulates DNA helicase activity.	115
Figure 4.10. Polymerase extension is dependent on helicase unwinding of the branch strand.....	118
Figure 5.1. Structure of thymidine and AZT.	126
Figure 5.2. Structure of HIV-RT with TAMs mutations.	127
Figure 5.3. Expression of HIV-RT.	132
Figure 5.4. Structure of MDCC.	134
Figure 5.5 Tandem column purification of HIV-RT.	135
Figure 5.6 ssDNA cellulose column purification of HIV-RT.....	136
Figure 5.7 Bio-Rex70 column purification of MDCC-labeled HIV-RT.	137

Figure 5.8. Chemical quench flow incorporation of dTTP and AZTTP by HIV-RT WT and TAMS mutant.	143
Figure 5.9. Global fitting of dTTP binding and incorporation by WT HIV-RT..	148
Figure 5.10. Temperature dependence of dTTP binding and incorporation by WT HIV-RT.	149
Figure 5.11. Global fitting of AZTTP binding and incorporation by WT HIV-RT.	151
Figure 5.12. Global fitting of dTTP binding and incorporation by TAMS HIV-RT.	153
Figure 6.1. Open and closed conformations of HIV-RT p66.	164
Figure 6.2. Global changes of HIV-RT structure with time.	165
Figure 6.3. Potential MDCC-labeling sites on HIV-RT.	167
Figure 6.4. Emission spectra of HIV-RT p66-C280S-E300C-MDCC.	172
Figure 6.5. Fluorescence Stopped-flow signal of HIV-RT p66-C280S-E300C-MDCC.	173
Figure 6.6. Fluorescence Stopped-flow signal of HIV-RT p66-C280S-Q334C- MDCC.....	174
Figure 6.7. Fluorescence Stopped-flow signal of HIV-RT p66-C280S-Q334C-MDCC at 4°C.	175

Chapter 1: Introduction

1.1 PROJECT SUMMARY

The work in this dissertation is aimed at evaluating the mechanisms of human mitochondrial DNA replication and HIV replication in order to gain a better understanding of nucleotide incorporation, specificity and discrimination against mismatches or nucleoside analogs used to treat HIV infections. To explore HIV replication, the kinetics of RNA-dependent DNA replication by HIV-1 reverse transcriptase (HIV-RT) were analyzed using pre-steady state kinetic methods to gain an insight into the discrimination of HIV-RT for correct nucleotides and for the nucleoside reverse transcriptase inhibitor (NRTI), AZT. Previous work on NRTIs found toxic side effects due to incorporation by the human mitochondrial DNA polymerase gamma (Pol γ) when these drugs were used in patients with HIV (1, 2). Our work continues to characterize the mitochondrial DNA replication by Pol γ and its partners in DNA replication. The goal of this project is to gain a detailed mechanistic understanding of these DNA polymerization reactions and the specificity of these enzymes and discrimination against nucleoside analogs. This work aids in the overall understanding of the mechanisms that these enzymes employ for DNA replication. The two-pronged approach of studying the viral HIV reverse transcriptase along with the human mitochondrial DNA polymerase allows for a more complex understanding of nucleotide analog effectiveness versus toxicity. Detailed mechanistic characterization of these two enzymes furthers our understanding of the diseases associated with mutations in mitochondrial Pol γ and potentially designing better targets for HIV-RT that will overcome the development of resistance and show lower toxicity. Chapter one provides a background of the enzymes studied in this research project as well as their relation to

human disease. In Chapter two, the study of six disease-associated mutations of mitochondrial DNA polymerase gamma is reported. Chapter three discusses the characterization of three active-site mutations of Pol γ and their effect on nucleotide specificity. Chapter four will expand the work on mitochondrial DNA replication by Pol γ to include the characterization of the mitochondrial DNA helicase. Chapter 5 will transition to the work done on HIV-RT by looking at the RNA-dependent DNA polymerase reaction by the wild-type enzyme as well as a set of resistance mutations (TAMS) seen clinically. The final chapter will discuss attempts to explore the conformational changes of HIV-RT by labeling the enzyme with a conformationally sensitive fluorophore based on predictions from molecular modeling.

1.2 MITOCHONDRIAL DNA REPLICATION

Mitochondria are complex organelles that are responsible for many diverse functions in the cell including production of ATP by oxidative phosphorylation, generation of reactive oxygen species that influence signaling pathways to control cell proliferation and differentiation, production of NADH, and regulation of Ca^{2+} , to name a few (3). Dysfunction of the mitochondrial processes is associated with a large number of heritable disease including neurodegenerative disorders, cardiomyopathies, cancer and obesity (3-8). Mammalian mitochondria contain greater than 1,500 proteins that differ in a tissue specific manner; however, all but 13 of these proteins are encoded by the nuclear genome and transported into the mitochondria (9).

Human mitochondrial DNA (mtDNA) is roughly 16,600 base pairs and contains 13 essential genes for proteins that are involved in the oxidative phosphorylation pathway leading to the production of cellular ATP, plus 22 tRNA and 2 rRNA genes required for mitochondrial protein synthesis (10). The circular mtDNA genome is organized into

nucleoids inside mitochondrial matrix with each mitochondrion DNA containing a high copy number and a mixed population of wild-type and mutant alleles (11). The proteins of the mitochondrial DNA replication machinery, all of which are encoded in the nucleus, translated in the cytosol and imported into the mitochondria, must faithfully maintain this genome. Deficiencies in mtDNA maintenance result in the accumulation of mutations and deletions, which have been associated with a number of neuromuscular degenerative disorders including, mtDNA depletion syndrome, Alpers syndrome, progressive external ophthalmoplegia (PEO), and sensory ataxic neuropathy, dysarthria, and ophthalmoparesis (SANDO) (5, 6, 12). The Human DNA Polymerase Gamma Mutation Database lists more than 200 mutations in Pol γ that have been seen in patients with mitochondrial disorders (13). Currently these mitochondrial diseases cannot be cured and treatment only involves measures to alleviate symptoms (14). It has also been suggested that mitochondrial dysfunction is associated with cancer, obesity, ageing and infertility (3, 7, 8, 15); therefore, a greater understanding of the proper maintenance of this mtDNA is of great value. In order to optimize treatment options and remedies for genetic mitochondrial diseases it will be necessary to understand the mechanistic basis for the physiological effects of disease mutations in the replisome machinery. This is a difficult task, as correlating mutations to biological phenotypes in mitochondrial disorders is often complex due to the high copy number of mtDNA and mixed population of mutant and wild-type alleles (known as heteroplasmy).

The mtDNA replication machinery that maintains the mtDNA is comprised of a nuclear-encoded DNA polymerase (polymerase gamma), single-stranded DNA binding protein (mtSSB), and a hexameric DNA helicase (aka Twinkle) (16-19). These proteins assemble at the replication fork and are responsible for the faithful replication of mtDNA in order to maintain its integrity (Figure 1.1). Defects in the enzymes of the mtDNA

replisome lead to an accumulation of mutations and deletions in the mitochondrial DNA and reduction of mtDNA content resulting in clinical symptoms of mitochondrial disorders that are often slow in onset and cumulative.

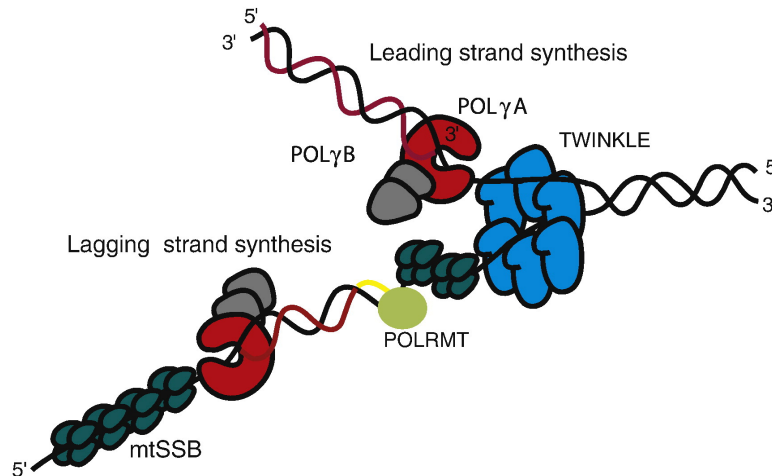


Figure 1.1 *Proteins at the mtDNA replication fork.* This figure, reproduced from (19), shows the mtDNA helicase (Twinkle) (blue), Pol γ A (red), Pol γ B (gray), mtSSB (dark green) and the mitochondrial RNA polymerase (POLRMT) (light green) at the replication fork where leading and lagging strand synthesis occurs.

Mutagenesis of mtDNA leads to mitochondrial diseases

Defects in mitochondria have been implicated in a variety of malignancies including degenerative diseases, aging and cancer (3, 7, 8, 15). Inherited mitochondrial diseases are genetically and molecularly complex due to the high copy number of mtDNA, the dynamics of the mitochondrial network and the interplay between mutations in nuclear and mitochondrial genomes. Mitochondrial diseases lead to a wide variety of clinical symptoms but primarily involve tissues that have high energy requirements and are affected by a reduction in cellular respiration (nerves, heart, muscle, renal and endocrine systems) (20). Point mutations and deletions in mtDNA can arise from spontaneous errors in DNA replication by Pol γ , as well as chemical damage from reactive oxygen species produced during respiration. Due to the high copy number of

mtDNA, a certain level of mtDNA mutations can be tolerated but once a phenotypic threshold of mutations is exceeded, mitochondrial dysfunction occurs and leads to clinical symptoms of mitochondrial diseases. Many mitochondrial disorders are cumulative and delayed in onset so that many do not present until later in life. Mutations arising from errors by Pol γ are rare because the enzyme has a moderately high fidelity. The fidelity of polymerization by the Pol γ results in one error in 280,000 base pairs, (21) which is further increased another 4- to 18-fold by the 5'-3' exonuclease activity of Pol γ , resulting in one error in 1 – 20 million base pairs on average (22). Pol γ also plays a role in the efficient base excision repair system in mitochondria, by filling the gap after the damaged base has been removed and cleaving the 5'-deoxyribose phosphate before ligation of the repaired DNA (23). Mitochondria lack a mechanism for nucleotide or ribonucleotide excision repair and there is little evidence for a mismatch repair pathway (24-28). Ultimately, unrepaired mutations that persist in mtDNA or depletion of mtDNA can lead to mitochondrial diseases, with a large number of these diseases linked to deficiencies in *POLG* encoding Pol γ A.

Mutations in Pol γ have the potential to lead to decreased polymerization rates and decreased discrimination against incorrect or oxidatively damaged nucleotides, leading to decreased fidelity of the enzyme. The current theory for *POLG*-related diseases suggests that defects in Pol γ result in oxidative stress that leads to further mtDNA damage and a cycle of cumulative defects that eventually lead to the clinically observable symptoms of the disease (7, 8). The *POLG*-related diseases relevant to this work are described below.

Progressive External Ophthalmoplegia (PEO). PEO is characterized by a progressive, adult-onset weakness of the extraocular eye muscles that results in ptosis and loss of eye movements (29). PEO can occur with autosomal dominant (ad) or recessive (ar) mutations in *POLG* and leads to the accumulation of multiple mtDNA deletions in

skeletal tissue. This disease has also been linked to mutations in the nuclear gene for the mtDNA helicase (*C10ORF2*) (30, 31). Other symptoms of this disease include exercise intolerance, cataracts, hearing loss, sensory ataxia, neuropathy, dysarthria, myopathy, Parkinsonism and premature ovarian failure (29, 32-35).

Alpers Syndrome. This autosomal recessive disorder, also referred to as Alpers-Huttenlocher syndrome, often occurs in infants and children who appear to be healthy before the onset of the disease. Symptoms of this syndrome include seizures, developmental regression and dysfunction of the liver (36). Progression of the disease ultimately leads to liver failure and early death. Patients with Alpers syndrome often show normal mitochondrial DNA content early in the disease process with mitochondrial DNA deletions and depletion accumulating during progression of the disease (37, 38). Pathogenic mutations in both Pol γ and the mtDNA helicase have been linked to Alpers syndrome.

SANDO. Sensory Ataxic Neuropathy, Dysarthria and Ophthalmoparesis (SANDO) is another *POLG*-associated mitochondrial disease related to dysfunction in the eyes, similar to PEO. This unique syndrome includes the coexistence of symptoms in ocular, sensory and speech systems. Additionally, biopsy of skeletal muscle from SANDO patients revealed ragged red fibers and mitochondrial DNA deletions (39). This is an autosomal recessive disorder and shows wide variation in phenotype within families presenting the disease. Additional symptoms can include myopathy, seizures and hearing loss (40).

Overall, mutations in Pol γ are associated with progressive diseases that lead to mitochondria dysfunction with a wide range and severity of symptoms. This work aims to characterize DNA replication by wild-type and mutants of Pol γ to better understand a biochemical basis for these diseases.

Mode of mitochondrial DNA replication

The exact mode of mitochondrial DNA replication is not fully understood and is still a topic of great debate in the field. Historically, the mechanism of mtDNA replication was considered to occur by a continuous, asymmetric, strand displacement mode (SDM), as outlined in Figure 1.2A (19). Leading-strand synthesis begins from an RNA-polymerase synthesized primer at the OH origin of replication site and proceeds unidirectionally, displacing the single stranded DNA to form the D-loop structure. The helicase and polymerase proceed and at some point the OL site is exposed so that the lagging-strand synthesis can be initiated by synthesis of a primer by the RNA-polymerase followed by the extension of the primer by Pol γ . In this model, mtSSB binds to the single stranded regions of DNA to protect it from degradation.

A more recent hypothesis for the mode of mtDNA replication has come from the work by Holt and coworkers using two-dimensional agarose gel electrophoresis (2D-AGE) methods to monitor replication intermediates (41, 42). The authors of this study found evidence for RNaseH-sensitive replication intermediates that led them to develop the model in Figure 1.2B (left path). In this model, referred to as RITOLS (ribonucleotide incorporation throughout the lagging strand), replication initiates from one single origin and proceeds in a strand coupled mode where the leading strand is synthesized while the lagging strand is simultaneously protected by the binding of RNA. Once the lagging-strand origin is unwound, replacement of the lagging-strand RNA with DNA occurs.

In a similar proposed mode for replication, Figure 1.2B (right path), the replication is thought to proceed in a strand-coupled mode. In this model, the replication initiates at an origin and proceeds bidirectionally in a mode that results in fully double stranded intermediates (41, 43, 44).

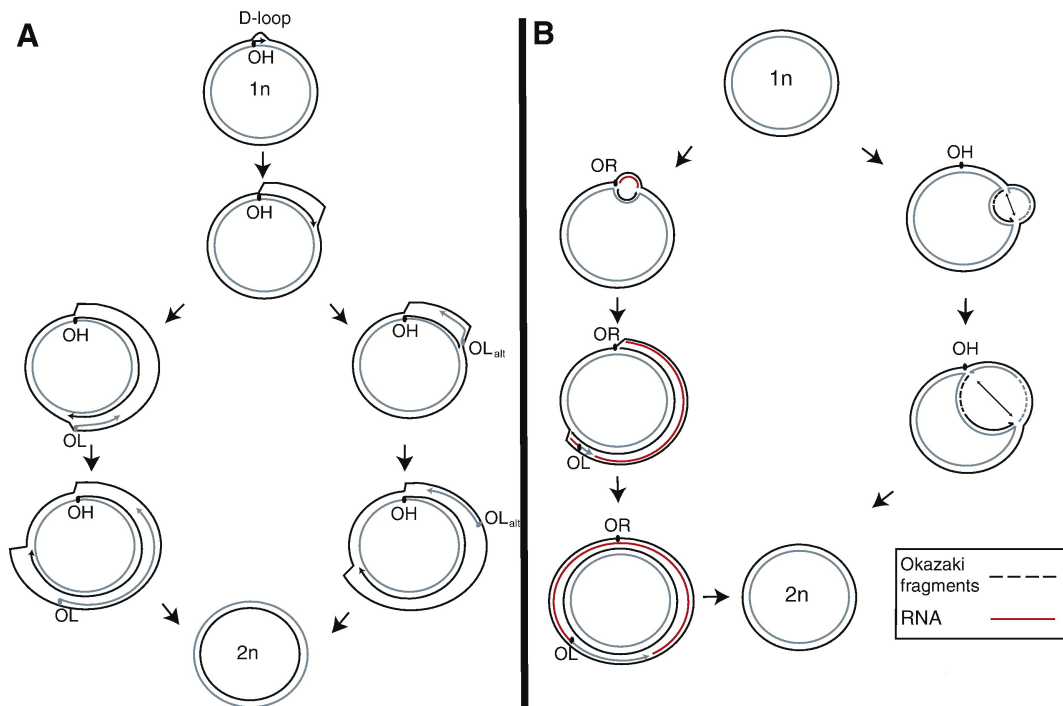


Figure 1.2 *Proposed modes of mtDNA replication.* Reproduced from (19) this figure shows the three proposed modes of mammalian mtDNA replication. A. Strand-displacement mode. B (left path). RITOLS – ribonucleotide incorporation throughout the lagging strand. B (right path). Strand-coupled mode.

At this point the exact mode of mtDNA replication is still being debated, with the three predominate candidates having experimental data to support their hypotheses. It is also possible that there is the existence of more than one replication mode utilized by mitochondria and the modes are tissue or environmentally specific.

Mitochondrial DNA polymerase gamma

DNA polymerase gamma (Pol γ) belongs to the family A of DNA polymerases and is heterotrimer, containing the 140 kDa catalytic subunit (Pol γ A) and a dimer of the 55 kDa processivity subunit (Pol γ B). Pol γ A is encoded by *POLG* at chromosomal locus 15q25, and the Pol γ B subunit is encoded by *POLG2* at chromosomal locus 17q24.1. The catalytic subunit contains domains for the polymerase (pol) and exonuclease (exo)

activities that are separated by a linker. A recent crystal structure of Pol γ (45), Figure 1.3, shows that the pol domain has the canonical structure resembling a “right-hand” that is characteristic to most polymerases with palm, fingers, and thumb subdomains that form the DNA binding groove and leads to the polymerase active site (46, 47).

The crystal structure of the ternary complex (Pol γ , DNA and nucleotide) has not been solved; however the ternary structure of the homologous T7 DNA polymerase can be used to provide insight into the functions of the active site residues (47). The holoenzyme of Pol γ catalyzes DNA synthesis in the 5' to 3' direction and also contains a 3' to 5' exonuclease domain, which provides a proofreading function (22, 48). *In vitro* measurements of polymerization on a primer/template DNA substrate by Pol γ have reported polymerization rates of 45 s^{-1} and a K_d for DNA of 10 nM (49). The Johnson laboratory has previously studied the DNA polymerization specificity, efficiency, fidelity, processivity and proofreading of wild-type Pol γ and several point mutations in Pol γ (21, 22, 48-57). The work presented here continues these studies to further understand the role of single point mutations in the clinical effects seen in heritable diseases.

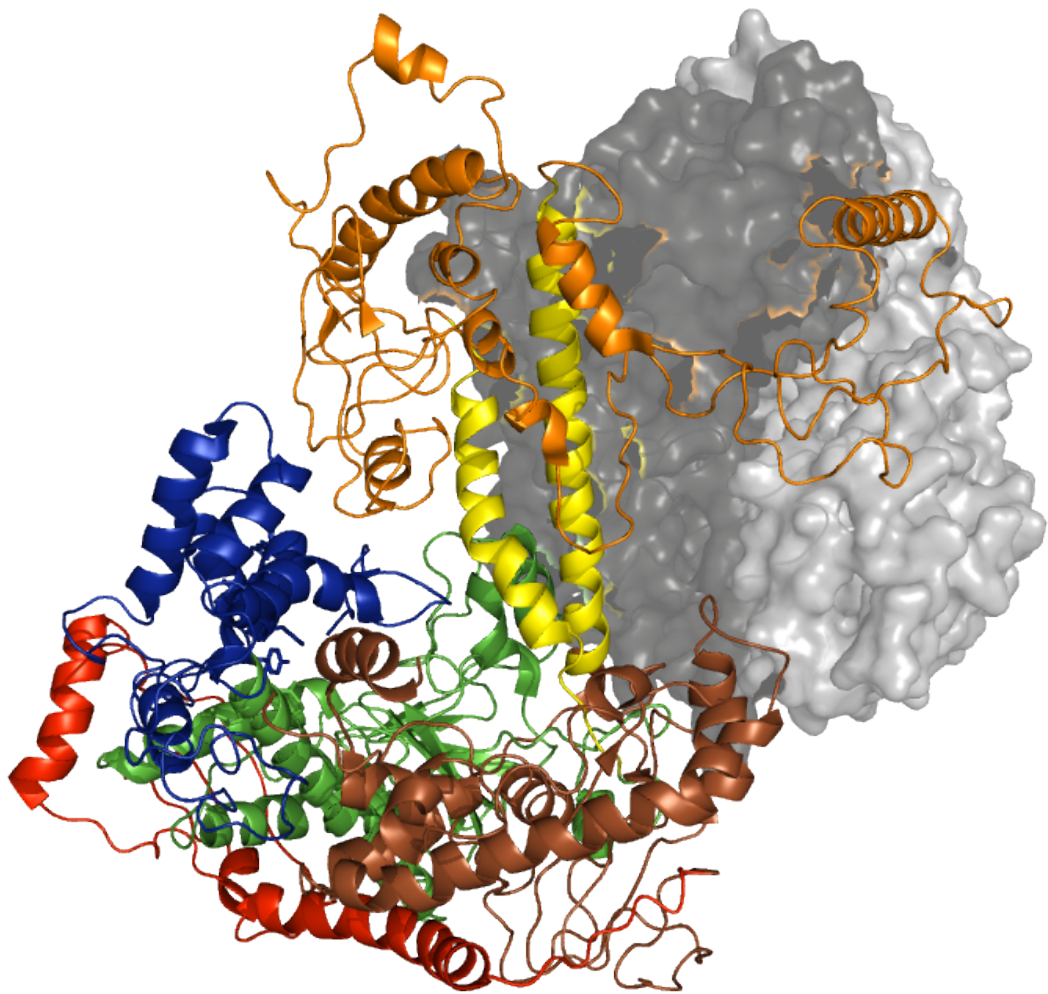


Figure 1.3 *The crystal structure of Pol γ (PDB:3IKM, (45))* The polymerase domain of the Pol γ A subunit shows the “right hand” configuration with the fingers subdomain (blue), palm subdomain (green), and thumb subdomain (yellow). The Pol γ A subunit also contains the N-terminal mitochondrial localization signal (MLS) (red) and exonuclease domain (brown). The spacer domain of Pol γ A is shown in orange with its accessory interacting subdomain (AID) contacting the proximal monomer of Pol γ B (dark gray surface). The distal monomer of Pol γ B is shown as the light gray surface.

Point mutations of Pol γ and their relation to disease

As described above, mutations in Pol γ A have been associated with several mitochondrial disorders including PEO, Alpers syndrome and SANDO. Below is a list of point mutations on Pol γ A that I have explored in this work and their relation to mitochondrial diseases. The locations of these residues near the polymerase active site are shown in Figure 1.4 on the structure of the homologous T7 DNA polymerase (47).

E895A. This residue is involved in the hydrogen-bonding network under the incoming nucleotide and is highly conserved in Pol γ across species and in family A DNA polymerases (45). Mutations at this position are rarely seen in the population with one case of myopathic myelodysplastic syndrome (MDS) where this position was mutated to a glycine (58).

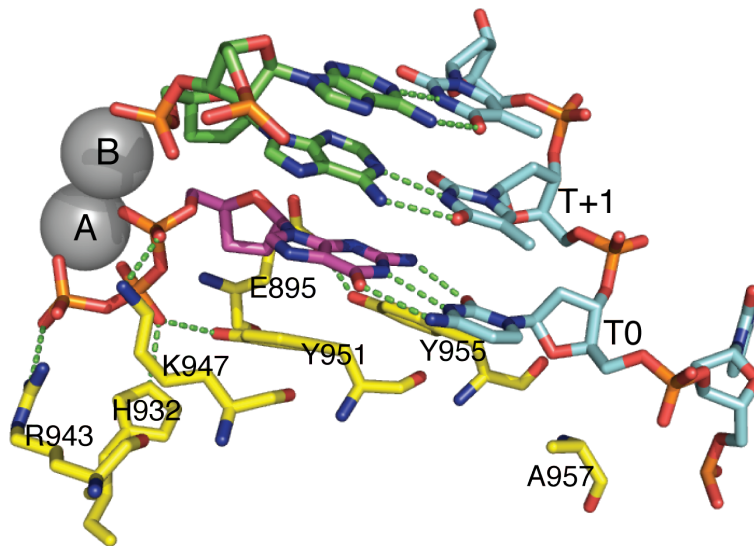


Figure 1.4 *Disease-associated residues near the polymerase active site.* The structure of T7 DNA polymerase (PDB: 1T7P, (47)) is used to model the locations of residues associated with mitochondrial diseases (yellow) that are found near the active site. The T7 structure contains the incoming dNTP (magenta) with the coordinating metal ions A and B, the primer strand (green) and the template strand (cyan). Numbering shows the homologous residues on Pol γ .

H932Y. Histidine at position 932 binds to the beta phosphate of the incoming nucleotide (45). Mutation to a tyrosine has been shown to be associated with autosomal recessive Progressive External Ophthalmoplegia (PEO) as well as Sensory Ataxic Neuropathy, Dysarthria, and Ophthalmoparesis (SANDO) (59-61).

R943H. Arginine 943 is expected to interact with the gamma phosphate of the incoming nucleotide and its mutation to a histidine has been associated with severe clinical phenotype in PEO and premature ovarian failure (34, 62, 63).

K947A. This mutation is not associated with any diseases however, K947R has been associated with PEO and ovarian failure in one case (64). Lysine 947 binds to the alpha phosphate of the incoming dNTP, and the K947A mutation was examined to determine the role of this interaction (45).

Y951F. This active site mutation has not been associated with any diseases. However the mutation Y951N has been seen in one case to be associated with peripheral neuropathy (61). Tyrosine 951 binds the ribose of the incoming nucleotide and is involved in the discrimination of dideoxy nucleotides (45). The Y951 at this position is responsible for the toxic side effects of dideoxy nucleotides in the mitochondria, which are incorporated more slowly by the Y951F mutant (65).

R953C. Arginine 953 is involved in the nucleotide binding pocket and has been associated with autosomal dominant PEO (35, 61, 66).

A957S. Alanine 957 appears to be part of the nucleotide binding pocket and the mutation to a serine has been associated with autosomal dominant PEO (62). In the clinical cases reported, of the six heterozygote individuals, five displayed a low penetrance of the disease with milder symptoms of PEO and a late-onset of the disease. One of the six heterozygote individuals displayed more aggressive PEO with a more

typical adult-onset of disease. Only one homozygote was reported and that patient was severely affected, showing a high amount of mtDNA deletions.

R1096C. This mutation is associated with PEO, Alpers syndrome, encephalopathy, SANDO and seizures (61, 67-73). The R1096 residue is located away from the active site in what is known as the partitioning loop between the palm and fingers subdomains of Pol γ (45). Clinically this mutation is seen as both a homozygote and as a compound heterozygote with other mutations. The age of onset of disease in patients with this mutation varies widely from <1 year to 55 years of age. In the four homozygote R1096C cases reported, all patients showed an onset of symptoms in age 2 or younger (61, 70) while the compound heterozygotes had a later age of onset of disease (61, 67-73).

Mitochondrial DNA SSB and helicase

In addition to Pol γ , the mtDNA replisome contains mtSSB, which is a non-catalytic protein that binds to single stranded DNA as a tetramer to prevent re-annealing and protect the ssDNA from damage by nucleases. More recently, it has been suggested that *E. coli* SSB may play a more complex role in replication, recombination and repair while interacting with at least 14 other proteins (74).

Ahead of Pol γ and mtSSB at the replication fork is the mtDNA helicase, which unwinds the downstream double stranded DNA to single stranded DNA in the 5' to 3' direction (75). The mtDNA helicase, which was discovered in a screen for mutations linked to autosomal dominant PEO, has structural similarity to phage T7 gp4 helicase/primase although no primase activity has been shown in human mtDNA helicase (31, 76). The mtDNA helicase monomer (72 kDa) binds to DNA in a hexameric form and unwinds dsDNA in a nucleotide-dependent manner.

Previous studies attempting to reconstitute the mtDNA replisome have failed to produce a quantitative analysis of helicase unwinding and polymerization at the replication fork. Rolling-circle replication assays (76, 77) that monitor polymerization by incorporation of radiolabeled dCTP into the growing primer strand show polymerization following helicase unwinding but only a small fraction, $\sim 0.1\%$, of the primers are extended. In published studies, the incorporation of the labeled dNTP into the growing strand amplified the signal to allow detection of very little product even though the results suggest that there is only a small fraction of active complexes. Also of questionable significance, dsDNA unwinding assays have shown helicase dependent strand displacement of 20 base pairs (bp) of duplex, while a similar assay extending the duplex to a length of 55 bp resulted in no strand displacement (77). It is questionable as to whether this assay provided a measure of true helicase unwinding activity, or simply strand displacement due to binding of the helicase to the branch strand and destabilizing the unstable 20bp duplex.

In order to successfully understand the mechanistic basis for disease arising to mutations in the replisome machinery, it is necessary to quantitatively reconstitute the replisome and understand the coordination between the helicase and the polymerase. This is necessary to accurately examine disease mutations in these enzymes that may affect the interactions of the proteins at the replication fork and reliable replication of mtDNA. For example, there are specific point mutations on Pol γ associated with Alpers syndrome, that have been hypothesized to be involved in contacts between the polymerase and other components of the replisome (78). Specifically, these mutations are on the surface of Pol γ and far away from the DNA binding site and active site. It is suggested that these surface mutations could be interfering with protein-protein interactions between the polymerase and SSB or the polymerase and the helicase. Understanding the relationship

between such biochemical changes in mutant enzymes and the clinical phenotypes that they are associated with will require rigorous analysis based on a more complete understanding of the mechanism of DNA replication by the mtDNA replisome.

Along with its association with heritable diseases, the mtDNA polymerase has been shown to be susceptible to inhibition by certain nucleoside reverse transcriptase inhibitors (NRTIs) that are used to target HIV (1, 2, 79). These NRTIs used in anti-HIV therapies are nucleoside analogs that cause chain termination and their incorporation by Pol γ leads to the cellular toxicity of these drugs. The work in The Johnson laboratory on HIV reverse transcriptase (HIV-RT) is complemented by work on Pol γ in order to advance our understanding of the molecular basis for the effectiveness for HIV-RT vs. the mitochondrial toxicity of an inhibitor. A greater understanding of these effects can be used in the rational design of antiviral agents that are more selective for HIV-RT.

1.3 HIV REVERSE TRANSCRIPTASE

HIV reverse transcriptase (HIV-RT) plays a key role in the HIV lifecycle by copying single stranded viral RNA into double stranded DNA before it can be integrated into the host genome. To accomplish this task HIV-RT has 3 enzymatic activities: RNA template-dependent DNA polymerization, DNA template-dependent DNA polymerization and RNase H activity. With this work, it is our goal to better understand the mechanism of RNA template-dependent DNA polymerization and its role in nucleotide selectivity for natural nucleotides versus nucleoside analogs (NRTIs). DNA polymerization on a DNA/RNA template has been shown to be faster and have a higher fidelity of replication than that of DNA/DNA templates (80) and studies presented here also show interesting differences in RNA-dependent DNA polymerization. These differences may contribute to mechanisms of nucleotide selectivity and resistance that

differ from those observed with DNA template-dependent DNA polymerization. It is therefore important to measure the effect of a DNA/RNA template on NRTI inhibition and resistance mechanisms. This work applies innovative pre-steady state kinetic methods to studies on RNA-dependent DNA polymerization to provide a more detailed explanation of the kinetics of nucleotide binding and incorporation based on pre-steady state rapid quench kinetic studies and stopped-flow fluorescence methods.

Replication of the HIV single-stranded RNA genome

To accomplish the conversion of single stranded viral RNA into linear double stranded DNA, HIV-RT catalyzes RNA- and DNA-dependent DNA polymerization and RNase H activities. The resulting double stranded viral DNA is then integrated into the host genome by the enzyme HIV integrase and the viral replication cycle can continue.

The process of reverse transcriptase activity was first discovered in 1970 by Baltimore and Temin and Mizutani (81, 82) who observed RNA-dependent DNA polymerization activity in retroviral particles. This process in HIV was described by Charneau et al. in 1994 (83) and the currently accepted mechanism for HIV viral replication is outlined in Figure 1.5 from a review by Gotte et al. (84). Viral RNA genome replication begins with priming of the (+) strand RNA genome by a host $tRNA_{Lys,3}$ at the primer binding site and RNA-dependent DNA polymerization from this primer by HIV-RT towards the 5' end of the viral RNA. HIV-RT also performs RNase H activity during this reverse transcription to digest the viral RNA and result in a single stranded (-) DNA product. This single stranded DNA is then involved in the first strand transfer reaction where it shifts to the 3' end of the viral RNA by hybridizing with the complementary R region. Following this strand transfer step, RNA-dependent DNA polymerization can continue and complete the synthesis of the (-) strand DNA. RNase H

digestion also continues, but certain segments of the viral (+) RNA are resistant to degradation and remain in duplex with the (-) strand DNA. These RNase H resistant regions are purine-rich and are termed polypurine tract regions (PPT). Synthesis of the (+) DNA strand uses these PPT regions as primers for DNA-dependent DNA polymerization by HIV-RT. This process proceeds to synthesize the (+) strand DNA from the templating (-) strand DNA until it passes the tRNA_{Lys,3} which is degraded by the RNaseH activity. Replication of and removal of the tRNA_{Lys,3} sequence provides a 3'-overhang of the (+) strand DNA that is complementary to the primer binding site and the DNA duplex circularizes in the second strand transfer step. This circularization allows for the final synthesis to be completed and the circular intermediate is subsequently resolved by either strand displacement by RT or repair and ligation to produce the linear duplex. This double stranded DNA duplex can then migrate into the nucleus of the host cell and be integrated in to the genome.

Clearly, HIV-RT plays a critical and essential role in the replication of the viral RNA genome therefore a detailed mechanistic understanding of its catalytic activities is necessary to aid our attempts to inhibit this enzyme in patients infected with HIV.

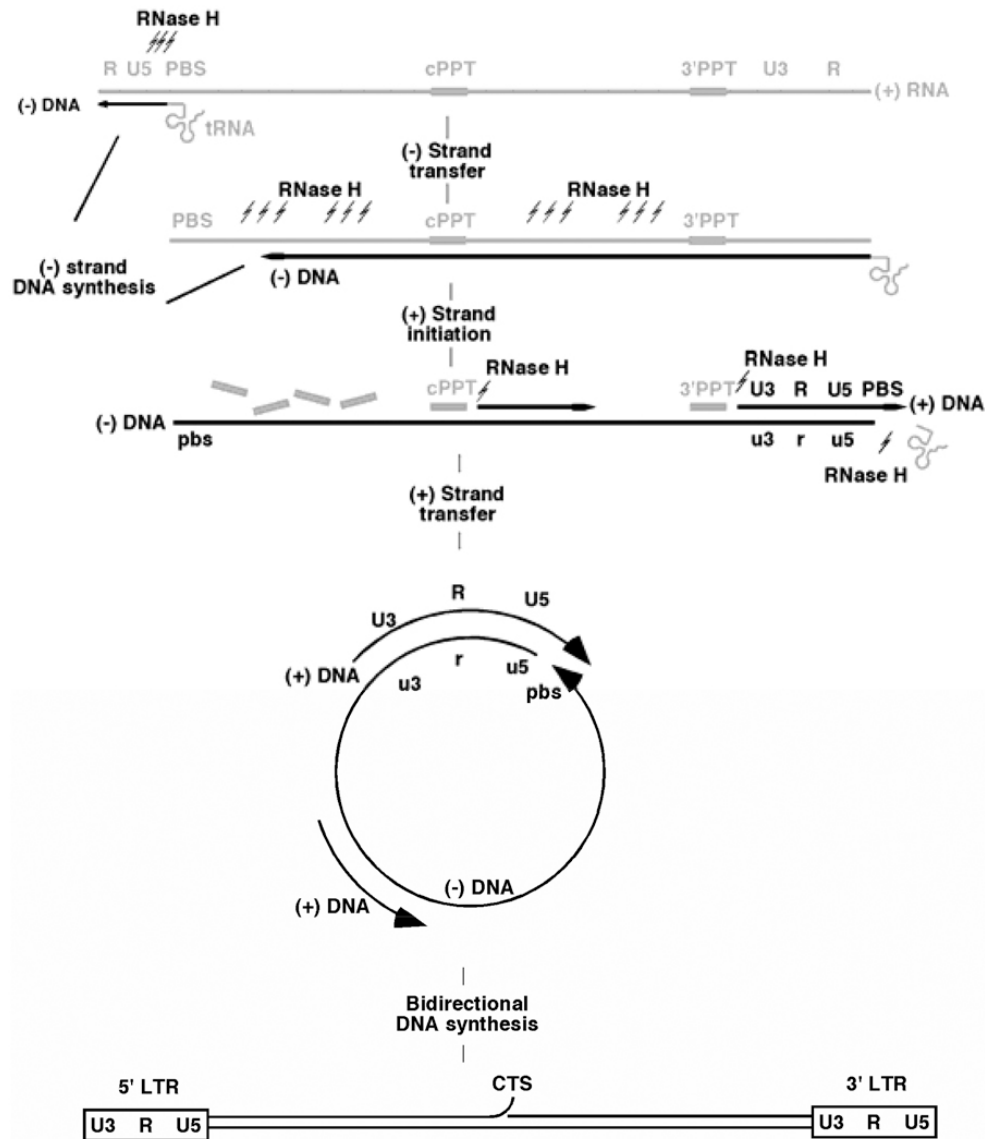


Figure 1.5 HIV Genome Replication. This figure, reproduced from (84), outlines the replication of the viral single stranded RNA genome to double stranded DNA before integration into the host genome. Synthesis of the (-) strand DNA by RT is initiated from the host tRNA_{Lys,3} and RNA-dependent DNA polymerization proceeds while RNase H activity is degrading segments of the (+) strand RNA between the polypurine tracts. Following a strand transfer, the newly synthesized single stranded (-) strand DNA is shifted to the 3'-end of the (+) strand RNA to complete (-) strand synthesis. Synthesis of the (+) strand is initiated from the polypurine tracts which act as primers for DNA-dependent DNA polymerization by RT through the tRNA primer. A second strand transfer event then leads to a circularization by annealing of the complementary primer binding site sequences and synthesis of the double stranded DNA is completed.

HIV reverse transcriptase structure

HIV-RT is a heterodimer of a 66 kDa subunit (p66) and a 51 kDa subunit (p51). The p66 subunit contains the enzymatic active sites for DNA polymerization and RNase H activity, while the smaller p51 subunit plays a structural role. p66 is separated into two domains, the polymerase domain and the RNase H domain. Within the polymerase domain there are four subdomains that resemble parts of a right hand: fingers, palm, thumb and connection (Figure 1.6). The palm subdomain contains the polymerase active site with three catalytic carboxylates, two of which are part of the highly conserved YXDD motif found in retroviral reverse transcriptases (85).

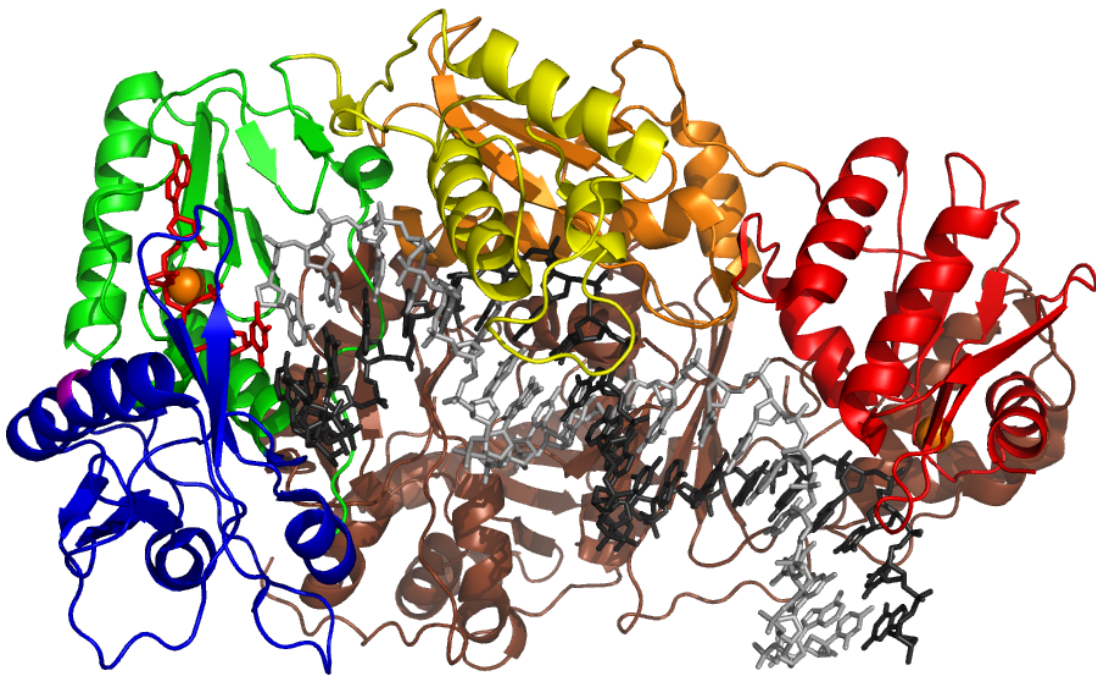


Figure 1.6 *Structure of HIV Reverse Transcriptase.* The structure of HIV-RT (PDB: 1RTD (86)) contains the p66 catalytic subunit which shows the “right hand” configuration containing the fingers subdomain (blue), palm subdomain (green), and thumb subdomain (yellow). The connection subdomain (orange) links the thumb subdomain with the RNaseH domain (red) of p66. The non-catalytic p51 accessory subunit is shown in brown. The crystal structure contains the duplex DNA showing the primer strand in light gray and the template strand in black.

HIV Reverse Transcriptase Inhibitors and resistance mutations

Due to its critical role in viral lifecycle, HIV-RT is a common target for anti-HIV therapies. The enzyme is targeted with nucleoside analog RT inhibitors (NRTIs) and non-nucleoside RT inhibitors (NNRTIs) (87, 88). NRTIs are nucleoside analogs lacking the 3'-OH and therefore act as substrates for the enzyme that cause chain termination (89). Alternatively, NNRTIs bind in a hydrophobic pocket near the polymerase active site and act as noncompetitive inhibitors that block chemistry (90, 91). Targeting HIV-RT with NRTIs inhibitors has been successful because RT is a low fidelity enzyme that will readily incorporate nucleotide analogues and lacks a proofreading exonuclease activity. However, because the enzyme is error prone and replicates so quickly, RT will evolve resistance to the inhibitors by increasing its discrimination against the nucleotide analogs. To try to combat the high rate of development of resistance in the clinic, it has been necessary to simultaneously attack the virus with multiple drugs, or a “drug cocktail”. In particular, highly active antiretroviral therapy (HAART), the current treatment method, combines at least three drugs to attempt to suppress viral replication and slow the rate of resistance (88). This method is effective at saving lives but it is important to note that it does not cure HIV infection and the therapy is a life-long treatment.

There are two known methods of discrimination against inhibitors employed by HIV-RT. The first is an exclusion mechanism where the resistance mutation causes increased discrimination for the drug reducing the rate of incorporation of the inhibitor (86, 92, 93). The second method is an excision mechanism. In this case the discrimination for the inhibitor is not increased, but instead the mutation(s) increase the rate of excision of the NRTI after it has been incorporated (94-97). This is the case with the TAMs (thymidine analog mutations) mutations that arise in from NRTI therapy and confer resistance to the thymidine analog AZT (3'-azido-3'-deoxythymidine). The TAMs

mutations increase the binding of ATP, which can be used as a pyrophosphate donor to excise the AZT and unblock the primer terminus in a reaction analogous to pyrophosphorolysis (96, 98, 99). A recent crystal structure of HIV-RT cross-linked to an AZT-terminated primer strand supports this hypothesis by suggesting that these mutations create an ATP binding site with high affinity (100). In Chapter 5, the kinetics of RNA-dependent DNA polymerization by HIV-RT were examined in order to better understand the mechanistic basis for the effectiveness of inhibitors and the evolution of resistance. By better understanding the mechanism of HIV-RT polymerization and development of resistance to NRTIs, we can possibly develop drugs that are more effective in blocking replication of the virus.

Chapter 2: Characterization of Mitochondrial DNA Polymerase Gamma Disease Mutations

2.1 INTRODUCTION

Mutations in the nuclearly-encoded mitochondrial DNA polymerase (Pol γ) lead to a wide range of mitochondrial disorders, including progressive external ophthalmoplegia (PEO), Alpers syndrome, Parkinsonism, male infertility, and sensory ataxic neuropathy, dysarthria and ophthalmoparesis (SANDO) (5, 6, 12, 101). Mutations lead to diseases of widely varying severity and age of onset with more severe symptoms occurring with the earliest ages. The reported clinical data for mutations in *POLG* have been compiled in The Human DNA Polymerase Gamma Mutation database (13) with a list of more than 200 mutations. Two recent reports from the Kaguni Lab have attempted to organize 136 of these pathogenic mutations into five functional clusters based upon structural analysis of Pol γ A and previously published biochemical data on these mutants (Figure 2.1) (78, 102). However, both the clinical data and biochemical data are not sufficient to have full confidence in these general clusters of mutations, but it is an important theory to consider when studying these mutations. Five of the six mutations studied in this chapter are predicted by Kaguni's analysis to belong in Cluster 1 and one mutation studied here was classified into Cluster 3. Cluster 1 mutations are located in the N-terminal domain (NTD), Exo and Pol domains and are predicted to be associated with a severe phenotype due to a reduction in polymerase activity. Mutations classified into Cluster 1 are also predicted to be dominant due to their ability to compete with wild-type Pol γ for dNTP binding but are not efficient at polymerization. Cluster 3 residues are

¹ Parts of this chapter were adapted from published paper under maiden name of J.L. McKenzie: Batabyal, D., McKenzie, J. L., and Johnson, K. A. (2010) Role of histidine 932 of the human mitochondrial DNA polymerase in nucleotide discrimination and inherited disease, *J Biol Chem* 285, 34191-34201. D.B. and J.L.M designed experiments, collected data and analyzed data. K.A.J. supervised the project.

located on the partitioning loop between the polymerase and exonuclease domains and are thought to contribute critical functions and therefore mutations are associated with a severe disease phenotype. This chapter will report the biochemical characterization of six disease mutations of Pol γ . In some cases, *in vitro* steady state assays have been reported but the results of these simple screens are often inconsistent (57, 103). Steady state kinetic analysis of polymerases often greatly underestimates the effect of a mutation because the slow rate of DNA release limits the steady state rate. This rate limiting DNA release can mask a significant effect on the rate of chemistry for a given mutation. It is therefore important to characterize these mutations in Pol γ under pre-steady state conditions. Below I will summarize several mutations selected for detailed study.

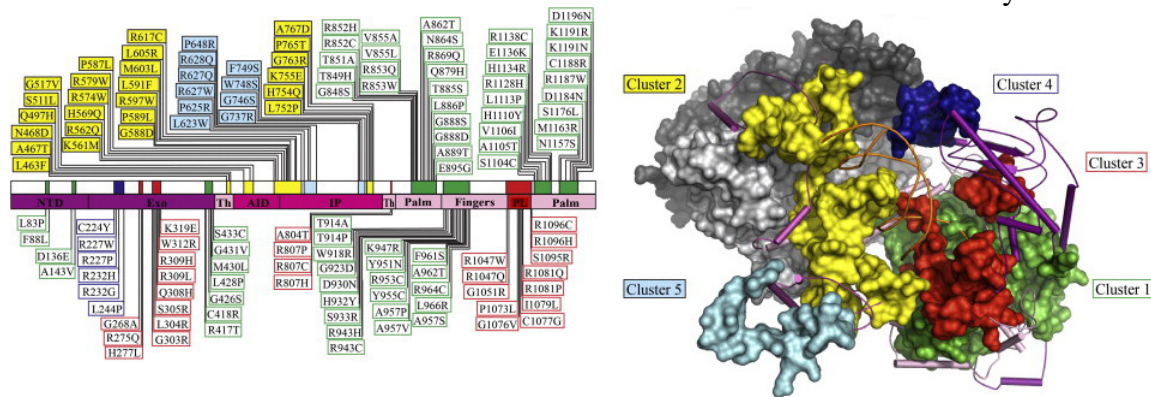


Figure 2.1 Clustering of POLG disease mutations. This figure from Farnum et al (102) displays 136 pathogenic mutations on the gene for Pol γ A and the location of the 5 clusters that these mutations are assigned to on the protein structure. Mutations are colored according to the cluster they have been assigned to.

H932Y/A. Histidine at position 932 binds to the beta phosphate of the incoming nucleotide (45) and its mutation to a tyrosine has been shown to be associated with autosomal recessive Progressive External Ophthalmoplegia (PEO) as well as Sensory Ataxic Neuropathy, Dysarthria, and Ophthalmoparesis (SANDO) (59-61). A preliminary

steady state analysis has been performed on the H932Y mutant of Pol γ suggesting a 200-fold decrease in nucleotide binding affinity and only a mild decrease in catalysis compared to wild-type (104). However, these steady state assays did not fully evaluate the role of the histidine residue at position 932 in nucleotide selectivity. Additionally, work in this same study on the homologous yeast mitochondrial polymerase, Mip1, containing the homologous mutation (H734Y) showed an increase in petite frequency suggesting defects in mitochondrial DNA replication.

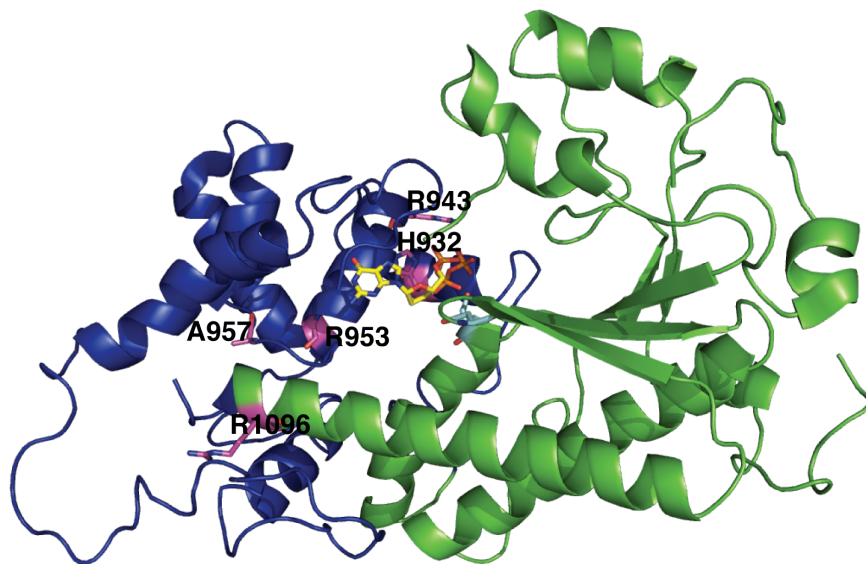


Figure 2.2 Location of disease mutations on Pol γ A. The crystal structure of Pol γ A (PDB: 3IKM (45)) is labeled to illustrate the location of the disease mutations studied in this chapter. The mutations (magenta) are located on the fingers (blue) and palm (green) subdomains near the active site. The two catalytic aspartic acids D890 and D1135 are shown in cyan on the palm subdomain. The structure for the incoming nucleotide bound at the active site is modeled based on alignment of the active site with the homologous T7 DNA polymerase (PDB: 1T7P (47)).

R943H. Arginine 943 interacts with the gamma phosphate of the incoming nucleotide and its mutation to a histidine has been associated with severe clinical phenotype in autosomal dominant PEO and premature ovarian failure (34, 62, 63). In

three clinical cases of patients with PEO harboring this mutation, two homozygous patients were age 30 and one heterozygous patient was 63 when the severe PEO symptoms developed. Preliminary steady state measurements have been made on the R943H mutant of Pol γ *in vitro* indicating in a 475-fold decrease in k_{cat}/K_m coming largely from the 83-fold increase in K_m (105).

R953C. R953 is involved in the nucleotide binding pocket and the mutation to cysteine has been associated with PEO (35, 61, 66). There have been four clinical cases of this mutation being associated with PEO where the patients were homozygous for R953C and all presented symptoms around age 20. The two other cases of this mutation were seen as compound heterozygotes with symptoms presenting at age 22 and 51.

A957S. This residue appears to be part of the nucleotide binding pocket and the mutation to a serine has been associated with autosomal dominant PEO (62) In the clinical cases reported, of the six heterozygote individuals, five displayed a low penetrance of the disease with milder symptoms of PEO and a late-onset of the disease. One of the six heterozygote individuals displayed more aggressive PEO with a more typical adult-onset of the disease. Only one homozygote was reported and that patient was severely affected, showing a high amount of mtDNA deletions. Biochemical assays measuring the steady state kinetics of this mutant *in vitro* described only a 4-fold decrease in k_{cat}/K_m (105). A more recent report (106), also suggests a mild effect of this mutation with a 1.7-fold decrease in k_{cat}/K_m compared to wild-type.

R1096C. This mutation is associated with PEO, Alpers syndrome, cerebellar ataxia and sensory neuropathy (61, 67-73). The R1096 residue is located away from the active site in what is described as the partitioning loop between the palm and fingers subdomains of Pol γ (45). Clinically this mutation is seen as both a homozygote and as a compound heterozygote with other mutations. The age of onset of disease in patients with

this mutation varies widely from <1 year to 55 years of age. In the four homozygous R1096C cases reported, all patients showed an onset of symptoms at age 2 or younger (61, 70). The compound heterozygotes had a later age of onset of disease (61, 67-73).

This chapter will characterize the six mutations of Pol γ listed above that have been associated with human mitochondrial disorders. The goal of this work is to analyze the biochemical effect of these point mutations in order to gain a better understanding of the observed clinical phenotypes in order to make progress towards establishing a molecular basis for mitochondrial diseases.

The work in this chapter on wild-type, H932Y and H932A Pol γ has been published in The Journal of Biological Chemistry in October 2010 (55). This work has been adapted for this dissertation.

2.2 MATERIALS AND METHODS

Site directed mutagenesis of Pol γ A

For this section of work, the clone of Pol γ A in the pUC19.1 was constructed to delete the first 66 amino acids from the N-terminus. This Δ 66 deletion, removes the mitochondrial localization sequence as well a polyglutamine tract of unknown function. The clone also contained the two mutations, D198A and E200A, in the exonuclease domain that render the enzyme exonuclease deficient (exo-) for use in nucleotide misincorporation assays (107). Site-directed mutagenesis was performed using the PCR mutagenic primers shown in Table 2.1 to make the H932Y, H932A, R943H, R953C, A957S, and R1096C mutants in the Δ 66 Pol γ A exo- background. All sequences were confirmed by sequencing the Pol γ A gene in the pUC19.1 plasmid using the sequencing primers listed in Table 2.2.

Table 2.1. *Mutagenic primers for Pol γ A Disease Mutants*

H932A

Forward: 5' -CGTGGCACCGACCTGGCTAGCAAAAACCGCAAC-3'

Reverse: 5' -GTTGCGGTTTTGCTAGCCAGGTCGGTGCCACG-3'

H932Y

Forward: 5' -CGTGGCACCGACCTGTATAGCAAAAACCGCAA-3'

Reverse: 5' -TTGCGGTTTTGCTATACAGGTCGGTGCCACG-3'

R943H

Forward: 5' -CGACTGTGGGCATTTTCGCATGAACATGCAAAGATTTT-3'

Reverse: 5' -AAAATCTTTGCATGTTCATGCGAAATGCCACAGTCG-3'

R953C

Forward: 5' -CAAAGATTTTCAATTACGGTTGTATTTACGGCGCAGGTCAG-3'

Reverse: 5' -CTGACCTGCGCCGTAAATACAACCGTAATTGAAAATCTTTG-3'

A957S

Forward: 5' -GGTCGTATTTACGGCTCAGGTCAGCCGTTTCG-3'

Reverse: 5' -CGAACGGCTGACCTGAGCCGTAAATACGACC-3'

R1096C

Forward: 5' -GAGTTCATGACCAGCTGTGTCAACTGGGTTCG-3'

Reverse: 5' -CGACCCAGTTGACACAGCTGGTCATGAACTC-3'

*mutated codons are underlined

Table 2.2. *Sequencing primers for Pol γ A*

Seq Primer 1	5' -GTAAGCGGATGCCGGGAGCAGACAA-3'
Seq Primer 2	5' -GTTCCGGTGGCGATCCCAGAGGAA-3'
Seq Primer 3	5' -AACCCACGAGGTGTTCCAGCAGCAA-3'
Seq Primer 4	5' -CGCGATAACCTGGCGAAACTGCCAA-3'
Seq Primer 5	5' -CCATTACGCGCCGTGCAGTTGAA-3'
Seq Primer 6	5' -GTGGCACGGAGAGCGAGATGTTTAACAA-3'

Baculovirus expression of Pol γ A

The recombinant Pol γ A clones were inserted into the pBacPAK9 transfer vector of the BacPAK Baculovirus Expression System (Clontech) by restriction digest of the pUC19.1 vector at the BglII and NotI (NEB) sites and subsequent ligation with the digested pBacPAK9. Recombinant virus was then generated by co-transfecting the pBacPAK9 containing the Pol γ A gene and the Bsu36I-digested BacPAK6 viral DNA. The homologous recombination event was performed in *Spodoptera frugiperda* SF9 cells and resulted in a recombinant baculovirus that expresses Pol γ A. SF9 cells were maintained in Sf-900 II SFM media (Gibco) supplemented with 10% v/v Fetal Bovine Serum (Gibco), 100 units/ml Penicillin (Sigma-Aldrich), and 100 μ g/ml Streptomycin (Sigma-Aldrich). After performing the co-transfection, viral plaque assays were performed to obtain individual viral plaques, which were then amplified to high viral titers. Expression of Pol γ A in SF9 cells was confirmed on 6-well tissue culture plates and analyzed by SDS-PAGE (Figure 2.3) before expression was scaled up.

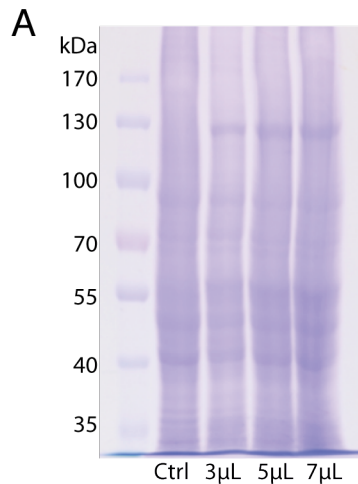


Figure 2.3 *Baculovirus expression of Pol γ A in SF9 cells.*

Coomassie blue stained SDS-PAGE of lysed SF9 cells expressing Pol γ A (140 kDa) for 3 days post infection with amplified virus stock. Control lane (Ctrl) contains sample from uninfected SF9 cells and subsequent lanes were loaded with increasing volumes of sample (3-7 μ L) from cells infected with baculovirus.

For large-scale expression, a monolayer of cells in a 150-cm² flask was infected with the amplified virus stock at a multiplicity of infection greater than 10. After 72 hours of infection, cells were removed from the 150-cm² flask and added to a suspension culture

containing log-phase cells at a concentration of 1×10^6 cells/ml. The infected suspension was then incubated at 27°C for 72 hours before harvesting by centrifugation at 1,500xg for 20 minutes at 4°C. The cell pellet was then flash frozen in liquid nitrogen and stored at -80°C until purification.

Purification of Pol γ A

Cell pellets from baculovirus expression of Pol γ A in SF9 cells were thawed and resuspended in *Pol γ A Lysis Buffer* (0.32 M sucrose, 10 mM HEPES pH 7.5, 0.5% v/v NP-40, 3 mM CaCl₂, 2 mM MgAc.4H₂O, 0.1 mM EDTA, 5mM 2-mercaptoethanol and protease inhibitor cocktail V, EDTA-free (AG Scientific)) by stirring on ice for 1 hour. The suspension was then centrifuged using a JS4.3 rotor (Beckman) at 1,500xg for 25 minutes. A 3M KCl solution was then added dropwise to the supernatant to obtain a final concentration of 0.5 M KCl. After stirring for 15 minutes on ice in the presence of 0.5 M KCl, the solution was ultracentrifuged at 31,000 rpm for 35 minutes. The supernatant was then incubated with Ni-NTA agarose resin (Qiagen) by stirring on ice at 4°C for 30 minutes. The nickel resin was equilibrated in *Pol γ A Nickel Equilibration Buffer* (20 mM HEPES pH 7.5, 5 mM imidazole pH 8, 0.2 M KCl, 5% glycerol). After binding to the Ni-NTA, the resin was washed with *Pol γ A Nickel Wash Buffer* (20 mM HEPES pH 7.5, 20 mM imidazole pH 8, 0.1 M KCl, 5% glycerol). Pol γ A was then eluted with *Pol γ A Nickel Elution Buffer* (20 mM HEPES pH 7.5, 200 mM imidazole pH 8, 0.05 M KCl, 5% glycerol) while collecting fractions. Fractions were analyzed by SDS-PAGE (Figure 2.4) and those containing Pol γ A were pooled and diluted to 30 mM KCl with *Pol γ A Nickel Dilution Buffer* (20 mM HEPES pH 7.5, 1 mM EDTA pH 8, 5% glycerol).

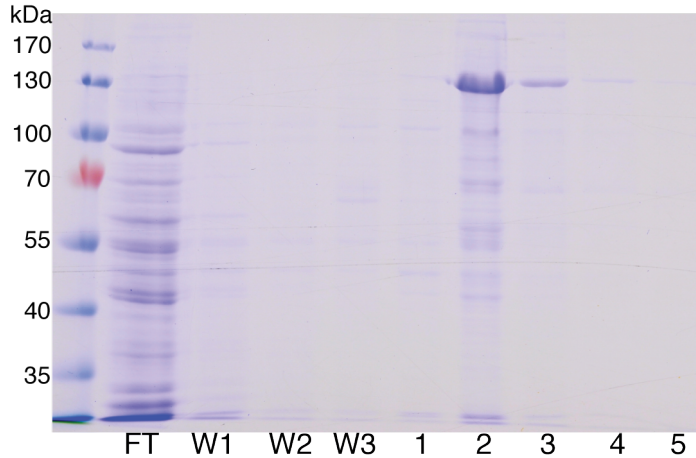


Figure 2.4 Nickel-NTA column purification of *Pol γA*. SDS-PAGE analysis of the flow-through (FT), washes (W1, W2, W3) and fractions from nickel-NTA column show *Pol γA* is present in fractions 2 and 3.

The fractions from the nickel column were then pumped at 1 mL/minute onto an SP Sepharose column (GE Healthcare) equilibrated in *Pol γA SP Buffer A* (20 mM HEPES pH 7.5, 30 mM KCl, 1 mM EDTA pH 8, 5 mM 2-mercaptoethanol, 5% glycerol) using the AKTA Purifier (GE Healthcare). After loading, the column was then washed with *Pol γA SP Buffer A* for 5 column volumes. The protein was eluted from the SP column with a linear gradient from 0-70% *Pol γA SP Buffer B* (20 mM HEPES pH 7.5, 700 mM KCl, 1 mM EDTA pH 8, 5 mM 2-mercaptoethanol, 5% glycerol) at 1 mL/minute over 8.5 column volumes. 1 mL fractions were collected from SP column and the absorbance at 280 nm and 260 nm was recorded. The fractions were then analyzed by SDS-PAGE (Figure 2.5) and those containing *Pol γA* were pooled and concentrated using a vivaspin sample concentrator (GE Life Sciences). The protein concentration was then measured by A_{280} using the extinction coefficient $\epsilon_{280} = 243,7900 \text{ M}^{-1}\text{cm}^{-1}$, previously determined (108). Experiments were all performed on the reconstituted holo-enzyme (*Pol*

γ) by combining the catalytic subunit Pol γ A and the accessory subunit Pol γ B with a 4:1 molar excess of Pol γ B:Pol γ A.

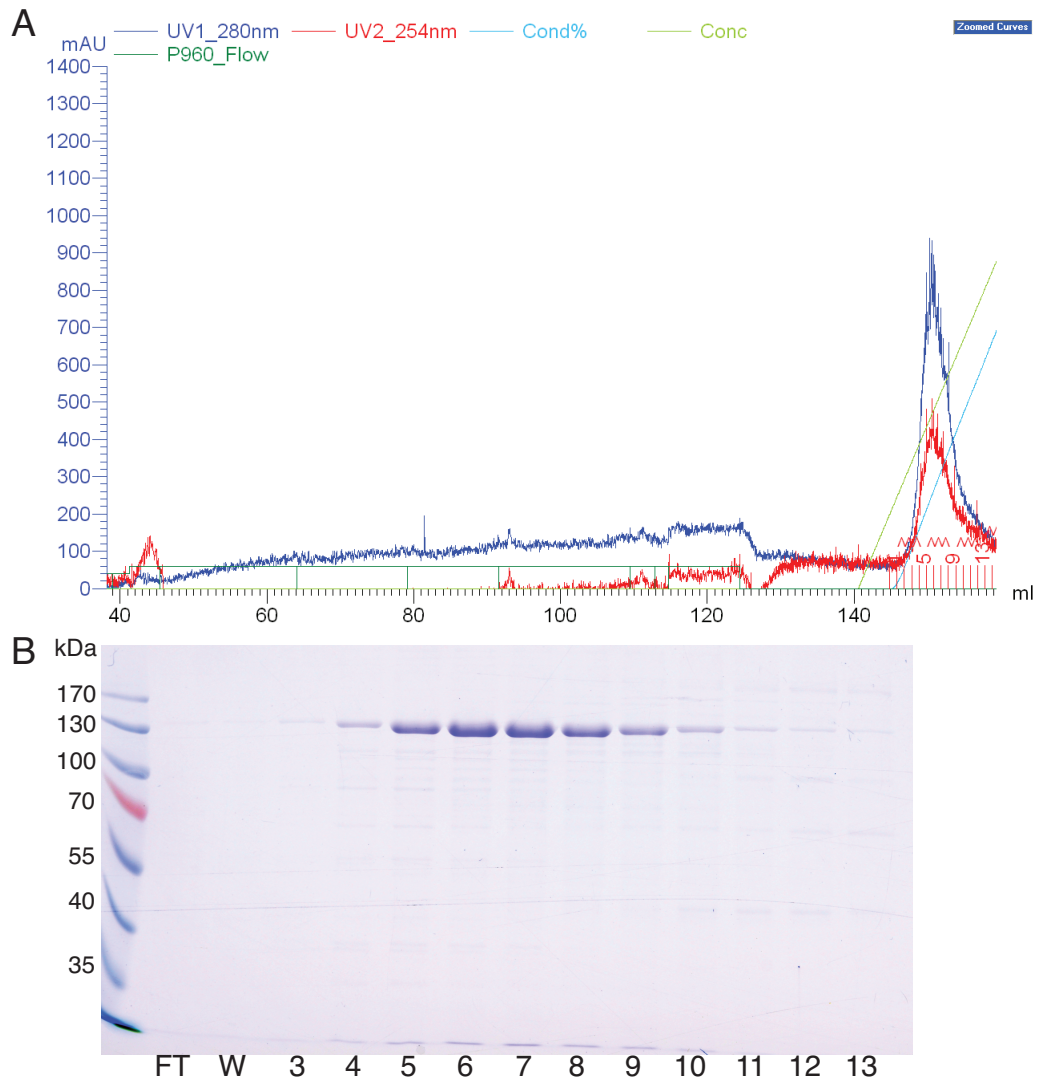


Figure 2.5 *SP sepharose column purification of Pol γ A.* (A) SP sepharose column chromatography of Pol γ A from pooled Nickel-NTA fractions. Absorbance at 280 nm (blue) and 254 nm (red) were monitored to detect protein and DNA respectively. After loading onto the SP column, Pol γ A was eluted from the column with a linear gradient from 0-70% *Pol γ A SP Buffer B* and conductivity percentage was monitored (light blue). (B) SDS-PAGE analysis of the flow-through (FT), wash (W) and fractions 3-13 confirm the presence of Pol γ A in fractions 4-10.

Cloning, expression and purification of Pol γ B

The accessory subunit, Pol γ B, used in these studies has the first 25 amino acids truncated from the N-terminal end and is modified at the C-terminus to have a His tag added for purification. The gene sequence was cloned into pET43.1a vector and transformed in *E. coli* Rosetta (DE3) (Novagen). A 250 ml starter culture of LB medium containing 50 μ g/ml ampicillin and 34 μ g/ml chloramphenicol was inoculated with a single colony transformant with the vector containing Pol γ B. The starter culture was grown at 37°C with shaking at 150 rpm overnight. After overnight incubation, the starter culture was used to inoculate a large-scale 1L LB medium culture to OD₆₀₀ of 0.1, which was incubated at 37°C with shaking at 100 rpm. Once the optical density at 600 nm reached 0.6, the protein expression was induced by the addition of 1mM isopropyl- β -D-thiogalactopyranoside (IPTG) and expression continued at 25°C for 6 hours. Cells were then harvested by centrifugation at 3,500 rpm and 4°C using a Beckman JLA8.1 rotor and subsequently frozen at -80°C. Protein purification was performed as described previously (55, 109). The thawed cell pellet was resuspended in *Pol γ B Lysis Buffer* (20 mM Tris-HCl pH 8.0, 500 mM NaCl, 50 mM imidazole, 0.1% Triton X-100, protease inhibitors (Roche)) and incubated with lysozyme (0.3 mg/ml) for 15 minutes on ice while stirring. The suspension was then sonicated for 20 minutes on ice. The resulting cell lysate was centrifuged at 15,000 rpm for 20 minutes in a Beckman 45Ti rotor to remove the debris. A 10% Polyethyleneimine (PEI) solution was added dropwise to the supernatant to a final concentration of 0.1% followed by ultracentrifugation at 40,000 rpm for 30 minutes in a Beckman 45Ti rotor. The supernatant was stirred for 30 minutes on ice with 5 mL Ni-NTA resin (Qiagen) equilibrated in *Pol γ B Binding Buffer* (20 mM Tris-HCl pH 8, 500 mM NaCl, 50 mM imidazole pH 8). The protein was then eluted in 6 mL fractions with *Pol γ B Nickel Elution Buffer* (20 mM Tris-HCl pH 8, 500 mM NaCl,

250 mM imidazole pH 8). SDS-PAGE analysis of fractions was performed and fractions containing Pol γ B were pooled, concentrated by centrifugation and injected onto a S200 Superdex gel filtration column (Amersham Biosciences) equilibrated in *Pol γ B S200 Buffer* (20 mM Tris-HCl pH 8, 500 mM NaCl). Fractions from the gel filtration column were analyzed by SDS-PAGE and pooled before dialysis into storage buffer containing 50 mM Tris-HCl pH 8, 100 mM NaCl, 1 mM dithiothreitol (DTT), 2.5 mM EDTA, 50% glycerol. Protein concentration was determined by A_{280} using the extinction coefficient, $\epsilon_{280} = 71,940 \text{ M}^{-1}\text{cm}^{-1}$ (108). Aliquots of the protein were flash frozen in liquid nitrogen and stored at -80°C .

Preparation of substrate DNA

The DNA substrates used in these studies were purchased as DNA oligomers from Integrated DNA Technologies (IDT) and purified by 15% denaturing polyacrylamide gel electrophoresis. Sequences of all substrate DNA oligomers are listed in Table 2.3. The primer oligonucleotide used was 25 nucleotides (25-mer) and the template strand was 45 nucleotides (45-mer). These sequences were selected for consistency with previous studies from our lab (49, 56).

For quench flow assays, the 5' end of the primer oligomer was ^{32}P -labeled using T4 polynucleotide kinase (New England Biolabs) and $\gamma\text{-}^{32}\text{P}\text{-ATP}$ according to the manufacturers protocol. After ^{32}P labeling, the reaction was heated to 95°C for 5 minutes and the labeled DNA was purified using a Bio-Spin P-6 gel column (Bio-Rad) to remove the excess $\gamma\text{-}^{32}\text{P}\text{-ATP}$. The concentration of the purified $^{32}\text{P}\text{-5}'$ -labeled primer was determined by TLC.

Duplex DNA substrates were formed by incubating the 25-mer primer with the 45-mer template at a 1:1 molar ratio in an *Annealing Buffer* (10 mM Tris-HCl pH 7.5, 50

mM NaCl, 1 mM EDTA) and heating to 95°C for 5 minutes before allowing to slowly cool to room temperature.

Table 2.3 DNA primer-template sequences for Pol γ

<u>25/45mer</u>	
25-mer	5' -GCCTCGCAGCCGTCCAACCAACTCA
45-mer	3' -CGGAGCGTCGGCAGGTTGGTTGAGTTGGAGCTAGGTTACGGCAGG

Correct nucleotide incorporation assays

Chemical quench flow experiments measuring single nucleotide incorporation assays were performed at 37 °C in a *Pol γ Reaction Buffer* containing 50 mM Tris-HCl (pH 7.5), 100 mM NaCl, 12.5 mM MgCl₂ with a RQF-3 rapid-quench-flow apparatus (KinTek Corp). All experiments measuring incorporation of the correct nucleotide (dATP) used the 5'-³²P-labeled 25/45mer primer-template duplex sequence listed in Table 2.3. The incorporation of dATP was measured by rapidly mixing a preformed enzyme-DNA complex (150 nM Pol γ A, 600 nM Pol γ B, 75 nM 5'-³²P-labeled 25/45mer DNA) with an equal volume of Mg-dATP²⁻ at various concentrations (0.2, 0.5, 1.5, 3, 5.5, and 8.5 μ M dATP for wild-type). The final concentration of MgCl₂ was 12.5 mM. The reactions were quenched by mixing with 0.5 M EDTA after various time intervals (0-1 second for wild-type). All concentrations listed are final (after mixing to start the reaction).

After quenching, the reactions were mixed with denaturing PAGE loading dye (0.25% bromophenol blue, 0.25% xylene cyanol) and separated on a 15% denaturing polyacrylamide sequencing gel. After drying the gel was exposed to a storage phosphor

screen and the bands were quantified using a Typhoon scanner (GE) and ImageQuant 5.0 (Molecular Dynamics). The concentration of the product formed over time was calculated as the product of the concentration of substrate ^{32}P -labeled DNA added times the fraction of material in the 26-mer band. Data collected were fit by global data fitting methods described below.

Nucleotide misincorporation assays

Misincorporation assays were performed in a similar assay as described above for correct dNTP incorporation; however, the formation of a mismatch often required longer time scales and higher concentrations of the incorrect dNTP. For time scales greater than 5 seconds, manual hand mixing was done instead of using the rapid-quench-flow instrument. In all assays, a maximum of 5 mM dNTP (final concentration after mixing) was not exceeded in order to avoid complications due to nonspecific inhibition (*II*, *III*). For misincorporation experiments a preformed enzyme-DNA complex (150 nM Pol γA , 600 nM Pol γB , 75 nM $5'$ - ^{32}P -labeled 25/45mer DNA) with an equal volume of Mg-dNTP $^{2-}$ at various concentrations (0.2, 0.5, 1.5, 3, 5.5, and 8.5 μM dATP for wild-type) in *Pol γ Reaction Buffer*. When noted, misincorporation was monitored in the presence of pyrophosphate (PPi) by including 0-50 μM NaPPi in the Mg-dNTP $^{2-}$ mix. After various time intervals from (0 – 1.5 hours, in some cases) the reactions were quenched with 0.5 M EDTA and the products were analyzed on a 15% denaturing polyacrylamide sequencing gel. When multiple misincorporation events occurred the product was calculated as the sum of all the bands above 25-mer divided by the total of bands including 25-mer. Data collected were fit by global data fitting methods described below.

Active site titration with DNA

Chemical quench assays measuring the K_d for DNA-binding were performed by preforming an enzyme-DNA complex with a fixed concentration of Pol γ and increasing concentrations of 5'- ^{32}P -labeled 25/45mer DNA (100 nM Pol γA , 400 nM Pol γB , 10-700 nM 5'- ^{32}P -labeled 25/45mer DNA). These were allowed to pre-equilibrate on ice for 10 minutes, then warmed to 37°C and reacted with an equal volume of 250 μM dATP in *Pol γ Reaction Buffer* + 12.5 mM MgCl_2 at 37°C for 0.15 seconds. The reactions were quenched with 0.5 M EDTA and the products were analyzed on a 15% denaturing polyacrylamide sequencing gel. The amount of 26-mer product formed after 0.15 seconds was calculated as the product of the concentration of substrate ^{32}P -labeled DNA added times the fraction of material in the 26-mer band. The 26-mer product was plotted as a function of 5'- ^{32}P -labeled 25/45mer DNA substrate concentration ($[\text{DNA}]$) and the data were fitted to a quadratic equation (Equation 2.1) to define the concentration of enzyme (E_0) and the K_d for DNA using non-linear regression (GraFit5, Erithacus).

Equation 2.1

$$[E \cdot \text{DNA}] = \frac{(E_0 + D_0 + K_d) - \sqrt{(E_0 + D_0 + K_d)^2 - 4E_0D_0}}{2}$$

Global data fitting

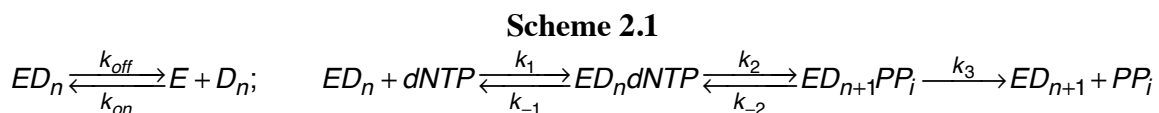
The Global data fitting throughout this work was performed using the KinTek Explorer simulation software (KinTek Corp). This program allows the data to be fit to a hypothesized model based on numerical integration of the rate equations with no simplifying assumptions (112). The process of global data fitting involves inputting the reaction model, the experimental concentrations of enzyme and substrates, scaling factors appropriate for each experimental observable, and estimates of rates for the reaction

steps. The KinTek Explorer program then allows for a refinement and a final convergence to the best-fit value for each parameter using nonlinear regression based on numerical integration of the rate equations. In this process, data are fit directly to the model so that both the rates and amplitude information are included in the fit. This eliminates any simplifying assumptions as are typically required to derive equations in conventional data fitting. Additionally, multiple experiments are simultaneously fit to the same set of rate constants for a given model. This ensures that the proposed model accounts for all of the data sets obtained. Error analysis by the program is comprehensive, in that it gives the standard error values for each parameter, as well as a confidence contour analysis. This pairwise error analysis method examines the dependence of χ^2 on a pair of parameters to create a 3D confidence contour that shows the relationship between parameters and to outline the level to which parameters are constrained by the data (112, 113). This allows for a reliable estimate of errors of fitted parameters and determines how well constrained the parameters are by the data. The data in this chapter were fit to either Scheme 2.1 or Scheme 2.2 as indicated. In these fits, the previously determined rates of DNA binding and release were used in the model ($K_{d,DNA}=10$ nM, $k_{off,DNA} = 0.02$ s⁻¹ (114). Additionally, the equilibrium constant for the initial complex formation was estimated by assuming diffusion-limited nucleotide binding ($k_1=100$ μ M⁻¹s⁻¹) and allowing the dissociation rate to vary during fitting. During global fitting of data within a concentration series, a small background correction (less than 10% of the signal) was applied to individual traces based upon optimal fitting the data to the model. The parameters in the data tables are presented as the best fit values, standard error values, as well as the upper and lower limits for each parameter as determined by the confidence contour analysis. These upper and lower limits are derived from a χ^2 threshold limit of 10%, or $\text{Chi}^2_{\text{min}}/\text{Chi}^2_{x,y} = 1.1$.

2.3 RESULTS

Kinetics of correct incorporation

The kinetics of incorporation of the correct nucleotide (dATP) were explored using rapid quench flow methods to measure the apparent nucleotide dissociation constant ($K_{d,app}$) and the maximum rate of incorporation (k_{pol}) by the wild-type enzyme as well as the six mutants. For these single turnover assays an enzyme-DNA (25/45mer) complex was formed and subsequently mixed with various concentrations of the correct nucleotide, Mg-dATP²⁻, for various time intervals and quenched with 500 mM EDTA. The formation of 26-mer product over time at various nucleotide concentrations was then fit by simulation using the KinTek Global Explorer Program. The expanded model for DNA polymerization is described in Scheme 2.1.

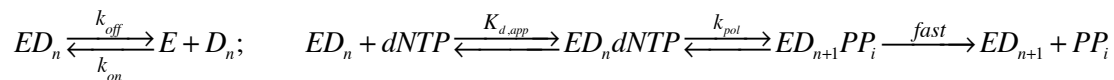


In this scheme the ground state binding of nucleotide to the enzyme-DNA complex (ED_n) is in a rapid equilibrium ($K_1=k_1/k_{-1}$) and is followed by the chemistry step k_2 . After chemistry, the pyrophosphate release and translocation steps occur to allow binding of the next nucleotide. In these experiments, the next template base is a mismatch with dATP, so binding is weak and reaction slow. Therefore our experimental design allows us to perform single turnover kinetic analysis.

In most cases, this scheme can be reduced to a more simplified form of the polymerization model (Scheme 2.2). In Scheme 2.2, fast rates of pyrophosphate release

and translocation for wild-type Pol γ and most mutants allows k_2 to be neglected and therefore the apparent K_d ($K_{d,app}$) = k_{-1}/k_1 , and $k_{pol} = k_2$ (110, 115).

Scheme 2.2



Additionally, the specificity constant governing each sequential nucleotide incorporation, k_{cat}/K_m , is equal to $k_{pol}/K_{d,app}$. The data for correct incorporation by wild-type and the Pol γ mutants could be fit to this simplified model in Scheme 2.2 and the global fitting results are summarized in Table 2.4 and displayed in Figure 2.6.

Table 2.4 *Pol γ Kinetic Parameters of dATP Incorporation*

	$K_{d,app}$ μM	k_{pol} s^{-1}	$k_{pol}/K_{d,app}$ $\mu M^{-1}s^{-1}$	Fold Change
WT	0.7 ± 0.14 (0.62 - 0.84)	30 ± 2 (29 - 33)	43 ± 9	-
H932Y	103 ± 15 (97 - 110)	28.6 ± 2.9 (27 - 30)	0.3 ± 0.05	143
H932A	39 ± 6.4 (39 - 49)	23 ± 2.8 (23 - 27)	0.6 ± 0.1	72
R943H	149 ± 19 (137 - 187)	29.9 ± 3 (27.9 - 36.3)	0.2 ± 0.03	215
R953C	0.63 ± 0.22 (0.42 - 0.99)	77.8 ± 11 (67 - 97)	123 ± 46	0.35
A957S	1.2 ± 0.26 (0.96 - 1.55)	29 ± 2.1 (27 - 32)	24 ± 5.5	1.8
R1096C	0.13 ± 0.07 (0.1 - 0.17)	4.6 ± 0.9 (4.2 - 5.1)	35 ± 20	1.2

This table summarizes the kinetic parameters derived in globally fitting data to Scheme 2.2 to define the kinetics of incorporation of dATP by wild-type and mutant forms of Pol γ . Data for the wild-type, H932Y and H932A enzymes are from (116). Numbers in parenthesis give the lower and upper limits derived from the confidence contour analysis in fitting the data.

The parameters determined by global fitting of the dATP incorporation by wild-type enzyme are in agreement with previously published data from our lab (49, 117) and give a $k_{\text{pol}}/K_{\text{d,app}}$ of $43 \pm 9 \mu\text{M}^{-1}\text{s}^{-1}$ (Table 2.4 and Figure 2.6A). The H932Y mutant (Figure 2.6B) showed a maximum rate of incorporation of 28.6 s^{-1} , which is similar to that of the wild-type enzyme at 30 s^{-1} (Figure 2.6A). However, the 143-fold change in the specificity constant comes from the drastically decreased K_{d} for nucleotide binding from $0.7 \mu\text{M}$ for wild-type to $103 \mu\text{M}$ for H932Y. The case is similar for the alanine mutation at position 932, though not as severe with a 72-fold decrease in $k_{\text{pol}}/K_{\text{d,app}}$. The R943H mutant showed a similar trend to H932Y with no effect seen in the rate of nucleotide incorporation (29.9 s^{-1}) and a decrease in $K_{\text{d,app}}$, this time by over 200-fold. This resulted in a 215-fold decrease in $k_{\text{pol}}/K_{\text{d,app}}$ for the R943H mutant compared to wild-type Pol γ . Both the R953C and the A957S mutants were less drastic in their effects on k_{pol} and $K_{\text{d,app}}$. The R953C mutant, shown in Figure 2.6C, surprisingly showed a 2-fold increase in k_{pol} and a very slight decrease in $K_{\text{d,app}}$. This led to a specificity constant that was almost 3-fold greater than that of the wild-type enzyme. The A957S mutant showed kinetics very close to wild-type with only a 1.8-fold change in $k_{\text{pol}}/K_{\text{d,app}}$. R1096C (Figure 2.6D) also showed a small change in specificity constant (1.2-fold) but this was due to a 6.5-fold decrease in k_{pol} which was offset by the 5.4 fold decrease in $K_{\text{d,app}}$.

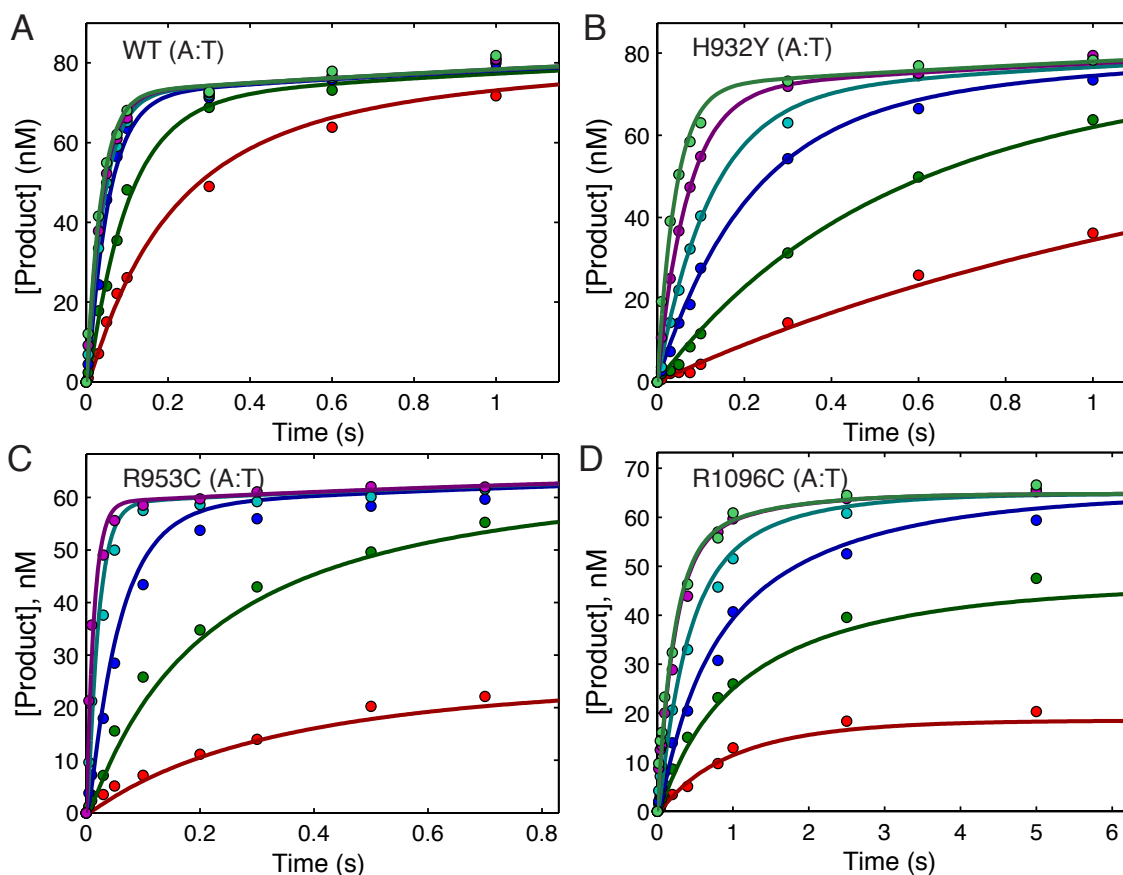


Figure 2.6. Correct incorporation of dATP by wild-type and mutants of Pol γ A. For each concentration series, a preformed enzyme-DNA complex was rapidly mixed with MgCl_2 and various concentrations of dATP. In each experiment, the final concentrations of enzyme and DNA after mixing were 150-175 nM and 75-100 nM, respectively. Results of the global fitting to Scheme 2.2 are shown and in each case the concentration of active enzyme was adjusted to fit the amplitude of the curves. (A) Incorporation of dATP by wild-type (WT) Pol γ at various concentrations (0.2, 0.5, 1.5, 3, 5.5, and 8.5 μM) was globally fit yielding k_{pol} of $30 \pm 2 \text{ s}^{-1}$ and $K_{\text{d,app}}$ of $0.7 \pm 0.14 \mu\text{M}$. (B) Incorporation of dATP by H932Y Pol γ at various concentrations (2.5, 7.5, 20, 40, 100, and 500 μM) was globally fit yielding k_{pol} of $28.6 \pm 2.9 \text{ s}^{-1}$ and $K_{\text{d,app}}$ of $103 \pm 15 \mu\text{M}$. (C) Incorporation of dATP by R953C Pol γ at various concentrations (0.025, 0.1, 0.4, 2 and 20 μM) was globally fit yielding k_{pol} of $77.8 \pm 11 \text{ s}^{-1}$ and $K_{\text{d,app}}$ of $0.63 \pm 0.22 \mu\text{M}$. (D) Incorporation of dATP by R1096C Pol γ at various concentrations (0.02, 0.05, 0.1, 0.25, 5 and 500 μM) was globally fit yielding k_{pol} of $4.6 \pm 0.9 \text{ s}^{-1}$ and $K_{\text{d,app}}$ of $0.13 \pm 0.07 \mu\text{M}$.

Kinetics of DNA binding

In certain cases where the kinetics of DNA binding were hypothesized to be affected by mutants, an active site titration with various concentrations of DNA was performed.

The active site titration of A957S was fit to a quadratic equation (Equation 2.1) to yield a K_d for DNA of 12.8 nM. This is close to the value of 9.9 nM previously determined for wild-type that was used in the global fitting of all mutants (49).

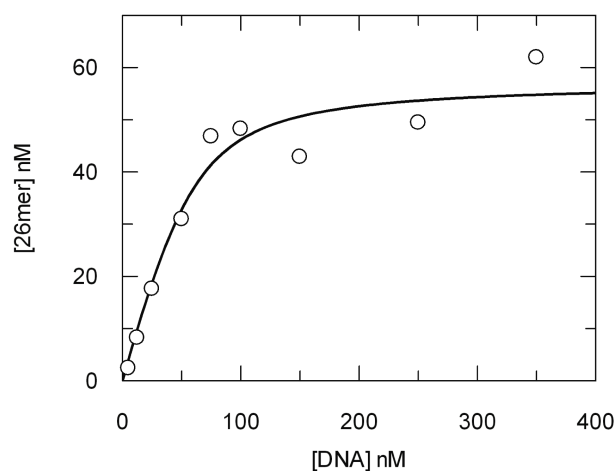


Figure 2.7 Active site titration of A957S mutant. All concentrations listed are final. 100 nM enzyme was preincubated with increasing concentrations of 25/45mer (10, 25, 50, 100, 150, 200, 300, 500 and 700 nM) and rapidly mixed with $MgCl_2$ and 250 μM dATP. The reactions were quenched after 0.15 seconds with 500 mM EDTA. Quantification of the concentration of 26mer was calculated as described in the materials and methods section and plotted as a function of DNA concentration. Data were fit to the quadratic equation (Equation 2.1) yielding a $K_{d,DNA} = 12.8 \pm 5.9$ and an active enzyme concentration of 57 ± 4.1 nM.

Kinetics of misincorporation

The kinetics of misincorporation of TTP, dCTP and dGTP opposite a templating TMP of the 25/45mer template were measured to explore the discrimination of the Pol γ

mutants against mismatches. These studies were carried out in a similar fashion to those for correct nucleotide incorporation where a preformed enzyme-DNA complex was preincubated with an excess of Pol γ over DNA to insure single turnover conditions. This complex was then rapidly mixed with various concentrations of incorrect nucleotide (TTP, dCTP or dGTP) and $MgCl_2$. The time course of product formation was then plotted and fit globally to a model for DNA polymerization. With some mutants of Pol γ , multiple misincorporations were seen where multiple nucleotides were incorporated onto the primer strand and resulted in products of up to 35 nucleotides long. When this occurred, all of the extended primers, 26 nucleotides and greater, were summed and quantified as the total product that was then plotted versus time. The results for wild-type enzyme and most mutants could be fit using the minimal model described in Scheme 2.2 for correct nucleotide incorporation.

In these cases, the global fitting resulted in a best-fit value for $1/K_1$ as the nucleotide dissociation constant ($K_{d,app}$) and k_2 as the maximum rate of nucleotide incorporation (k_{pol}). As was described above, the ratio of these $k_{pol}/K_{d,app}$, gives the specificity constant governing nucleotide incorporation, k_{cat}/K_m . In some cases, misincorporation by mutants required an expanded model (Scheme 2.1) to account for the trends seen in the data. Specifically, some of the data showed that the amplitude of product formation was concentration dependent. The minimal model in Scheme 2.2 does not allow for an amplitude dependence on concentration because the fast, largely irreversible step of pyrophosphate release after chemistry drives the reaction forward even at low nucleotide concentrations. An amplitude dependence on concentration suggests that the chemistry step is reversible and comes to an equilibrium that is linked to nucleotide binding. For this to occur, the pyrophosphate release step after chemistry must be slow or readily reversible. This phenomenon has been seen previously with Pol γ in

the incorporation of 8-oxo-dGTP and AZT-triphosphate (118, 119). When this trend in the data was seen, the expanded model (Scheme 2.1) was used to fit the data where the reversible rate of chemistry, k_{-2} is greater than zero and k_3 the pyrophosphate release step is slow relative to k_2 .

The best-fit values of the wild-type misincorporation data and data for the 6 mutants studied in this chapter are summarized in Table 2.5. Experiments that could be fit with the minimal model for nucleotide incorporation have the k_{-2} set to 0 (because it is not defined by the data) and the k_3 step listed as *fast* (relative to k_2). For those mutants requiring the expanded model including a reversible chemistry step and slow pyrophosphate release, the best-fit values for k_{-2} and k_3 are listed. Table 2.6 shows the k_{cat} , K_m , k_{cat}/K_m and discrimination values for each enzyme. For those fitted with the minimal model of Scheme 2.2, the $k_2=k_{cat}$, $1/K_1=K_m$ and the k_{cat}/K_m is therefore equal to $k_2/(1/K_1)$. For situations where the expanded 3-step model of Scheme 2.1 was required, Equations (Eqn) 2.2, 2.3 and 2.4 were used to obtain values for k_{cat} , K_m and k_{cat}/K_m . The discrimination was calculated as the k_{cat}/K_m for correct nucleotide divide by the k_{cat}/K_m for a mismatch nucleotide.

$$\text{Eqn 2.2} \quad k_{cat} = \frac{k_2 k_3}{k_2 + k_{-2} + k_3}$$

$$\text{Eqn 2.3} \quad K_m = \frac{k_2 k_3 + k_{-1}(k_{-2} + k_3)}{k_1(k_2 + k_{-2} + k_3)}$$

$$\text{Eqn 2.4} \quad k_{cat} / K_m = \frac{k_1 k_2 k_3}{k_2 k_3 + k_{-1} k_{-2} + k_{-1} k_3}$$

The misincorporation of TTP, dCTP and dGTP by wild-type enzyme were all fit to the minimal model in Scheme 2.2. These misincorporation assays have been previously described for wild-type Pol γ (21), however they were repeated in this study for accurate comparison with the six mutants. Figure 2.8 shows the polyacrylamide gel showing incorporation of a T:T mismatch by wild-type enzyme and the data for the full

concentration series are plotted in Figure 2.10A. The discrimination for TTP, dCTP and dGTP are 430,000, 717,000, and 8,600 respectively. Consistent with previously published misincorporation results (21), the discrimination by wild-type Pol γ for mismatches comes from both greatly reduced k_{cat} values and increased K_{m} values.

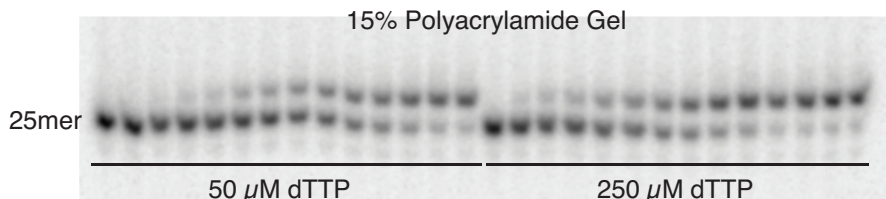


Figure 2.8 Formation of a T:T mismatch by wild-type *exo*⁻ Pol γ . All concentrations listed are final. 100 nM enzyme was preincubated with 75 nM 25/45mer DNA and subsequently mixed with MgCl_2 and various concentrations of dTTP before quenching with 500 mM EDTA. Products from incorporation of 50 μM and 250 μM dTTP are shown on a 15% polyacrylamide sequencing gel. For each concentration of dTTP, time points were taken from 0 – 1200 seconds and the formation of a 26mer T:T mismatch was observed.

The H932Y and H932A mutants both showed interesting results for a T:T and C:T mismatch. These data required fitting to the expanded the model in Scheme 2.1 that allowed for reversible chemistry and slow pyrophosphate release. Figure 2.10B shows an attempt to fit the data to the minimal model in Scheme 2.2 with the dashed lines. It is clear that this fit cannot account for the amplitude dependence that is seen in the data. The expanded model of Scheme 2.1 is able to fit the trends seen in the data (solid lines). H932Y/A also differed from wild-type in the formation of a T:T mismatch by forming multiple misincorporations over this time scale and at these dTTP concentrations. This is displayed in Figure 2.9 which shows the formation of products up to 31-nucleotides in length. The formation of a C:T mismatch by H932Y and H932A also suggested a slow pyrophosphate release step leading to a reversible chemistry step. In both cases, H932Y

and A, the release of pyrophosphate is 0.0003 to 0.0005 s⁻¹. These lead to very low values for k_{cat}/K_m , but when the decreased k_{cat}/K_m for dATP is considered, the calculated value for discrimination does not vary greatly from wild-type. For H932Y, the discrimination for TTP is down to 150,000 from 430,000 for wild-type, the discrimination for dCTP is comparable (750,000 vs 717,000) and the discrimination for dGTP is slightly lower at 6,000 compared to 8,600 for wild-type. Overall, mutations H932Y/A did not have a significant effect on the enzyme fidelity of incorporation.

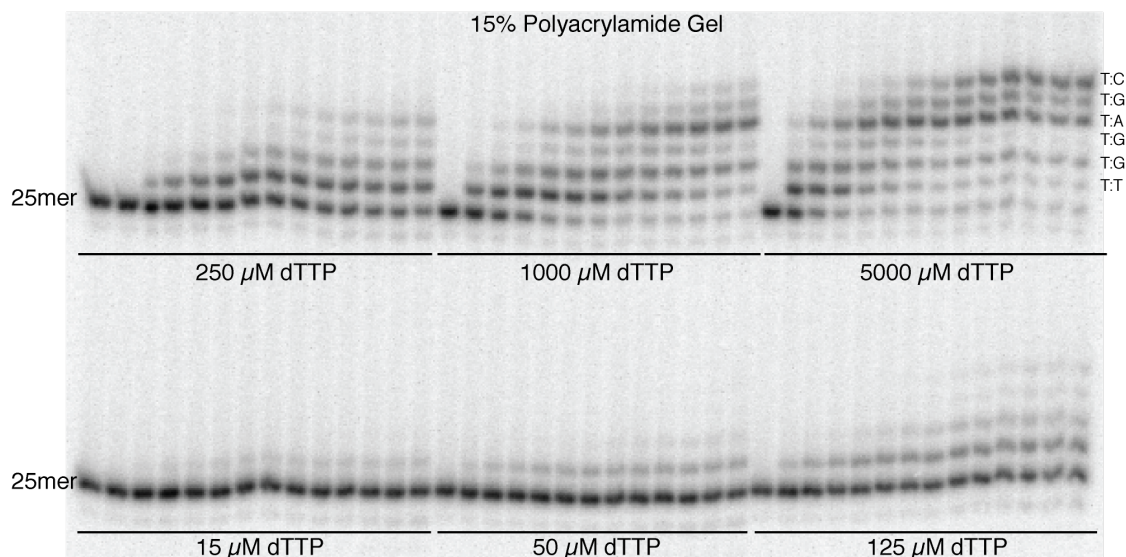


Figure 2.9 Misincorporation of dTTP by *Pol γexo- H932Y* mutant. All concentrations listed are final. 150 nM enzyme was preincubated with 75 nM 25/45mer DNA and subsequently mixed with MgCl₂ and various concentrations of dTTP before quenching with 500 mM EDTA. Products from incorporation of dTTP were resolved on a 15% polyacrylamide sequencing gel. For each concentration of dTTP, time points were taken from 0 – 1200 seconds. At concentrations greater than 125 μM dTTP, formation of multiple incorporations past the T:T mismatch were observed with products up to a 31mer observed. The right axis on the 5000 μM dTTP concentration displays the mismatch formed according to the templating base of the DNA substrate as it corresponds to each band.

The R943H mutant was similar to the mutation of the histidine at position 932 in that the misincorporation of TTP and dCTP required steps for slow pyrophosphate release and reversible chemistry. These effects led to a decrease in discrimination of TTP from 430,000 for wild-type to 95,000 for R943H. Alternatively, the discrimination against dCTP was increased from 717,000 for wild-type to 2,000,000 for R943H.

The misincorporation data for the remaining mutants studied here, R953C, A957S, and R1096C, were fit to the minimal model in Scheme 2.2. R953C showed an increase in the discrimination for all mismatches largely due to the increases in K_m that were seen for the mismatched nucleotides with that mutant. The A957S showed discrimination values similar to those for wild-type enzyme. The R1096C mutant had a decrease in the discrimination against TTP and dCTP while obtaining comparable values against discrimination of dGTP.

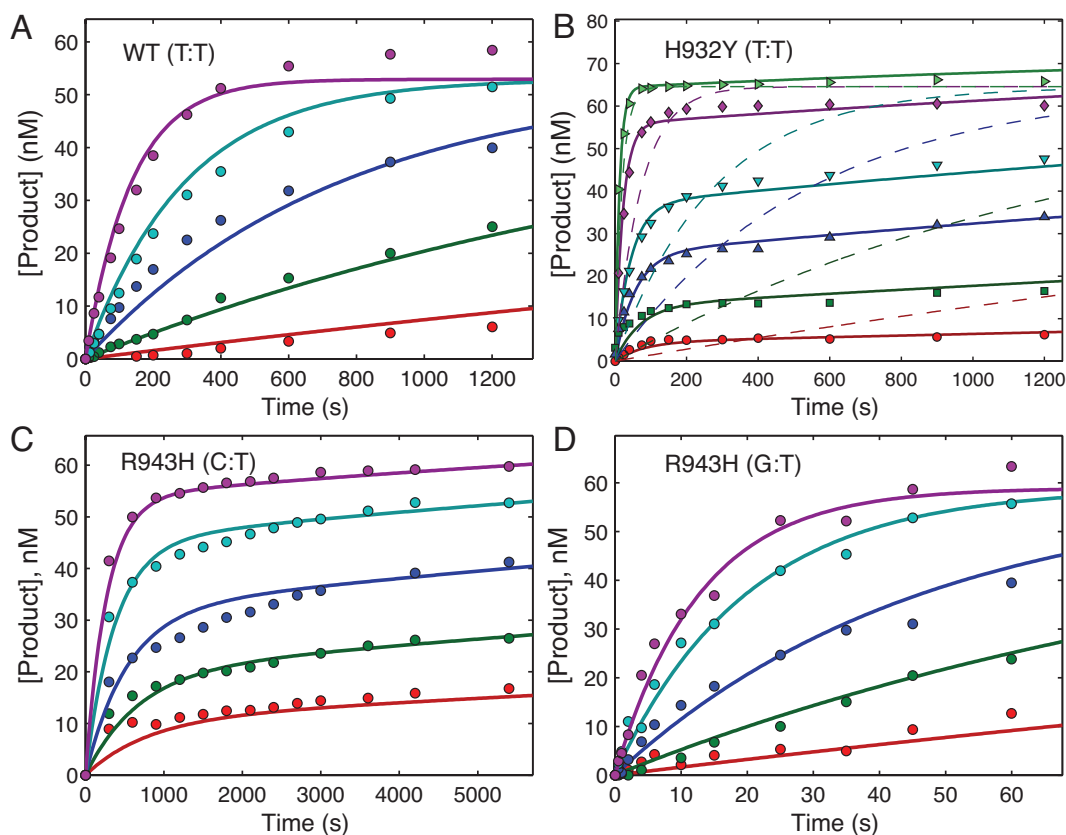


Figure 2.10 Misincorporation by wild-type and mutant *exo* Pol γ . For each concentration series, a preformed enzyme-DNA complex was rapidly mixed with MgCl_2 and various concentrations of incorrect nucleotide. In each experiment, the final concentrations of enzyme and DNA after mixing were 150-175 nM and 75-100 nM, respectively. The time course of product formation was then fit globally and in each case the concentration of active enzyme was adjusted to fit the amplitude of the curves. (A) Incorporation of dTTP by wild-type (WT) Pol γ at various concentrations (1.5, 5, 15, 50, 250 μM) was globally fit to Scheme 2.2 yielding k_{pol} of $0.01 \pm 0.004 \text{ s}^{-1}$ and $K_{\text{d,app}}$ of $81.8 \pm 10.9 \mu\text{M}$. (B) Incorporation of dTTP by H932Y Pol γ at various concentrations (15, 50, 125, 250, 1000 and 5000 μM) was globally fit to Scheme 2.1 (solid lines) yielding $K_{\text{d,app}}$ of $1634 \pm 482 \mu\text{M}$, $k_2 = 0.09 \pm 0.03 \text{ s}^{-1}$, $k_{-2} = 0.009 \pm 0.005 \text{ s}^{-1}$ and $k_3 = 0.0003 \pm 0.0008 \text{ s}^{-1}$. Attempts to fit the model described in Scheme 2.2 are shown as the dashed lines that do not account for the concentration dependence of the rate and amplitude seen in the data. (C) Incorporation of dCTP by R943H Pol γ at various concentrations (350, 750, 1500, 3000 and 5000 μM) was globally fit to Scheme 2.1 yielding $K_{\text{d,app}}$ of $>17000 \mu\text{M}$, $k_2 = 0.08 \pm 0.004 \text{ s}^{-1}$, $k_{-2} = 0.001 \pm 0.001 \text{ s}^{-1}$ and $k_3 \leq 0.0004 \text{ s}^{-1}$. (D) Incorporation of dGTP by R943H Pol γ at various concentrations (150, 500, 1200, 3000 and 5000 μM) was globally fit to Scheme 2.2 yielding k_{pol} of $0.49 \pm 0.06 \text{ s}^{-1}$ and $K_{\text{d,app}}$ of $>13,000 \mu\text{M}$.

Table 2.5 *Pol γ Kinetic Parameters of Misincorporation*

	$1/K_1$	k_2	k_2	k_3
	μM	s^{-1}	s^{-1}	s^{-1}
WT				
TTP	81.8 ± 10.9 (40 - 90)	0.01 ± 0.004 (0.006 - 0.01)	(0)	fast
dCTP	1030 ± 193 (810 - 1300)	0.06 ± 0.018 (0.05 - 0.08)	(0)	fast
dGTP	1300 ± 1600 (836 - 4100)	6.6 ± 7.4 (4.5 - 20)	(0)	fast
H932Y				
TTP	1634 ± 482 (1330 - 4800)	0.09 ± 0.03 (0.08 - 0.22)	0.009 ± 0.005 (0.007 - 0.02)	0.0003 ± 0.0008 (1.3×10^{-9} - 0.001)
dCTP	22200 ± 3420 (17800 - 6.7×10^{11})	0.02 ± 0.005 (0.015 - 8.3×10^5)	0.0004 ± 0.003 (0.0002 - 0.002)	0.0003 ± 0.002 (2.8×10^{-8} - 0.001)
dGTP	24000 ± 9600 (18300 - 1.5×10^5)	1.2 ± 0.4 (1 - 7)	(0)	fast
H932A				
TTP	9400 ± 2700 (7000 - 1.7×10^5)	0.47 ± 0.15 (0.35 - 11.5)	0.013 ± 0.0056 (0.01 - 0.02)	0.0003 ± 0.0004 (2×10^{-5} - 0.0008)
dCTP	40900 ± 9470 (26000 - 1.9×10^5 *)	0.038 ± 0.012 (0.02 - 0.18)	0.0009 ± 0.0006 (0.0005 - 0.0017)	0.0005 ± 0.001 (0.0002 - 0.0008)
dGTP	5150 ± 1500 (4100 - 10000)	0.27 ± 0.06 (0.23 - 0.45)	(0)	fast
R943H				
TTP	1350 ± 82 (1350 - 2110)	0.02 ± 0.002 (0.02 - 0.04)	0.006 ± 0.002 (0.005 - 0.013)	0.001 ± 0.003 (0.0009 - 0.002)
dCTP	>17000	0.08 ± 0.004 (0.02 - 1)	0.001 ± 0.001 (0.0009 - 0.006)	≤ 0.0004 (5×10^{-5} - 0.0004)
dGTP	>13000	0.49 ± 0.06 (0.3 - 2.33*)	(0)	fast

Table 2.5 Continued Pol γ Kinetic Parameters of Misincorporation

	$1/K_1$	k_2	k_{-2}	k_3
	μM	s^{-1}	s^{-1}	s^{-1}
R953C				
TTP	2860 ± 980 (2260 - 5830)	0.16 ± 0.05 (0.13 - 0.31)	(0)	fast
dCTP	>24000	0.96 ± 0.07 (0.49 - 8.97*)	(0)	fast
dGTP	>1850	3.46 ± 0.97 (2.77 - 6.97)	(0)	fast
A957S				
TTP	1390 ± 317 (812 - 1650)	0.096 ± 0.03 (0.06 - 0.1)	(0)	fast
dCTP	3270 ± 1000 (2980 - 4370)	0.08 ± 0.03 (0.08 - 0.11)	(0)	fast
dGTP	1560 ± 560 (995 - 2430)	2.9 ± 0.98 (2 - 4.5)	(0)	fast
R1096C				
TTP	967 ± 408 (667-1770)	0.29 ± 0.11 (0.22-0.5)	(0)	fast
dCTP	444 ± 195 (355-498)	0.097 ± 0.046 (0.08-0.1)	(0)	fast
dGTP	327 ± 150 (283-402)	1.18 ± 0.4 (1-1.35)	(0)	fast

This table summarizes the kinetic parameters derived in globally fitting data to define the kinetics of misincorporation against a template dT by wild-type and mutant forms of Pol γ . Numbers in parenthesis give the lower and upper limits derived from the confidence contour analysis in fitting the data. * denotes that no boundary was found during the confidence contour search; the number given defines the most extreme value examined. Data for the wild-type, H932Y and H932A enzyme were obtained from (116).

Table 2.6 *Pol γ Kinetic Parameters of Misincorporation*

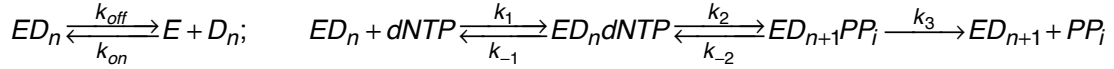
	k_{cat}	K_m	k_{cat}/K_m	Discrimination
	s^{-1}	μM	$\mu M^{-1} s^{-1}$	
WT (del66)				
TTP	0.01 ± 0.004	81.8 ± 10.9	0.0001 ± 0.00005	430,000
dCTP	0.06 ± 0.018	1030 ± 193	0.00006 ± 0.00002	717,000
dGTP	6.6 ± 7.4	1300 ± 1600	0.005 ± 0.008	8,600
H932Y				
TTP	0.0003 ± 0.0007	153 ± 105	0.000002 ± 0.000005	150,000
dCTP	0.0003 ± 0.002	750 ± 3875	0.0000004 ± 0.000003	750,000
dGTP	1.2 ± 0.4	24000 ± 9600	0.00005 ± 0.00003	6,000
H932A				
TTP	0.0003 ± 0.0004	260 ± 150	0.000001 ± 0.000002	600,000
dCTP	0.0005 ± 0.001	1450 ± 1330	0.0000003 ± 0.0000007	2,000,000
dGTP	0.27 ± 0.06	5150 ± 1500	0.00005 ± 0.00002	12,000
R943H				
TTP	0.0007 ± 0.002	350 ± 189	$2.1 \times 10^{-6} \pm 6.4 \times 10^{-6}$	95,000
dCTP	$8.9 \times 10^{-5} \pm 0.6 \times 10^{-5}$	1750 ± 1605	$5 \times 10^{-8} \pm 4.6 \times 10^{-8}$	4,000,000
dGTP	0.49 ± 0.06	≥ 13000	$2.3 \times 10^{-5} \pm 0.28 \times 10^{-5}$	8,700
R953C				
TTP	0.16 ± 0.05	2860 ± 980	$5.6 \times 10^{-5} \pm 2.5 \times 10^{-5}$	2,500,000
dCTP	0.96 ± 0.07	>24000	$2 \times 10^{-5} \pm 0.1 \times 10^{-5}$	6,150,000
dGTP	3.46 ± 0.97	>1850	0.001 ± 0.0004	120,000
A957S				
TTP	0.096 ± 0.03	1390 ± 317	$7 \times 10^{-5} \pm 2.6 \times 10^{-5}$	340,000
dCTP	0.08 ± 0.03	3270 ± 1000	$2.4 \times 10^{-5} \pm 1.2 \times 10^{-5}$	1,000,000
dGTP	0.097 ± 0.046	444 ± 195	0.0018 ± 0.0008	13,000
R1096C				
TTP	0.29 ± 0.11	967 ± 408	0.0003 ± 0.00017	117,000
dCTP	0.097 ± 0.046	444 ± 195	0.0002 ± 0.0001	175,000
dGTP	1.86 ± 0.83	265 ± 150	0.007 ± 0.005	9,700

The table summarizes the k_{cat} and K_m values governing misincorporation by mutant forms of Pol γ , calculated from the data in Table 2.5. Data for the wild-type, H932Y and H932A enzymes are from (116). Discrimination was calculated as the ratio of k_{cat}/K_m values for correct versus mismatched dNTP.

2.4 DISCUSSION

For each of these mutants we have characterized of the effect of the mutation by conducting single turnover rapid quench flow experiments and fitting our data to a model for the pathway of DNA polymerization, shown in Scheme 2.1.

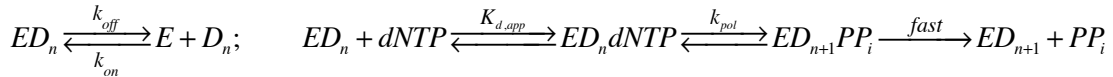
Scheme 2.1.



Pathway of DNA polymerization. Pol γ data fit is to the model shown above. The initial binding of nucleotide is in a rapid equilibrium therefore we assume $k_1 = 100 \mu\text{M}^{-1}\text{s}^{-1}$ and from the fitted value of k_{-1} we can compute $K_d = k_{-1}/k_1$. In most cases, $k_3 \gg k_{-2}$, so k_{cat} is determined solely by k_2 and $K_m = k_{-1}/k_1$. In some cases, k_3 appears to be rate limiting and we can obtain estimates of k_{-1} , k_2 , k_{-2} and k_3 . In all cases, our comprehensive modeling includes DNA binding and release with $k_{\text{on}} = 2 \mu\text{M}^{-1}\text{s}^{-1}$ and $k_{\text{off}} = 0.02 \text{ s}^{-1}$ based on previous measurements (114).

In the simplest form of this model, the ground state binding of nucleotide to the enzyme-DNA complex is in a rapid equilibrium and the polymerization rate is governed by the singled rate limiting step k_2 , followed by steps after chemistry presumed to be fast (pyrophosphate release and translocation) (110, 115). The fast rates of translocation and pyrophosphate release for wild-type Pol γ and most mutants allows k_{-2} to be neglected (Scheme 2.2) and therefore the apparent K_d ($K_{d,\text{app}}$) = k_{-1}/k_1 , and $k_{\text{pol}} = k_2$, and, the specificity constant governing nucleotide incorporation, k_{cat}/K_m , is defined by $k_{\text{pol}}/K_{d,\text{app}}$.

Scheme 2.2



Upon analysis of the quench flow data monitoring nucleotide incorporation, it became evident that the simple model (Scheme 2.2) could not account for the trends seen in the data. In particular, several cases of nucleotide misincorporation showed an amplitude dependence on nucleotide concentration. We have interpreted this as a reversible chemistry step that is thermodynamically linked to nucleotide binding and

therefore requires a slow step following chemistry. Previous studies on Pol γ have seen this with 8-oxo-dG and AZT incorporation as a mechanism to reduce incorporation of these compounds (118, 119). In the cases where the amplitude dependence of the nucleotide incorporation concentration series was seen, we utilized the expanded fitting model to allow chemistry to be reversible ($k_{-2} > 0$) and k_3 to be a variable parameter. These fits resulted in a slow step for k_3 relative to the rate of chemistry. In this chapter, the kinetics of incorporation of a mismatched nucleotide were also examined to investigate the fidelity of these various mutants.

Relating biochemical characterization to clinical phenotype

H932Y/A mutants

Histidine at position 932 is positioned near the active site to form a hydrogen bond with the β -phosphate of the incoming dNTP during polymerization by Pol γ . The presumed role for this residue is based on alignment of the amino acids near the active site with the homologous T7 DNA polymerase where the crystal structure of the ternary complex is available (45, 47). H932 is conserved throughout DNA polymerases (104) and mutation of this position to a tyrosine is seen in patients with mitochondrial disorders (59-61). In particular, the Human DNA Polymerase Gamma Mutation Database (13) lists four reported cases of the H932Y missense mutation in clinical studies (59-61). These patients all exhibited a late onset of Pol γ deficiencies (PEO, myopathy of upper limbs, mtDNA depletion, peripheral neuropathy) that presented in individuals 20-40 years old. The characterization of this H932Y mutant and the alanine mutant give some insight into the mechanistic basis for clinical features that are seen in patients harboring this mutation.

Disruption of the hydrogen bonding interaction between H932 and the β -phosphate of the incoming nucleotide by the mutation to a tyrosine residue resulted in a decrease in specificity constant for Pol γ by 140-fold. This drastic decrease in k_{cat}/K_m comes predominantly from a change in the $K_{\text{d,app}}$ for the enzyme which was increased to 103 μM from the 0.7 μM $K_{\text{d,app}}$ for wild-type enzyme. The H932Y mutation did not significantly affect the k_{pol} value. These results show the importance of this residue in nucleotide incorporation particularly by enhancing the binding of the nucleotide to the active site. In a case where this hydrogen bonding is lacking, nucleotide binding is decreased but the overall rate of polymerization is not affected and is possibly accommodated by the binding of the nearby Y951 that is also hypothesized to form a hydrogen bond to the β -phosphate. The mutation of the H932 residue may not interfere with the stabilization of the transition state of the reaction that is required for catalysis, which is accomplished predominantly by the Mg^{2+} ions and K947 binding to the α -phosphate. Our comparison of the H932Y mutant with the H932A mutant showed that the tyrosine had a more drastic effect than the alanine, suggesting that the presence of the tyrosine at this position may lead to steric effects that are more unfavorable than caused by alanine.

Analysis of the enzyme fidelity of the H932Y and H932A mutants did not reveal a significant difference in the discrimination of the enzyme against mismatches in single turnover studies. However, other differences were seen in misincorporation kinetics that differed significantly from that of wild-type. H932Y and H932A mutants both readily catalyzed the incorporation of multiple mismatches, which would have significant physiological effects over time and could lead to progressive and cumulative mutations in the mitochondrial DNA. It is important to note that these experiments were performed in an exonuclease deficient enzyme and therefore the contribution of the exonuclease to the

fidelity of the enzyme was not analyzed. However, stalling of a polymerase after misincorporation is a key kinetic determinant of exonuclease specificity. Thus, incorporation after a mismatch would decrease overall fidelity.

The mutants of H932 and the R943H mutation were the only cases that required the model to be expanded to include a slow pyrophosphate release step following chemistry during nucleotide misincorporation. Generally the steps of pyrophosphate release and translocation after chemistry are presumed to be fast and perhaps limited by a conformational change of the enzyme from the closed to open state (*110, 115*). Because the histidine at position 932 is predicted to be involved in hydrogen bonding with the β -phosphate of the incoming nucleotide and to stabilize the negative charge of the pyrophosphate, it is somewhat surprising that mutation of this residue appears to slow pyrophosphate release rather than accelerate it. The same is true for the R943 residue that hydrogen bonds with the γ -phosphate. It is possible that these residues are involved in the conformational change step that is presumed to limit pyrophosphate release after chemistry. Without the stabilizing interaction of these positively charged residues with the pyrophosphate leaving group, perhaps the conformational change is slowed. In these studies, the slow pyrophosphate release was only seen in the T:T and C:T mismatches for these mutants and not in the G:T mismatch or for correct incorporation of A:T. It appears that this result only occurs in the pyrimidine:pyrimidine base pairs and not in the purine:pyrimidine cases, including the formation of the G:T wobble. This suggests that the structure of DNA containing the pyrimidine:pyrimidine base pair and the mutations at position 932 or 943 lead to a slower pyrophosphate release possibly by slowing the rate of the conformational change from closed to the open form of the enzyme.

R943H mutant

The arginine at position 943 is involved in hydrogen bonding with the γ -phosphate of the incoming nucleotide during DNA polymerization by Pol γ (45). Mutation of this residue to a histidine is associated with the most severe clinical phenotypes of autosomal dominant PEO. The disease is often late in onset with cases of patients in their 30s or 60s. The R943H mutation is often found as a compound heterozygote and in most cases appears to be fully penetrant; meaning every person who has the mutation shows symptoms for PEO. This missense mutation has also been associated with premature ovarian failure.

These results show that the R943H mutation severely affects the specificity of the enzyme resulting in a k_{cat}/K_m value that is 215-fold lower than that of wild-type enzyme. This decrease in k_{cat}/K_m comes exclusively from a decrease in $K_{\text{d,app}}$ and the k_{pol} is comparable to wild-type Pol γ . This is consistent with the proposed role for this residue to bind to the γ -phosphate of the incoming nucleotide and a disruption in that bonding interaction severely affects the nucleotide binding. Analysis of enzyme fidelity reveals a 4.5-fold decrease in discrimination for T:T mismatches and surprisingly, compared to wild-type the R943H mutation increases the discrimination 5.5-fold for a C:T mismatch. The fitting of data collected for these two mismatches T:T and C:T with this mutant also required the slow pyrophosphate release step that was described above for H932Y.

R953C mutant

Clinically the reported cases of the R953C mutation in Pol γ involve patients greater than age 20 who have been diagnosed with PEO (35, 61, 66). This mutation has been seen as a compound heterozygote with other mutations in Pol γ and is associated with autosomal dominant PEO. Additionally, in 2012 three cases were reported of patients that were homozygous for this missense mutation and were diagnosed with

autosomal recessive PEO (66). The residue at position 953 is positioned in an alpha helix of the fingers subdomain near the active site of Pol γ (45). The characterization of the R953C mutant revealed a surprising increase in k_{cat}/K_m of 2.8-fold compared to wild-type enzyme. This increase in specificity constant comes largely from a 2.6-fold increase in k_{pol} by this Pol γ mutant. Examination of the fidelity of this mutant also was surprising and revealed that the discrimination values for T:T, C:T and G:T mismatches were all increased compared to wild-type by at least 5-fold. For the T:T and C:T mismatches, the k_{cat} values were actually higher than the wild-type k_{cat} values for formation of these mismatches, but the mutant had much weaker binding of the mismatches as reflected in the higher $K_{\text{d,app}}$ values. The lack of deficiency of this mutant seen in these single turnover nucleotide incorporation studies leads to the hypothesis that perhaps this mutant is involved in disrupting an interaction of Pol γ with other proteins at the replisome, potentially the helicase. This has yet to be tested. Also, the less severe clinical phenotype seen with this mutant is supported by this characterization. Furthermore, the fact that the mutation is present as a homozygote in patients that develop deficiencies that are late in onset suggests that this mutation is not hugely detrimental to mtDNA replication.

A957S mutant

The A957 residue is positioned on a loop of the fingers subdomain of Pol γ and is predicted to be part of the nucleotide-binding pocket (Figure 2.2) (45). It is also in a close proximity to the template strand of DNA based on alignment of Pol γ with the T7 DNA polymerase structure containing nucleotide and DNA (47). Mutation of this residue from an alanine to a serine is associated with cases of autosomal dominant PEO. The mutation appears to have a low penetrance and results in milder symptoms of PEO. In one study (62), seven cases of this A957S mutation were reported. There were six heterozygotes

examined and five of those six showed late-onset PEO symptoms and just 1 showed symptoms representing the typical PEO. Also reported was one case of a homozygous individual who was severely affected by PEO. The analysis of this mutation presented here reveals k_{pol} , $K_{\text{d,app}}$, $k_{\text{cat}}/K_{\text{m}}$, and $K_{\text{d,DNA}}$ values that are all very similar to wild-type poly. Analysis of the fidelity of this A957S mutant also showed very wild-type values for discrimination of T:T, C:T and G:T mismatches. This biochemical analysis correlates well with the low penetrance of this mutation in clinical studies and the less severe phenotypes that are seen. However, this mutation does lead to a late onset clinical phenotype that is not explained by its wild-type-like activity in our assay. It is possible that this A957S mutation could interfere with interactions of Pol γ with other proteins in the replisome at the replication fork of mtDNA.

R1096C mutant

The arginine residue at position 1096 in Pol γ is located away from the active site at the junction between the palm and fingers subdomains of the protein (Figure 2.2) (45). Mutation of this residue to a cysteine has been associated with several Pol γ disorders including PEO, Alpers, seizures, encephalopathy and SANDO (61, 67-73). One case of a R1096H mutation has also been seen clinically (68). In these clinically reported cases, the average age of disease onset is 18 years old (see Appendix) but the ages of patients range from 5 months to 55 years. The mutation is often found as a compound heterozygote with other mutations in Pol γ , possibly accounting for the variable age of onset, but homozygous forms have also been observed. The four homozygotes that were observed all had an early age of onset with symptoms occurring at 5 months, 8 months, 1 year and 2 years old (61, 70). The ages of the compound heterozygotes ranged from 2-55 (61, 68-73). Analysis of the R1096C mutant in the studies presented in this chapter revealed that

for dATP incorporation the k_{pol} was decreased 6.5-fold from wild-type and the $K_{d,app}$ was also decreased 5-fold to yield a modest 1.2-fold decrease in the overall k_{cat}/K_m value. The misincorporation data for R1096C showed that the misincorporation of a T:T mismatch was almost 30-fold faster than wild-type but this was offset by the weaker binding of the T:T mismatch to give an overall decrease in discrimination. The discrimination of C:T mismatch was also decreased compared to wild-type but the G:T mismatch was very similar to that of wild-type Pol γ . Overall the characterization of this mutant relates to its clinical phenotype seen where the mutation does not appear to be severe and could account for the slow onset of phenotype in the heterozygous case. Also this mutation has more clinically reported cases than the other mutants here so it is more tolerated in the population.

Summary of all mutants

In general, the variable phenotypes of *POLG*-related mitochondrial disorders are genetically and biochemically difficult to explain (6). The diseases that manifest from mutations in the gene for Pol γ are often slow in onset and likely due to the accumulation of mutations over time; however, in some cases mutations lead to a severe clinical phenotype and death within two years of birth (64). The variability in phenotype can be attributed to the high copy number of mtDNA in the cell and the heterozygosity of the two *POLG* alleles. Most mammalian cells contain hundreds of mitochondria and each mitochondria is estimated to be contain somewhere between 2-10 copies of mtDNA (120, 121). Therefore the mtDNA copy number in a mammalian cell can range from 1,000 – 10,000 copies and the regulation of such is not well understood (122). Additionally, the regulation of Pol γ expression in the nucleus is not well understood. It could be that in many cases where one mutant allele is present, the other allele is upregulated such that

the wild-type enzyme is more abundant. In this case, the mutant polymerase therefore wouldn't significantly interfere with efficient polymerization, other than to possibly bind to primer template regions and block wild-type binding. The off-rate of Pol γ is shown to be 0.02 s^{-1} (114), therefore a polymerase would fall off the DNA every 30 seconds and a new, potentially wild-type polymerase, would have the opportunity to bind. Many of the clinical reports of mutations in Pol γ are found as compound heterozygotes, coexisting with another mutation on the other Pol γ allele, which adds to the variability in complementation and ultimately disease severity.

As an initial summary of all mutants, Figure 2.11 shows the individual contributions of K_d and k_{pol} to changes in enzyme specificity due to a mutation in Pol γ . Data from Table 2.4 was used to plot the effect of each mutation on catalytic efficiency of Pol γ on a free energy scale, revealing that most of the effects on enzyme efficiency are due to a decrease in K_d for the mutants (dark color). The R943H mutant showed the most drastic effect of these disease mutants followed by the mutation of the histidine at position 932. In the case of R953C, the negative free energy value represents the increase in k_{pol}/K_d seen by this mutant largely from its increase in k_{pol} (light color). This summary of the net specificity for each mutant does generally relate to the clinically observed phenotypes for each mutant (R943H most severe, A957S wild-type-like activity), however recent work suggests that the increased mutation frequency of mutants in Pol γ is the primary effect leading to defects in mitochondria (123). Therefore a more robust characterization of mutants must include effects on fidelity of Pol γ mutants.

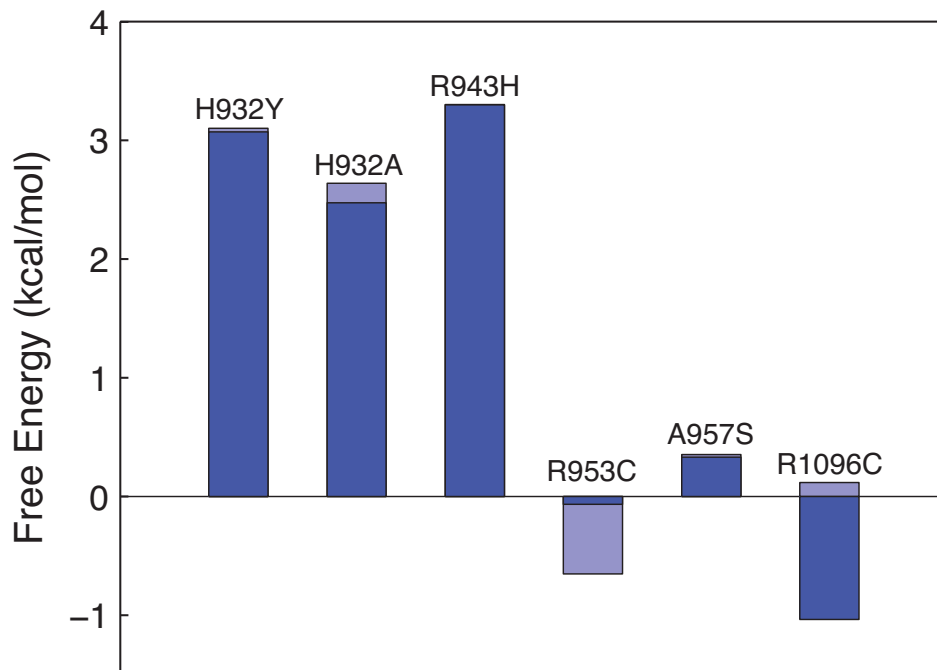


Figure 2.11. Contributions of K_d and k_{pol} to specificity displayed on a free energy scale.

The Y-axis displays free energy $\Delta\Delta G = RT \ln(R)$, where R is the ratio of K_d or k_{pol} values. On this scale, a positive $\Delta\Delta G$ equals the free energy difference favoring the wild-type over the mutant, whereas a negative value that the mutant is favored over the wild-type. K_d values for each mutant divided by the K_d for the WT ($K_{d\text{ mut}}/K_{d\text{ WT}}$), and the corresponding ratios of k_{pol} values $k_{pol,WT}/k_{pol,mut}$ are shown. Values represent the contributions of ground-state binding (K_d , darker color) and rate of polymerization (k_{pol} , lighter color) to the net specificity (k_{pol}/K_d), represented by the sum of the two.

Figure 2.12 shows a simple diagram in attempt to understand the effects of each mutation in Pol γ on DNA replication in the cell, taking into account a decreased polymerization rate and an increase in mutation frequency. This example supposes that a slow enzyme may be less detrimental than a fast enzyme in generating errors. The numbers for rates and discrimination were selected for ease of explaining the relative effects of a mutant vs. a wild-type enzyme in the cell. The illustration shows that, in the

simplest case after 1000 seconds, a mutant polymerase with a 100-fold decrease in rate of polymerization and a 100-fold decrease in discrimination would result in 1000 bp replicated containing 1 error. This is in contrast to the wild-type case, which would result in 100,000 bp replicated containing 1 error. One can imagine how a mutant polymerase, such as the one in this example could be compensated by the wild-type polymerase such that it is able to sustain life, but over time it's effects could be detrimental to mitochondrial function due to the accumulation of mutations.

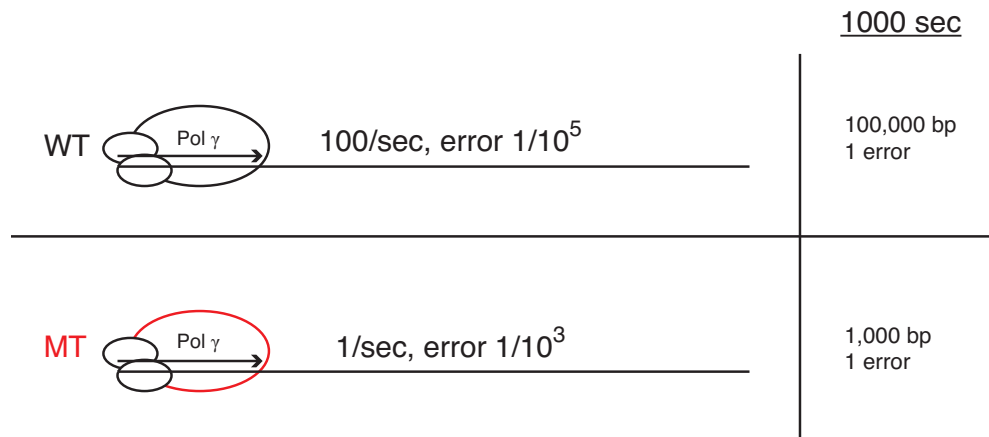


Figure 2.12. Comparison of wild-type and mutant *Pol γ*. The illustration above displays a simple example of the relative effects on k_{cat} and discrimination that result from a mutation in *Pol γ*.

Figure 2.13 displays two proposals for a calculation of a “Mutation Severity Index” for *POLG*-related diseases, using data presented for the mutants in this chapter. This analysis is an attempt to apply a quantitative basis to physiological effects of these mutation in *Pol γ*. Figure 2.13A displays the simple explanation where a slow enzyme making errors is not as detrimental to mtDNA as a fast enzyme (described by Figure 2.12). Under this assumption, the Mutation Severity Index value would be calculated as the fold change in discrimination for mutant divided by the fold change in k_{cat} ($(D_{wt}/D_{mt})/(k_{cat,wt}/k_{cat,mt})$). In this case, a decrease in discrimination could be offset by a

comparable decrease in k_{cat} . The rationale for this is that the more error prone enzyme would not have as much opportunity for misincorporation compared to the wild-type simply because it has a slower rate of polymerization and has less incorporation events overall. Therefore, based on this rationale, a value close to one for this ratio would represent the case where the discrimination is offset by the k_{cat} changes. This calculated Mutation Severity Index value is shown in Figure 2.13A for all mutants, with all mutants other than H932Y giving values less than 1. Plotting these as a function of the average age of disease onset in heterozygote individuals based on available clinical data is shown in Figure 2.14C. The average age of onset in heterozygote individuals was used and homozygote ages were excluded to facilitate the comparison of values and due to the lack of homozygous data in some cases (see Appendix for clinical data). The plot in Figure 2.14C does not show a correlation between the Age of onset and this calculation for Mutation Severity Index. Therefore, a counter scoring function for Mutation Severity Index is proposed below.

An alternative interpretation of the relationship between the discrimination and k_{cat} for a mutant, is that Mutation Severity Index value would be better described by the product of the change in discrimination and change in k_{cat} compared to wild-type, as described in 2.13B. In this case, a defect in discrimination by a mutant would be compounded by a defect in the k_{cat} . This was the case for R1096C where the 6.5-fold decrease in k_{cat} and the 3.8-fold decrease in discrimination compared to wild-type were multiplied resulting in a Mutation Severity Index value of 25. In the case of R953C, the increase in k_{cat} and increase in discrimination compared to wild-type, led to a calculation of 0.05 for the Mutation Severity Index using this calculation. The calculated values for Mutation Severity Index are plotted as a function as the age of disease-onset in heterozygotes in 2.14D. There is a negative correlation between the Mutation Severity

Index calculated in this way and the age of onset, with the Pol γ mutation R1096C having the lowest average age of onset and the highest Mutation Severity Index value.

Overall, relating *in vitro* biochemical data with clinical phenotypes for mutations in *POLG* is a complex process. The relationships outlined in this chapter show the need for more biochemical and clinical data in order to fully assess the physiological consequences of mutations in Pol γ .

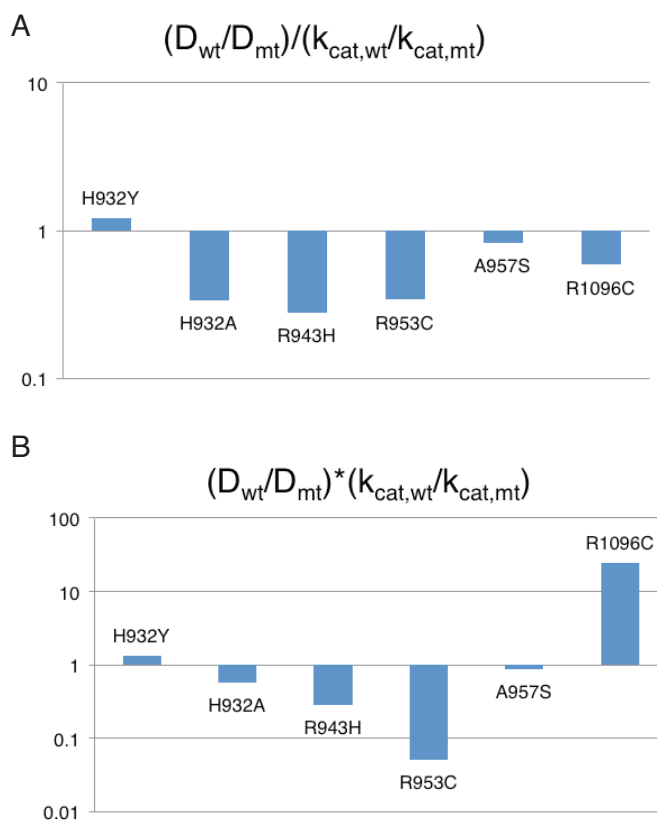


Figure 2.13. Calculating a Mutation Severity Index for Pol γ mutants. Bar graphs show the relationship between the fold changes in discrimination and k_{cat} for mutants of Pol γ versus wild-type on a log scale. (A) The fold change in discrimination divided by the fold change in k_{cat} gives values of less than 1 for all mutants other than H932Y. (B) The product of the fold change in discrimination and the fold change in k_{cat} gives the shows the most drastic changes with R1096C and R953C.

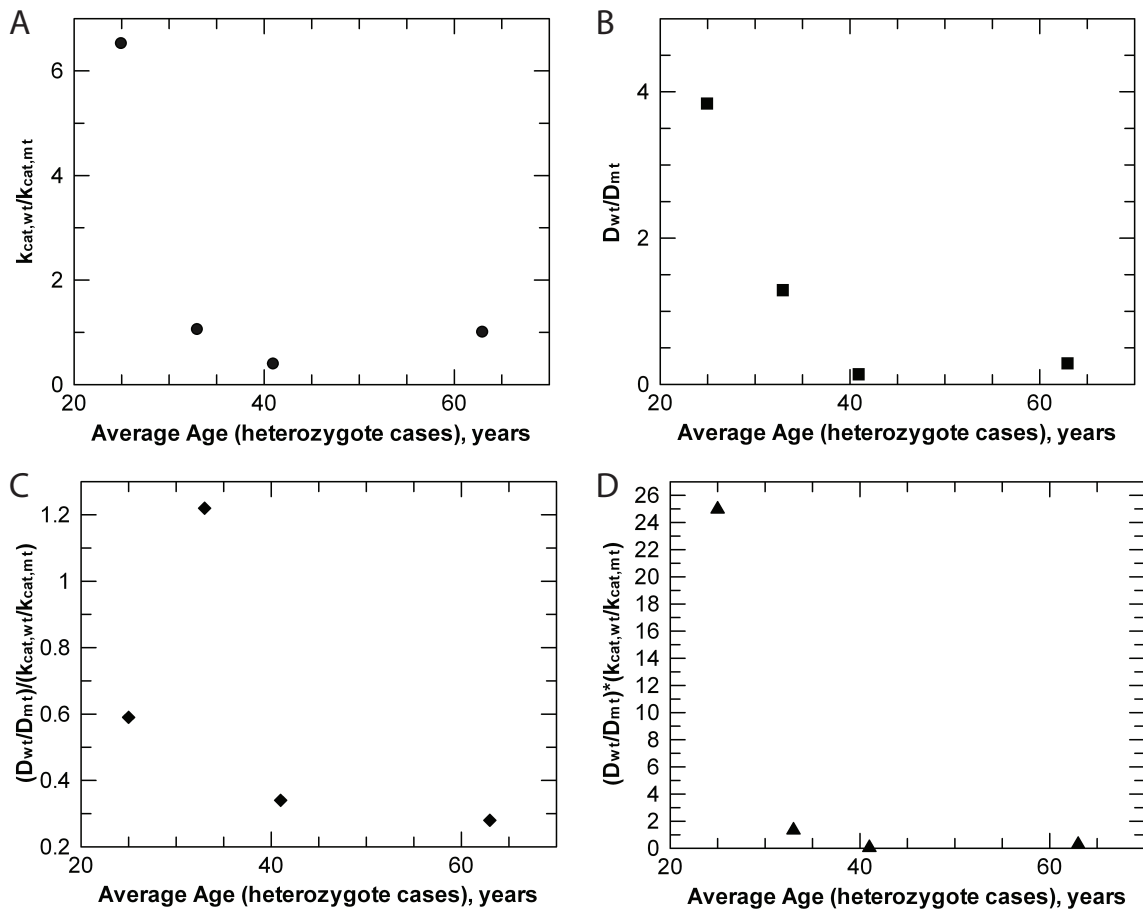


Figure 2.14. *Relating biochemical parameters in POLG mutants to age of onset of disease.* Each plot displays the biochemically-determined parameter on the y-axis versus the average age of disease onset in patients harboring heterozygous mutations in *POLG*. Average age of disease onset for heterozygote cases are as follows: H932Y = 33 years, R943H = 63 years, R953C = 41 years, R1096C = 25 years. (See appendix for clinically reported cases and ages) A. Fold change in k_{cat} (wild-type/mutant). B. Fold change in discrimination (wild-type/mutant). C. The fold change in discrimination divided by the fold change in k_{cat} . D. The product of the fold change in discrimination and the fold change in k_{cat} .

Chapter 3: Characterization of Mitochondrial DNA Polymerase Gamma Active Site Mutations

3.1 INTRODUCTION

This chapter explores three active site residues of Pol γ and their role in nucleotide incorporation, specificity and discrimination. The active site of the polymerase domain in Pol γ is formed by residues in the fingers subdomain and the palm subdomain that come together during the conformational change that occurs upon nucleotide binding (45). This conformational change brings together the positively charged residues of the fingers subdomain to bind the negatively charged triphosphate of the incoming dNTP and align it with the catalytic aspartic acids (D890 and D1135). The crystal structure of Pol γ A (45) suggests that residues E895 and Q1102 of the palm subdomain along with Y951 and Y955 of the fingers subdomain are involved in binding of the nucleotide. The E895 residue is involved in the hydrogen-bonding network under the incoming nucleotide and is highly conserved in Pol γ across species and in family A DNA polymerases (45). The Y951 residue is located on the O helix of the fingers subdomain and has been suggested to bind the ribose of the incoming nucleotide. This residue is involved in the discrimination of dideoxy nucleotides and is responsible for the toxic side effects of dideoxy nucleotides in the mitochondria (124, 125). The third residue studied in this chapter is K947, which binds to the alpha phosphate of the incoming dNTP (45). The relevant active site residues in Pol γ are shown on the crystal structure of the homologous T7 DNA polymerase in Figure 3.1 (47).

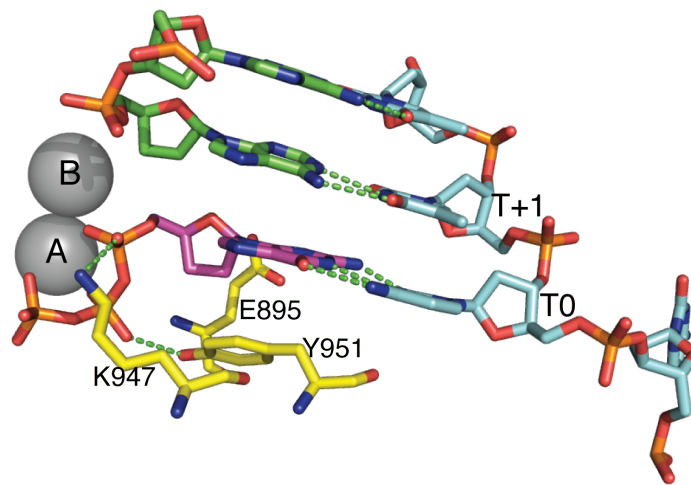


Figure 3.1 *Active site residues of Pol γ .* Homologous structure of T7 DNA polymerase (PDB: 1T7P) showing the conserved residues of the Pol γ active site explored in this chapter. Incoming nucleotide is magenta, template strand is cyan, primer strand is green, active site residues are yellow and labeled with Pol γ amino acid numbers.

Mutations of these residues are rarely seen clinically

The three residues studied in this chapter are absolutely conserved in Pol γ across species and highly conserved within family A DNA polymerases. The few clinical cases that have been reported involving these residues show clinical phenotypes in patients of a young age and in the case of E895G the patient only survived for 36 hours after birth. The conservation of these active site residues along with the clinical data suggests that mutation of these residues are severe and in most cases they are likely to be lethal. Below I will summarize several mutations of active site residues selected for detailed study.

E895A. Residue E895 is involved in the hydrogen-bonding network under the incoming nucleotide (Figure 3.1). Mutations at this position are rarely seen in the population with one case of myopathic myelodysplastic syndrome (MDS) where this position is mutated to a glycine. This mutation E895G was found in a heterozygous

newborn that died soon after birth with generalized floppiness (muscle weakness) and 20% liver mtDNA depletion (58).

K947A. This mutation is not associated with any diseases however, *K947R* has been associated with PEO, facial weakness, proximal myopathy and ovarian failure in one case of a patient who showed symptoms at age 18. The mutation was seen as a compound heterozygote in this patient (64). Lysine 947 binds to the alpha phosphate of the incoming dNTP, and the *K947A* mutation was examined to determine the role of this interaction (45).

Y951F. The mutation of tyrosine 951 to phenylalanine has not been associated with any diseases, however the mutation *Y951N* has been seen in two cases of peripheral neuropathy in patients 22 and 23 years old (61). Tyrosine 951 binds the ribose of the incoming nucleotide and is involved in the discrimination of dideoxy nucleotides (45). The *Y951* at this position is responsible for the toxic side effects of dideoxy nucleotides in the mitochondria, which are incorporated more slowly by the *Y951F* mutant (65).

This chapter will characterize the three mutations of Pol γ listed above that are located near the polymerase active site of Pol γ . The goal of this work is to analyze the biochemical effect of these point mutations in order to gain a better understanding of the role of these residues in catalysis.

3.2 MATERIALS AND METHODS

Cloning expression and purification.

Accessory subunit Pol γ B

The accessory subunit of Pol γ , Pol γ B used in these studies has the first 25 amino acids truncated from the N-terminal end and is modified at the C-terminus to have a His

tag added for purification, as is described in Chapter 2. The protein was expressed in *E. coli* BL21 (DE3) from New England Biolabs. After harvesting the cells, the protein was purified by sequential application of Ni-NTA (Novagen) and Superdex 200 (Amersham Biosciences) columns as described previously (55) and above in Chapter 2.

Catalytic subunit Pol γ A

The clone for the wild-type exonuclease deficient C terminus His tagged Pol γ A was maintained in pUC 19.1 and lacked the first 66 amino acid from the N-terminus as was described in detail in Chapter 2. The exonuclease deficient enzyme with mutations D198A and E200A was used in the studies in this section of work. The mutagenesis of Pol γ A in the pUC19.1 vector was performed using site directed mutagenesis; the PCR mutagenic primers listed in Table 3.1.

Table 3.1 *Mutagenic primers for Pol γ A Active Site Mutants*

E895A

Forward: 5' -ATGTTGACAGCCAGGCGTTGTGGATTGCCGC-3'

Reverse: 5' -GCGCAATCCACAACCGCCTGGCTGTCAACAT-3'

K947A

Forward: 5' -GGCATTTCGCGTGAACATGCAGCGATTTTCAATTACGGTCGTAT-3'

Reverse: 5' -ATACGACCGTAATTGAAAATCGCTGCATGTTCACGCGAAATGCC-3'

Y951F

Forward: 5' -GCGTGAACATGCAAAGATTTTCAATTTCGGTCGTAT-3'

Reverse: 5' -CGTAAATACGACCGAAATTGAAAATCTTTGCATGTT-3'

*mutated codons are underlined

Once mutagenic sequences were confirmed, the Pol γ A clones were transferred to the pBacPak9 transfer vector by a double restriction digest followed by ligation. A recombinant baculovirus expressing each mutant in SF9 insect cells at high viral titers

were then optimized for protein expression before large scale expression occurred. Large scale expression in Sf9 insect cells was followed by the protein purification procedure outlined in detail in Chapter 2. The purification included the sequential application of lysates to a Ni-NTA and an SP Sepharose column. Cell pellets from baculovirus expression of Pol γ A in SF9 cells were thawed and resuspended by stirring in *Pol γ A Lysis Buffer* (0.32 M sucrose, 10 mM HEPES pH 7.5, 0.5% v/v NP-40, 3 mM CaCl₂, 2 mM MgAc.4H₂O, 0.1 mM EDTA, 5mM 2-mercaptoethanol and protease inhibitor cocktail V, EDTA-free (AG Scientific)). The suspension was then centrifuged using a JS4.3 rotor (Beckman) at 1,500xg for 25 minutes. A 3M KCl solution was then added dropwise to the supernatant to obtain a final concentration of 0.5 M KCl. After stirring for 15 minutes on ice in the presence of 0.5 M KCl, the solution was ultracentrifuged at 31,000 rpm for 35 minutes. The supernatant was then incubated with Ni-NTA agarose resin (Qiagen) equilibrated in *Pol γ A Nickel Equilibration Buffer* (20 mM HEPES pH 7.5, 5 mM imidazole pH 8, 0.2 M KCl, 5% glycerol). After binding to the Ni-NTA, the resin was washed with *Pol γ A Nickel Wash Buffer* (20 mM HEPES pH 7.5, 20 mM imidazole pH 8, 0.1 M KCl, 5% glycerol) and eluted with *Pol γ A Nickel Elution Buffer* (20 mM HEPES pH 7.5, 200 mM imidazole pH 8, 0.05 M KCl, 5% glycerol). Fractions were analyzed by SDS-PAGE and those containing Pol γ A were pooled and diluted to 30 mM KCl with *Pol γ A Nickel Dilution Buffer* (20 mM HEPES pH 7.5, 1 mM EDTA pH 8, 5% glycerol). The fractions from the nickel column were then loaded onto an SP Sepharose column (GE Healthcare) equilibrated in *Pol γ A SP Buffer A* (20 mM HEPES pH 7.5, 30 mM KCl, 1 mM EDTA pH 8, 5 mM 2-mercaptoethanol, 5% glycerol) using the AKTA Purifier (GE Healthcare). After loading, the column was then washed with *Pol γ A SP Buffer A* and eluted with a linear gradient from 0-70% *Pol γ A SP Buffer B* (20 mM HEPES pH 7.5, 700 mM KCl, 1 mM EDTA pH 8, 5 mM 2-mercaptoethanol, 5%

glycerol). 1 mL fractions were collected from SP column and the absorbance at 280 nm and 260 nm was recorded. The fractions were then analyzed by SDS-PAGE and those containing Pol γ A were pooled and concentrated using a vivaspin sample concentrator (GE Life Sciences). The protein concentration was then measured by A_{280} using the extinction coefficient $\epsilon_{280} = 243,7900 \text{ M}^{-1}\text{cm}^{-1}$, previously determined (108). Experiments were all performed on the reconstituted holo-enzyme (Pol γ) by combining the catalytic subunit Pol γ A and the accessory subunit Pol γ B with a 4:1 molar excess of Pol γ B:Pol γ A.

Preparation of substrate DNA

DNA substrates were purchased from Integrated DNA Technologies (IDT) and purified by 15% denaturing polyacrylamide gel electrophoresis. Sequences of 25-mer primer and 45-mer template DNA oligomers are listed in Table 3.2.

Table 3.2 DNA primer-template sequences for Pol γ

<u>25/45mer</u>	
25-mer	5' -GCCTCGCAGCCGTCCAACCAACTCA
45-mer	3' -CGGAGCGTCGGCAGGTTGGTTGAGTTGGAGCTAGGTTACGGCAGG

For quench flow assays, the 5' end of the primer oligomer was ^{32}P -labeled using T4 polynucleotide kinase (New England Biolabs) and γ - ^{32}P -ATP according to the manufacturers protocol. After ^{32}P labeling, the reaction was heated to 95°C for 5 minutes and purified using a Bio-Spin P-6 gel column (Bio-Rad) to remove the excess γ - ^{32}P -ATP. The concentration of the purified ^{32}P -5'-labeled primer was determined by TLC.

Duplex DNA substrates were formed by incubating the 25-mer primer with the 45-mer template at a 1:1 molar ratio in an *Annealing Buffer* (10 mM Tris-HCl pH 7.5, 50

mM NaCl, 1 mM EDTA) and heating to 95°C for 5 minutes before allowing to slowly cool to room temperature.

Kinetics of correct nucleotide incorporation

Chemical-quench flow assays were performed to measure the incorporation of correct nucleotide by mutants of Pol γ . These experiments were conducted at 37°C in *Pol γ Reaction Buffer* (50 mM Tris-HCl (pH 7.5), 100 mM NaCl, 12.5 mM MgCl₂) using a RQF-3 rapid-quench-flow apparatus (KinTek Corp). For these single turnover experiments, preformed enzyme-DNA complex (150 nM Pol γ A, 600 nM Pol γ B, 75 nM 5'-³²P-labeled 25/45mer DNA) was mixed rapidly with an equal volume of Mg-dATP²⁻ at various concentrations (0.2, 0.5, 1.5, 3, 5.5, and 8.5 μ M dATP for WT). The final concentration of MgCl₂ was 12.5 mM. After various time intervals, the reactions were quenched by mixing with 0.5 M EDTA. All concentrations listed are final.

After quenching, the reactions were mixed with denaturing PAGE loading dye (0.25% bromophenol blue, 0.25% xylene cyanol) and separated on a 15% denaturing polyacrylamide sequencing gel. The dried gel was then exposed to a storage phosphor screen and the bands were quantified using a Typhoon scanner (GE) and ImageQuant 5.0 (Molecular Dynamics). The concentration of the product formed over time was calculated as the product of the concentration of substrate ³²P-labeled DNA added times the fraction of material in the 26-mer band. Data collected were fit by global data fitting methods described below and in Chapter 2.

Nucleotide misincorporation assays

Misincorporation assays were performed in a similar assay as described above for correct dNTP incorporation, however the formation of a mismatch often required longer

time scales and higher concentrations of the incorrect dNTP. For time scales greater than 5 seconds, manual hand mixing was done instead of using the rapid-quench-flow instrument. In all assays, a maximum of 5 mM dNTP (final concentration after mixing) was not exceeded in order to avoid complications due to nonspecific inhibition (110, 111). For misincorporation experiments a preformed enzyme-DNA complex (150 nM Pol γ A, 600 nM Pol γ B, 75 nM 5'-³²P-labeled 25/45mer DNA) with an equal volume of Mg-dNTP²⁻ at various concentrations (0.2, 0.5, 1.5, 3, 5.5, and 8.5 μ M dATP for WT) in *Pol γ Reaction Buffer*. Reactions were quenched with 0.5 M EDTA after various time intervals from (0 – 1.5 hours, in some cases) and the products were analyzed on a 15% denaturing polyacrylamide sequencing gel. Data collected were fit by global data fitting methods described below and in Chapter 2.

Pyrophosphate Release Assay

Pyrophosphate release was measured in a stopped-flow coupled assay as described previously (119, 126) using an AutoSF-120 series stopped-flow instrument from KinTek Corp. For this assay, 100 nM Pol γ was preincubated with 90 nM 25-mer/45mer DNA duplex in the presence of 1.5 μ M E. coli phosphate binding protein (PBP) with MDCC (7-Diethylamino-3-(((2-Maleimidyl)ethyl)amino)carbonyl)-coumarin) label at mutated Cys197, 100 μ M 7-methylguanosine (Sigma), 0.02 units/ml purine nucleoside phosphorylase (Sigma), and 0.6 μ M yeast inorganic pyrophosphatase (PPase) (Sigma) in *Pol γ reaction buffer* for 15 minutes at 37°C. The reaction was then started by mixing with a solution containing various concentrations of dATP in the presence of 100 μ M 7-methylguanosine (Sigma), 0.02 units/ml purine nucleoside phosphorylase (Sigma), and 0.6 μ M yeast inorganic pyrophosphatase (Sigma) in *Pol γ reaction buffer*. The MDCC fluorophore on PBP was excited at 425 nm and the change in

fluorescence was measured as a function of time using a 475 nm single-band bandpass filter (Semrock).

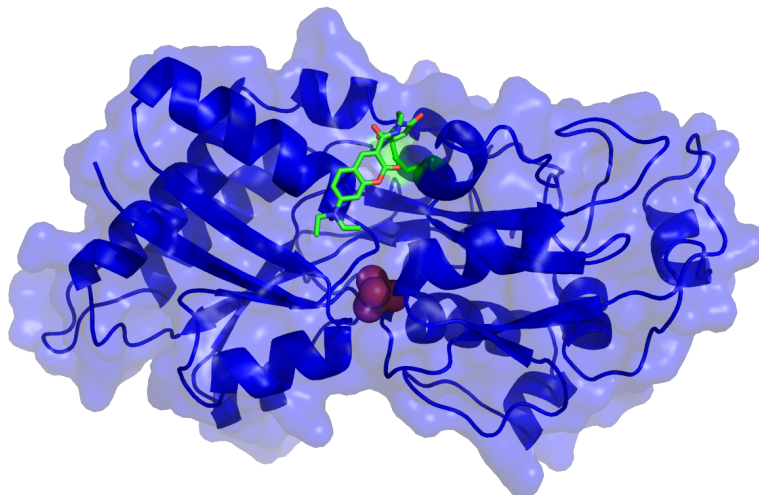


Figure 3.2. *Crystal structure of MDCC-PBP.* (PDB: 1A54) (127) The structure of phosphate binding protein from *E. coli* is shown with the labeling site mutation A197C and labeled with MDCC. The MDCC coumarin fluorophore is displayed in green and is located in the hydrophobic groove on the surface of the molecule near the phosphate binding site which in this case is bound by a dihydrogenphosphate ion (pink spheres).

Control experiments for phosphate binding to PBP-MDCC as well as pyrophosphate hydrolysis by PPase followed by subsequent phosphate binding to PBP-MDCC were performed to ensure that these rates were sufficiently fast so that the coupled assay measures the rate of pyrophosphate release by Pol γ .

Pyrophosphate Release Controls

Phosphate binding to PBP-MDCC. For this assay, 3 μM *E. coli* phosphate binding protein (PBP) with MDCC label, was preincubated with 200 μM 7-methylguanosine (Sigma) and 0.04 units/ml purine nucleoside phosphorylase (Sigma) in *Pol γ reaction buffer* for 15 minutes at 37°C. The reaction was then started by mixing with a solution containing various concentrations of Na_2HPO_4 (0.2, 0.5, 1, 2, 3, and 5 μM) in *Pol γ Reaction Buffer*.

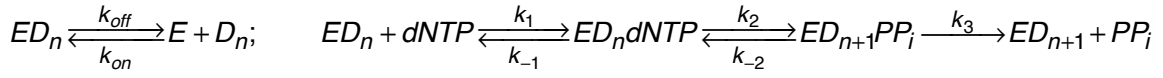
Pyrophosphate hydrolysis followed by phosphate binding to PBP-MDCC. For this assay, 3 μM *E. coli* phosphate binding protein (PBP) with MDCC label, was preincubated with 100 μM 7-methylguanosine (Sigma), 0.02 units/ml purine nucleoside phosphorylase (Sigma) and 1.2 μM yeast inorganic pyrophosphatase (PPase) (Sigma) in *reaction buffer* for 15 minutes at 37°C. The reaction was then started by mixing with a solution containing various concentrations of NaPP_i (0.05, 0.2, 0.4, 0.6 and 0.8 μM) in the presence of 100 μM 7-methylguanosine (Sigma) and 0.02 units/ml purine nucleoside phosphorylase (Sigma) in *Pol γ Reaction Buffer*.

For both assays, the MDCC fluorophore on PBP was excited at 425 nm and the change in fluorescence was measured as a function of time using a 475 nm single-band bandpass filter (Semrock).

Global data fitting

Data from chemical quench flow and stopped flow experiments were fit globally using the KinTek Explorer simulation software (Kintek Corp). The details of this fitting are described in Chapter 2. Briefly, the fitting by simulation involves inputting a model sequence of reaction steps, initial estimates of rate constants, the experimental setup and after trial and refinement, a final convergence to the best fit value for each parameter is obtained by nonlinear regression based upon numerical integration of the rate equations (112, 113). Two models were used in the fitting of data in this chapter.

Scheme 3.1



Scheme 3.1 is the expanded model for nucleotide binding and incorporation that includes a rate of pyrophosphate release (k_3) that is slow and allows the rate of chemistry k_2 to be reversible and include the k_{-2} step. When the expanded model of Scheme 3.1 is used for fitting and the contributions of k_{-2} and k_3 cannot be neglected, k_{cat} , K_m and k_{cat}/K_m were calculated according to Equations (Eqn) 3.1, 3.2 and 3.3.

$$\text{Eqn 3.1} \quad k_{cat} = \frac{k_2 k_3}{k_2 + k_{-2} + k_3}$$

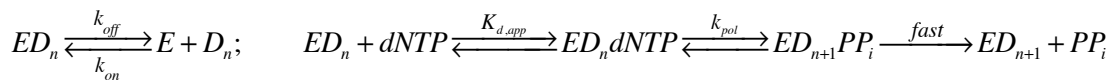
$$\text{Eqn 3.2} \quad K_m = \frac{k_2 k_3 + k_{-1}(k_{-2} + k_3)}{k_1(k_2 + k_{-2} + k_3)}$$

$$\text{Eqn 3.3} \quad k_{cat} / K_m = \frac{k_1 k_2 k_3}{k_2 k_3 + k_{-1} k_{-2} + k_{-1} k_3}$$

As was the case in Chapter 2, the previously determined rates of DNA binding and release were used in the model ($K_{d,DNA}=10\text{nM}$, $k_{off,DNA} = 0.02 \text{ s}^{-1}$) (114). Additionally, the equilibrium constant for the initial complex formation was estimated by assuming diffusion-limited nucleotide binding ($k_1=100 \mu\text{M}^{-1}\text{s}^{-1}$) and allowing the dissociation rate to vary during fitting.

Scheme 3.2 shows the minimal model for nucleotide incorporation that assumes the binding of the nucleotide is in a rapid equilibrium and the rates after chemistry are fast so that the reverse of chemistry can be neglected. By fitting the concentration dependence of the rate of polymerization to the model of Scheme 3.2, an apparent nucleotide dissociation constant ($K_{d,app}$) is obtained along with a maximum rate of nucleotide incorporation (k_{pol}).

Scheme 3.2



As was described in Chapter 2, in the simple model of Scheme 3.2 the specificity constant (k_{cat}/K_m) is defined as the ratio of $k_{\text{pol}}/K_{\text{d,app}}$. In this case, the term from quench flow experiments is reported as an apparent K_d and would equal the true K_d if the binding occurred in a single step. Because we are measuring the concentration dependence of incorporation and not the actual ground state binding of the nucleotide, then there are in multiple steps involving a conformational change of the enzyme (128, 129), this apparent K_d is more accurately defined as a Michaelis constant.

In experiments of this chapter, when noted, the pyrophosphate release stopped flow experiments were fit globally with chemical quench flow data to determine the rate of pyrophosphate release (Scheme 3.1, k_3). The control experiments for the coupled assay measuring pyrophosphate release were included in the global fitting of the data collected for the Pol γ mutants and the model was adapted to include steps for pyrophosphate hydrolysis by PPase and phosphate binding to PBP-MDCC.

In the results tables, the standard error values are reported for each parameter along with the upper and lower limits for each fitted parameter. These limits are derived from a threshold in the confidence contours as described in Chapter 2 ($\text{Chi}_{\text{min}}^2/\text{Chi}_{x,y}^2 = 1.1$) (113).

3.3 RESULTS

Kinetics of correct incorporation

The kinetics of incorporation of the correct nucleotide (dATP) for the three Pol γ active site mutants (E895A, Y951F and K947A) were explored using rapid quench flow methods to measure the apparent nucleotide dissociation constant (K_d) and the maximum rate of incorporation (k_{pol}). The results are summarized in Table 3.3 and 3.4.

Table 3.3 *Pol γ Kinetic Parameters of dATP Incorporation*

	$1/K1$	k_2	k_{-2}	k_3
	μM	s^{-1}	s^{-1}	s^{-1}
WT				
dATP	0.7 ± 0.14 (0.62 - 0.84)	30 ± 2 (29 - 33)	0	<i>fast</i>
E895A				
dATP	17 ± 0.3 (13 - 17.6)	2.4 ± 0.04 (2.2 - 3.1)	1.9 ± 0.07 (1.6 - 3.5)	0.4 ± 0.005 (0.34 - 0.47)
Y951F				
dATP	1.6 ± 0.1 (1.3 - 1.2)	6.9 ± 0.1 (6.4 - 7.6)	0	<i>fast</i>
K947A				
dATP	1320 ± 230 (1130 - 1780)	5.2 ± 0.6 (4.6 - 6.3)	0	<i>fast</i>

This table summarizes the kinetic parameters derived in globally fitting data to Scheme 3.1 and 3.2 to define the kinetics of incorporation of dATP by wild-type and mutant forms of Pol γ . Data for the wild-type enzymes is from (116). Numbers in parenthesis give the lower and upper limits derived from the confidence contour analysis in fitting the data.

Table 3.4 *Pol γ Kinetic Parameters of dATP Incorporation*

	K_d μM	k_{pol} s^{-1}	$k_{pol}/K_{d,app}$ $\mu M^{-1} s^{-1}$	Fold Change
WT				
dATP	0.7 ± 0.14	30 ± 2	43 ± 9	-
E895A				
dATP	8.3 ± 0.3	0.2 ± 0.005	0.024 ± 0.001	1790
Y951F				
dATP	1.6 ± 0.1	6.9 ± 0.1	4.3 ± 0.3	10
K947A				
dATP	1320 ± 230	5.2 ± 0.6	0.004 ± 0.0008	11000

This table summarizes the kinetic parameters derived in globally fitting data to Scheme 3.1 and 3.2 to define the kinetics of incorporation of dATP by wild-type and mutant forms of Pol γ . Data for the wild-type enzymes is from (116). Numbers in parenthesis give the lower and upper limits derived from the confidence contour analysis in fitting the data.

The data for dATP incorporation by the Y951F mutant were fit to the simple model (Scheme 3.2) for nucleotide incorporation and showed a 4.3-fold decrease in k_{pol} and a 2.3-fold increase in $K_{d,app}$ relative to wild-type. This resulted in a 10-fold decrease in the specificity constant compared to wild-type. Slow pyrophosphate release was not required to fit the dATP incorporation data for this mutant (Figure 3.3A and C). The quench flow data and stopped flow PP_i release data for Y951F were globally fit to the model shown in Scheme 3.2 with fast pyrophosphate release. The K947A mutant was also fit to the simple model in Scheme 3.2 and is consistent with fast pyrophosphate

release. The fitting of the K947A data resulted in a modest decrease in k_{pol} by 5.7-fold but a drastic increase in $K_{\text{d,app}}$ by 1880-fold, leading to a 11,000-fold decrease in the specificity constant as compared to wild-type. Alternatively, the data for E895A showed an amplitude dependence on nucleotide concentration and the expanded model with slow pyrophosphate release was used for fitting (Scheme 3.1). This was further supported when the pyrophosphate release experiment was added to the quench flow data and both were fit to the model in Scheme 3.1. These two datasets included in the global fit for E895A are shown in Figure 3.3B and D. The fitting of these data for E895A resulted in a value for $1/K_1=17 \mu\text{M}$, $k_2=2.4 \text{ s}^{-1}$, $k_{-2}=1.9\text{s}^{-1}$, and $k_3= 0.4 \text{ s}^{-1}$. These rates lead to a k_{cat}/K_m value of $0.02 \mu\text{M}^{-1}\text{s}^{-1}$ which is 2,150-fold lower than that of wild-type enzyme. The data in Figure 3.4 show the control experiments included in global fits of Y951F dATP incorporation and E895A incorporation that utilized pyrophosphate release experiments. The pyrophosphate release assay could not be used in the case of K947A because the dATP concentrations required to saturate binding for this mutant exceeded the limit of the coupled assay due to the apparent direct binding of dATP to MDCC-PBP above concentrations of 1 mM dATP.

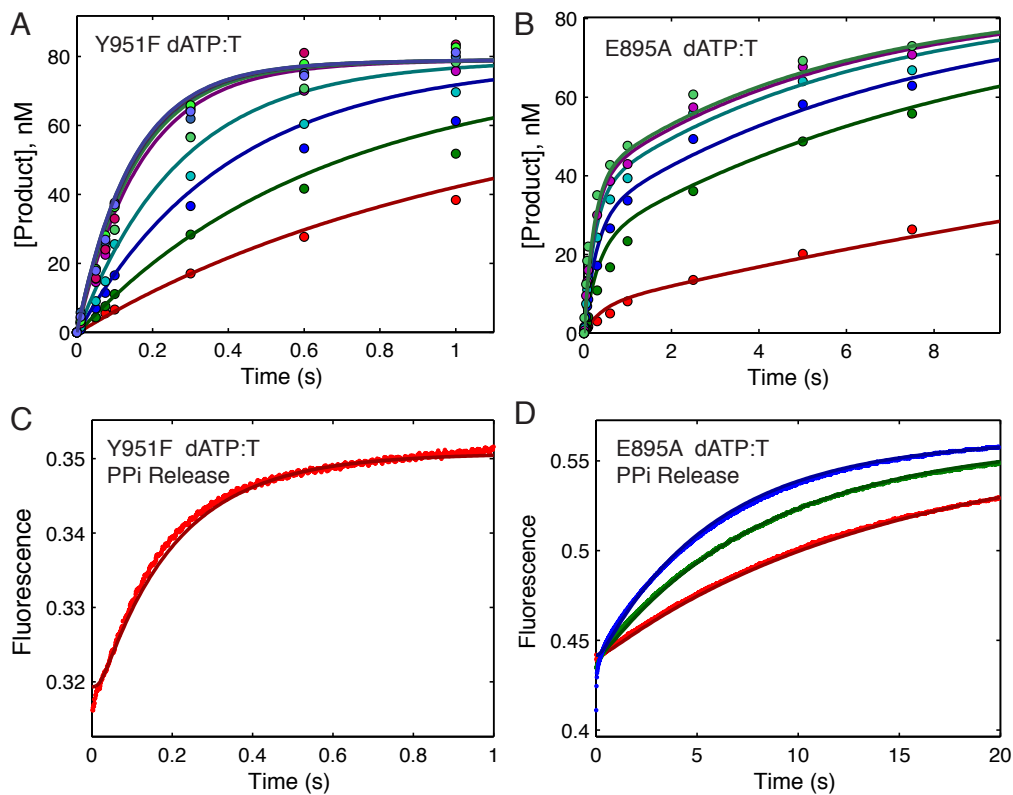


Figure 3.3 Kinetics of incorporation of dATP for the Y951F and E895A mutants. For each concentration series, an enzyme-DNA complex was rapidly mixed with MgCl_2 and various concentrations of dATP. In each experiment, the final concentrations of enzyme and DNA after mixing were 150-175 nM and 75-100 nM, respectively. Results of the global fitting are shown and in each case the concentration of active enzyme was adjusted to fit the amplitude of the curves in the quench flow experiment. (A) Incorporation of dATP by Y951F exo- Pol γ at various concentrations (0.25, 0.5, 1, 2, 10, 20, 50, 100, 250 and 500 μM) by quench flow methods. (B) Incorporation of dATP for E895A exo- Pol γ at various concentrations (2, 12.5, 25, 75, 200, and 500 μM) by quench flow methods. (C) Incorporation of dATP and release of pyrophosphate by Y951F exo- Pol γ at 5 μM dATP measured by stopped flow methods using PBP-MDCC. The data in A and B, along with pyrophosphate release control experiments (Figure 3.4), were globally fit to the mechanism shown in Scheme 3.2, yielding an apparent K_d of $1.6 \pm 0.1 \mu\text{M}$ and k_{pol} of $6.9 \pm 0.1 \text{ s}^{-1}$. (D) Incorporation of dATP and release of pyrophosphate by E895A exo- Pol γ at 5, 15 and 100 μM dATP measured by stopped flow methods using PBP-MDCC. The data in C and D, along with pyrophosphate release control experiments were fit to the mechanism shown in Scheme 3.1, yielding an apparent K_d of $17 \pm 0.3 \mu\text{M}$, k_2 of $2.4 \pm 0.04 \text{ s}^{-1}$, k_2 of $1.9 \pm 0.07 \text{ s}^{-1}$, and k_3 of $0.4 \pm 0.005 \text{ s}^{-1}$.

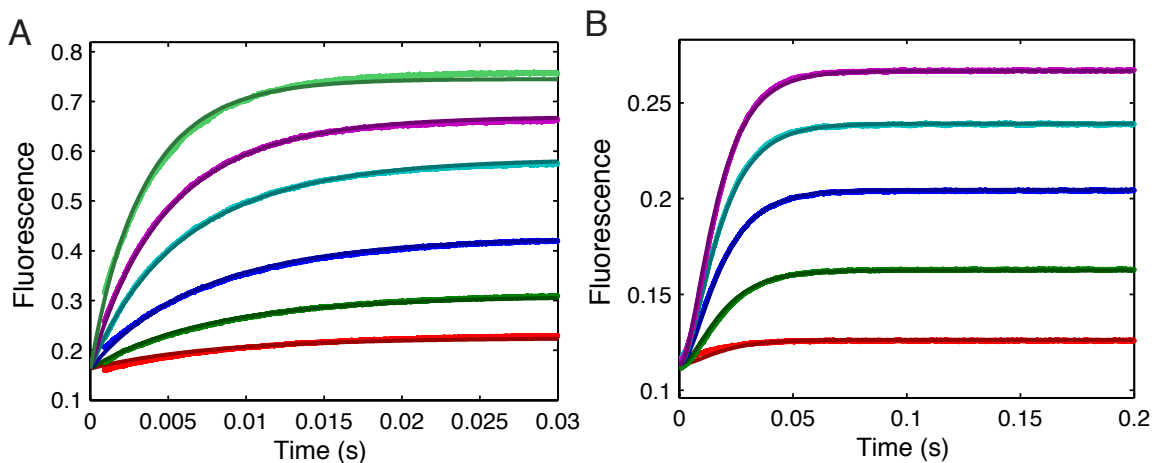


Figure 3.4 Stopped flow controls for pyrophosphate release assay. A. Phosphate binding to PBP-MDCC. For this assay, 3 μM *E. coli* phosphate binding protein (PBP) with MDCC label, was preincubated with 200 μM 7-methylguanosine (Sigma) and 0.04 units/ml purine nucleoside phosphorylase (Sigma) in *Pol γ Reaction Buffer* for 15 minutes at 37°C. The reaction was then started by mixing with a solution containing various concentrations of Na_2HPO_4 (0.2, 0.5, 1, 2, 3, and 5 μM) in *reaction buffer B*. Pyrophosphate hydrolysis followed by phosphate binding to PBP-MDCC. For this assay, 3 μM *E. coli* phosphate binding protein (PBP) with MDCC label, was preincubated with 100 μM 7-methylguanosine (Sigma), 0.02 units/ml purine nucleoside phosphorylase (Sigma) and 1.2 μM yeast inorganic pyrophosphatase (PPase) (Sigma) in *Pol γ Reaction Buffer* for 15 minutes at 37°C. The reaction was then started by mixing with a solution containing various concentrations of NaPP_i (0.05, 0.2, 0.4, 0.6 and 0.8 μM) in the presence of 100 μM 7-methylguanosine (Sigma) and 0.02 units/ml purine nucleoside phosphorylase (Sigma) in *Pol γ Reaction Buffer*. For both assays, the MDCC fluorophore on PBP was excited at 425 nm and the change in fluorescence was measured as a function of time using a 475 nm single-band bandpass filter (Semrock).

Nucleotide Misincorporation Assays

Chemical quench flow assays were performed on Pol γ to monitor the incorporation of mismatches in order to investigate the discrimination of the Pol γ mutants against mismatches. All of the mutants were prepared in the background of an exonuclease deficient variant and lacked significant proofreading ability so that the rates of misincorporation could be measured (22, 49). Misincorporation assays measured the amount of 25-mer DNA primer extended by the polymerase upon mixing with various concentrations of the incorrect nucleotide and MgCl_2 for different time intervals. The results plotting the accumulation of product over time were fit to the models from either Scheme 3.1 or Scheme 3.2. In all cases, the minimal model (Scheme 3.2) was first used in an attempt to fit the data, and in cases when an amplitude dependence on nucleotide concentration was observed, the expanded model in Scheme 3.1 was applied. The results of the fitting are shown in Table 3.5 and summarized in Table 3.6. For each of the 3 mutants tested, the formation of a T:T mismatch and a G:T mismatch required the fitting to the model in Scheme 3.1 to allow for a slow pyrophosphate release step with reversible chemistry. This was seen in the H932Y, H932A and R943H misincorporation results described in Chapter 2 as well as the E895A correct nucleotide incorporation described above. However, the formation of the C:T mismatches by the three mutants of this chapter did not require this expanded model and could be fit to the minimal model with fast pyrophosphate release (Scheme 3.2). The E895A mutant showed a 10-fold reduction in the discrimination of dTTP on a templating TMP compared to that of wild-type (43,000 vs. 430,000) (Figure 3.5A). This mutation also showed a significant decrease in the discrimination for dCTP:TMP with a 27-fold decrease in discrimination compared to that of wild-type. The discrimination for a G:T mismatch by E895A did not significantly

differ from that of wild-type despite the requirement in the model for the slow pyrophosphate release step with the E895A mutant and not for the wild-type.

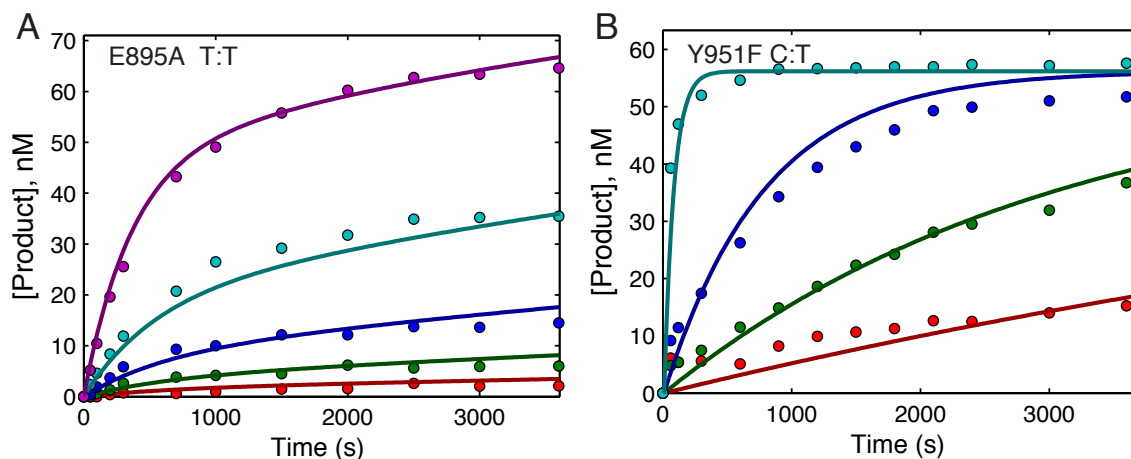


Figure 3.5 Kinetics of misincorporation by the E895A and Y951F mutants. All concentrations listed are final. 150 nM enzyme was preincubated with 75 nM 25/45mer DNA and subsequently mixed with Mg^{2+} and various concentrations of incorrect nucleotide. (A) Formation of a T:T mismatch by E895A exo^- Pol γ at each TTP concentration (20, 50, 125, 375 and 5000 μM) was fit globally to the mechanism shown in Scheme 3.1, yielding an apparent K_d of $1090 \pm 110 \mu M$, k_2 of $0.0018 \pm 0.0007 s^{-1}$, k_2 of $0.001 \pm 0.0005 s^{-1}$, and k_3 of $\leq 0.0004 s^{-1}$. (B) Formation of a C:T mismatch by Y951F exo^- Pol γ at each dCTP concentration (30, 100, 400 and 5000 μM) was fit globally to the mechanism shown in Scheme 3.2 yielding an apparent K_d of $>10,000 \mu M$ and a k_{pol} of $> 0.04 s^{-1}$.

The Y951F mutation showed an increase in discrimination against the C:T and G:T mismatches and only a 1.5-fold decrease in discrimination for the T:T mismatch. In the case of the C:T mismatch for this mutant (Figure 3.5B), the nucleotide binding was so weak that only a lower limit of $K_{d,app}$ could be determined, as well as a lower limit for k_{pol} . Nonetheless, the ratio of these as $k_{pol}/K_{d,app}$ value was well determined based on the concentration dependence of the rate. In the misincorporation assays, a maximum concentration of 5 mM nucleotide was not exceeded in order to minimize complications

from non-specific inhibition at high nucleotide concentrations that have been seen previously (110, 111).

With the K947A mutant, only the formation of a T:T mismatch and a G:T mismatch could be monitored because in the C:T misincorporation experiment very little product was formed and could not be quantified. The T:T mismatch showed a very significant decrease in discrimination with the K947A mutant having a 90-fold decrease in discrimination. The discrimination of a G:T mismatch was also significantly decreased by 18-fold with this mutant.

Table 3.5 *Pol γ Kinetic Parameters of Misincorporation*

	$1/K_1$	k_2	k_{-2}	k_3
	μM	s^{-1}	s^{-1}	s^{-1}
WT				
TTP	81.8 ± 10.9 (40 - 90)	0.01 ± 0.004 (0.006 - 0.01)	(0)	<i>fast</i>
dCTP	1030 ± 193 (810 - 1300)	0.06 ± 0.018 (0.05 - 0.08)	(0)	<i>fast</i>
dGTP	1300 ± 1600 (836 - 4100)	6.6 ± 7.4 (4.5 - 20)	(0)	<i>fast</i>
E895A				
TTP	1090 ± 110 (810 - 1180)	0.0018 ± 0.0007 (0.0013 - 0.0019)	0.001 ± 0.0005 (0.0005 - 0.0015)	≤ 0.0004
dCTP	650 ± 110 (560 - 1360)	0.0005 ± 0.0002 (0.0004 - 0.0007)	(0)	<i>fast</i>
dGTP	800 ± 120 (767 - 1470)	0.004 ± 0.001 (0.0035 - 0.0063)	0.0015 ± 0.0005 (0.0006 - 0.0038)	≤ 0.0019 (2.5×10^{-8} - 0.0016)
Y951F				
TTP	1500 ± 500 (930 - 2700)	0.36 ± 0.03 (0.3 - 0.6)	0.03 ± 0.009 (0.025 - 0.13)	≤ 0.002
dCTP	>10000	>0.04 (0.04 - 0.6)	(0)	<i>fast</i>
dGTP	1350 ± 200 (1140 - 1590)	1.03 ± 0.13 (0.91 - 1.2)	0.33 ± 0.1 (0.25 - 0.45)	0.11 ± 0.03 (0.08 - 0.14)
K947A				
TTP	≥ 7000	0.01 ± 0.007 (0.007 - 0.1)	0.0018 ± 0.0013 (0.0005 - 0.003)	≤ 0.0025
dCTP	-	-	-	-
dGTP	> 2400	0.03 ± 0.005 (0.004 - 0.4)	0.0009 ± 0.0005 (0.0002 - 0.003)	≤ 0.002

This table summarizes the kinetic parameters derived in globally fitting data to define the kinetics of misincorporation against a template dT by wild-type and mutant forms of Pol γ . Numbers in parenthesis give the lower and upper limits derived from the confidence contour analysis in fitting the data. Data for the wild-type enzyme was obtained from (116).

Table 3.6 *Pol γ Kinetic Parameters of Misincorporation*

	k_{cat} s^{-1}	K_m μM	k_{cat}/K_m $\mu M^{-1} s^{-1}$	Discrimination
WT				
TTP	0.01 ± 0.004	81.8 ± 10.9	0.0001 ± 0.00005	430,000
dCTP	0.06 ± 0.018	1030 ± 193	0.00006 ± 0.00002	717,000
dGTP	6.6 ± 7.4	1300 ± 1600	0.005 ± 0.008	8,600
E895A				
TTP	0.0002 ± 0.0001	475 ± 220	$4.7 \times 10^{-7} \pm 3.1 \times 10^{-7}$	43,000
dCTP	0.0005 ± 0.0002	650 ± 110	$7.7 \times 10^{-7} \pm 3.3 \times 10^{-7}$	26,000
dGTP	0.001 ± 0.0003	370 ± 95	$2.8 \times 10^{-6} \pm 1.1 \times 10^{-6}$	7,000
Y951F				
TTP	0.0018 ± 0.0002	122 ± 54	$1.5 \times 10^{-5} \pm 0.7 \times 10^{-5}$	290,000
dCTP	>0.04	>10000	$3.6 \times 10^{-6} \pm 0.5 \times 10^{-6}$	1,200,000
dGTP	0.08 ± 0.02	400 ± 130	$0.0002 \pm 8 \times 10^{-5}$	22,000
K947A				
TTP	0.0017 ± 0.0015	2100 ± 1200	$8.3 \times 10^{-7} \pm 8.6 \times 10^{-7}$	4,800
dCTP	-	-	-	-
dGTP	0.0018 ± 0.0004	210 ± 48	$8.6 \times 10^{-6} \pm 2.7 \times 10^{-6}$	470

The table summarizes the k_{cat} and K_m values governing misincorporation by mutant forms of Pol γ , calculated from the data in Table 3.5. Data for the wild-type enzyme is from (116). Discrimination was calculated as the ratio of k_{cat}/K_m values for correct versus mismatched dNTP.

3.4 DISCUSSION

The active site mutations studied here were explored to gain a better understanding of the role of these conserved residues in the kinetics of nucleotide incorporation. The three residues probed, E895, Y951 and K947 are hypothesized to be involved in alignment of the incoming nucleotide at the active site of Pol γ and therefore understanding the effect of mutation of these residues will provide an important contribution to the knowledge of their role in polymerization. Previous studies have been reported on these residues in Pol γ , however their steady state assays have overlooked

details that were revealed in these pre-steady state assays and derived incorrect values for key kinetic parameters (130). Figure 3.6 displays a summary of all mutants from this chapter, showing the individual contributions of K_d and k_{pol} to changes in enzyme specificity due to a mutation in Pol γ . Data from Table 3.4 was used to plot the effect of each mutation on catalytic efficiency of Pol γ on a free energy scale. This figure reveals the most drastic effect on enzyme specificity was in the K947A mutant and was largely due to a decrease in K_d for the mutant (dark color). The large change in specificity constant for the E895A mutant was largely due to the decrease in k_{pol} compared to wild-type but the increase in $K_{d,app}$ also contributed to the defect of this mutant.

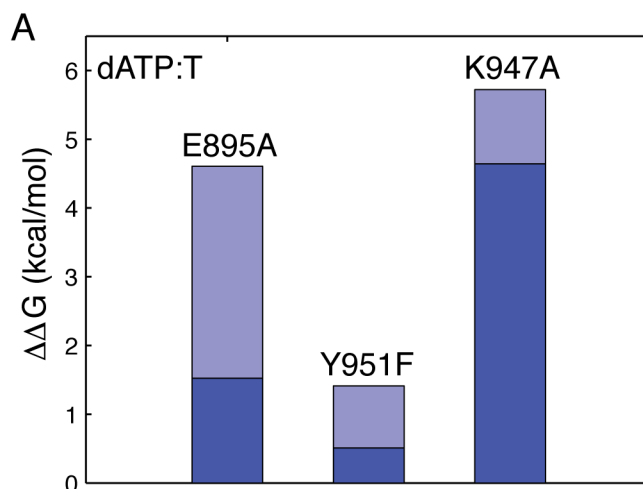


Figure 3.6. Contributions of K_d and k_{pol} to specificity displayed on a free energy scale.

The Y-axis displays free energy $\Delta\Delta G = RT \ln(R)$, where R is the ratio of K_d or k_{pol} values. On this scale, a positive $\Delta\Delta G$ equals the free energy difference favoring the WT over the mutant, whereas a negative value would indicate that the mutant is favored over the WT. K_d values for each mutant divided by the K_d for the WT ($K_d \text{ mut}/K_d \text{ WT}$), and the corresponding ratios of k_{pol} values $k_{pol} \text{ WT}/k_{pol} \text{ mut}$ are shown. Values represent the contributions of ground-state binding (K_d , darker color) and rate of polymerization (k_{pol} , lighter color) to the net specificity (k_{pol}/K_d), represented by the sum of the two.

Mutation E895A

A 2003 study on this mutation of Pol γ (130) reported that the k_{cat} for this mutant was 0.49 s^{-1} , the K_{m} was $140 \text{ }\mu\text{M}$ and the $k_{\text{cat}}/K_{\text{m}}$ was $0.003 \text{ }\mu\text{M}^{-1}\text{s}^{-1}$. This same study reported values for the wild-type enzyme that were $k_{\text{cat}} = 3.7 \text{ s}^{-1}$, the K_{m} was $2.6 \text{ }\mu\text{M}$ and the $k_{\text{cat}}/K_{\text{m}}$ was $1.4 \text{ }\mu\text{M}^{-1}\text{s}^{-1}$, which differs substantially from recently published results from the same group (106) where $k_{\text{cat}} = 72 \text{ s}^{-1}$, the K_{m} was $2.1 \text{ }\mu\text{M}$ and the $k_{\text{cat}}/K_{\text{m}}$ was $34 \text{ }\mu\text{M}^{-1}\text{s}^{-1}$. The group's results for E895A suggest a 466-fold change $k_{\text{cat}}/K_{\text{m}}$ from wild-type to mutant. However, the steady state assays used in this work do not give any information about the chemistry step of the reaction because steady state rates are governed by the rate of DNA release and therefore the effect of the mutation is not fully realized in these types of studies. The pre-steady state kinetic assays in the work presented here measuring the kinetics of single nucleotide incorporation and rigorous global fitting of the data to a model, reveal unique features of these mutants that are not seen with wild-type enzyme or in steady state assays. The data here shows a 1790-fold decrease in $k_{\text{pol}}/K_{\text{d,app}}$ for E895A (Figure 3.6) and the presence of slow pyrophosphate release after chemistry (Figure 3.3B and D). The amplitude dependence of the quench flow data and the measurement of pyrophosphate release in the stopped flow assay using *E. coli* phosphate binding protein affirm the step of slow pyrophosphate release following correct nucleotide incorporation to be 0.4 s^{-1} . In misincorporation experiments the formation of a T:T mismatch as well as a G:T mismatch also required slow pyrophosphate release steps but these were considerably slower at $<0.0019 \text{ s}^{-1}$. The overall fidelity of E895A mutant was mildly affected with the discrimination for a T:T mismatch decreased 10-fold compared to wild-type and the discrimination for C:T mismatch decreased 27-fold. The discrimination for a G:T mismatch was comparable to that of wild-type.

Mutation Y951F

The 2003 study mentioned above on E895A also examined Y951F (130). Using steady state methods the authors showed the k_{cat} for this mutant was 1.8 s^{-1} , the K_m was $2 \text{ }\mu\text{M}$ and the k_{cat}/K_m was $0.9 \text{ }\mu\text{M}^{-1}\text{s}^{-1}$. Which compared to their values for wild-type Pol γ , did not suggest a large change due to this mutation. Their results suggested a 1.5-fold change in k_{cat}/K_m from wild-type to mutant whereas the work here suggests a slightly more significant, 10-fold change coming from a 2-fold increase in K_m and a 5-fold decrease in k_{cat} . Overall the mutation did not drastically affect the k_{pol} or $K_{\text{d,app}}$ of the enzyme, possibly due to the presence of the H932 residue that also interacts with the β -phosphate of the incoming nucleotide. The mutation of the H932 residue to tyrosine (results in Chapter 2) resulted in a much more drastic effect on $K_{\text{d,app}}$ with a 100-fold change compared to wild-type, and no significant effect on k_{cat} . The results characterizing the residues interacting with the β -phosphate suggest that in the absence of the histidine at position 932, the tyrosine at position 951 can still stabilize the transition state of the reaction and therefore the k_{cat} is not reduced. However, in the absence of the tyrosine at position 951, the transition state is not as well stabilized and the k_{cat} is reduced. The histidine at position 932 showed a more important role in nucleotide binding affinity than Y951, but their roles appear to be complementary in their interactions with the incoming nucleotide.

Mutation K947A

Mutation of K947 to alanine showed the most drastic effect and therefore suggests an important role for this residue in polymerization. This residue is thought to interact with the α -phosphate of the incoming nucleotide and act to stabilize the developing negative charge of the transition state during nucleotide incorporation (45). The removal of the positively charge lysine at this position renders this residue unable to stabilize the

negatively charge of the transition state and therefore the rate of chemistry is reduced 6-fold. Even more dramatically affected is the nucleotide binding which was reduced 1,885-fold. This indicates that the interaction of the lysine at position 947 with the incoming nucleotide plays a key role in the affinity of the nucleotide. The fidelity of this mutant was also drastically affected due to large changes in both the K_m and the k_{cat} for formation of mismatches. Overall this mutation had a very dramatic effect on nucleotide incorporation.

Relating active site mutations to disease mutations

The results of the characterization of these three mutants can be applied to gain a better understanding of not only the role of these residues in polymerization but also a better understanding of the very few clinically reported cases of mutations at these residues. Of these mutants, the Y951F mutation showed the least effect on k_{cat}/K_m as well as the least change in fidelity. This correlates with the disease mutations of Y951N that have been reported in two cases (61). In these cases, 2 patients in their young 20s showed symptoms of peripheral neuropathy. No other mutations at this residue have been reported. A slightly more affected patient was seen carrying the K947R mutation and presented symptoms of adult onset PEO at 18 years old (64). Our studies confirm the high importance of this residue and it perhaps makes sense that the only clinically tolerated mutation of this lysine is to an arginine. Our alanine mutant showed drastic effects on the specificity constant for nucleotide incorporation and the fidelity, however it is possible that the mutation to an arginine may be less detrimental, but this would need to be tested. Finally the most detrimental of the disease mutations of these residues is the report of the E895G mutation that was found as a compound heterozygote in a patient that died 36-hours after birth (58). Our results suggested a 1790-fold decrease in

specificity constant for this mutant. The clinical results suggest that this mutant was able to function as a compound heterozygote at least for the fetus to survive and for the baby to be delivered but that the mutation was indeed lethal in the newborn.

Figure 3.7 displays the two proposals for a calculation of a “Mutation Severity Index” for *POLG*-related diseases that was described for the disease-associated mutations in Chapter 2. Using data presented for the mutants in this chapter, these analyses are an attempt to apply a quantitative basis to physiological effects of these mutations in Pol γ . Figure 3.7A displays the simple explanation where a slow enzyme making errors is not as detrimental to mtDNA as a fast enzyme. Under this assumption, the Mutation Severity Index value would be calculated as the fold change in discrimination for mutant divided by the fold change in k_{cat} ($(D_{wt}/D_{mt})/(k_{cat,wt}/k_{cat,mt})$). In this case, a decrease in discrimination could be offset by a comparable decrease in k_{cat} . This calculated Mutation Severity Index value is shown in Figure 3.7A for all mutants of this chapter, with the K947A mutant having the largest calculated value due to the large decrease in discrimination by the mutant (146-fold) compared to wild-type and the modest decrease in k_{cat} (5-fold).

An alternative interpretation of the relationship between the discrimination and k_{cat} for disease-associated mutations presented in Chapter 2, was that Mutation Severity Index value would be better described by the product of the change in discrimination and change in k_{cat} compared to wild-type (3.7B). In this case, a defect in discrimination by a mutant would be compounded by a defect in the k_{cat} . In this case, all of the active site mutants studied in this chapter result in a calculated index value greater than 1 with K947A having the largest effect.

Overall, the pre-steady state characterization of these active site residues indicate the importance of these residues in nucleotide binding, incorporation and pyrophosphate

release. It is not surprising that there are very few clinical reports of mutations at these residues and those that do occur are rare and exhibit a severe disease phenotype.

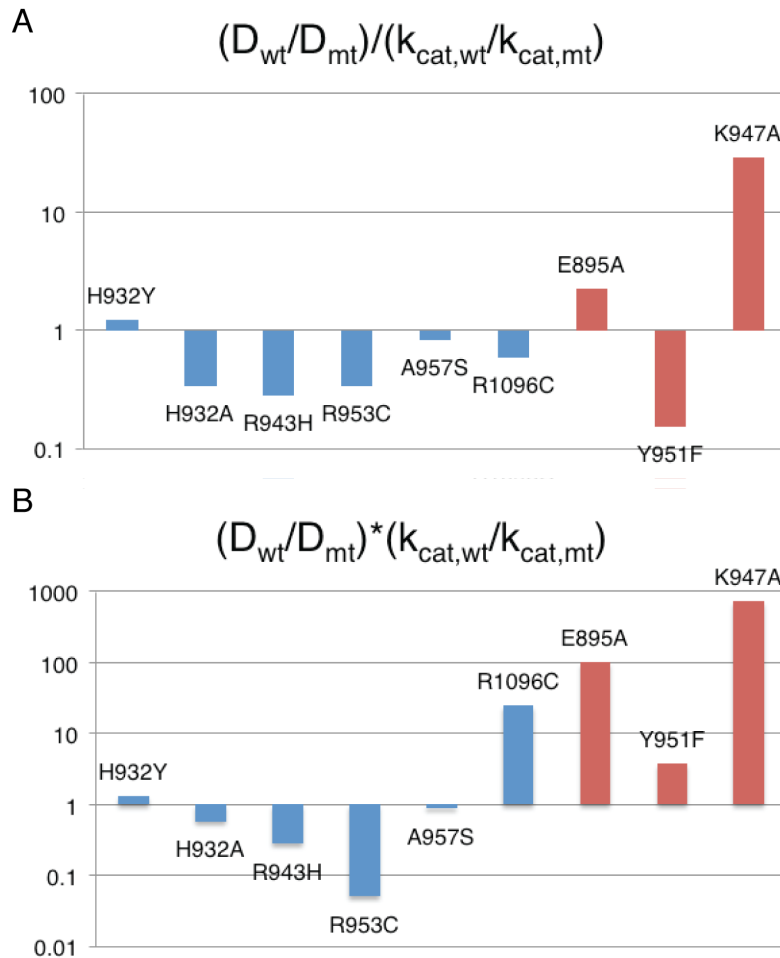


Figure 3.7. *Calculating a Mutation Severity Index for Pol γ mutants.* Modified from Figure 2.13 (blue) to include mutants from this chapter (red). Bar graphs show the relationship between the fold changes in discrimination and k_{cat} for mutants of Pol γ versus wild-type on a log scale. (A) The fold change in discrimination divided by the fold change in k_{cat} . (B) The product of the fold change in discrimination and the fold change in k_{cat} .

Chapter 4: Reconstitution of the Human Mitochondrial DNA Replisome

4.1 INTRODUCTION

The mtDNA replisome is comprised of a nuclearly-encoded DNA polymerase (polymerase gamma), single-stranded DNA binding protein (SSB), and a hexameric DNA helicase (16, 17). These proteins assemble at the replication fork and carry out replication of the mtDNA. DNA polymerase gamma (Pol γ) is a heterotrimer, containing the catalytic subunit (Pol γ A) and a dimer of the processivity subunit (Pol γ B). The holoenzyme of Pol γ catalyzes DNA synthesis in the 5' to 3' direction and also contains a 3' to 5' exonuclease domain, which provides a proofreading function (22, 48). In vitro measurements of polymerization on a primer/template DNA substrate by Pol γ have reported polymerization rates of 45 s⁻¹ and a K_d for DNA of 10 nM (49). SSB is a non-catalytic protein that binds to single stranded DNA as a tetramer to protect the ssDNA from damage by nucleases. Ahead of Pol γ and SSB at the replication fork is the mtDNA helicase, which unwinds the downstream double stranded DNA to single stranded DNA by movement along the displaced strand in the 5' to 3' direction (75). The mtDNA helicase, which was discovered in a screen for mutations linked to autosomal dominant PEO, has structural similarity to phage T7 gp4 helicase/primase although no primase activity has been shown in human mtDNA helicase (31). The mtDNA helicase binds to DNA in a hexameric form and unwinds dsDNA in an NTP-dependent manner. Previous studies attempting to reconstitute the mtDNA replisome have failed to provide a quantitative analysis of helicase unwinding and polymerization at the replication fork. Rolling-circle replication assays (76, 77, 131), that monitor polymerization by incorporation of radiolabeled dCTP into the growing primer strand show polymerization following helicase unwinding but only a small fraction, ~ 0.1%, of the primers are extended. In published studies following the incorporation of the labeled dNTP into the

growing strand the signal was enhanced to allow observation of product even though only a small fraction of complexes were active. Also of questionable significance, dsDNA unwinding assays have shown helicase dependent strand displacement of 20 base pairs (bp) of duplex, while an assay extending the duplex to a length of 55bp observed no strand displacement (77). It is questionable as to whether this assay provided a measure of true helicase unwinding activity, or simply strand displacement that could be due to binding of the helicase to the branch strand thereby destabilizing the unstable 20bp duplex. In order to successfully understand the mechanistic basis for disease mutations in the replisome machinery, it will be necessary to quantitatively reconstitute the replisome and understand the coordination between the helicase and the polymerase.

This chapter reports the results of reconstituting the mtDNA replisome in high yield by successfully assembling the replication complex containing Pol γ and the helicase on a synthetic oligonucleotide that resembles a replication fork, as shown in Figure 4.1. The modeled complex in panel A of this figure shows the crystal structure of Pol γ with the DNA modeled by overlaying with the homologous T7 DNAP-DNA structure (45, 132). To represent the helicase, we used the structure of the highly homologous T7 gp4 helicase/primase (1Q57.pdb, (133)) and extended the DNA to resemble the replication fork. This model illustrates one plausible arrangement of the helicase and polymerase on the replication fork with the helicase at the base of the fork and the polymerase at the end of the primer strand and presents a more realistic view than the cartoons typically portrayed.

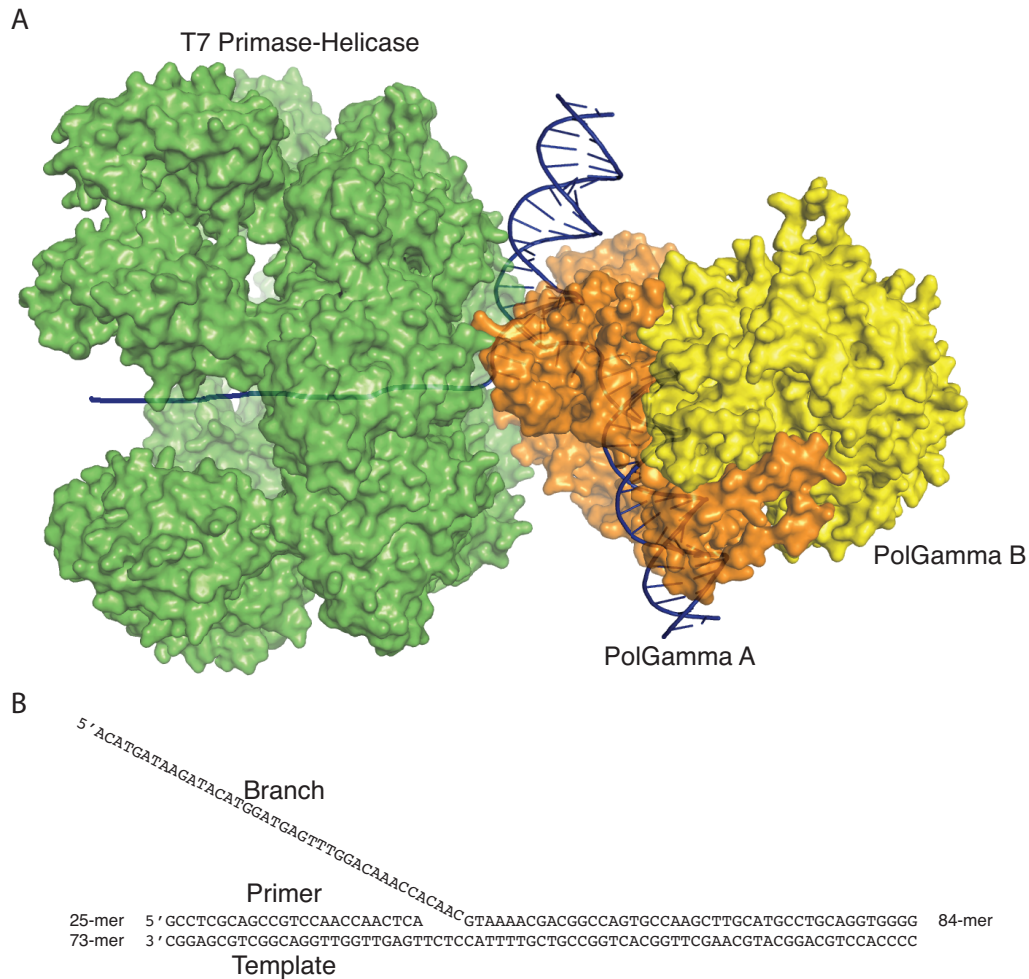


Figure 4.1. *Reconstitution of the mtDNA Replication fork.* (A) In this figure, the T7 Primase-Helicase structure, 1Q57.pdb (133) is shown to represent the mtDNA helicase in relation to Pol γ at the replication fork. The Pol γ structure shows the Pol γ A large subunit and the Pol γ B small subunit bound to DNA primer and template strands, which have been modeled in using the crystal structure of T7 DNA polymerase, 1T7P.pdb (45, 134). We have extended this stretch of DNA to display a possible configuration of the dsDNA downstream of the polymerase being unwound by the helicase. (B) The DNA substrate used for helicase and Pol γ assays consists of a 25-nucleotide primer strand annealed to a 73-nucleotide template strand. A branch strand of 84 nucleotides is annealed to the primer-template, giving a gap of 4 nucleotides before 44 base pairs of duplex DNA.

4.2 MATERIALS AND METHODS

Cloning, expression and purification of Pol γ A

For the clone for Pol γ A used in this section of work we truncated the first 25 amino acids from the N-terminus (Δ 25), to remove the mitochondrial localization sequence but retaining the polyglutamine tract that had been removed in previous studies on the Δ 66 construct (55). As was the case in previous chapters, the clone for Pol γ A contained a C-terminal His tag. The clone was constructed in pUC 19.1 and transferred to pBacPak9 by restriction digestion and subsequent ligation. Once in pBacPak9 the clone was then transferred to baculovirus by recombination with BacPak6 viral DNA (Clontech). Protein expression in SF9 cells and purification methods were followed as described previously (55) and in Chapter 2. Briefly, recombinant viral DNA was used to infect SF9 cells and cells were harvested 72 hours after infection. Protein was then purified from the cell pellet by stirring in *Lysis buffer* (0.32 M sucrose, 10 mM HEPES, pH 7.5, 0.5% NP-40, 3 mM CaCl₂, 2 mM MgAc.4H₂O, 0.1 mM EDTA and protease inhibitor cocktail from A. G. Scientific Inc.), centrifugation at 1,500xg for 10 minutes, slowly increasing the salt concentration to 500 mM KCl, and ultracentrifugation at 31,000 x g RCF for 30 minutes. The supernatant was then passed over a Ni-NTA column (Qiagen), followed by a cation exchange SP Sepharose column (GE Healthcare). Lastly, as a modification to our previously described procedure in Chapters 2 and 3, an anion exchange HiTrap Capto Q column (GE Healthcare) was used for a final purification step. Fractions from the SP Sepharose column were pooled and loaded onto the HiTrap Capto Q column. After washing with *Buffer A* (20 mM HEPES pH 7.5, 30 mM KCl, 1 mM EDTA, 5% glycerol, 5 mM β -ME), the protein was eluted with a 0-100% linear gradient of *Buffer B* (20 mM HEPES pH 7.5, 700 mM KCl, 1 mM EDTA, 5% glycerol, 5 mM β -ME) over 16 column volumes collecting 1 ml fractions. After analysis with 8% SDS-

PAGE, the protein was pooled, concentrated with a Centricon ultrafiltration unit (50KDa MWCO, Millipore), and dialyzed into *Storage Buffer* (50 mM Tris-HCl pH 7.5, 100 mM NaCl, 2.5 mM EDTA pH 8.0, 50% glycerol, 1 mM DTT). Protein was then divided into small aliquots, flash frozen in liquid nitrogen and stored at -80°C. All experiments containing Pol γ were performed with a reconstituted holo-enzyme formed by pre-incubating with a 4:1 molar excess of Pol γ B over Pol γ A. All references to Pol γ refer to the reconstituted holo-enzyme.

Cloning, expression and purification of Pol γ B

The Pol γ B small subunit was expressed and purified as described previously (55) and in Chapter 2. The Pol γ B protein lacks the first 25 amino acids from the N-terminal end, thus removing the mitochondrial localization sequence, and is C-terminal His tagged.

Cloning, expression and purification of mtDNA Helicase

The human mitochondrial DNA Helicase with an N-terminal His tag and lacking the first 43 amino acids, was cloned into pCIts ind+ plasmid and expressed in C2984H cells. The large-scale expression (6 L) was induced at an OD of 4.7 with temperature change to 37°C and addition of Nalidixic acid to a final concentration of 50 μ g/ml (Figure 4.2). The cultures were then grown overnight to a final OD of 13.7 and pelleted at 6,500 x g for 20 minutes at 4°C.

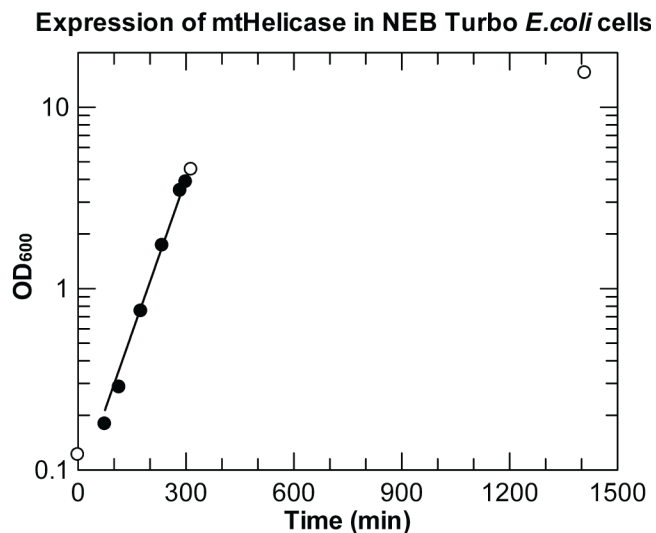


Figure 4.2. *Growth kinetics of E. coli expressing mtDNA Helicase.* Cultures of NEB Turbo *E. coli* expressing mtDNA helicase were grown at 30°C to an induction density of 4.7 OD₆₀₀/mL which was reached in 300 minutes (filled circles). Cultures were induced with a temperature shift to 37°C and the addition of 50 µg/ml nalidixic acid and grown overnight (filled circles) before harvesting by centrifugation.

For protein purification, the cell pellet was re-suspended in 5 volumes (5 mL/gm) of *Lysis buffer* (50 mM Tris-HCl pH 7.5, 50 mM NaCl, 20 mM imidazole, 5 mM MgCl₂·6H₂O, 0.1 mM PMSF, 10% Glycerol, 0.5% Nonidet-P40) for 20 minutes. A Dounce A homogenizer was used to ensure uniform suspension. Lysozyme was then added to the suspension to a final concentration of 50 µg/ml and stirred on ice for 15 minutes. The NaCl concentration was then brought to 500 mM and 1 mM ATP was added to the cell lysate before sonicating for 15 minutes. This was followed by centrifugation to pellet the debris at 55,000 x g RCF for 30 minutes at 4°C in a Beckman 45Ti. The supernatant then incubated for 20 minutes on ice with Ni-Sepharose beads (GE Healthcare) pre-equilibrated with *Lysis buffer* + 1 mM ATP + 500 mM NaCl. The Ni-Sepharose beads were then pelleted at 700 x g RCF for 20 minutes at 4°C. The pelleted

beads and minimal residual supernatant volume were transferred to a jacketed column with water bath set to 4°C and allowed to pack. The column (Figure 4.3) was then washed with 10 column volumes of *Lysis buffer* + 1 mM ATP + 500 mM NaCl. Next, the column was washed with 5 column volumes of *Nickel Column Wash 1* (30 mM Tris-HCl pH 7.5, 20% Glycerol, 0.5% Nonidet-P40, 1 mM β-ME, 5 mM MgCl₂·6H₂O, 0.1 mM PMSF, 0.2 mM ATP, 0.5 M NaCl, 20 mM imidazole) followed by a wash with *Nickel Column Wash 2* (30 mM Tris-HCl pH 7.5, 20% Glycerol, 0.5% Nonidet-P40, 1 mM β-ME, 5 mM MgCl₂·6H₂O, 0.1 mM PMSF, 0.2 mM ATP, 350 mM NaCl, 20 mM imidazole). The protein was then eluted with a linear gradient from 0-100% *Nickel Column Elution Buffer* (30 mM Tris-HCl pH 7.5, 20% Glycerol, 0.5% Nonidet-P40, 1 mM β-ME, 5 mM MgCl₂·6H₂O, 0.1 mM PMSF, 0.2 mM ATP, 350 mM NaCl, 250 mM imidazole) over 5 column volumes. Fractions were collected and the peak fractions were pooled for further purification on 3 tandem columns (Figure 4.4): Q-Sepharose (1 mL) followed by two Heparin Sepharose columns (1 mL each). Columns were washed with 10 column volumes of *Heparin Column Buffer A* (30 mM Tris-HCl pH 7.5, 20% Glycerol, 0.5% Nonidet-P40, 1 mM β-ME, 5 mM MgCl₂·6H₂O, 0.1 mM PMSF, 350 mM NaCl, 0.2 mM ATP) and the Q-column was removed. The protein was then eluted off of the Heparin Sepharose columns with a steep gradient to *Heparin Column Buffer B* (30 mM Tris-HCl pH 7.5, 20% Glycerol, 0.5% Nonidet-P40, 1 mM β-ME, 5 mM MgCl₂·6H₂O, 0.1 mM PMSF, 1 M NaCl, 0.2 mM ATP). The helicase peak eluted at about 550-600 mM NaCl and fractions were pooled, concentration estimated by Bradford assay, aliquoted and flash frozen in liquid nitrogen. Protein was stored at -80°C until used in assays.

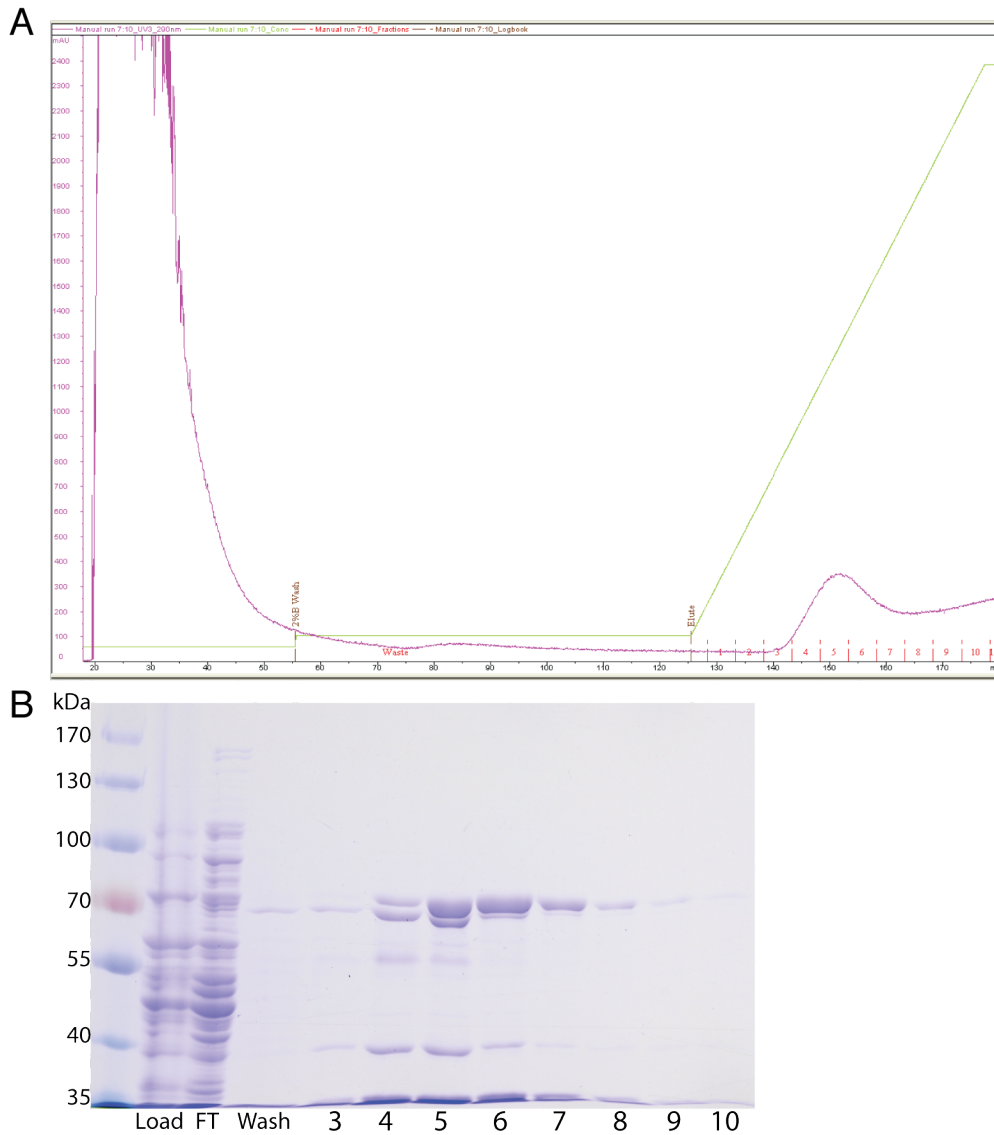


Figure 4.3 *Nickel sepharose column purification of mtDNA helicase.* (A) Nickel sepharose column chromatography of mtDNA helicase from cell lysate. Absorbance at 290 nm (magenta) was monitored to detect protein and avoid any additional absorbance from the presence of ATP in the buffer. After loading onto the Nickel column, mtDNA helicase was eluted from the column with a linear gradient from 0-100% *Nickel Column Elution Buffer* (green). (B) SDS-PAGE analysis of the loaded lysate (Load), flow-through (FT), wash and fractions 3-10 confirm the presence of mtDNA helicase in fractions 4-7.

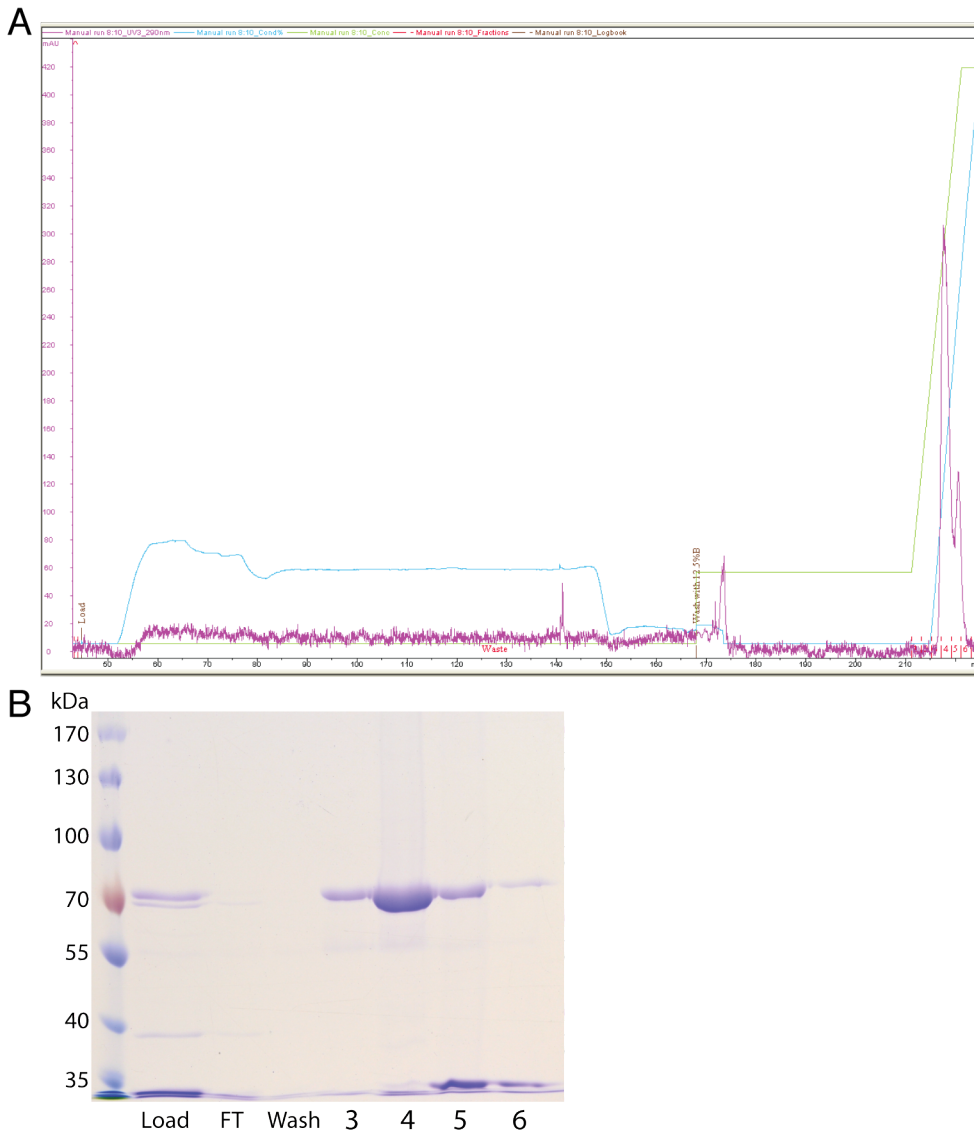


Figure 4.4 *Tandem column purification of mtDNA helicase.* Tandem Q sepharose and heparin sepharose column chromatography of mtDNA helicase from nickel sepharose fractions. Absorbance at 290 nm (magenta) was monitored to detect protein and avoid any additional absorbance from the presence of ATP in the buffer. After loading onto the tandem columns, the Q sepharose column was removed and the mtDNA helicase was eluted from the heparin columns with a linear gradient from 0-100% *Heparin Column B Buffer* (green). (B) SDS-PAGE analysis of the loaded sample (Load), flow-through (FT), wash and fractions 3-6 confirm the presence of mtDNA helicase in fractions 3-5.

Cloning of mtDNA Helicase trimer

In an attempt to overcome the difficulties in assembly of the hexameric helicase, the original $\Delta 43$ helicase gene in the pcI^{ts} expression plasmid was altered to express two (mtHelicase dimer) or three helicase (mtHelicase trimer) genes in tandem with a flexible linker domain between each subunit. This technique was adapted from work on other hexameric DNA translocases (*135-139*). A flow chart of this cloning process is outlined in Figures 4.5-4.8. The first step in constructing these clones was to add two additional restriction sites at the 3' end of the mtHelicase gene (Figure 4.5). For this, mtHelicase oligomer #1 and #2 (Table 4.1) were used in a PCR reaction to generate a 736 bp amplicon that was then restriction digested with NotI/NcoI (NEB). This digested amplicon was then ligated to the $pcI^{\text{ts}}_{\Delta 43}$ helicase plasmid, which had also been digested by NotI/NcoI.

Table 4.1 Oligomers for construction of mtHelicase trimer

Oligomer #

1	5' -AGATAT GCGGCCG CTTACTTAAT GCTAGC ATAATAACT GAATTC CTTTGAACGCTTGGAGGTGT-3'
2	5' -TCATGCTGACACAGTTTGCCGA-3'
3	5' -TGTATATCT CATATGGGTACC ACTCTCCAAGCCTTGGATATGCCAGTGTTCCTGTAA-3'
4	5' -TACAATATA AAGCTTGCTAGC CTTTGAACGCTTGGAGGTGTCTGGCTGGTCGGGA-3'
5	5' -TACAATATA AAGCTTGCGGCCG <u>C</u> TTACTTTGAACGCTTGGAGGTGTCTGGCTGGTCGGGA-3' 5' -
6	TATGGAATTC GGCGGCGGTTCCGAGGGCGGTGGTTCAGAAGGCGGTTCCGGTGGTGGCGGTAGCGAAG- 3' 5' -
7	CTGCCACCACCTTCGCTACCGCCACCACCGGAACCGCCTTCTGAACCACCGCCCTCGGAACCGCCGCC GA ATTCCA -3'
8	5' -GTGGTGGCAGCGAAGGTGGCAGCGGTGGTGGTAGCGAAGGCGGTAGCGGTGGTAGCGAAGGTGGCG- 3'
9	5' - GTACCGCCAC CTTCGCTACCACCGCTACCGCCTTCGCTACCACCACCGCTGCCACCTTCG-3' 5' -
10	TATGGCTAGC GGCGGCGGTTCCGAGGGCGGTGGTTCAGAAGGCGGTTCCGGTGGTGGCGGTAGCGAAG- 3' 5' -
11	CTGCCACCACCTTCGCTACCGCCACCACCGGAACCGCCTTCTGAACCACCGCCCTCGGAACCGCCGCC GC TAGCCA -3'

*Restriction sites are in bold. Stop codon is underlined.

A copy of the $\Delta 43$ helicase gene was amplified from the original pCl^{is} _{$\Delta 43$ helicase} plasmid in a PCR reaction using Primer #3 and #4 (Figure 4.6A). These primers included sequences to add NdeI and KpnI restriction sites to the 5' end of the gene and HindIII and NotI sites to the 3' end of the gene. The PCR product was then cut with NdeI/HindIII and ligated with a NdeI/HindIII digest of an empty pUC19.1 plasmid. This resulted in what we refer to as “Gene 2 minus linker”. The same process was repeated with Primers #3 and #5 to generate “Gene 3 minus linker” but this time Primer #5 added the sequence coding for a stop codon at the 5' end of the gene before the HindIII and NotI restriction sites (Figure 4.7A).

The DNA sequence coding for the 44 amino acid linker sequence between gene 1 and gene 2 of the helicase trimer

(EFGGGSEGGGSEGGSGGGGSEGGGSEGGSGGGSEGGSGGSEGGG)

was constructed by annealing the two oligomers #6 and 7 and separately annealing oligomers #8 and 9 by heating to 95°C for 5 minutes in *Annealing Buffer* (10 mM Tris-HCl pH 7.5, 50 mM NaCl, 1 mM EDTA) and then allowing to cool slowly to room temperature. The two duplexes were then ligated to give the full sequence for the 44 amino acid linker between helicase gene 1 and helicase gene 2 of the trimer (“linker 1-2”) (Figure 4.6B). The sequence of this “linker 1-2” was engineered to contain an NdeI digested overhang at the 3’ end and a Acc65I digested overhang at the 5’end. This was then able to be ligated with a NdeI/Acc65I digested “Gene 2 minus linker” to result in “Gene 2 plus linker” (Figure 4.6B). This process was then repeated for the linker to insert between helicase gene 2 and helicase gene 3 of the trimer. Oligomers #10 and 11 were annealed and separately oligomers #8 and #9 from above were annealed. The two duplexes of #10/11 and #8/9 were ligated and resulted in the full sequence for the linker between gene 2 and gene 3 of the helicase trimer (“linker 2-3”).

(EFGGGSEGGGSEGGSGGGGSEGGGSEGGSGGGSEGGSGGSEGGG)

The sequence of this “linker 2-3” was also engineered to contain an NdeI digested overhang at the 3’ end and a Acc65I digested overhang at the 5’end. This was then able to be ligated with a NdeI/Acc65I digested “Gene 3 minus linker” to result in “Gene 3 plus linker” (Figure 4.7B). Sequences were confirmed for “Gene 3 plus linker” in the pUC19 plasmid and the “Gene 2 plus linker” in a separate pUC19 plasmid. The following double restriction digests were made to prepare for the final ligation of the 3 genes: EcoRI/NotI digest of pCl^{ts}_Δ43helicase; EcoRI/NheI digest of pUC19_Gene2PlusLinker; NheI/NotI digest of pUC19_Gene3PlusLinker. A tripartite ligation (Figure 4.8) was performed of

these 3 digests to form the final clone containing 3 helicase genes in tandem each separated by a 43 amino acid flexible linker.

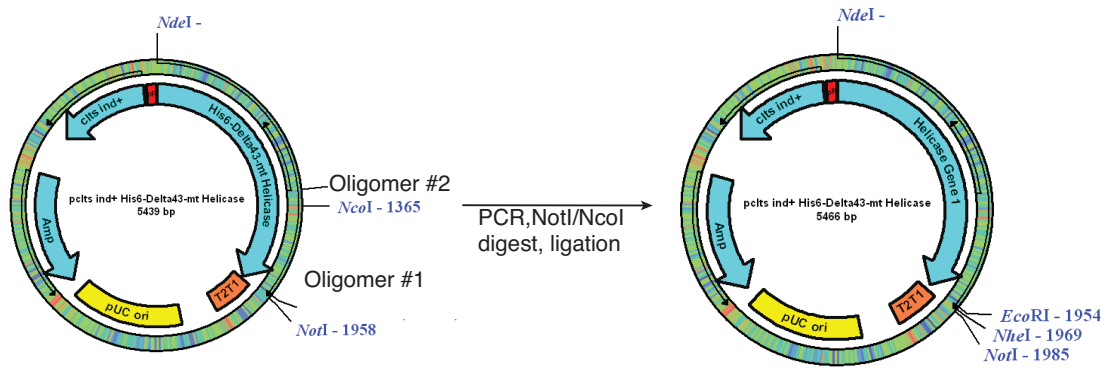


Figure 4.5 Cloning of *mtHelicase* trimer – adding gene insertion sites. Additional insertion sites were added to the expression plasmid pCl^{ts} containing the mtDNA helicase gene.

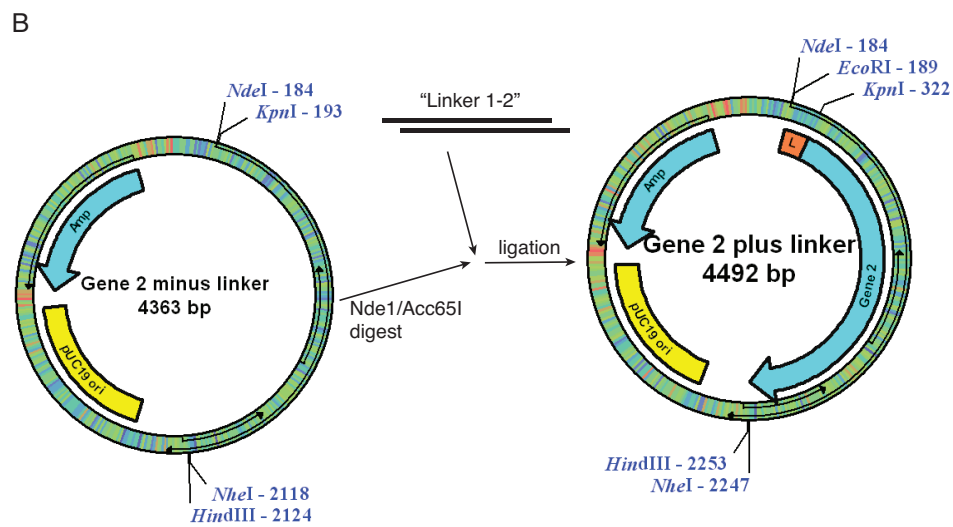
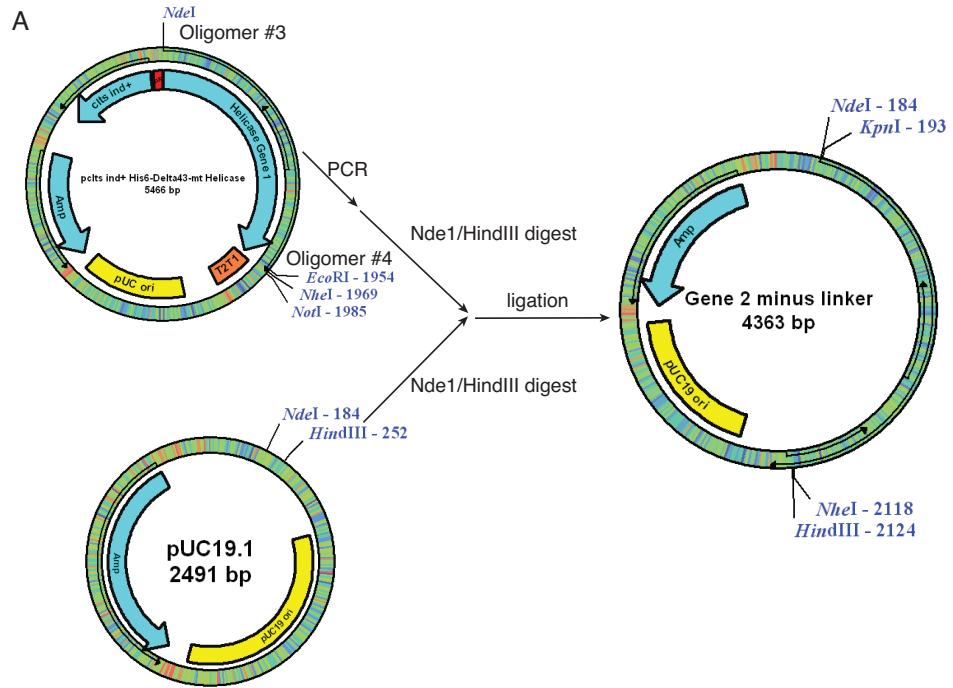


Figure 4.6 Cloning of mtHelicase trimer – construction of gene 2. (A) Scheme to transfer mtHelicase gene to cloning vector pUC19.1 while adding KpnI restriction site to 5'-end of gene. (B) Scheme to add Linker 1-2 to 5'-end of gene 2 by digestion with NdeI and KpnI.

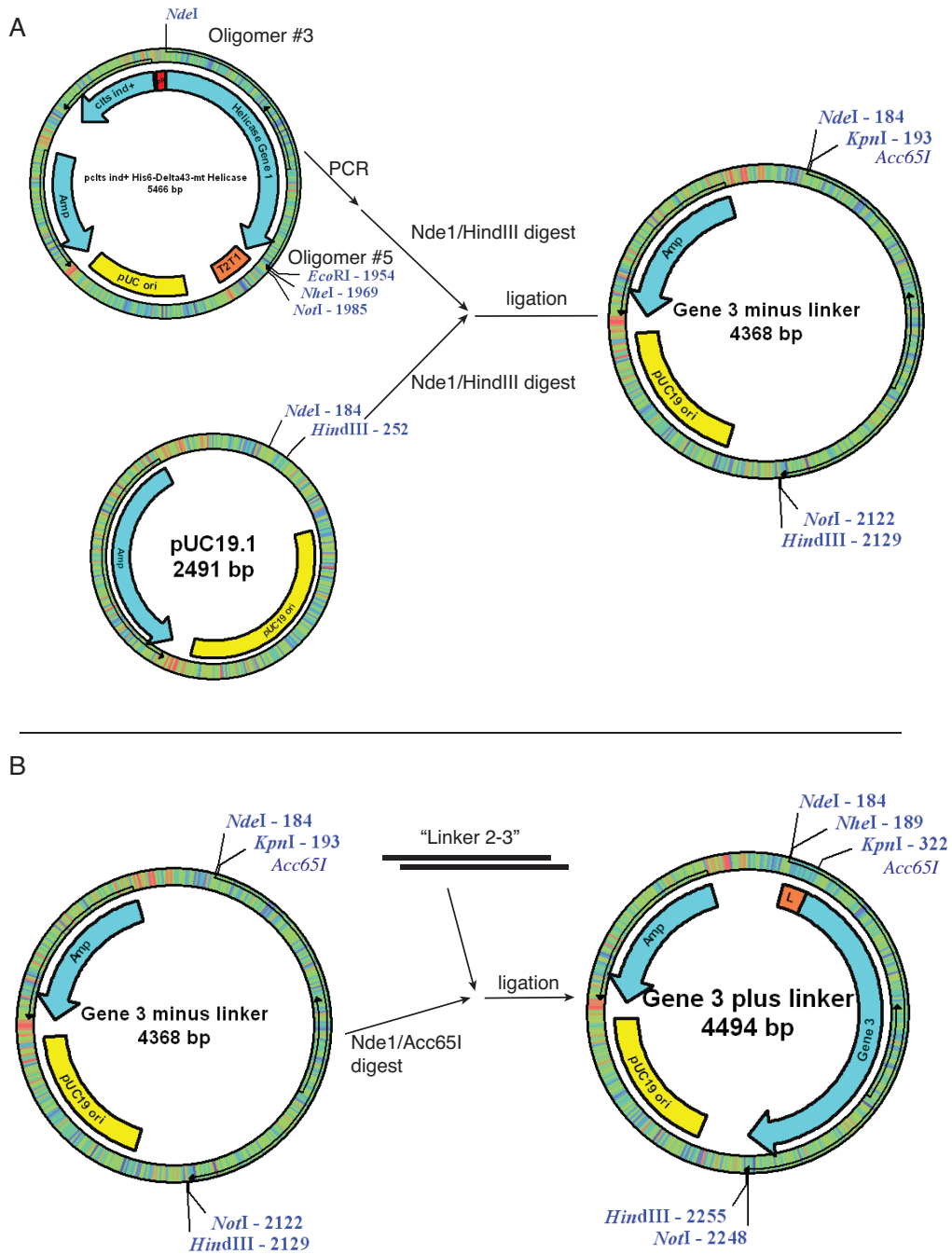


Figure 4.7 Cloning of *mtHelicase* trimer – construction of gene 3. (A) Scheme to transfer *mtHelicase* gene to cloning vector pUC19.1 while adding *KpnI* restriction site to 5'-end of gene and *NotI* site to 3'-end of the gene. (B) Scheme to add Linker 2-3 to 5'-end of gene 3 by digestion with *NdeI* and *KpnI*.

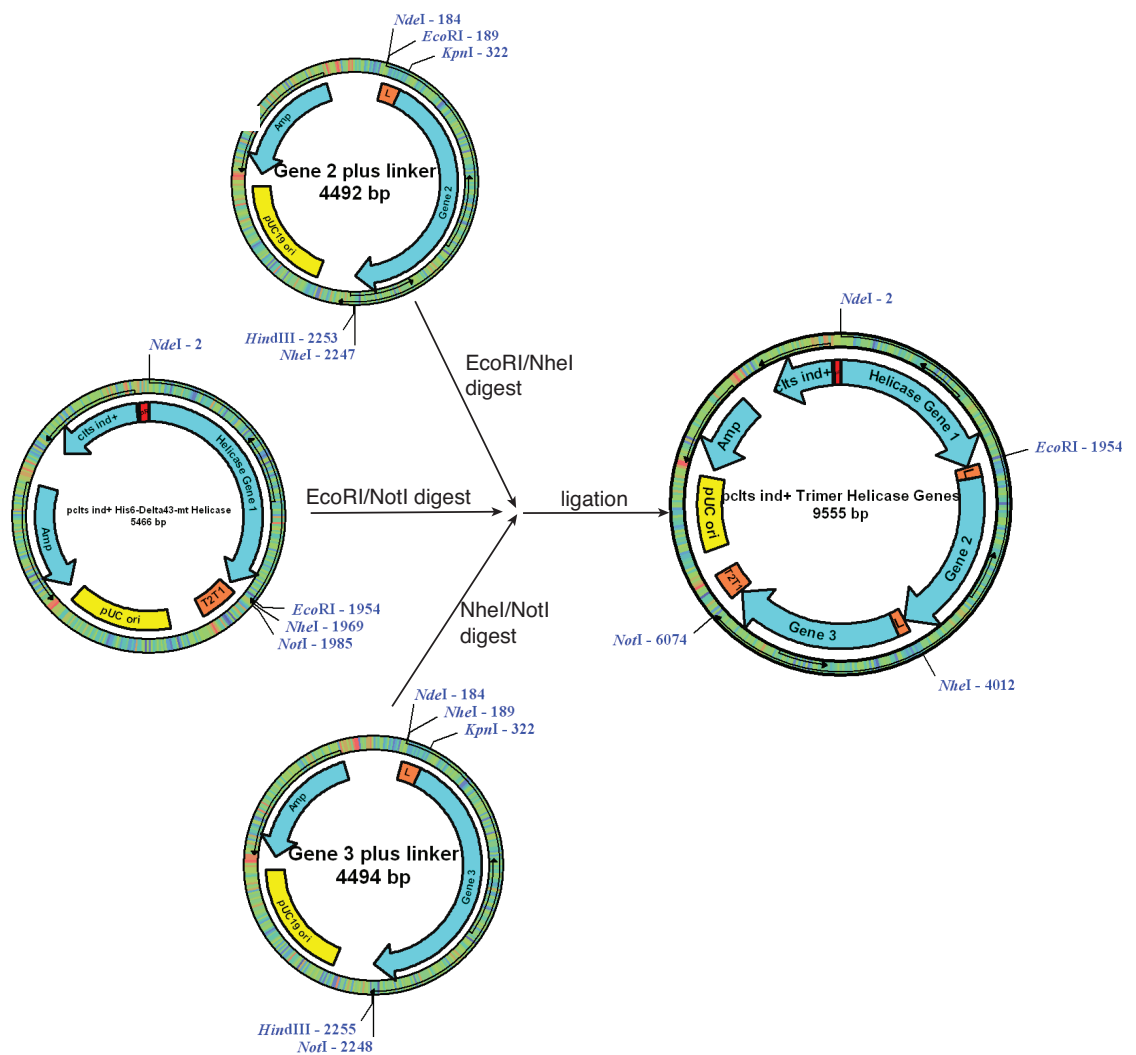


Figure 4.8 Cloning of *mtHelicase* trimer – tripartite ligation. Scheme to ligate genes 1, 2 and 3 of the mtDNA Helicase trimer.

Preparation of DNA substrates

Oligonucleotides were synthesized by Integrated DNA Technologies (IDT, Inc.) and PAGE purified using a 10-15% polyacrylamide denaturing gel. To form the 25/73/84 DNA substrate a 25-nt primer strand (5' GCC TCG CAG CCG TCC AAC CAA CTC A

3'), 73-nt template strand (5' CCC CAC CTG CAG GCA TGC AAG CTT GGC ACT GGC CGT CGT TTT ACC TCT TGA GTT GGT TGG ACG GCT GCG AGG C 3') and 84-nt branch strand (5' ACA TGA TAA GAT ACA TGG ATG AGT TTG GAC AAA CCA CAA CGT AAA ACG ACG GCC AGT GCC AAG CTT GCA TGC CTG CAG GTG GGG 3') were annealed. Oligomers were annealed by heating to 95°C for 5 minutes and then allowing to cool slowly to room temperature. DNA substrates were 5'-³²P-labeled, as noted, using T4 polynucleotide kinase (Invitrogen).

Table 4.2 *Substrates for replisome assays*

25/73(-br)

25-mer	5' -GCCTCGCAGCCGTCCAACCAACTCA
73-mer	3' -CGGAGCGTCGGCAGGTTGGTTGAGTTCTCCATTTTGCTGCCGGTCACGGTTCG <u>AACGTACGGACGTCCACCCC</u>

25/73/84

25-mer	5' -GCCTCGCAGCCGTCCAACCAACTCA
73-mer	3' -CGGAGCGTCGGCAGGTTGGTTGAGTTCTCCATTTTGCTGCCGGTCACGGTTC GAACGTACGGACGTCCACCCC
84-mer	5' - ACATGATAAGATACATGGATGAGTTTGGACAAACCACAAC GTAAAACGACG GCCAGTGCCAAGCTTGCATGCCTGCAGGTGGGG

r25/73/84

r25-mer	5' -GCCUCGCAGCCGUCCAACCAACUCA
73-mer	3' -CGGAGCGTCGGCAGGTTGGTTGAGTTCTCCATTTTGCTGCCGGTCACGGTT CGAACGTACGGACGTCCACCCC
84-mer	5' - ACATGATAAGATACATGGATGAGTTTGGACAAACCACAAC GTAAAACGACGGC CAGTGCCAAGCTTGCATGCCTGCAGGTGGGG

25/73/84agag

25-mer	5' -GCCTCGCAGCCGTCCAACCAACTCA
73-mer(agag)	3' -CGGAGCGTCGGCAGGTTGGTTGAGTAGAGCATTTTGCTGCCGGTCACGGTTCG AACGTACGGACGTCCACCCC
84-mer	5' - ACATGATAAGATACATGGATGAGTTTGGACAAACCACAAC GTAAAACGACGG CCAGTGCCAAGCTTGCATGCCTGCAGGTGGGG

Table 4.2 Continued *Substrates for replisome assays*

<u>25/73/84-8ntgap</u>	
25-mer	5' –GCCTCGCAGCCGTCCAACCAACTCA 3' –CGGAGCGTCGGCAGGTTGGTTGAGTTCTCCATTTTGCTGCCGGTCACGGT
73-mer	TCGAACGTACGGACGTCCACCCC
84-mer	5' – ACATGATAAGATACATGGATGAGTTTGGACAAACCACAACCAGGAACGACG GCCAGTGCCAAGCTTGCATGCCTGCAGGTGGGG
<u>25/89/84-20ntgap</u>	
25-mer	5' –GCCTCGCAGCCGTCCAACCAACTCA 3' –CGGAGCGTCGGCAGGTTGGTTGAGTAGAGGAGAAGAGAGGGAGAGCATTTTG
89-mer	CTGCCGGTCACGGTTCGAACGTACGGACGTCCACCCC
84-mer	5' – ACATGATAAGATACATGGATGAGTTTGGACAAACCACAACGTAAAACGACGGC CAGTGCCAAGCTTGCATGCCTGCAGGTGGGG
<u>25/89/84-20ntgap with primer on branch</u>	
25-mer	5' –GCCTCGCAGCCGTCCAACCAACTCA 3' –CGGAGCGTCGGCAGGTTGGTTGAGTAGAGGAGAAGAGAGGGAGAGCATTT
89-mer	TGCTGCCGGTCACGGTTCGAACGTACGGACGTCCACCCC
84-mer	5' – ACATGATAAGATACATGGATGAGTTTGGACAAACCACAACGTAAAACGACG GCCAGTGCCAAGCTTGCATGCCTGCAGGTGGGG
20-mer	3' –TGTACTATTCTATGTACCTA

*5' branch overhang is shown in bold. Single stranded template gap is underlined.

Helicase Unwinding Assays

Helicase unwinding of the branched DNA substrate shown in Figure 4.9 was monitored by 5'-³²P-labeling of the 84-nt branch strand and monitoring the conversion of double to single strand DNA on a gel under non-denaturing conditions. For the reaction in the absence of polymerase, the helicase (20 nM hexamer) was pre-incubated with 15 nM 25/73/84 DNA substrate at 37°C for 5 minutes in the *Reaction Buffer* (20 mM Tris-HCl pH 7.5, 100 mM NaCl, 10% glycerol, 100 µg/ml BSA, and 4 mM DTT). The reaction was started by mixing with 5 mM “free” MgCl₂, 3 mM ATP and 150 nM unlabeled 84-nt branch strand DNA to serve as a trap. For the reaction in the presence of

the polymerase, 20 nM helicase hexamer was pre-incubated with 15 nM 25/73/84 DNA substrate, 15 nM Pol γ A, 60 nM Pol γ B, and 0.5 mM EDTA at 37°C for 5 minutes in reaction buffer. The reaction was then started by the addition of 5 mM “free” MgCl₂, 3 mM ATP, 250 μ M dATP, 250 μ M dGTP, and 150 nM unlabeled 84-nt branch strand DNA to serve as a trap. At each time point, the reaction was stopped by the addition of the Stop Solution (90 mM EDTA, 30% glycerol, 1% SDS, 0.25% Xylene Cyanol, 0.25% Bromophenol Blue). Single stranded DNA products were resolved from the duplexed DNA substrate on a 10% polyacrylamide non-denaturing gel. The concentration of product formed was calculated as the percentage of ssDNA at each time point multiplied by the initial DNA concentration.

Replisome Assays

A branched DNA substrate was used in order to measure polymerase extension based on helicase unwinding. This 25/73/84 DNA substrate, shown in Figure 4.1B, consists of a 25-nt primer strand, 73-nt template strand and an 84-nt branch strand. In the presence of the branch strand, the polymerase can extend the primer by only 4 nucleotides while displacement of the branch by the helicase will allow formation of a 73mer. To measure full extension, the 25-nt primer strand was 5'-³²P-labeled using T4 polynucleotide kinase (Invitrogen) and then annealed to the 73-nt template strand along with the 84-nt branch strand by heating to 95°C for 5 minutes and then slowly cooling to room temperature. In the “Polymerase Start” reaction setup, 50 nM 25/73/84 DNA substrate was pre-incubated with 500 nM helicase hexamer at 37°C for 30 or 60 minutes in reaction buffer containing 20 mM Tris-HCl pH 7.5, 100 mM NaCl, 5 mM “free” MgCl₂, 10% glycerol, 100 μ g/ml BSA, 4 mM DTT and 3 mM ATP. After pre-incubation, the reaction was then started by mixing with 100 nM Pol γ A, 400 nM Pol γ B and all 4

dNTPs at 250 μ M each. Alternatively in the “dNTP Start” reaction setup, 50 nM 25/73/84 DNA substrate was pre-incubated with 500 nM helicase hexamer, 100 nM Pol γ A, 400 nM Pol γ B, 250 μ M dATP and 250 μ M dGTP at 37°C for 30 minutes in the reaction buffer. The reaction was then started by mixing dCTP and TTP at 250 μ M each. At each time point, the reaction was stopped by mixing with Stop Solution containing, 166 mM EDTA, 0.25% Xylene Cyanol and 0.25% Bromophenol Blue. The reaction products were resolved on a 15% polyacrylamide denaturing gel and the amount of product formed at each time point was analyzed using the ImageQuant software (GE Healthcare). The concentration of product formed was calculated as the percentage of 73mer product multiplied by the initial DNA concentration.

4.3 RESULTS

Kinetics of helicase unwinding

Previous studies have not been able to show unwinding of more than 20 base pairs by the mtDNA helicase in a helicase unwinding assay (77). To probe this inconsistency, we optimized a radiometric assay to monitor helicase unwinding of 44 base pairs of duplexed DNA. After pre-incubation of the helicase and the 25/73/84 DNA substrate, the unwinding reaction was started by the addition of ATP and Mg^{2+} . It was necessary to add excess unlabeled 84-nt branch strand to the reaction to serve as a trap and prevent re-annealing of the unwound radiolabeled strand. The three necessary controls shown in Figure 4.9A explore the behavior of the dsDNA substrate in the absence of helicase, the re-annealing of the heat denatured DNA substrate over the time course of the reaction and also the re-annealing of the heat denatured DNA substrate during loading onto the native polyacrylamide gel. There is a small amount of re-annealing seen in these controls.

Helicase unwinding of this 44 base pair substrate is slow in the absence of polymerase with the formation only 0.12 nM product after 60 minutes of reaction time. The kinetics of unwinding with the helicase alone is displayed in Figure 4.9B; the data were fit to a linear equation giving an unwinding rate of 0.002 min^{-1} .

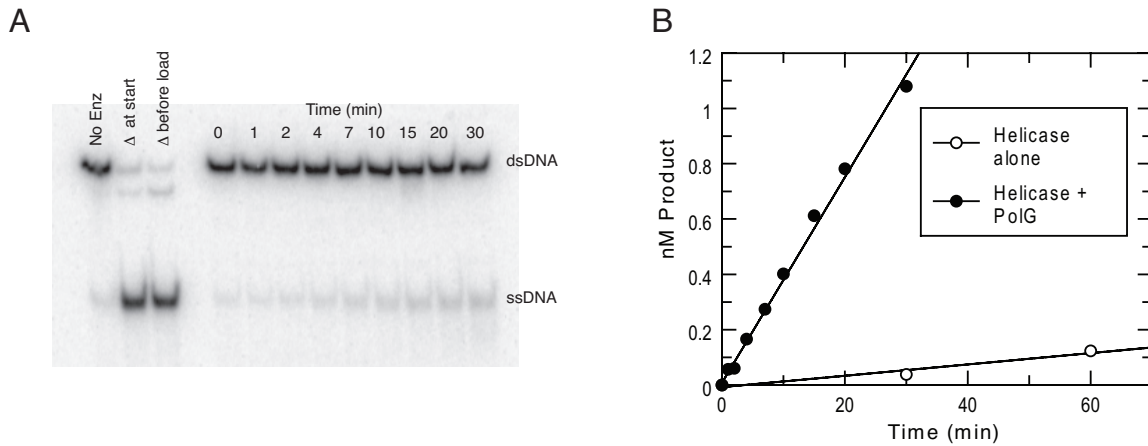


Figure 4.9. *Pol γ stimulates DNA helicase activity.* (A) Unwinding of the branch strand was monitored by ^{32}P -labeling the 5' end of the 84-mer branch strand. A no enzyme control shows the duplex DNA before enzyme was added. Controls for re-annealing of ssDNA were heated to 95°C for 5 minutes at the start of the reaction time course, and also heated to 95° for 5 minutes just before loading on the gel. For the reaction, 20 nM helicase hexamer was pre-incubated with 15 nM primer-template-branch DNA, 15 nM Pol γ , and 0.5 mM EDTA for 5 minutes. The reaction was started by the addition of 5 mM “free” Mg^{2+} , 3 mM ATP, 250 μM dATP, 250 μM dGTP, and 150 nM unlabeled 84-mer branch strand DNA. ssDNA products unwound by helicase were resolved on a non-denaturing 10% polyacrylamide gel. The reaction was performed at 37°C and the reaction buffer contained 20 mM Tris-HCl, pH 7.5, 100 mM NaCl, 5 mM MgCl_2 , 10% Glycerol, 100 $\mu\text{g}/\text{ml}$ BSA, 4 mM DTT, and 3 mM ATP. All concentrations noted are final concentrations after mixing. (B) The time course of ssDNA product formation is plotted and fit to a linear equation giving a slope of 0.037 min^{-1} in the presence of the Pol γ (filled circles) and 0.002 min^{-1} in the absence of Pol γ (open circles).

Kinetics helicase unwinding in the presence of polymerase.

Helicase unwinding assays performed in the presence of the polymerase show an 18.5 fold increase in the rate of unwinding. In these assays we used the same experimental setup described above when monitoring unwinding of the helicase alone. To test the effect of Pol γ on helicase unwinding, Pol γ was included in the pre-incubation and the reaction was started with the addition of ATP, Mg^{2+} , dATP and dGTP. The two dNTPs were included allows the polymerase to extend the primer by five nucleotides based on the sequence of the 73-mer template DNA. The 10% native polyacrylamide gel from this assay is shown in Figure 4.9A and displays the formation of ssDNA product over the time course of 30 minutes. These data are then plotted in Figure 4.9B (filled circles) as the concentration (nM) of product formed over time in the presence of helicase and Pol γ . A linear fit to these data gives a helicase unwinding rate of 0.037 min^{-1} in the presence of the polymerase. This marked increase in unwinding rate in the presence of the polymerase suggests that the polymerase stimulates unwinding by the helicase, perhaps by assisting in loading of assembly of the helicase on the branch strand. In a follow-up experiment where all 4 dNTPs were added to the reaction mix in order to allow full length extension of the primer by Pol γ there was no significant difference seen in the rate of unwinding (data not shown). The kinetics support the hypothesis that the polymerase aids in assembly or loading of the helicase, which appears to be rate-limiting in the assay.

Kinetics of mtDNA Replisome

In order to reconstitute the mtDNA replisome and monitor polymerization following helicase unwinding, we again used the branched DNA substrate shown in Figure 4.1B. In this radiometric assay, we are able to monitor extension of the 5'- ^{32}P -

labeled 25-nt primer strand by the polymerase. Extension of the primer to 29-nt by Pol γ is unimpeded, but further extension to the full length 73-nt is dependent on displacement of the 84-nt branch strand. As shown in Figure 4.10A, Pol γ is able to rapidly extend the 25-nt primer to the full-length product in the absence of the branch strand (-br) in less than 10 seconds. Alternatively, with the branch strand present and in the absence of the helicase (-hel), after 10 minutes the polymerase can extend the primer by 4 nucleotides right up to the fork junction. There is a small amount of product formed showing polymerization up to \sim 38-nt into the forked structure, but after 10 minutes there is no significant formation of full length product indicating that the polymerase cannot completely displace the branch strand on its own. When the helicase is pre-incubated (for 30 or 60 minutes) with the branched DNA substrate and then mixed with the polymerase and dNTPs (Pol Start), there is formation of full length 73-mer product over the time course of 10 minutes. The time course of product formation after a 30 minute pre-incubation is plotted in Figure 4.10B and a fit of the data to a single exponential equation gives a rate of 0.0015 s^{-1} with an amplitude of 33 nM (66% efficiency). As is displayed on the gel in Figure 4.10A, there is no significant difference in rate or amplitude of product formation when the incubation time is extended to 60 minutes.

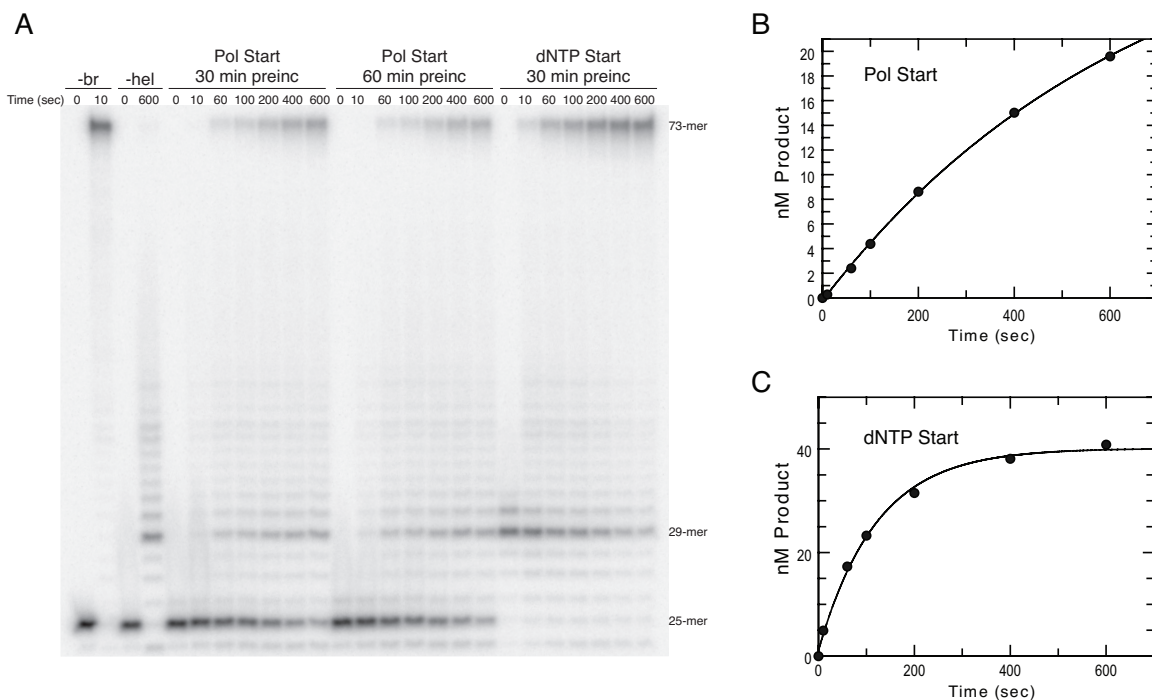


Figure 4.10. *Polymerase extension is dependent on helicase unwinding of the branch strand.*

In all cases DNA, Pol γ and dNTPs are present at a final concentration of 50 nM, 100 nM and 250 μ M each, respectively. (A) Primer extension was monitored by 32 P-labeling the 5' end of the 25-mer primer strand. At each time point the reaction was quenched in a solution of 500 mM EDTA and formamide loading dye solution, and products were then separated on a denaturing 15% polyacrylamide gel. For the -branch strand control (-br), primer-template DNA (25/73) lacking the branch strand was mixed with Pol γ and all 4 dNTPs. For the -helicase (-hel) control, primer-template-branch DNA (25/73/84) was mixed with Pol γ and all 4 dNTPs. To analyze polymerization following unwinding of the branch strand, primer-template-branch DNA was pre-incubated with 500 nM helicase hexamer for 30 or 60 minutes, then mixed with Pol γ and all 4 dNTPs (Pol Start). Alternatively in a dNTP Start, primer-template-branch DNA was pre-incubated with 500 nM helicase hexamer, Pol γ , dATP and dGTP for 30 minutes, then mixed with dCTP and TTP to start the reaction. All concentrations noted are final concentrations after mixing. (B) Data from gel shown in panel A Polymerase Start, 30 minute pre-incubation. Formation of 73-mer product was plotted over time and fit to a single exponential equation resulting in a rate of 0.0015 s^{-1} with an amplitude of 33 nM. (C) Data from gel shown in panel A dNTP Start, 30 minute pre-incubation. Formation of 73-mer product was plotted over time and fit to a single exponential equation resulting in a rate of 0.0083 s^{-1} and an amplitude of 39 nM.

In an alternative pre-incubation strategy, we performed a “dNTP Start” where the 25/73/84 DNA substrate was pre-incubated with helicase, Pol γ , dATP and dGTP for 30 minutes. This allowed the polymerase to extend the 25-nt primer to 29 nucleotides as is shown in the 0 time point on the gel in Figure 4.10A – dNTP Start. After mixing in the two remaining dNTPs (dCTP and TTP), extension of the 29-nt primer is dependent on helicase unwinding of the branch strand. The time course of product formation under these conditions is plotted in Figure 4.10C and a fit to a single exponential equation gave a rate of 0.0083 s^{-1} and an amplitude of 39 nM. This reaction proceeds to ~80% completion with a half-life of 84 seconds. As was suggested in the helicase assays, it appears that pre-incubation with the helicase and the polymerase results in a faster unwinding rate that is likely due to the ability of Pol γ to assist with assembly and/or binding of the helicase.

Alternative assembly strategies

Preincubation of the helicase, polymerase and DNA under a variety of conditions and for varying lengths of time failed to further increase the rate or amplitude of the observed extension reaction (data not shown). Below is a summary of the alternative assembly strategies that were explored in an attempt to reach a point where helicase unwinding and polymerization are the rate limiting steps.

In an attempt to optimize assembly of the replisome we examined the time dependence of pre-incubation by pre-incubating for up to 3 hours. We observed that longer pre-incubation times resulted in less overall product formed, perhaps due to a contaminating exonuclease. We also examined the reactions under various helicase concentrations with the hypothesis that high concentrations of helicase may be inhibitory

due to binding on the duplex DNA. We tested a range of helicase concentrations (data not shown) from 67 nM helicase hexamer to 3 μ M helicase hexamer and saw no significant difference in amount of total product formed. Other attempts were made to optimize the buffer conditions by varying the Mg^{2+} concentration (5 - 20 mM free Mg^{2+}), NaCl concentration (20 - 100 mM); salt ion used (50 - 150 mM KOAc), and buffer pH (6.5 – 8.5). We found that the optimal buffer conditions to be as reported above (5 mM free Mg^{2+} , 100 mM NaCl, no significant change with KOAc, and pH 7.5). We observed the effects of different NTPs for example UTP showed no significant increase in product formed compared to ATP. Also in the absence of ATP, there was still 73mer product formed, due to the ability of the helicase to utilize dNTPs (131). However, interestingly ATP- γ -S was shown to be an inhibitor resulting in no 73mer product formation even in the presence of dNTPs.

As an alternative attempt to increase assembly of the replisome at the forked DNA substrate we used a 25-nt RNA primer instead of the 25-nt DNA primer. This was working under the hypothesis that in vivo the helicase initiates replication from an RNA primer at the origin of H-strand replication (140, 141). The use of the RNA primer resulted in a lower amplitude of product formation and no significant increase in rate.

Additionally, we modified the DNA substrate to have an 8- or 20-nt gap instead of the 4-nt gap that is present on the 25/73/84 DNA substrate. Based on our model in Figure 1, it appears that Pol γ and the helicase can be in close proximity to each other in the orientation that we have placed them in, but it is possible that a larger gap between the two would be necessary for assembly of the replisome. With the larger gaps in our synthetic replication fork (8- or 20-nt), again we saw no appreciable difference in the rate of product formation.

Finally, we attempted to increase assembly of the helicase by cloning and expressing covalently linked dimers and trimers of the helicase. The purification of these multimers was complicated by proteolysis of the multimers leading to monomers in the purification. A purified fraction containing 4% mtHelicase trimers (remainder was cleaved to dimer and monomeric forms) was tested in the replisome assay on the 25/73/84 DNA substrate and there was no apparent polymerization following unwinding of the branch strand. Expression and purification methods for the helicase trimer and dimer need to be optimized in the future to obtain intact helicase multimers to determine the effectiveness of this technique.

4.4 DISCUSSION

Pol γ stimulates DNA helicase activity

We have successfully shown unwinding of 44 base pairs of duplex DNA by the mtDNA helicase and demonstrated that this unwinding rate is increased in the presence of Pol γ . Previous studies have suggested unwinding of 20bp by mtDNA helicase but paradoxically have failed to show unwinding of a 55bp substrate (77). It is possible that the observed formation of the ssDNA product was attributable to destabilization of the weak 20bp substrate by binding of the helicase to the branch strand, not unwinding activity. This would explain the lack of unwinding seen with a more stable 55bp substrate. The uncertainty of what was being measured in these assays was not taken into account in several similar assays, such as one used to screen multiple disease mutations of the helicase (142). In this case, the DNA substrate for the helicase-unwinding assay only contained 18bp for unwinding and thus the assay may not measure helicase activity at all. In order to accurately observe and quantify the effects of disease mutations one

must first establish an accurate assay for helicase unwinding and know what is being measured.

Kinetics of mtDNA Replisome

We have successfully assembled the mtDNA replisome at our forked DNA substrate. Our results show polymerization that is dependent on unwinding of the branch strand DNA by the helicase. By pre-incubating the helicase and polymerase with the DNA substrate, we have achieved helicase unwinding followed by polymerization that proceeds to ~80% completion at a rate of 0.0083 s⁻¹. However, the observed unwinding rates that we obtained appear to be limited by initiation of unwinding by either assembly or binding of the helicase because we fail to see any intermediates in the reaction. In the Pol Start reactions, the gel shown in Figure 4.10A shows conversion of the 25-mer to the 29-mer and then further conversion to the 73-mer that is dependent on helicase unwinding. However, there are no significant intermediate bands between the 29-mer and the 73-mer suggesting that once the helicase is assembled there is rapid unwinding followed by rapid polymerization. Our single exponential rates of product formation are therefore limited by the rate of initiation. The same is true for the dNTP Start reaction where the starting material is at the 29-mer and once initiated, we see rapid conversion to 73-mer products.

This project will require continued efforts to achieve a higher fraction of assembly during pre-incubation. This would allow us to start the reaction and simultaneously measure rates of primer extension with rates of ATP hydrolysis by the helicase to quantify the coupling of ATP turnover during unwinding. Successful initiation of the replisome during pre-incubation with our assay will also afford measurements of the

effects of single point mutations on the polymerase and helicase as they act at the replication fork. Our previous studies have examined mutations at the active site of Pol γ (55, 143) and a reconstituted replisome fork will allow for the examination of residues outside of the Pol γ active site that are important in the coordination between the polymerase, helicase and mtSSB. This will ultimately provide a better understanding of the mechanistic basis for the physiological consequences of mitochondrial disease mutations.

Chapter 5: Characterization of HIV Reverse Transcriptase Nucleotide incorporation on a DNA/RNA substrate by WT and TAMS mutant

5.1 INTRODUCTION

The work presented here has examined the kinetics of RNA-dependent DNA polymerization by HIV-RT in order to understand the mechanistic basis for the effectiveness of inhibitors and the evolution of resistance. Extensive work in the Johnson lab has been done to study DNA-dependent DNA polymerization and it is still ongoing (90, 144-146), but it is important to study the differences seen in RNA-dependent DNA polymerization. By better understanding the mechanism of HIV-RT polymerization and development of resistance to NRTIs, we can facilitate the development of drugs that are more effective in blocking replication of the virus. We have combined traditional pre-steady state experiments with newly developed experiments involving an environmentally sensitive fluorophore to obtain rates for individual steps governing RNA-dependent DNA polymerization. Using methods similar to those shown for labeling T7 DNA polymerase (129), we have adapted the method to fluorescently label HIV-RT on the fingers subdomain (128). The fluorophore provides a signal to monitor changes in conformation of the fingers subdomain in order to measure the rates of conformational changes. The MDCC (7-diethyl - lamino-3-(((2-maleimidyl)ethyl)amino)carbonyl) -coumarin) label, shown in magenta in Figure 5.2, is added to position 36 that is mutated from a glutamic acid to a cysteine by site directed mutagenesis. This places the fluorophore in an ideal location on the outside of the fingers subdomain on the αA helix. At this position, it can be used to detect conformational changes in the fingers subdomain from the “open” to “closed” state but likely does not interfere with the conformational

change (86, 146-148). Our labeling method does include the removal of one cysteine at position 280 by mutating to a serine, but it has been shown that this alteration is frequently found in naturally occurring HIV isolates (149) and therefore could also be considered wild-type. There is another naturally occurring cysteine in the enzyme that was not necessary to remove at position 38. This residue is highly conserved and buried in a hydrophobic pocket near the active site so it is not reactive with the MDCC label (150).

Using MDCC labeled HIV-RT we can perform stopped flow experiments to monitor changes in fluorescence over time under different reaction conditions. As an example, work with MDCC-labeled protein has been recently published (128) showing how the fluorescence signal monitors conformation changes during polymerization. In this work, stopped flow experiments showed a 30% increase in fluorescence upon DNA binding to HIV-RT followed by a 30% decrease in fluorescence upon formation of the ternary Enzyme-DNA-dNTP complex. These large changes in fluorescence are sufficient to accurately measure kinetic and equilibrium binding. The MDCC label was able to detect a change in fluorescence due to a conformational change of the enzyme induced by nucleotide binding and revealed a two step nucleotide binding model consisting of a weak rapid equilibrium binding to the open enzyme state, followed by a rapid conformational change to the closed enzyme state. This finding was able to resolve the mechanism by which HIV-RT discriminates against the nucleoside analog 3TC-TP which, in previous studies, had been shown to have a lower K_m than the natural nucleotide. In this work we study the six thymidine analog mutations (TAMs) that have been shown to give clinical resistance to AZT, the thymidine analog 3'-azido-3'-deoxythymidine (Figure 5.1 and 5.2).

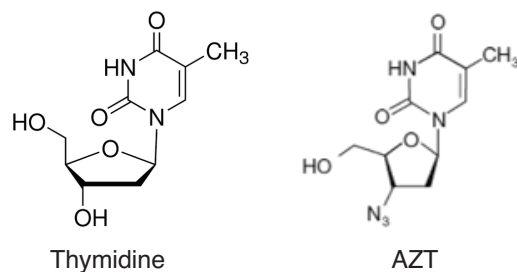


Figure 5.1. Structure of thymidine and AZT. AZT (3'-azido-3'-deoxythymidine) contains an azide group in place of the hydroxyl group at the 3' carbon of the ribose ring. The presence of the 3'-azido group does not allow for the 5' to 3' phosphodiester linkage and therefore AZT acts as a chain terminator.

AZT was the first drug approved to treat HIV in 1985 (151) and is still used today. It is given as a pro-drug and is converted to its triphosphate form by cellular kinases (152) before it can be incorporated into the DNA by HIV-RT in place of the natural thymidine triphosphate as an NRTI (nucleoside reverse transcriptase inhibitor). As can be seen in the structure (Figure 5.1), AZT lacks the free 3' OH; therefore, once it is incorporated into the growing DNA strand, chain termination occurs and polymerization can no longer continue.

Because treatment of HIV with NRTIs does not provide a cure for the virus, drug therapy must be life-long which ultimately leads problems of drug toxicity and development of resistance mutations in HIV-RT. With the treatment of AZT, patients commonly develop a group of mutations referred to as the Thymidine Analog Mutations (TAMs) (153, 154). Of the six TAMs mutations, the K70R and T215Y mutations have been shown to appear in patients relatively early after treatment with AZT and they serve as the primary mutations that confer resistance to AZT. The four remaining mutations (M41L, D67N, L210W, and K219Q) are considered secondary mutations that improve AZT resistance (155). The resistance mechanism thought to be employed by the TAMs mutant is ATP-dependent excision of the NRTI (94, 96, 156). Recent structural data

suggests that the TAMs mutations create a new ATP binding site to which ATP can bind and act as the pyrophosphate donor to excise the AZT from the terminated primer (100). It has also been suggested that once incorporated, an AZT terminated primer remains more often in the nucleotide binding site (pre-translocation) and not the primer binding site (post-translocation) so that it is readily accessible for pyrophosphorolysis (157). Once the AZT is excised the primer is rescued and can react with the correct nucleotide to continue polymerization.

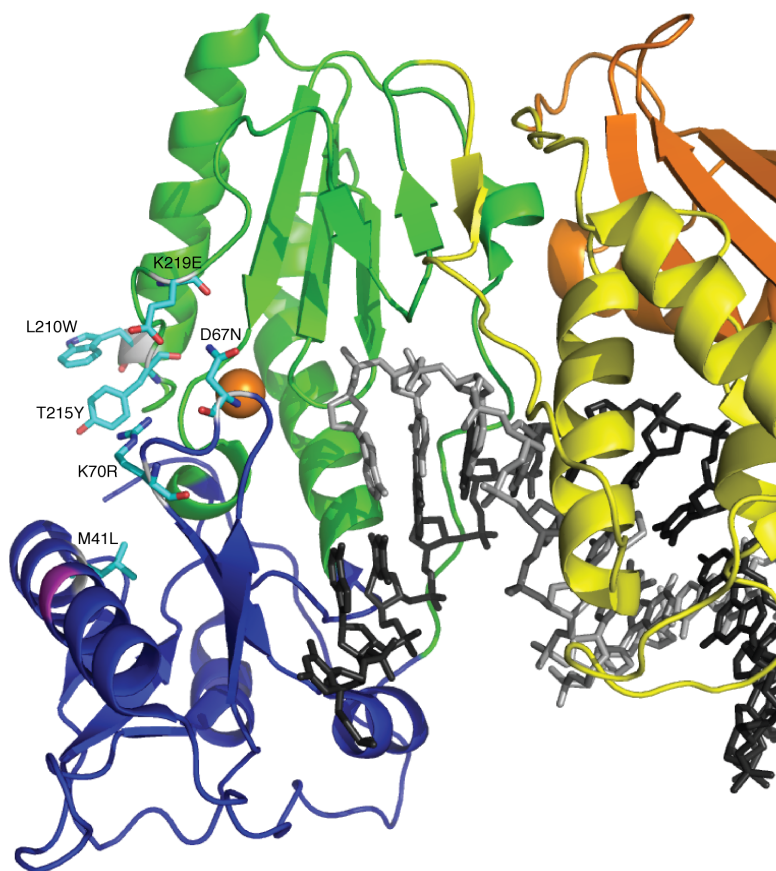


Figure 5.2. Structure of HIV-RT with TAMs mutations. Crystal structure of HIV-RT (PDB:3KLF) with the TAMs mutations shown in cyan (M41L, D67N, K70R, L210W, T215Y and K219Q). The fingers subdomain is shown in blue with the MDCC fluorophore position highlighted in magenta.

Kinetic studies have previously been performed on the TAMs mutant but none of the results can account for the strong resistance effects seen in the clinic (*153, 158, 159*). Published pre-steady state kinetic experiments with a DNA/RNA primer template have shown only a modest 2-fold decrease in selectivity for AZT incorporation by the TAMs mutant compared to the wild-type enzyme (*158*). In this work, pre-steady state rapid quench methods, stopped flow methods and global fitting methods are employed to more closely examine the specificity by the TAMs mutant.

5.2 MATERIALS AND METHODS

Site directed mutagenesis of HIV-RT

The catalytic subunit (p66) and the accessory subunit (p51) of HIV-1 RT strain HxB2 were cloned and expressed individually and combined at the purification step. The gene for the full-length p66 subunit used in previous studies by our lab (*146*), was maintained in a pET-21a ampR vector under the control of the T7lac promoter by which expression is induced with the addition of isopropyl- β -D-thiogalactopyranoside (IPTG). The p51 accessory subunit with the deletion of thirteen amino acids at the C-terminus (p51 Δ 13) was also under the control of a T7lac promoter in a separate pET-30a vector. This vector differs from pET-21a in its antibiotic resistance to kanamycin rather than ampicillin. No purification tags were added to either the p66 or p51 subunit. Site-directed PCR mutagenesis was utilized to introduce all of the mutations discussed in this work. For this chapter on RNA-dependent DNA polymerization it was necessary to perform experiments with a variant of HIV-RT that is deficient in RNase H activity. This allows the study of the DNA polymerization reaction exclusively, without the complication of

any RNase H activity while using a DNA/RNA substrate. A mutation of the glutamic acid residue at position 478 to a glutamine results in a defective RNase H function but wild-type reverse transcriptase activity (160). This mutation was therefore present in the p66 subunit in all experiments in this chapter. Other mutations added to RT in this chapter are the TAMs mutations in p66 along with the MDCC labeling site mutations in both p66 and p51 (p66-E36C/C280S, p51-C280S). For each 50 μ L mutagenesis reaction, 50 ng of parental dsDNA was mixed with 100 ng of forward and reverse primers, 1X cloned *Pfu* reaction buffer, 1 μ L of 10 mM dNTPs (Promega), and 2.5 units of *Pfu Turbo* DNA polymerase (Stratagene). The PCR amplification reaction was then performed with the following optimized thermal cycling conditions: 95°C for 5 minutes, followed by 18 cycles of 95°C for 30 seconds, 55°C for 1 minute, and 72°C for 8 minutes. A final extension step of 72°C for 15 minutes before final storage at 4°C. The PCR reaction was then transformed into Novablue (Novagen) *E. coli*. See Table 5.1 for primer sequences used for mutagenesis as well as the T7 promoter sequencing primers used to confirm the result of the mutagenesis.

Table 5.1 *Mutagenic primers for HIV-RT*

MDCC Labeling Site Mutations

p66-E36C

Forward: 5' -CATTGACAGAAGAAAAATAAAAGCATTAGTATGCATTTGTACAGA
GATGGAAAAGGAAG-3'
Reverse: 5' -CTTCCTTTTCCATCTCTGTACAAATGCATACTAATGCTTTTATTTTTT
CTTCTGTCAATG-3'

p66/p51-C280S

Forward: 5' -CCAGGGATTAAAGTAAGGCAATTATCTAAACTCCTTAGAGGAACCAAAGCACT-3'
Reverse: 5' -AGTGCTTTGGTTCCTCTAAGGAGTTTAGATAATTGCCTTACTTTAATCCCTGG-3'

RNaseH Deficiency Mutation

p66-E478Q

Forward: 5' -TGACACAACAAATCAGAAGACTCAGTTACAAGCAATTTATCTAG-3'
Reverse: 5' -CTAGATAAATTGCTTGTAACTGAGTCTTCTGATTTGTTGTGTCA-3'

TAMS Mutations

p66-M41L

Forward: 5' -CATTAGTATGCATTTGTACAGAGCTGGAAAAGGAAGGGAAAATTC-3'
Reverse: 5' -GAAATTTTCCCTTCCTTTTCCAGCTCTGTACAAATGCATACTAATG-3'

p66-D67N_K70R

Forward: 5' -CTCCAGTATTTGCCATAAAGAAAAAAACAGTACTCGCTGGAGAAAATT
AGTAGATTTCA-3'
Reverse: 5' -TGAAATCTACTAATTTTCTCCAGCGAGTACTGTTTTTTTTTCTTTATGGCA
AATACTGGAG-3'

p66-L210W_T215Y_K219E

Forward: 5' -GCTGAGACAACATCTGTGGAGGTGGGGACTTTACACACCAGACGAAAA
CATCAGAAAGA-3'
Reverse: 5' -TCTTTCTGATGTTTTTCGTCTGGTGTGTAAAGTCCCCACCTCCACAGATG
TTGTCTCAGC-3'

T7 Sequencing primers

Forward: 5' -TAATACGACTCACTATAGGG-3'
Reverse: 5' -GCTAGTTATTGCTCAGCGGT-3'

Expression of HIV-RT p66 and p51 subunits

Once sequencing with the T7 sequencing primers confirmed the correct sequence for a p66 or p51 gene, the plasmid was transformed into BL21(DE3) competent *E. coli* cells (EMD Millipore) by following the suppliers protocol for a standard transformation reaction. The transformation mix was subsequently plated on LB agar plates containing the correct antibiotic to select for either the pET21-a_p66 or pET-30a_p51 plasmid and incubated at 37°C overnight. The pET21-a_p66 plasmid was selected for using LB agar plates containing 100 µg/mL ampicillin and the pET30-a_p51 plasmid was selected for using LB agar plates containing 50 µg/ml kanamycin. An individual colony was then used to inoculate an overnight “starter culture” for the large-scale expression. The starter culture contained 250 mL of LB plus antibiotic (100 µg/mL Ampicillin or 50 µg/mL kanamycin). Once inoculated with a single transformant, the starter culture was incubated with shaking at 250 rpm at 37°C overnight. After >10 hours of growth, the OD₆₀₀ of the starter culture was measured by spectrophotometer and this was used to inoculate the large scale cultures consisting of 6 1L baffled-bottom Erlenmeyer flasks of LB plus antibiotic to an OD₆₀₀ of 0.1. The cultures were grown at 37°C with shaking at 150 rpm and the optical density was monitored until it reached an OD₆₀₀ of 0.6. At this point, the protein expression was induced by the addition of 0.5 mM IPTG to each flask. After induction, the incubation at 37°C and 150 rpm continued for 3 hours while monitoring the optical density. After 3 hours of growth the cells were then harvested by centrifugation at 4000xg for 20 minutes and the cell pellet was stored at -80°C until purification. A typical expression curve is shown in Figure 5.3 below. Figure 5.3B shows an 8% SDS-PAGE gel with samples from an expression of p66 pre- and post-induction with IPTG (lanes 1 and 2, respectively) and a separate expression of p51 pre- and post-induction with IPTG (lanes 3 and 4, respectively). Typically expressions resulted in 18g

of cell pellet per 6 liters of culture. For a typical purification of RT, 6 liters of culture were used to express p66 and 6 liters of culture were used to express p51.

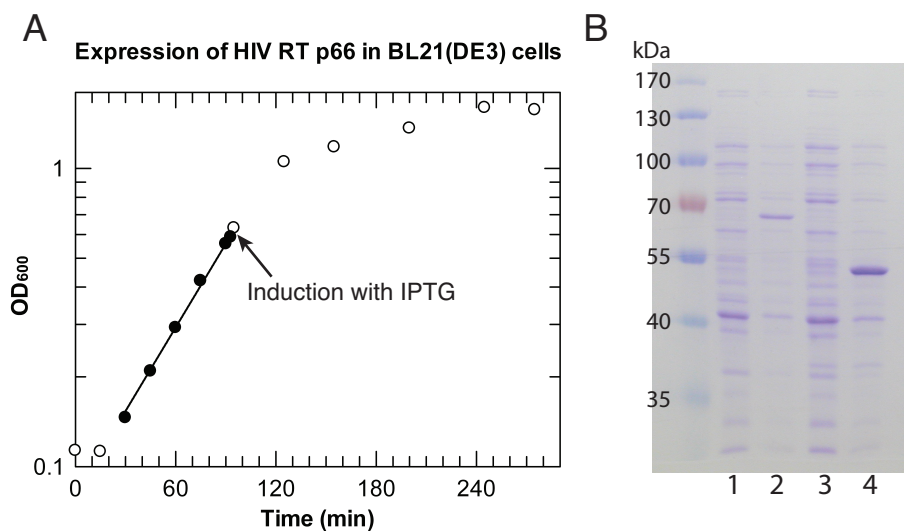


Figure 5.3. *Expression of HIV-RT.* (A) Growth kinetics of BL21(DE3) cells containing the expression plasmid pET21a expressing the p66 subunit of HIV-RT. Cultures were grown at 37°C to an OD₆₀₀ of 0.6 (filled circles) and induced with the addition of 0.5 mM IPTG. After induction, cultures were grown for 3 hours (open circles) before harvesting by centrifugation. (B) SDS-PAGE analysis of expression of subunits of HIV-RT. Lane 1 shows a sample from cultures containing the pET21a_p66 plasmid before induction and Lane 2 shows a sample from this culture 3 hours after induction with the expression of p66. Lane 3 shows a sample from cultures containing the pET30a_p51 plasmid before induction and Lane 4 shows a sample from this culture 3 hours after induction with the expression of p51.

The pre- and post-induction samples equal to 6 OD units of cells were then analyzed by SDS-PAGE as shown in Figure 5.3B. For this analysis, the 6 OD unit samples from p66-pre-induction, p66-post-induction, p51-pre-induction, and p51-post-induction were resuspended in 50 mM Tris-HCl pH 8 and 100 µg/ml lysozyme (Sigma-Aldrich) before incubation in a 37°C water bath for 10 minutes to lyse the cells. The lysate was then sonicated for 30 bursts (20% duty cycle, 1.5 output level) followed by

centrifugation at 10,000 rpm for 10 minutes. The supernatant was then mixed with SDS-PAGE loading dye and run on an 8% SDS-PAGE gel. Once stained with coomassie blue solution and destained the gel was scanned using an Odyssey CLx (LI-COR) to determine the relative densities of the p66-post-induction and p51-post-induction bands. This was then used to calculate the weights of each of the cell pellets to be mixed to obtain a 1:1 molar ratio of p66 and p51 during purification.

Purification and MDCC labeling of HIV-RT

The combined p66 and p51 cell pellets were resuspended in *RT Buffer A* (30 mM HEPES pH 7.9, 60 mM NaCl, 1 mM DTT, 0.1 mM EDTA) + protease inhibitor cocktail IV (AG Scientific). Cells were then lysed by sonication using a Branson sonifier 450 at 20% duty cycle, output 6 for 20 minutes while stirring on ice. The lysate was then cleared by ultracentrifugation at 40,000 rpm for 30 minutes at 4°C using a Beckman 45Ti rotor. The supernatant was then loaded onto a tandem setup of a Q sepharose (GE) column followed by a Bio-Rex 70 column (Bio-Rad) equilibrated in *RT Buffer A* (Figure 5.5). After loading, the Q sepharose column was removed and the Bio-Rex 70 column was washed with 2% *RT Buffer B* (30 mM HEPES pH 7.9, 1 M NaCl, 1 mM DTT, 0.1 mM EDTA). The protein was eluted from the Bio-Rex 70 column with a linear gradient from 2-47% *RT Buffer B* over five column volumes collecting 5 mL fractions. Fractions were analyzed by SDS-PAGE, pooled and diluted to the conductivity of *RT Buffer A* using *RT Buffer C* (30 mM HEPES pH 7.9, 1 mM DTT, 0.1 mM EDTA). The diluted protein was then loaded onto a single-stranded DNA cellulose column (Sigma Aldrich) equilibrated in *RT Buffer A* (Figure 5.6). After loading the column was washed with 2% *RT Buffer B* and eluted with a linear gradient from 2% to 47% *RT Buffer B* over five column volumes collecting 5 ml fractions. Fractions were analyzed by SDS-PAGE and selected fractions

were dialyzed against 2 L *MDCC Labeling Buffer* (30 mM HEPES pH 7.9, 250 mM NaCl, 0.1 mM EDTA, 1 mM Tris(2-carboxyethyl)phosphine hydrochloride (Sigma-Aldrich)) for 2 hours. Protein concentration was then estimated by absorbance using the $\epsilon_{280} = 260,450 \text{ M}^{-1}\text{cm}^{-1}$ and MDCC labeling reactions were setup by adding a 10-fold molar excess of MDCC (Figure 5.4) and incubating overnight at 4°C. The labeled protein was then purified from excess label by passing over the Bio-Rex 70 column in *RT Buffer A* and eluting with 30% *RT Buffer B* (Figure 5.7). Fractions were then pooled, concentrated using a Centricon ultrafiltration unit (30 KDa MWCO, Millipore), and dialyzed into *RT Storage Buffer* (50 mM Tris-HCl pH 7.5, 50 mM NaCl, 1 mM DTT, 0.1 mM EDTA). The final protein concentration was estimated by A_{280} , as above, flash frozen in liquid nitrogen and stored at -80°C.

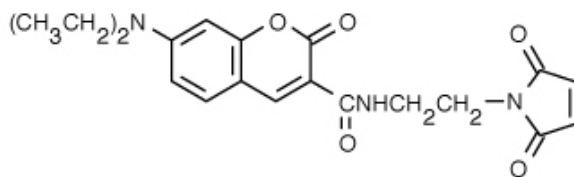


Figure 5.4. *Structure of MDCC.* MDCC (7-diethylamino-3-(((2-maleimidyl)ethyl)amino)carbonyl)coumarin is a thiol reactive coumarin that forms a covalent linkage through a thiol-maleimide bond. This fluorescent probe is environmentally sensitive and when excited with 425 nm light it gives an emission of about 470 nm.

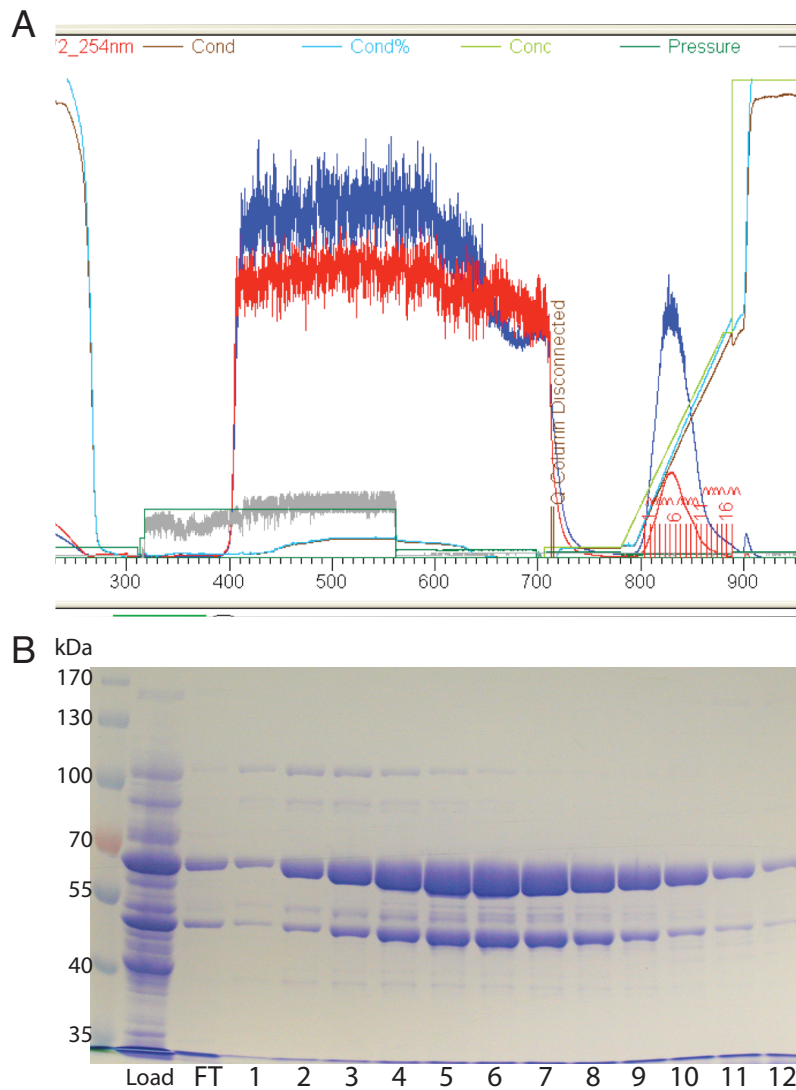


Figure 5.5 *Tandem column purification of HIV-RT.* (A) Tandem Q sepharose and Bio-Rex70 column chromatography of HIV-RT from cell lysate. Absorbance at 280 nm (blue) and 254 nm (red) was monitored to detect protein and DNA respectively. After loading onto tandem columns, the Q sepharose column was removed and the Bio-Rex 70 column was washed with 2% *RT Buffer B*. HIV-RT was eluted from the Bio-Rex70 column with a linear gradient from 2-47% *RT Buffer B* and conductivity percentage was monitored (light blue). (B) SDS-PAGE analysis of the loaded lysate (Load), flow-through (FT) and fractions 1-12 confirm the presence of HIV-RT p66 and p51 subunits in fractions 3-9.

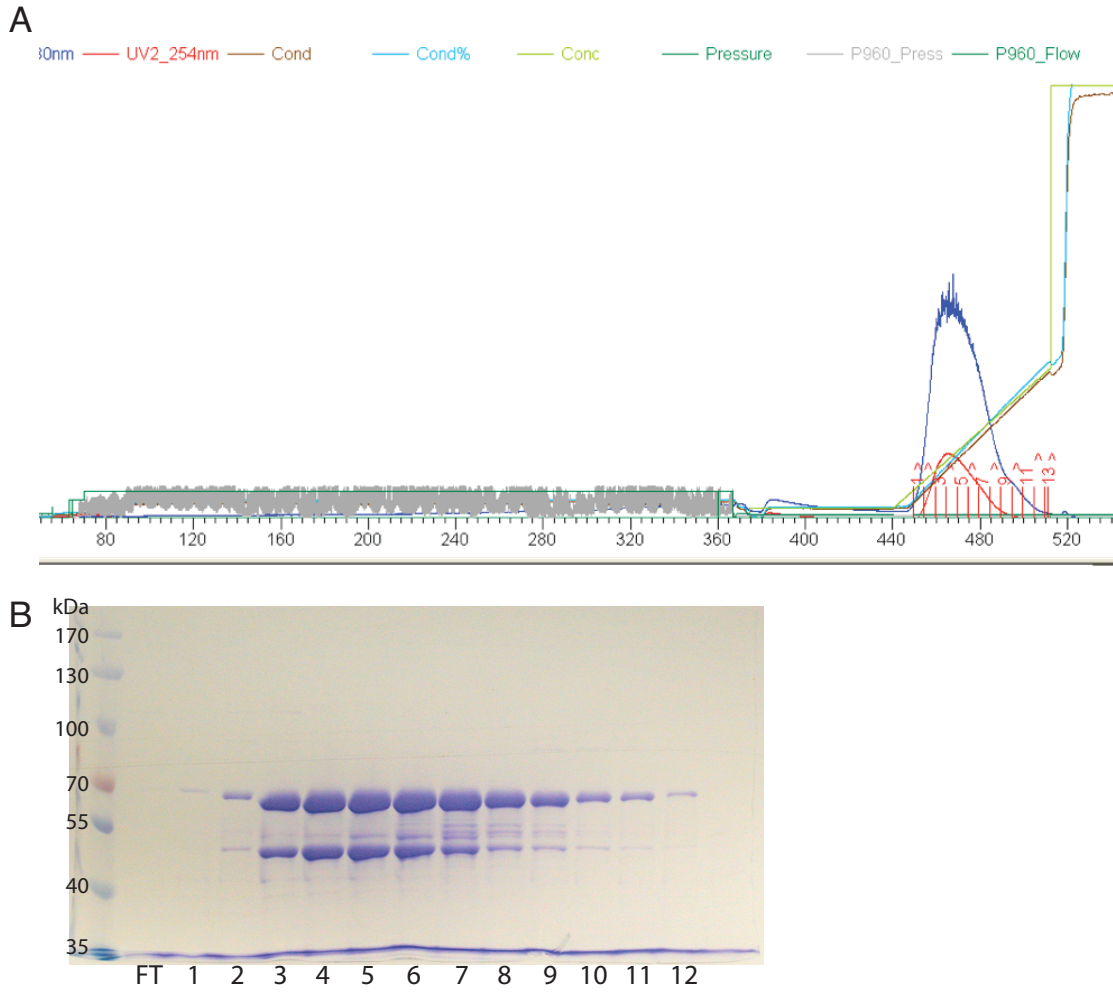


Figure 5.6 *ssDNA cellulose column purification of HIV-RT*. *ssDNA cellulose column chromatography of HIV-RT from Bio-Rex 70 fractions*. Absorbance at 280 nm (blue) and 254 nm (red) was monitored to detect protein and DNA respectively. After fractions from the Bio-Rex70 column were pooled, they were loaded onto *ssDNA cellulose column*. The *ssDNA cellulose column* was washed with 2% *RT Buffer B* and HIV-RT was eluted with a linear gradient from 2-47% *RT Buffer B* and conductivity percentage was monitored (light blue). (B) SDS-PAGE analysis of the flow-through (FT) and fractions 1-12 confirm the presence of HIV-RT p66 and p51 subunits in fractions 3-7.

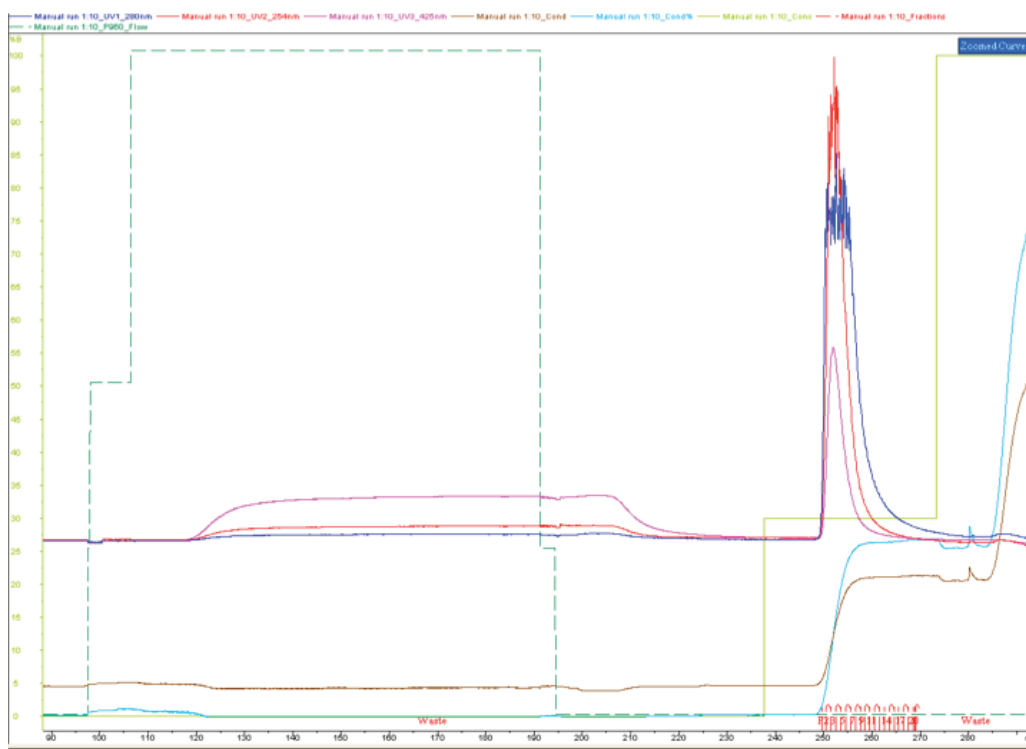


Figure 5.7 Bio-Rex70 column purification of MDCC-labeled HIV-RT. Bio-Rex70 column chromatography of HIV-RT from MDCC-labeled fractions. Absorbance at 280 nm (blue), 254 nm (red) and 425 nm (magenta) was monitored to detect protein, DNA and MDCC respectively. Overnight MDCC-labeling reactions of HIV-RT were loaded onto the Bio-Rex70 column and washed with *RT Buffer A* to remove the excess MDCC label. Labeled HIV-RT was eluted with 30% *RT Buffer B* and conductivity percentage was monitored (light blue).

Preparation of substrate DNA and RNA

DNA substrates were purchased from Integrated DNA Technologies (IDT) and purified by 15% denaturing polyacrylamide gel electrophoresis. RNA substrates were also purchased from IDT and were ordered HPLC-purified. Sequences of 25-mer DNA primer (d25mer) and 36-mer template RNA (r36mer) oligomers are listed in Table 5.2.

For quench flow assays, the 5' end of the primer oligomer was ^{32}P -labeled using T4 polynucleotide kinase (New England Biolabs) and $\gamma\text{-}^{32}\text{P}\text{-ATP}$ according to the manufacturers protocol. After ^{32}P labeling, the reaction was heated to 95°C for 5 minutes

and purified using a Bio-Spin P-6 gel column (Bio-Rad) to remove the excess γ - ^{32}P -ATP. The concentration of the purified ^{32}P -5'-labeled primer was determined by TLC.

Duplex DNA/RNA substrates were formed by incubating the d25mer primer with the r36mer template at a 1:1 molar ratio in an *Annealing Buffer* (10 mM Tris-HCl pH 7.5, 50 mM NaCl, 1 mM EDTA) and heating to 95°C for 5 minutes before allowing to slowly cool to room temperature.

All work with RNA was performed with DEPC-treated water in an RNA-free environment.

Synthesis of 2', 3'-dideoxyterminated dd26mer

In stopped flow assays measuring the binding of nucleotide without chemistry, a 2', 3'-dideoxy-terminated primer (dd25mer) was used such that chemistry was not possible on the primer lacking a 3'-OH. This dd25mer was synthesized in a reaction containing an oligomer with the first 24-nucleotides of the DNA primer sequence (5'-GCCTCGCAGCCGTCCTCAACCAACTC-3') annealed to a 45-mer DNA template 5'-GGACGGCATTGGATCGACGATGAGTTGGTTGGACGGCTGCGAGGC-3') to allow the incorporation of a ddATP versus the template dTMP. The synthesis reaction contained 560 μM 24/45mer DNA substrate, 500 μM HIV-RT, 10 units of pyrophosphatase (Sigma), and 1.5 mM ddATP (UBS). The reaction was incubated at 37°C for 2 hours in RT-buffer (50 mM Tris-HCl (pH 7.5), 100 mM potassium acetate, 0.1 mM EDTA) and 10 mM MgCl_2 . After incubation the reaction was terminated by phenol:chloroform extraction and purification of the dd25mer by ethanol precipitation followed by 15% denaturing PAGE.

Table 5.2 DNA-primer/RNA-template sequences for HIV-RT

<u>d25/r36mer</u>	
d25mer	5' -GCCTCGCAGCCGTCCAACCAACTCA
r36mer	3' -CGGAGCGUCGGCAGGUUGGUUGAGUAGCAGCUAGGU
<u>dd25/r36mer</u>	
dd25mer	5' -GCCTCGCAGCCGTCCAACCAACTCA _{dd}
r36mer	3' -CGGAGCGUCGGCAGGUUGGUUGAGUAGCAGCUAGGU

Quench flow kinetic assays

Chemical quench flow experiments measuring single nucleotide incorporation of TTP or AZTTP were performed at 37 °C in a 1X-RT-Buffer containing 50 mM Tris-HCl (pH 7.5), 100 mM potassium acetate, 0.1 mM EDTA with a RQF-3 rapid-quench-flow apparatus (KinTek Corp). Quench flow assays used 5'-³²P-labeled d25/r36mer primer-template duplex sequence listed in Table 5.2. The incorporation of TTP or AZTTP was measured by rapidly mixing a preformed enzyme-DNA complex (175 nM HIV-RT, 75 nM 5'-³²P-labeled d25/r36mer DNA/RNA) with an equal volume of Mg-TTP²⁻ or Mg-AZTTP²⁻ at various concentrations (0.1, 0.25, 0.5, 1.5, 10, and 100 μM TTP for wild-type HIV-RT). The final concentration of magnesium acetate was 10 mM. The reactions were quenched by mixing with 0.5 M EDTA after various time intervals (0-2 seconds for wild-type HIV-RT). All concentrations listed are final.

After quenching, the reactions were mixed with denaturing PAGE loading dye (0.25% bromophenol blue, 0.25% xylene cyanol) and separated on a 15% denaturing polyacrylamide sequencing gel. After drying the gel was exposed to a storage phosphor screen and the bands were quantified using a Typhoon scanner (GE) and ImageQuant 5.0 (Molecular Dynamics). The concentration of the product formed over time was calculated

as the product of the concentration of substrate ^{32}P -labeled DNA added times the fraction of material in the 26mer band. Data collected were fit by global data fitting methods described below.

Stopped flow nucleotide incorporation assays

Stopped flow experiments measuring incorporation of TTP or AZTTP were performed at 37 °C in a 1X-*RT-Buffer* containing 50 mM Tris-HCl (pH 7.5), 100 mM potassium acetate, 0.1 mM EDTA with a an AutoSF-120 series stopped-flow instrument from KinTek Corp. For this assay, 100 nM MDCC-labeled HIV-RT wild-type or mutant was preincubated with 150 nM d25/r36mer DNA/RNA duplex for 15 minutes at 37°C. The reaction was then started by mixing with a solution containing various concentrations of TTP or AZTTP in RT buffer supplemented with 10 mM magnesium acetate. The MDCC fluorophore on HIV-RT was excited at 425 nm and the fluorescence emission was measured as a function of time using a 475 nm single-band bandpass filter (Semrock).

Stopped flow nucleotide dissociation assays

Experiments measuring nucleotide dissociation from a dd25/r36mer ddDNA/RNA primer template were performed in the AutoSF-120 stopped-flow instrument in a similar manner as was described above. In this nucleotide dissociation assay, 100 nM MDCC-labeled HIV-RT wild-type or mutant was preincubated with 150 nM dd25/r36mer DNA/RNA duplex and 1.4 μM TTP or AZTTP for 15 minutes at 37°C. This was then rapidly mixed with a solution of *RT Buffer* containing a 5 μM unlabeled-HIV-RT trap to bind the dissociated nucleotide. An increase in MDCC-fluorescence was observed by exciting at 425 nm and monitoring emission at 475 nm as a function of time.

Global data fitting

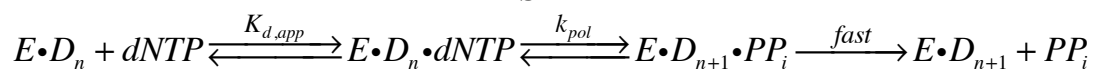
The chemical quench flow assays and stopped flow assays were fit to the models described in the subsequent results section using the Kintek Global Explorer program (Kintek Corp.). This fitting technique is outlined in detail in the methods section of Chapter 2.

5.3 RESULTS

Kinetics of nucleotide binding and incorporation by quench flow methods

In this work, both rapid chemical quench flow and stopped flow experiments were performed on the RNase H deficient, fluorescently labeled HIV-RT (MDCC-RT) on a DNA/RNA primer template. Here, to measure the kinetics of nucleotide binding and incorporation by quench flow methods, RNaseH deficient MDCC-RT and the MDCC-RT-TAMS mutants were each preincubated with the d25/r36mer substrate in reaction buffer to form an enzyme-DNA complex. The reactions were setup with an excess of enzyme over DNA/RNA template to afford single turnover conditions. This formed complex was then rapidly mixed with various concentrations of the correct nucleotide (TTP) or AZTTP and quenched with 0.5M EDTA after various time intervals in the rapid quench flow instrument RQF-3 to obtain the data shown in Figure 5.8. The amount of 26-mer product formed over time was plotted and globally fit using the model shown in Scheme 5.1.

Scheme 5.1



Fitting of just the quench flow experiments to the model for nucleotide incorporation in Scheme 5.1 allows for determination of the maximum rate of

incorporation (k_{pol}) and an apparent nucleotide dissociation constant ($K_{d,app}$). The model assumes that the polymerization step is a single rate-limiting step that follows a rapid equilibrium for nucleotide binding. These values were then used to calculate the specificity constant where $k_{cat}/K_m = k_{pol}/K_{d,app}$. The discrimination and resistance values were calculated according to Equation 5.1 and 5.2. The fitting results are summarized in Table 5.3. On the RNA/DNA substrate, the RNaseH deficient MDCC-labeled RT showed similar nucleotide incorporation kinetics to those that have been previously reported (158). The rate of polymerization k_{pol} was 78.6 s^{-1} and the apparent K_d for TTP was $13 \text{ }\mu\text{M}$. This yielded a specificity constant of $6 \text{ }\mu\text{M}^{-1}\text{s}^{-1}$. The results for the incorporation of AZTTP by RNaseH deficient MDCC-labeled RT, showed a slight reduction in k_{pol} to a value of 41.1 s^{-1} and a comparable $K_{d,app}$ of $13.9 \text{ }\mu\text{M}$. The resulting $k_{pol}/K_{d,app}$ determined by the quench flow studies was $2.9 \text{ }\mu\text{M}^{-1}\text{s}^{-1}$, therefore the discrimination ($(k_{pol}/K_{d,app})_{correct}/(k_{pol}/K_{d,app})_{NRTI}$) favoring TTP over AZTTP is 2.0. The RNaseH deficient MDCC-labeled RT containing the TAMS mutations had a 1.8-fold slower rate of incorporation, 42.5 s^{-1} , and similar $K_{d,app}$ of $14.7 \text{ }\mu\text{M}$ compared to wild-type incorporation of TTP. The quench flow analysis of the incorporation of AZTTP by the RNaseH deficient MDCC-labeled RT containing the TAMS mutations revealed an even further decrease of k_{pol} to a rate of 16.2 s^{-1} while maintaining the same apparent K_d . These results for the TAMS mutant lead to a discrimination factor of 2.6 for correct incorporation of TTP over AZTTP which when divided by the discrimination factor of 2.0 for the wild-type enzyme, leads to a resistance value of 1.3 by the TAMS mutant.

Equation 5.1

$$\text{Discrimination} = D = \frac{(k_{pol} / K_d)_{dNTP}}{(k_{pol} / K_d)_{NRTI}}$$

Equation 5.2

$$\text{Resistance} = \frac{D_{wt}}{D_{mutant}}$$

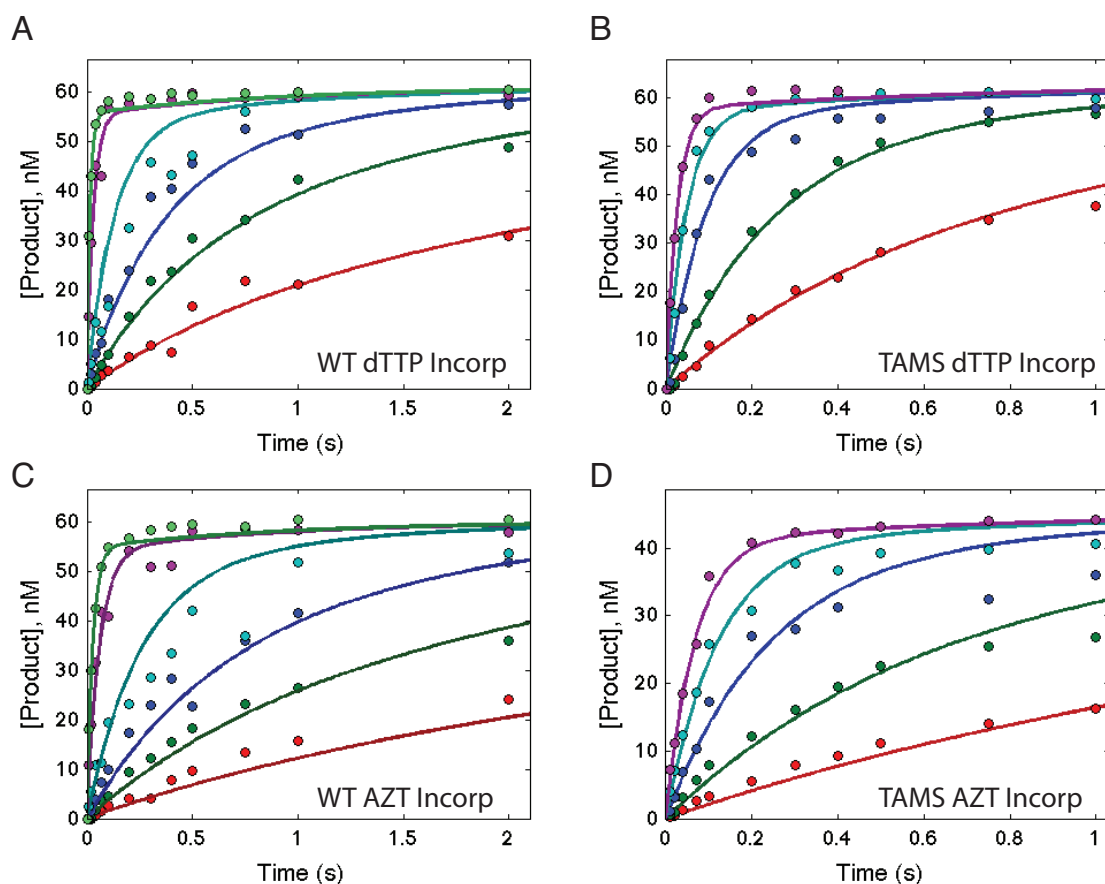


Figure 5.8. Chemical quench flow incorporation of *dTTP* and *AZTTP* by *HIV-RT* WT and *TAMS* mutant. All concentrations listed are final. (A) A preformed enzyme-DNA complex with 175 nM WT *HIV-RT* and 75 nM *d25/r36mer* DNA/RNA was rapidly mixed with increasing concentrations of *dTTP* (0.1, 0.25, 0.5, 1.5, 10 and 100 μM). The reactions were quenched by the addition of 0.5 M EDTA at times from 0 to 2 seconds. (B) A preformed enzyme-DNA complex with 175 nM *TAMS HIV-RT* and 75 nM *d25/r36mer* DNA/RNA was rapidly mixed with increasing concentrations of *dTTP* (0.5, 1.5, 5, 15 and 150 μM). The reactions were quenched by the addition of 0.5 M EDTA at times from 0 to 1 second. (C) A preformed enzyme-DNA complex with 175 nM WT *HIV-RT* and 75 nM *d25/r36mer* DNA/RNA was rapidly mixed with increasing concentrations of *AZTTP* (0.1, 0.25, 0.5, 1.5, 10 and 100 μM). The reactions were quenched by the addition of 0.5 M EDTA at times from 0 to 2 seconds. (D) A preformed enzyme-DNA complex with 175 nM *TAMS HIV-RT* and 75 nM *d25/r36mer* DNA/RNA was rapidly mixed with increasing concentrations of *AZTTP* (0.5, 1.5, 5, 15 and 150 μM). The reactions were quenched by the addition of 0.5 M EDTA at times from 0 to 1 second. In all experiments the formation of 26mer product over time was fit the model in Scheme 5.1 using Kintek Global Explorer. Parameters obtained in fitting are listed in Table 5.3.

Table 5.3 HIV-RT Incorporation parameters

	k_{pol} s^{-1}	$K_{\text{d, app}}$ μM	$k_{\text{pol}}/K_{\text{d, app}}$ $\mu\text{M}^{-1}\text{s}^{-1}$	Discrimination	Resistance
WT					
TTP	78.6 ± 18.6 (62.9 - 123)	13 ± 3.6 (10 - 21)	6 ± 2.2	2.0	-
AZTTP	41.1 ± 8.1 (34.9 - 64.3)	13.9 ± 3.3 (11 - 23)	2.9 ± 0.9		
TAMs					
TTP	42.5 ± 5 (34 - 54.3)	14.7 ± 2.3 (11.1 - 20.4)	2.9 ± 0.6	2.6	1.3
AZTTP	16.2 ± 2 (12.8 - 22.5)	14.5 ± 2.9 (11 - 24)	1.1 ± 0.3		

*Numbers in parenthesis give the lower and upper limits derived from the confidence contour analysis in fitting the data.

Kinetics of nucleotide binding and incorporation by stopped flow methods

The chemical quench flow assays described above allow determination of the apparent K_{d} and the k_{pol} for nucleotide binding and incorporation when fitting to the simple model in Scheme 5.1. This model assumes that the k_{pol} is a single rate-limiting step and the nucleotide binding occurred in a rapid equilibrium. However, previous studies have shown that for RT and other polymerases the nucleotide binding occurs with a minimum of two steps involving a weak equilibrium binding to the open state of the enzyme followed by a reversible conformational change step to a closed conformation of the enzyme before chemistry occurs (129, 161-163). Therefore the value obtained for nucleotide binding in quench flow assays is referred to as an apparent K_{d} . The apparent K_{d} value is a measure of the relative rates of substrate binding and incorporation, which makes it more similar to a Michaelis constant (K_{m}) rather than a measure of ground state nucleotide binding. To explore this two-step nucleotide binding we utilized the

fluorescent MDCC label on the mobile fingers subdomain of RT in the stopped flow instrument (146, 161). These studies were conducted by performing an enzyme-DNA/RNA complex where RNaseH deficient MDCC-RT and the MDCC-RT-TAMS mutants were each preincubated with the d25/r36mer substrate in reaction buffer. As with the quench flow studies, the reactions were setup with an excess of enzyme over DNA/RNA template to afford single turnover conditions. This formed complex was then rapidly mixed various concentrations of the correct nucleotide (TTP) or the NRTI AZTTP in the stopped flow instrument. The change in MDCC fluorescence over time was measured and the data were included in the global fitting of each mutant (Figures 5.9, 5.11-5.13).

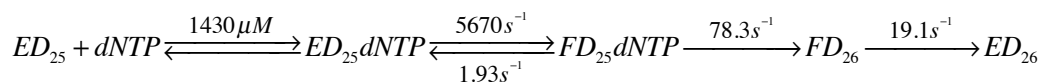
We also included in the global fits an experiment measuring nucleotide dissociation from the enzyme-ddDNA/RNA complex. This change in fluorescence represents the transition from the “closed” nucleotide bound state of the enzyme to the “open” nucleotide free state of the enzyme at a rate limited by the dissociation of the nucleotide.

Global fitting of HIV-RT wild-type TTP incorporation

Figure 5.9 shows the global fitting results for the quench flow and stopped flow experiments performed with wild-type HIV-RT and TTP. 5.9A shows the solid lines of the fitted curves on the data collected from TTP incorporation by HIV-RT monitored changes in fluorescence in the stopped flow instrument. 5.9B shows the global fit of the quench flow TTP incorporation data at six different nucleotide concentrations and 5.9C shows the fitting of the nucleotide dissociation stopped flow monitoring nucleotide release from a ternary complex with MDCC-labeled HIV-RT. The model used for fitting

these three experiments with wild-type HIV-RT is shown in Scheme 5.2 and best-fit values for each parameter are summarized in Table 5.4.

Scheme 5.2



This scheme includes two-step nucleotide binding model where the nucleotide first binds to the enzyme in the open conformation with a weak ground state binding ($1/K_1$) of $1430 \pm 4.4 \mu\text{M}$. This is followed by a fast conformational change to the closed state of the enzyme at $5670 \pm 660 \text{ s}^{-1}$ with a reverse rate of $1.93 \pm 0.006 \text{ s}^{-1}$. At 37°C , the rapid decrease in fluorescence in the stopped flow experiment representing the conformational change of the enzyme from “open” to “closed” was too fast to be fit accurately due to the dead-time of the instrument therefore a temperature dependence of this rate was measured at 5, 10, 15, 20 and 25°C and extrapolated to 37°C . This temperature dependence analysis is shown in Figure 5.10 where A is the rate of the fast phase, k_2 , versus concentration of TTP for the five temperatures tested. Figure 5.10B shows the Arrhenius plot of $\ln(k_{\text{max}})$ against the reciprocal of the absolute temperature relative to 37°C , $(1/T - 1/T_{37})$, so that a linear fit extrapolating a y-intercept representing the $\ln(k_{\text{max}})$ value at 37°C (T_{37}). This estimated a maximum rate of $5670 \pm 660 \text{ s}^{-1}$ that was consistent with initial global fitting analysis and therefore k_2 was locked at this value for the final global fit.

Following the fast conformational change, the model in scheme includes the step for chemistry at $78.3 \pm 0.15 \text{ s}^{-1}$ to form the FD_{26} complex. This is followed by a conformational change to a lower fluorescent state with a rate of 19.1 s^{-1} . The calculation

of k_{cat}/K_m using the values obtained in the global fit was determined using Equation 5.3 and the resulting specificity constant for TTP incorporation by wild-type HIV-RT on a DNA/RNA template is $3.7 \pm 0.74 \mu\text{M}^{-1}\text{s}^{-1}$ (Table 5.5). This value is within the error of the value that was obtained by fitting the quench flow experiment alone ($6 \pm 2.2 \mu\text{M}^{-1}\text{s}^{-1}$) (Table 5.3).

Equation 5.3

$$k_{cat} / K_m = \frac{k_1 k_2 k_3 k_4}{k_{-1} k_{-2} k_{-3} + k_{-1} k_{-2} k_4 + k_{-1} k_3 k_4 + k_2 k_3 k_4}$$

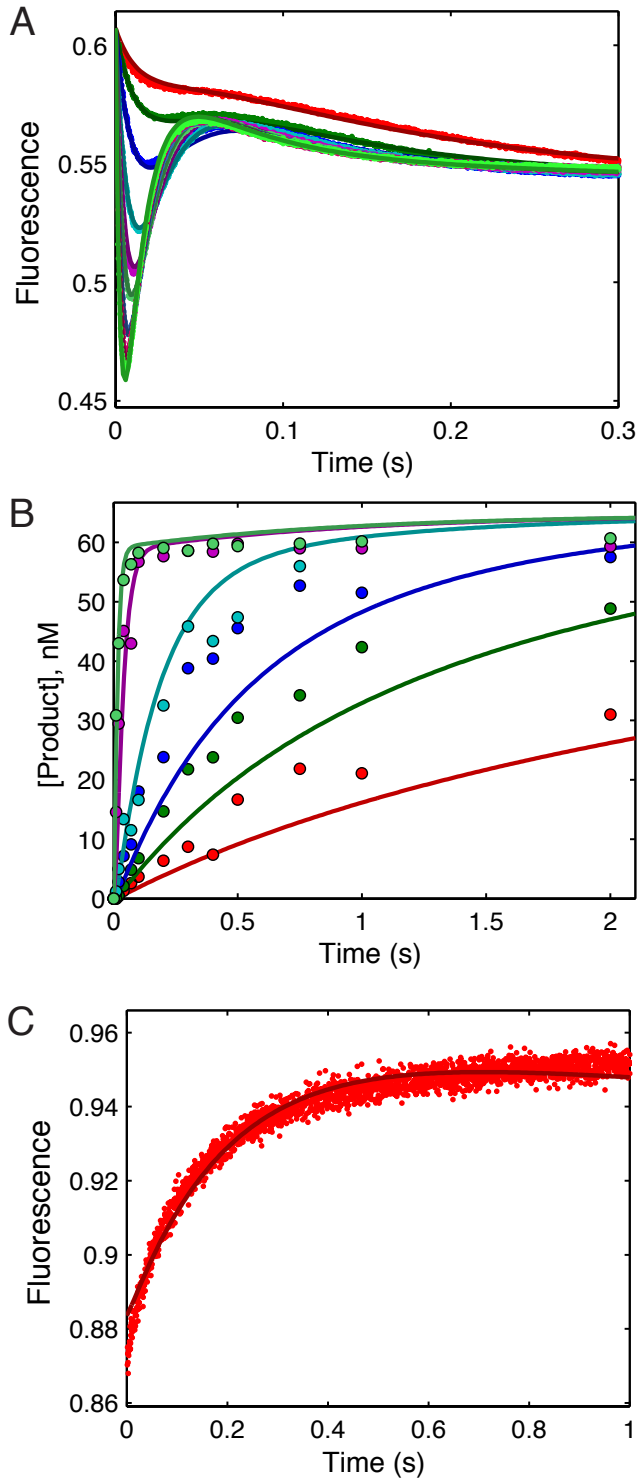


Figure 5.9. Global fitting of dTTP binding and incorporation by WT HIV-RT. (A) Fluorescence data from stopped-flow experiments monitoring MDCC fluorescence over time representing dTTP binding and incorporation. Preformed enzyme-DNA/RNA complex (200 nM HIV-RT WT, 300 nM d25/r36) was rapidly mixed with increasing concentrations of Mg²⁺ and dTTP (2.5, 5, 10, 20, 30, 40, 60, 80 and 100 μM). (B) Chemical quench flow data (shown in Figure 5.8) monitoring the incorporation of dTTP by HIV-RT WT over time. Preformed enzyme-DNA/RNA complex (175 nM HIV-RT WT, 75 nM d25/r36) was rapidly mixed with increasing concentrations of Mg²⁺ and dTTP (0.1, 0.25, 0.5, 1.5, 10 and 100 μM). (C) Fluorescence data from stopped-flow experiments measuring dTTP dissociation from the closed enzyme-DNA/RNA ternary complex. A preformed enzyme-DNA/RNA-dTTP complex (50 nM HIV-RT WT, 75 nM dd25/r36, 1.4 μM dTTP) was rapidly mixed with 600 nM unlabeled enzyme-ddDNA/RNA complex to serve as a trap. An increase in fluorescence representing the release of dTTP from the ternary complex was observed. Rate constants derived from the global fitting are described in Table 5.4.

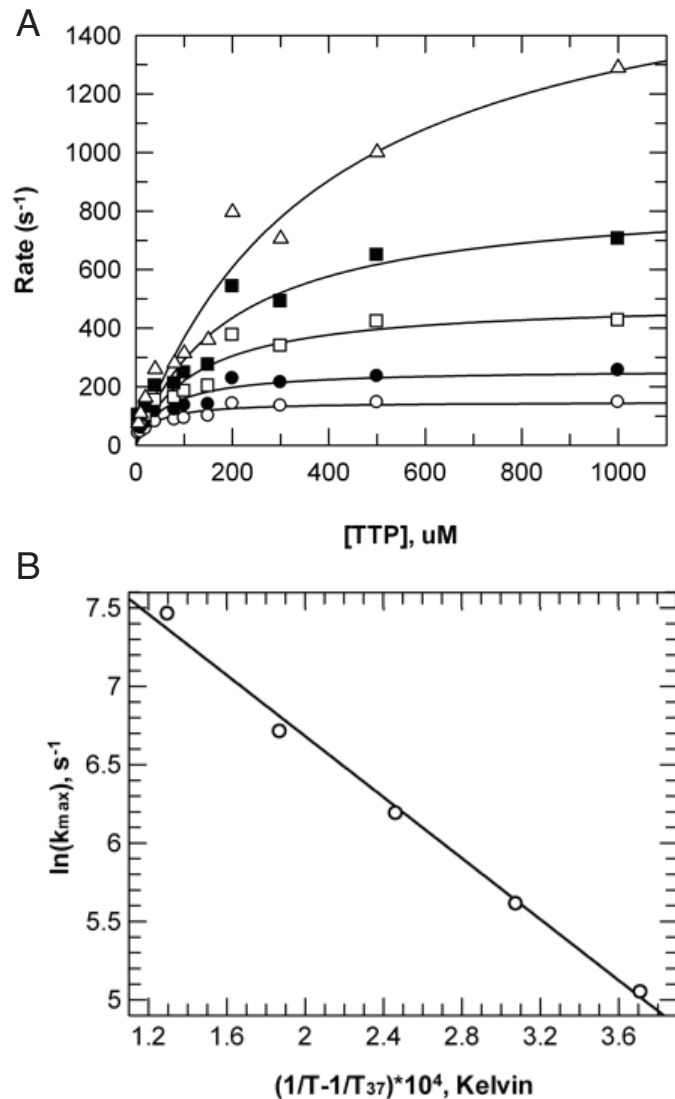
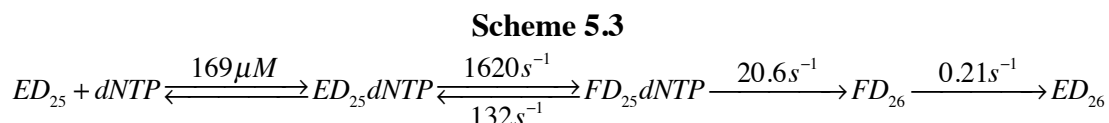


Figure 5.10. *Temperature dependence of dTTP binding and incorporation by WT HIV-RT.* (A) Stopped flow experiments measuring nucleotide binding and incorporation were performed at five different temperatures. The rate of the initial rapid decrease in fluorescence was plotted as a function of nucleotide concentration for each temperature (5°C (open circles), 10 °C (filled circles), 15 °C (open squares), 20 °C (filled squares) and 25 °C (open triangles)). These data were fit to a hyperbola to extract a maximum rate of the conformational change. (B) The natural logarithm of maximum rate determined from A was plotted versus the reciprocal of the absolute temperature minus the reciprocal of the absolute temperature at 37° ($1/T-1/T_{37}$). Fitting of this Arrhenius plot to a linear equation allows for extrapolation to a rate of $5673 \pm 658 \text{ s}^{-1}$ at 37°C.

Global fitting of HIV-RT wild-type AZTTP incorporation

Global fitting of the stopped flow and quench flow experiments for the incorporation of AZTTP by wild-type enzyme during RNA-dependent DNA polymerization is shown in Figure 5.11 and the best fit values are shown on the model Scheme 5.3 and in Table 5.4. The dissociation constant for the initial binding ($1/K_1$) of AZTTP is $169 \pm 2.2 \mu\text{M}$ and the rate of the conformational change is $1620 \pm 21 \text{ s}^{-1}$ with a reverse rate of $132 \pm 1.9 \text{ s}^{-1}$. The chemistry step following the fast conformational change is $20.6 \pm 0.08 \text{ s}^{-1}$ and the isomerization to a lower fluorescence state after chemistry is $0.21 \pm 0.0007 \text{ s}^{-1}$. These best fit values were used in Equation 5.3 to calculate the specificity constant ($k_{\text{cat}}/K_{\text{m}}$) for a 4-step reaction which is equal to $1.3 \pm 0.03 \mu\text{M}^{-1}\text{s}^{-1}$. The discrimination for TTP over AZTTP is therefore equal to $(k_{\text{cat}}/K_{\text{m}})_{\text{TTP}}/(k_{\text{cat}}/K_{\text{m}})_{\text{AZTTP}}$ and is equal to 2.8.



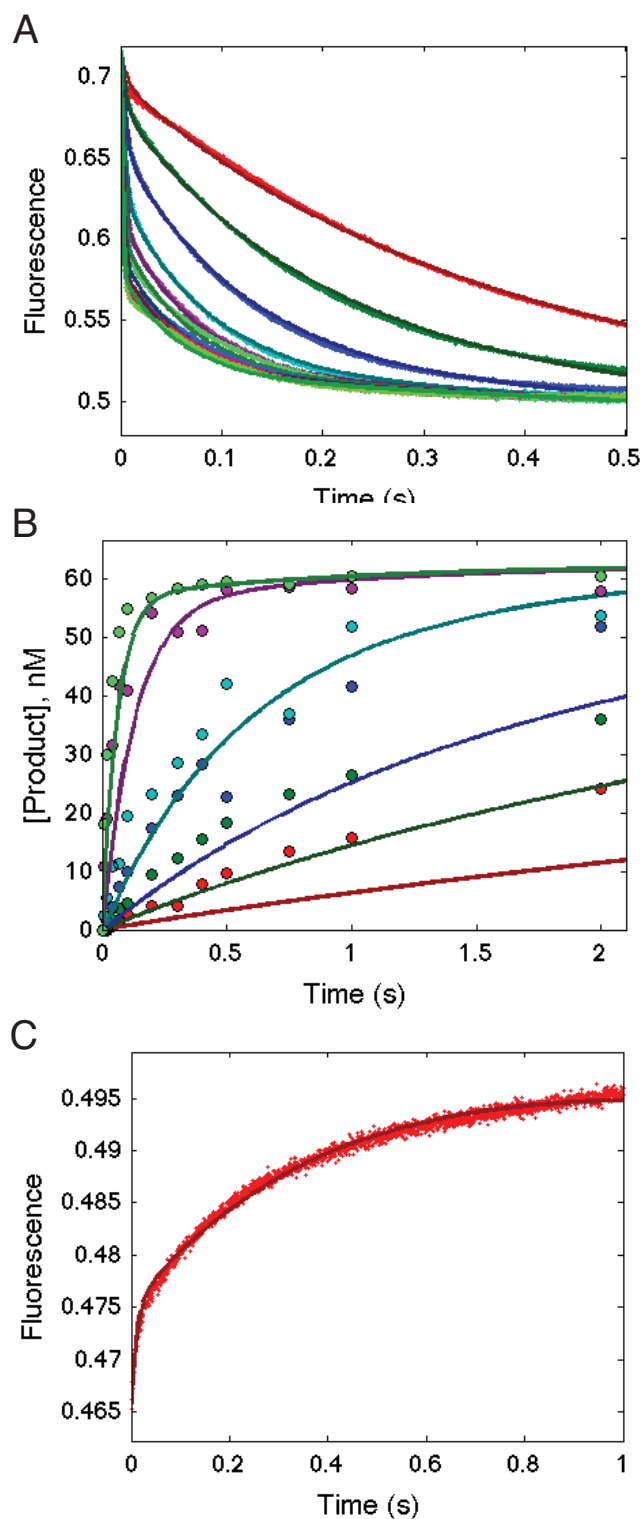
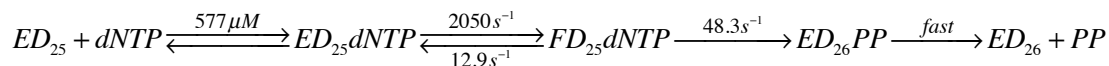


Figure 5.11. Global fitting of AZTTP binding and incorporation by WT HIV-RT. (A) Fluorescence data from stopped-flow experiments monitoring MDCC fluorescence over time representing AZTTP binding and incorporation. Preformed enzyme-DNA/RNA complex (200 nM HIV-RT WT, 400 nM d25/r36) was rapidly mixed with increasing concentrations of Mg^{2+} and AZTTP (2.5, 5, 10, 20, 30, 40, 60, 80 and 100 μM). (B) Chemical quench flow data (shown in Figure 5.8) monitoring the incorporation of AZTTP by HIV-RT WT over time. Preformed enzyme-DNA/RNA complex (175 nM HIV-RT WT, 75 nM d25/r36) was rapidly mixed with increasing concentrations of Mg^{2+} and dTTP (0.1, 0.25, 0.5, 1.5, 10 and 100 μM). (C) Fluorescence data from stopped-flow experiments measuring AZTTP dissociation from the closed enzyme-DNA/RNA ternary complex. A preformed enzyme-DNA/RNA-AZTTP complex (200 nM HIV-RT WT, 300 nM dd25/r36, 3.5 μM AZTTP) was rapidly mixed with 3.5 μM unlabeled enzyme-ddDNA/RNA complex to serve as a trap. An increase in fluorescence representing the release of AZTTP from the ternary complex was observed. Rate constants derived from the global fitting are described in Table 5.4.

Global fitting of HIV-RT TAMS TTP incorporation

Figure 5.12 shows the global fitting of TTP incorporation by the HIV-RT TAMS mutant during RNA-dependent DNA polymerization. These data are fit to the model shown in Scheme 5.4 and the summary of best-fit values are listed in Table 5.4. The first step of nucleotide binding to the HIV-RT TAMS mutant gives a value for $1/K_1$ of $577 \pm 87 \mu\text{M}$. This is followed by the fast conformational change of the enzyme from the open to closed conformation at a forward rate of $2050 \pm 315 \text{ s}^{-1}$ and a reverse rate of $12.9 \pm 0.04 \text{ s}^{-1}$. The chemistry step is $48.3 \pm 0.9 \text{ s}^{-1}$. The rates following chemistry are assumed to be fast (pyrophosphate release and translocation). The k_{cat}/K_m value of $2.7 \pm 0.8 \mu\text{M}^{-1}\text{s}^{-1}$ was calculated using Equation 5.4 for a 3-step reaction. This is a 1.4-fold decrease in k_{cat}/K_m compared to wild-type enzyme for the incorporation of TTP.

Scheme 5.4



Equation 5.4

$$k_{\text{cat}} / K_m = \frac{k_1 k_2 k_3}{k_2 k_3 + k_{-1} k_{-2} + k_{-1} k_3}$$

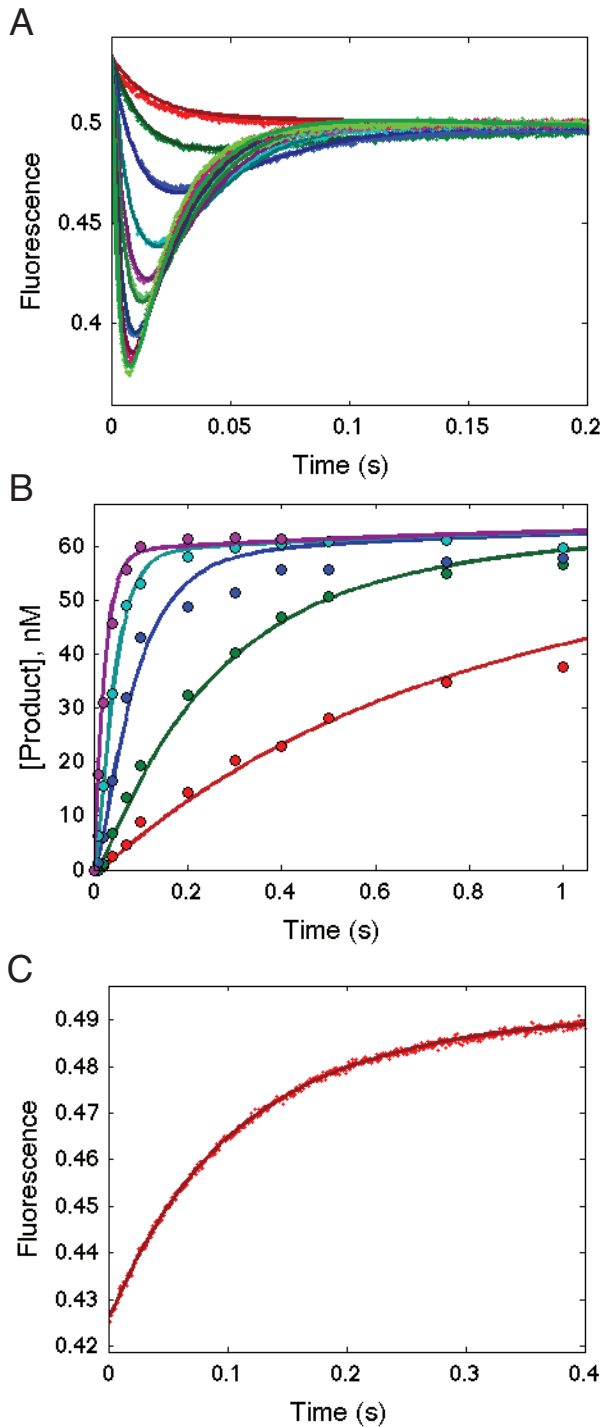
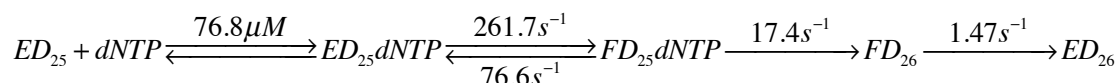


Figure 5.12. Global fitting of dTTP binding and incorporation by TAMS HIV-RT. (A) Fluorescence data from stopped-flow experiments monitoring MDCC fluorescence over time representing dTTP binding and incorporation. Preformed enzyme-DNA/RNA complex (200 nM HIV-RT TAMS, 300 nM d25/r36) was rapidly mixed with increasing concentrations of Mg^{2+} and dTTP (2.5, 5, 10, 20, 30, 40, 60, 80 and 100 μM). (B) Chemical quench flow data (shown in Figure 5.8) monitoring the incorporation of dTTP by HIV-RT TAMS over time. Preformed enzyme-DNA/RNA complex (175 nM HIV-RT TAMS, 75 nM d25/r36) was rapidly mixed with increasing concentrations of Mg^{2+} and dTTP (0.5, 1.5, 5, 15 and 150 μM). (C) Fluorescence data from stopped-flow experiments measuring dTTP dissociation from the closed enzyme-DNA/RNA ternary complex. A preformed enzyme-DNA/RNA-dTTP complex (50 nM HIV-RT TAMS, 75 nM dd25/r36, 1.75 μM dTTP) was rapidly mixed with 3.5 μM unlabeled enzyme-ddDNA/RNA complex to serve as a trap. An increase in fluorescence representing the release of dTTP from the ternary complex was observed. Rate constants derived from the global fitting are described in Table 5.4.

Global fitting of HIV-RT TAMS AZTTP incorporation

The global fitting of quench flow and stopped-flow data for the incorporation of AZTTP for the TAMS mutant of HIV-RT is shown in Figure 5.13 and the best fit values are summarized in Table 5.4. The data are fit to the model shown in Scheme 5.5 giving a $1/K_1 = 76.8 \pm 0.8 \mu\text{M}$, $k_2 = 261.7 \pm 2.2 \text{ s}^{-1}$, $k_{-2} = 76.6 \pm 0.6 \text{ s}^{-1}$, $k_3 = 17.4 \pm 0.08 \text{ s}^{-1}$ and $k_4 = 1.47 \pm 0.01 \text{ s}^{-1}$. Using Equation 5.3 for a 4-step reaction, these rate constants yield a k_{cat}/K_m value of $0.62 \pm 0.01 \mu\text{M}^{-1}\text{s}^{-1}$ which is 2-fold lower than the specificity constant for AZTTP incorporation by wild-type enzyme. For the TAMS mutant of HIV-RT, the discrimination for TTP over AZTTP is calculated as $(k_{\text{cat}}/K_m)_{\text{TTP}}/(k_{\text{cat}}/K_m)_{\text{AZTTP}}$ and is equal to 4.3. This discrimination constant compared to that of wild-type enzyme gives a 1.5-fold resistance to AZTTP by the TAMS mutant ($\text{Discrimination}_{\text{TAMS}}/\text{Discrimination}_{\text{wild-type}}$).

Scheme 5.5



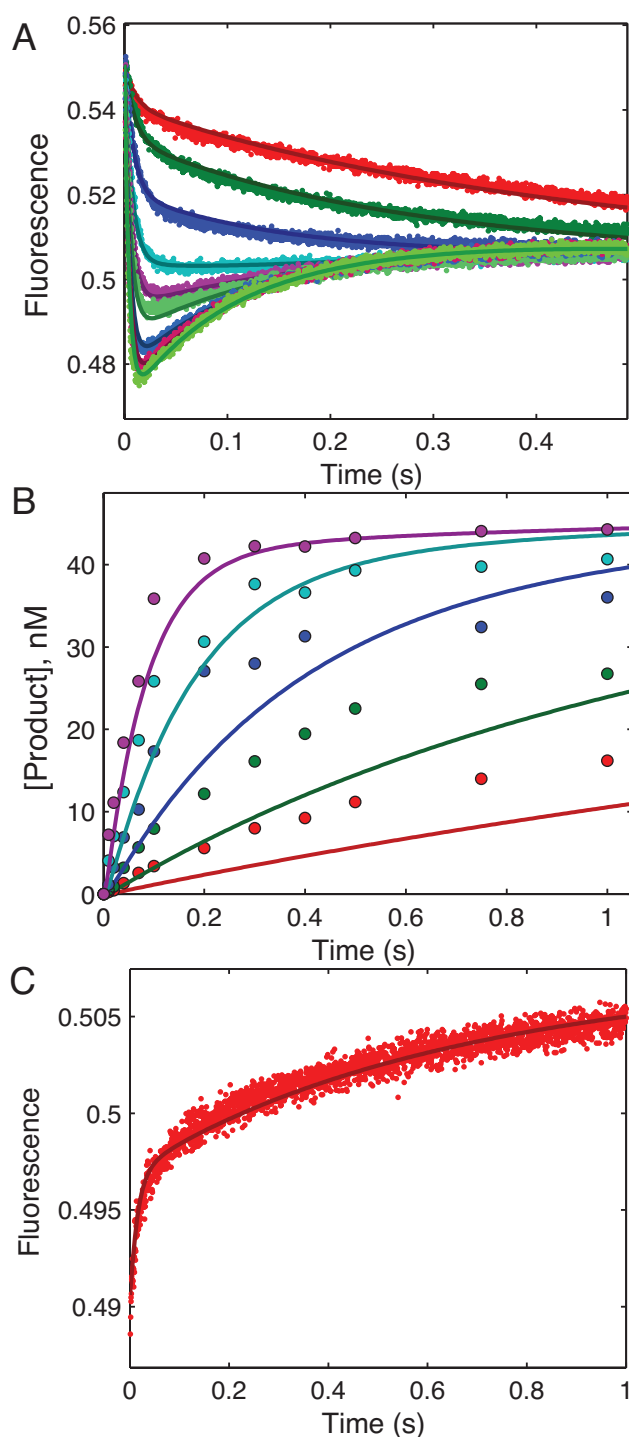


Figure 5.13. Global fitting of AZTTP binding and incorporation by TAMS HIV-RT.

(A) Fluorescence data from stopped-flow experiments monitoring MDCC fluorescence over time representing AZTTP binding and incorporation. Preformed enzyme-DNA/RNA complex (200 nM HIV-RT TAMS, 300 nM d25/r36) was rapidly mixed with increasing concentrations of Mg^{2+} and AZTTP (2.5, 5, 10, 20, 30, 40, 60, 80 and 100 μM). (B) Chemical quench flow data (shown in Figure 5.8) monitoring the incorporation of AZTTP by HIV-RT TAMS over time. Preformed enzyme-DNA/RNA complex (175 nM HIV-RT TAMS, 75 nM d25/r36) was rapidly mixed with increasing concentrations of Mg^{2+} and AZTTP (0.5, 1.5, 5, 15 and 150 μM). (C) Fluorescence data from stopped-flow experiments measuring AZTTP dissociation from the closed enzyme-DNA/RNA ternary complex. A preformed enzyme-DNA/RNA-AZTTP complex (300 nM HIV-RT TAMS, 200 nM dd25/r36, 5 μM AZTTP) was rapidly mixed with 5 μM unlabeled enzyme-ddDNA/RNA complex to serve as a trap. An increase in fluorescence representing the release of AZTTP from the ternary complex was observed. Rate constants derived from the global fitting are described in Table 5.4.

Table 5.4 Rate constants for TTP and AZTTP Incorporation by HIV-RT determined by global fitting

	$1/K_1$	k_2	k_{-2}	K_2	k_3	k_4
	μM	s^{-1}	s^{-1}		s^{-1}	s^{-1}
<u>WT</u>						
TTP	1430 ± 4.4 (1380 - 1490)	5670 ± 660 -	1.93 ± 0.006 (1.86 - 2)	2937 ± 342	78.3 ± 0.15 (76.3 - 80.2)	19.1 ± 0.06 (18.3 - 19.8)
AZTTP	169 ± 2.2 (135 - 212)	1620 ± 21 (1290-2020)	132 ± 1.9 (105 - 184)	12.2 ± 0.23	20.6 ± 0.08 (18.9 - 22.6)	0.21 ± 0.0007 (0.20 - 0.22)
<u>TAMs</u>						
TTP	577 ± 87 (96 - 5650)	2050 ± 315 (334 - 20700)	12.9 ± 0.04 (12.3 - 13.1)	158 ± 24.4	48.3 ± 0.9 (44.8 - 60.4)	-
AZTTP	76.8 ± 0.8 (60- 114)	261.7 ± 2.2 (232 - 333)	76.6 ± 0.6 (66.2 - 86.2)	3.4 ± 0.04	17.4 ± 0.08 (16.1 - 19.2)	1.47 ± 0.01 (1.18 - 1.73)

*Numbers in parenthesis give the lower and upper limits derived from the confidence contour analysis in fitting the data.

Table 5.5 Specificity, discrimination and resistance determined by global fitting

	k_{cat}	K_m	$K_{d,net}$	k_{cat}/K_m	Discrimination	Resistance
	s^{-1}	μM	μM	$\mu M^{-1} s^{-1}$		
<u>WT</u>						
TTP	77.2 ± 12.6	20.7 ± 2.4	0.48 ± 0.06	3.7 ± 0.74		
AZTTP	18.8 ± 0.34	14.7 ± 0.31	12.7 ± 0.3	1.3 ± 0.03	2.8	-
<u>TAMs</u>						
TTP	46.9 ± 10	17.2 ± 3.6	3.6 ± 0.9	2.7 ± 0.8		
AZTTP	12.8 ± 0.14	20.4 ± 0.3	17.4 ± 0.3	0.62 ± 0.01	4.3	1.5

*Numbers in parenthesis give the lower and upper limits derived from the confidence contour analysis in fitting the data.

5.4 DISCUSSION

The work here explores the RNA-dependent DNA polymerase reaction for wild-type HIV-RT as well as HIV-RT containing the TAMS mutations. In this work we studied the kinetics of incorporation of a correct TTP and the incorporation of AZTTP, which is a nucleoside reverse transcriptase inhibitor (NRTI). Previous work has been done in our lab to characterize the DNA-dependent DNA polymerase activity by these two enzyme forms on the two nucleotide substrates (159). The results here show differences in rates of incorporation and conformational changes compared to polymerization on a DNA/RNA primer-template. However, the overall analysis of discrimination against NRTIs by the TAMS mutant enzyme confirms the previous result that discrimination is only modestly affected by the mutations.

The initial analysis in this chapter using quench flow methods alone, revealed a modest 1.3 fold increase in discrimination of AZTTP over TTP by the TAMS mutant compared to wild-type HIV-RT. The quench flow data were fit to the simple one-step nucleotide binding model for nucleotide incorporation that assumes that nucleotide binding first occurs in a rapid equilibrium, is followed by a single-rate limiting polymerization step and the steps after nucleotide incorporation (pyrophosphate release, translocation) are fast.

Inclusion of stopped flow experiments in a global fit with the quench flow data allow for a characterization of the two-step nucleotide binding model by monitoring a change in fluorescence representing the conformational change of the enzyme upon nucleotide binding. The presence of the MDCC fluorophore that is covalently attached to the fingers subdomain of RT, results in a 27% decrease in fluorescence upon addition of nucleotide to monitor the isomerization from the “open” to “closed” state (146). A regain in fluorescence is then subsequently seen which is limited by the rate of chemistry. A

result observed in these studies and not in those monitoring DNA-dependent DNA polymerization, was a further isomerization to a lower fluorescent state of the enzyme after the chemistry step. This rate constant, k_4 , was seen for wild-type incorporation of TTP and AZTTP and for TAMS mutant incorporation of AZTTP. Stopped-flow studies revealed this isomerization to a different fluorescent state of the enzyme that was not seen with the TAMS mutant incorporation of TTP and could not be detected in the quench flow experiments because it occurs as an irreversible step after irreversible chemistry. It is possible that this observed isomerization could be a measure of pyrophosphate release or translocation but more studies must be done to explore these possibilities.

The global fit of stopped flow and quench flow data for TTP incorporation by wild-type enzyme was fit to the expanded 4-step model for nucleotide incorporation. This is described by an initial weak ground state binding of TTP to the open form of the enzyme ($1/K_1$) followed by a rapid isomerization to the closed state (k_2). This isomerization to the closed state is reversible and is followed by the chemistry step (k_3) followed by a subsequent isomerization step (k_4). Both the rate of chemistry and the isomerization after chemistry were irreversible, as the experimental setup did not provide information about the reverse of these steps. It is the relative rates of chemistry (k_3) and the reverse of the conformational change (k_2) that determine the specificity constant for nucleotide binding. For TTP incorporation by wild-type enzyme, the rate of the conformational change was determined to be 5670 s^{-1} which is 2-fold faster than the rate reported for the wild-type HIV-RT TTP incorporation on DNA/DNA primer template. An explanation for this faster conformational change with a DNA/RNA primer template could be the increase in interactions between the RNA template and the protein as was reported in crystal structures of HIV-RT with DNA/RNA primer template (164, 165).

With TTP incorporation the binding does not come to equilibrium due to the fast rate of chemistry relative to the reverse rate of the conformational change, $k_3 \gg k_{-2}$, therefore the $K_{d,app}$ estimates the ratio of the rates of product turnover to the formation of the closed complex and can be estimated as $k_3/(K_1k_2)$. This value $k_3/(K_1k_2)$ from the global fit parameters is determined to be $19.7 \mu\text{M}$ which is close to the value for $K_{d,app}$ determined by conventional fitting of the quench flow experiment of $13 \pm 3.6 \mu\text{M}$. This $K_{d,app}$ from the quench flow experiment however, does not equal the $K_{d,net}$ which is defined as $1/(K_1(1+K_2))$ (Equation 5.5) and in this case equals $0.48 \pm 0.06 \mu\text{M}$. The specificity constant k_{cat}/K_m is calculated to be $3.7 \mu\text{M}^{-1}\text{s}^{-1}$ is a product of the equilibrium constant governing nucleotide ground state binding and the forward rate of the conformational change and the equation for k_{cat}/K_m can be simplified to K_1k_2 which equals $3.9 \mu\text{M}^{-1}\text{s}^{-1}$. This simplification of the equation for k_{cat}/K_m can be used because of the fast rate of chemistry relative to the slow reverse of the conformational change ($k_3 \gg k_{-2}$). Overall the wild-type enzyme with TTP incorporation has a weak nucleotide binding that is then committed to chemistry by the presence of the fast conformational change step at 5670 s^{-1} followed by a rate of chemistry at 78.3 s^{-1} and the reverse rate of the conformational change at only 1.93 s^{-1} is not significant. This induced-fit model for nucleotide incorporation by RT is similar to that which was seen for the analysis of DNA-dependent DNA-polymerase activity (159).

Simplifying assumptions for calculation of specificity constant:

$$\text{If } k_3 \gg k_{-2}, \text{ then } k_{cat} / K_m = K_1k_2$$

$$\text{If } k_{-2} \gg k_3, \text{ then } k_{cat} / K_m = K_1K_2k_3$$

The case of AZTTP incorporation by wild-type enzyme differs from that of TTP incorporation by the fact that the reverse rate of the conformational change at 132 s^{-1} is significant relative to the rate of chemistry at 20.6 s^{-1} . This increase in the reverse rate and decrease of the rate of chemistry relative to wild-type enzyme allows the nucleotide binding to come to equilibrium before the chemistry step. In this case where $k_{-2} \gg k_3$, the measurement of the $K_{d,app}$ by the quench flow studies does equal to the $K_{d,net}$ and the K_m for the nucleotide binding ($13.9 \text{ }\mu\text{M} \approx 12.7 \text{ }\mu\text{M} \approx 14.7 \text{ }\mu\text{M}$, respectively) (Equations 5.5 and 5.6).

Equation 5.5

$$K_{d,net} = \frac{1}{K_1(1 + K_2)}$$

Equation 5.6

$$K_m = \frac{k_2k_3 + k_{-1}(k_{-2} + k_3)}{k_1(k_2 + k_{-2} + k_3)}$$

In this scenario the derivation of the specificity constant can be simplified to the product of the equilibrium constants and the rate of chemistry ($K_1K_2k_3$). This simplified equation gives a value of $1.5 \text{ }\mu\text{M}^{-1}\text{s}^{-1}$ while the expanded equation for specificity constant gives the value of $1.3 \text{ }\mu\text{M}^{-1}\text{s}^{-1}$. The incorporation of this NRTI therefore binds 8.5-fold more tightly in the initial ground state binding compared to the wild-type, however the slower conformational change step that comes to equilibrium before chemistry leads to a 26-fold weaker $K_{d,net}$ and a 1.3-fold lower specificity constant for nucleotide incorporation. This tighter ground-state binding for AZTTP is not too surprising as it was seen in the DNA-dependent DNA polymerization analysis and is likely due to the additional contacts formed between AZTTP and the nucleotide binding site (100).

Characterization of the TAMS mutant of HIV-RT with TTP incorporation revealed that the fast chemistry relative to the reverse of the conformational change step

was maintained as was seen in wild-type enzyme. However the equilibrium constant for the conformational change step was reduced from $K_2 = 2937$ for wild-type to $K_2 = 158$ for the TAMS mutant. In the mutant, the 48.3 s^{-1} rate for chemistry is faster than the reverse of the conformational change at 12.9 s^{-1} so the same simplifying assumptions that were applied for wild-type TTP incorporation can be applied here. Specifically, because $k_3 > k_{-2}$, the $K_{d,app}$ value of $14.7 \text{ }\mu\text{M}$ from the quench flow studies describes the ratio of the rates of product turnover to the rates of formation of the closed complex and is approximately equal to $k_3/(K_1k_2)$, which is calculated as $13.6 \text{ }\mu\text{M}$. The calculation of the K_m by Equation 5.6 is equal to $17.2 \text{ }\mu\text{M}$ and therefore the $K_{d,app}$ is more similar to the K_m than the net K_d . The equation for the $K_{d,net}$ (Equation 5.5) determines a value of $3.6 \text{ }\mu\text{M}$ for TTP binding to the TAMS mutant which is 7.5-fold weaker than the binding to wild-type enzyme. Therefore the binding affinity for correct nucleotide is sacrificed with the mutation to the TAMS mutant. Also the specificity constant, which is calculated to be $2.7 \text{ }\mu\text{M}^{-1}\text{s}^{-1}$ by the expanded Equation 5.4, is 1.4-fold lower than that for wild-type. As with wild-type, because the $k_3 > k_{-2}$ for the TAMS mutant, the calculation of k_{cat}/K_m can be approximated by the product of the equilibrium constant governing ground-state nucleotide binding and the forward rate of the conformational change, K_1k_2 which is equal to $3.6 \text{ }\mu\text{M}^{-1}\text{s}^{-1}$.

Although the TAMS mutant sacrifices a 1.4-fold reduction in the specificity constant for TTP incorporation compared to wild-type, the specificity constant for AZTTP is reduced 2-fold to give an increase in discrimination for AZTTP over TTP, and therefore a net resistance of 1.5-fold for this mutant. The TAMS mutations reduce the rate of the conformational change of the enzyme 6-fold compared to wild-type AZTTP incorporation which drastically affects the equilibrium of the conformational change step. Also the slight reduction in the rate of chemistry relative to wild-type contributes to the

decrease in k_{cat}/K_m for AZTTP incorporation by the TAMS mutant. This mutant showed the same pattern of relative values for rate constants with AZTTP incorporation that was seen with wild-type however the effect is even more extreme. Specifically, the conformational change step ($k_2 = 261.7 \text{ s}^{-1}$) comes to equilibrium with a reverse rate of 76.6 s^{-1} and is subsequently followed by the rate of chemistry at 17.4 s^{-1} . In this case where $k_2 \gg k_3$, the apparent K_d determined by quench flow studies ($14.5 \text{ }\mu\text{M}$) is approximates to the K_m calculated from the full Equation 5.6 ($20.4 \text{ }\mu\text{M}$) and also the $K_{d,\text{net}}$ which was calculated to be $17.4 \text{ }\mu\text{M}$ (Equation 5.5).

Overall this characterization of RNA-dependent DNA-polymerase activity by wild-type HIV-RT and the TAMS mutant of HIV-RT shows that the TAMS mutations lead to a slower rate of chemistry and an increased $K_{d,\text{net}}$ compared to wild-type which results in a modest 1.5-fold increase in discrimination of AZTTP over TTP. This result is similar to the effects seen in the characterization of DNA-dependent DNA-polymerization (159). The stopped flow studies monitoring the polymerization reaction on an RNA template however did reveal an additional isomerization step following chemistry that was not seen on a DNA template.

Chapter 6: HIV Reverse Transcriptase Labeling Site Mutations

6.1 INTRODUCTION

Previous studies and the work outlined in Chapter 5 have shown the importance of the conformational change in HIV-RT upon nucleotide binding in determination of specificity and discrimination of nucleotides (166). This nucleotide-induced conformational change has been monitored using an environmentally sensitive fluorophore (MDCC) on the fingers subdomain of HIV-RT and has revealed that the fast isomerization from open to closed complex commits the enzyme to carrying forward the substrate to incorporation into the growing DNA primer. With wild-type enzyme on a DNA/DNA primer-template (159) and a DNA/RNA primer-template (Chapter 5), the initial weak nucleotide binding to the open conformation is in a rapid equilibrium and the subsequent isomerization to the closed conformation on a millisecond timescale leads to a large change in structure and is responsible for determining the specificity constant for the correct nucleotide. Stopped-flow experiments monitoring this reaction by the MDCC labeled protein have proved to be very valuable in establishing the rate of the induced-fit mechanism for HIV-RT and T7 DNA polymerase (146, 159, 161).

A recent paper from Kirmizialtin, et al. has performed molecular dynamics simulations to illustrate global changes in structure of HIV-RT from the open to closed states (167). Figure 6.1 shows the p66 subunit of HIV-RT in the open (gray) and closed (blue) states. This structure shows the incoming dNTP (magenta) bound at the active site near the two catalytic magnesium ions in yellow. The primer and template DNA are shown in green and cyan.

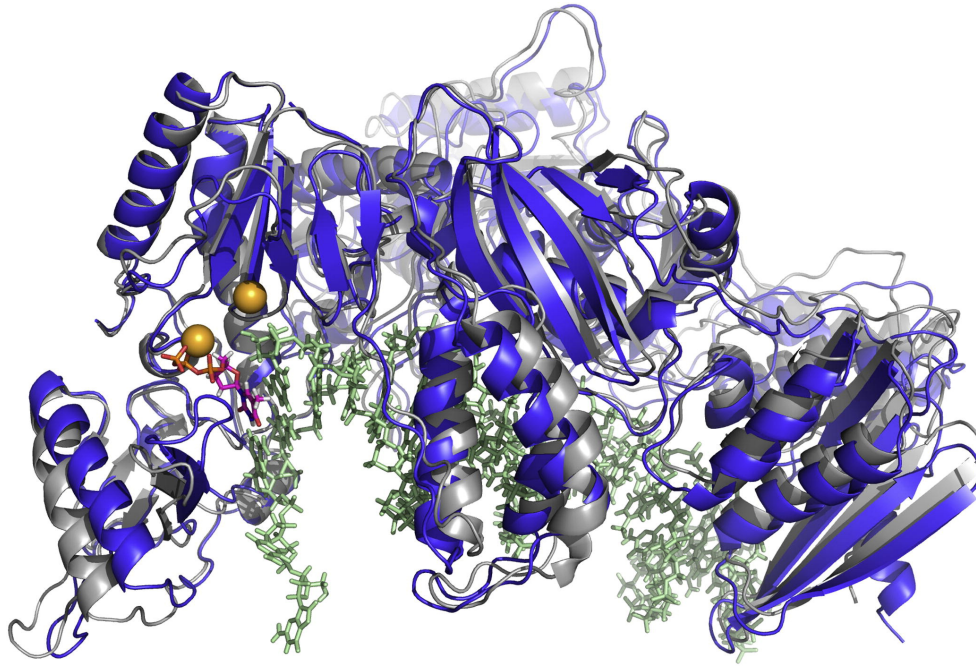


Figure 6.1. *Open and closed conformations of HIV-RT p66.* This figure from Kirmizialtin et al (167), shows an overlay of open (gray) and closed (blue) conformations of the HIV-RT p66 subunit. The crystal structure of HIV-RT and primer template was used to model the open complex (PDB: 1J5O (92)) while a crystal structure of the ternary complex with enzyme, primer template DNA and nucleotide was used to model the closed complex (PDB: 1RTD (86)) The incoming nucleotide is shown in magenta, the DNA primer and template strands are shown in green, and the two catalytic magnesium ions are displayed as yellow spheres.

Using these two endpoint structures of the open and closed complexes, computer simulation was used to model the changes in structure of the enzyme over time between these two endpoints. The global changes that were observed in the p66 catalytic subunit are outlined in Figure 6.2, which shows the difference in the protein states as a function of amino acid residue and time relative to the initial open structure. The largest change was seen in the fingers subdomain but significant movement was detected throughout the enzyme. The fingers subdomain contains positively charged residues that make contact with the negatively charged triphosphate of the incoming nucleotide to align the nucleotide substrate at the active site for catalysis and the large conformational change of

this domain was expected. The thumb and palm subdomains showed the next largest changes in conformation while the connection and RNase H domains appeared to be more rigid. The most mobile regions of the protein were often found in flexible loop domains and less movement was seen in beta sheets and alpha helices.

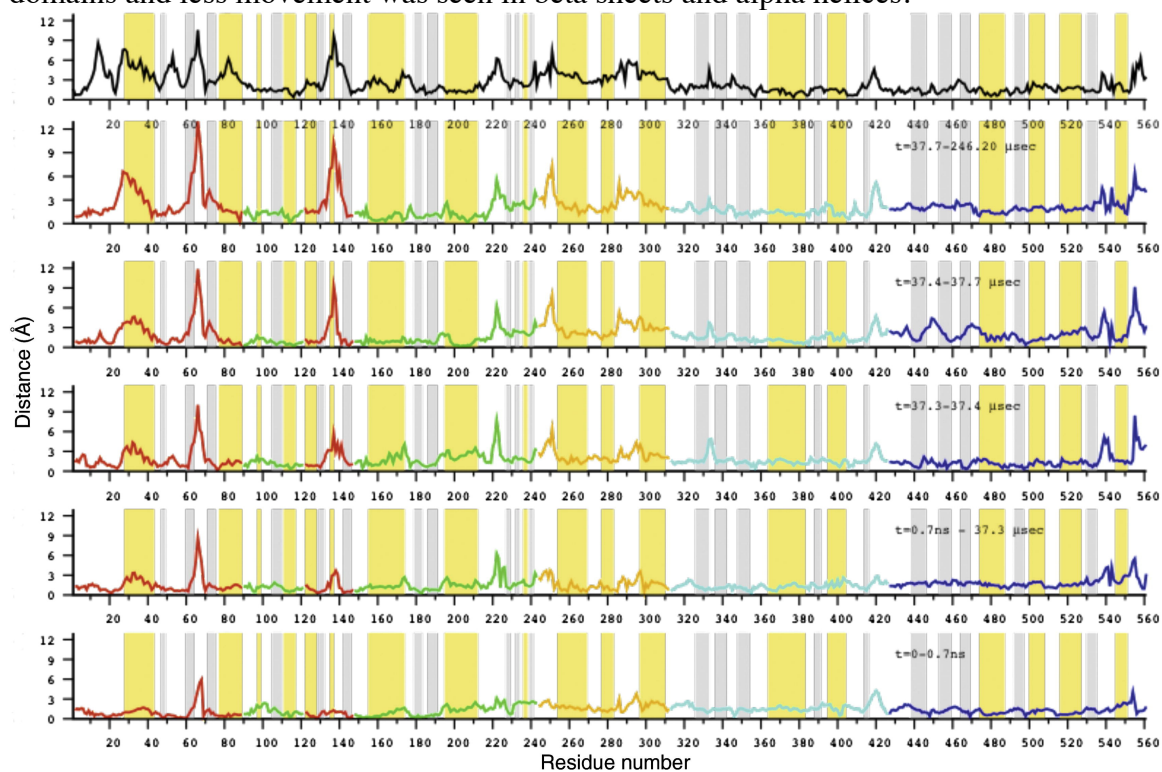


Figure 6.2. *Global changes of HIV-RT structure with time.* This figure, also from Kirmizialtin et al (167), shows the residue number of HIV-RT p66 subunit on the x-axis versus the average root mean square deviation of alpha carbons with respect to the open conformation of the enzyme on the y-axis. The top plot with the black line represents the difference between the open and closed conformations of the enzyme as a function of residue number. The lower five plots represent the difference in structure at a given time (t) versus the open conformation. The lines are color coded to represent the subdomains of the protein: red-fingers, orange-thumb, green-palm, cyan-connection and blue-RNaseH. The gray and yellow shaded regions of each plot represent regions of beta-sheet and alpha helices, respectively.

The work presented in this chapter aims to explore regions of HIV-RT distant from the active site, which were predicted to be highly mobile by the molecular dynamic simulations with conformational changes possibly linked to nucleotide binding (167). Mobility of these residues and regions of the protein were explored using the fluorescent probe previously used to monitor the conformational change of the fingers subdomain (146). Residues chosen for mutation to cysteine and subsequent labeling with an MDCC fluorophore (summarized in Table 6.1) were selected based on the following criteria: 1. The residue is on a mobile region of the protein as predicted by the molecular dynamics simulation 2. The residue is distant from the active site 3. The residue is not highly conserved. Three residues on the thumb subdomain and one residue on the connection subdomain of p66 were studied. Additionally on p66, two residues in the RNaseH domain were analyzed. Finally, two residues on the p51 subunit were studied which were predicted to have changes in conformation during nucleotide incorporation.

Table 6.1 *Residues selected for cysteine mutagenesis and MDCC labeling*

Subunit	Residue	Location
p66	Q242C	Thumb subdomain
p66	E300C	Thumb subdomain
p66	K311C	Thumb subdomain
p66	Q334C	Connection subdomain
p66	L517C	RnaseH domain
p66	E523C	RnaseH domain
p51	Q91C	p51 opposite side from p66 interface
p51	R358C	p51 near connection subdomain of p66

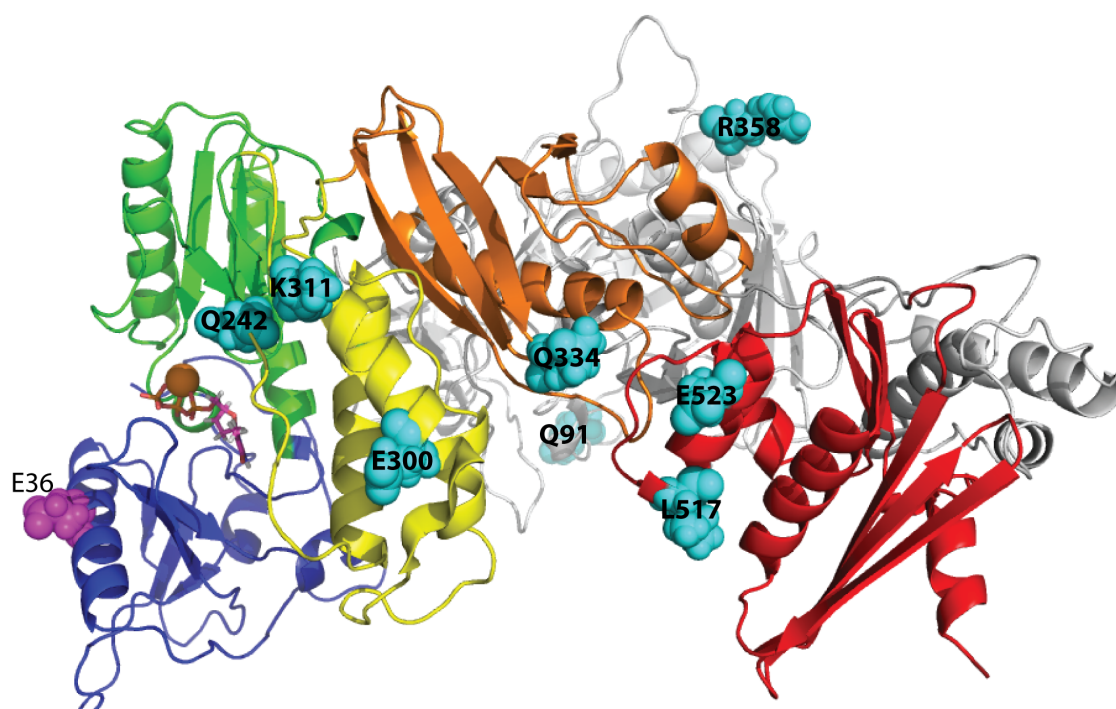


Figure 6.3. *Potential MDCC-labeling sites on HIV-RT.* The MDCC-fluorophore labeling sites studied in this chapter are shown as cyan spheres on the structure of HIV-RT (PDB: 1RTD). The previously used position for MDCC-labeling (E36), is shown in magenta on the fingers subdomain (blue). The potential labeling sites are found on the thumb subdomain (yellow), the connection domain (orange) and the RNaseH domain (red) of p66. The non-catalytic p51 accessory subunit is shown in gray and contains two potential labeling sites Q91 and R358. No labeling sites were studied on the palm subdomain (green).

6.2 MATERIALS AND METHODS

Site directed mutagenesis of HIV-RT

The catalytic subunit p66 and the accessory subunit p51 of HIV-1 RT strain HxB2 were cloned and expressed individually in the same vectors as described in Chapter 5. However, in this section of work the p66 subunit, which was in the pET21a expression vector, did not contain the E36C mutation for the labeling position on the fingers subdomain used previously. To test the six proposed MDCC-labeling sites on p66, the full length wild-type p66 sequence with the C280S mutation was used for site directed

mutagenesis using the primers listed in Table 6.2. For each 50 μ L mutagenesis reaction, 50 ng of parental dsDNA was mixed with 100 ng of forward and reverse primers, 1X cloned *Pfu* reaction buffer, 1 μ l of 10 mM dNTPs (Promega), and 2.5 units of *Pfu Turbo* DNA polymerase (Stratagene). The PCR amplification reaction was then performed with the following optimized thermal cycling conditions: 95°C for 5 minutes, followed by 18 cycles of 95°C for 30 seconds, 55°C for 1 minute, and 72°C for 8 minutes. A final extension step of 72°C for 15 minutes before final storage at 4°C. The PCR reaction was then transformed into Novablue (Novagen) *E. coli* and a miniprep procedure (Qiagen) was performed to isolate the plasmid DNA. In cases where a labeling site was explored on the p51 accessory subunit the same procedure was performed on the pET30a plasmid containing sequence for the p51 subunit with the 13 amino acid C-terminal deletion and the C280S mutation, as was used in Chapter 5. See Table 6.2 for mutagenic primer sequences used for mutagenesis and Table 5.1 for the T7 promoter sequencing primers used to confirm the mutagenesis.

Table 6.2 *Mutagenic primers for HIV-RT labeling site mutants*

p66-Q242C

Forward: 5' -CCTGATAAATGGACAGTATGCCCTTATAGTGCTGCCAGAAAAAG-3'

Reverse: 5' -CTTTTTCTGGCAGCACTATAGGGCATACTGTCCATTTATCAGG-3'

p66-Q334C

Forward: 5' -ATACAGAAGCAGGGGTGCGCCAATGGACATAT-3'

Reverse: 5' -ATATGTCCATTGGCCGCACCCCTGCTTCTGTAT-3'

p66-K311C

Forward: 5' -AACAGAGAGATTCTATGCGAACCAGTACATGGA-3'

Reverse: 5' -TCCATGTACTGGTTCGCATAGAATCTCTCTGTT-3'

p66-L517C

Forward: 5' -GATCAAAGTGAATCAGAGTGCGTCAATCAAATAATAGAGC-3'

Reverse: 5' -GCTCTATTATTTGATTGACCGCACTCTGATTCACTTTGATC-3'

p66-E300C

Forward: 5' -CTAACAGAAGAAGCATGCCTAGAACTGGCAGAA-3'

Reverse: 5' -TTCTGCCAGTTCTAGGCATGTCTTCTTCTGTAG-3'

p66-E523C

Forward: 5' -GAGTTAGTCAATCAAATAATATGCCCAGTTAATAAAAAAGGAAAAGG-3'

Reverse: 5' -CCTTTTCCTTTTTTATTAACTGGCATATTATTTGATTGACTAACTC-3'

p51-R358C

Forward: 5' -AAATATGCAAGAATGTGCGGTGCCACACTAAT-3'

Reverse: 5' -ATTAGTGTGGGCACCGCACATTCTTGCATATTT-3'

p51-Q91C

Forward: 5' -GACTTCTGGGAAGTTTGCTTAGGAATACCACAT-3'

Reverse: 5' -ATGTGGTATTCCTAAGCAAACTTCCCAGAAAGTC-3'

mutated codons are underlined

Expression, purification and MDCC-labeling of HIV-RT

The catalytic subunit p66 and the accessory subunit p51 of HIV-1 RT strain HxB2 were expressed individually in the same vectors as described in Chapter 5. The purification and MDCC labeling was also performed as described in detail in Chapter 5 using Q-sepharose, Bio-rex 70 and ssDNA-cellulose columns for purification.

Preparation of substrate DNA

DNA substrates were purchased from Integrated DNA Technologies (IDT) and purified by 15% denaturing polyacrylamide gel electrophoresis. Sequences of 25-mer DNA primer, dideoxy-terminated 26-mer primer and 45-mer template oligomers are listed in Table 6.3.

Duplex substrates were formed by incubating the 25mer primer with the 45mer template at a 1:1 molar ratio in an *Annealing Buffer* (10 mM Tris-HCl pH 7.5, 50 mM NaCl, 1 mM EDTA) and heating to 95°C for 5 minutes before allowing to slowly cool to room temperature.

Table 6.3 *Primer template sequences for HIV-RT labeling mutants*

25/45mer

25-mer	5' -GCCTCGCAGCCGTCCAACCAACTCA
45-mer	3' -CGGAGCGTCGGCAGGTTGGTTGAGTTGGAGCTAGGTTACGGCAGG

dd26/45mer

dd26-mer	5' -GCCTCGCAGCCGTCCAACCAACTCAT _{dd}
45-mer	3' -CGGAGCGTCGGCAGGTTGGTTGAGTAGCAGCTAGGTTACGGCAGG

Fluorimeter assay measuring substrate binding

To measure the changes in fluorescence of the MDCC-labeled mutants of HIV-RT upon substrate binding, fluorescence emission was measured in a steady-state fluorimeter (Photon Technologies Inc). The fluorophore was excited at 425 nm and emission was monitored from 450 – 550 nm. First, the cuvette containing *RT-Buffer* (50

mM Tris-HCl (pH 7.5), 100 mM potassium acetate, 0.1 mM EDTA) supplemented with 10 mM magnesium acetate was scanned as a base-line sample. MDCC-labeled HIV-RT was then added to the cuvette at a final concentration of 400 nM and the sample was scanned again. The dideoxy-terminated primer-template DNA substrate (Table 6.3) was then added to the sample and it was scanned again. A final scan was done after the addition of the correct nucleotide (dCTP) at a final concentration of 100 μ M.

Stopped flow assay measuring nucleotide incorporation

Stopped flow experiments measuring incorporation nucleotide by the MDCC-labeled HIV-RT were performed at 37 °C in a 1X-*RT-Buffer* containing 50 mM Tris-HCl (pH 7.5), 100 mM potassium acetate, 0.1 mM EDTA with a an AutoSF-120 series stopped-flow instrument from KinTek Corp. For these assays, 100 nM MDCC-labeled HIV-RT wild-type or mutant was preincubated with 150 nM 25/45mer DNA for 15 minutes at 37°C. The reaction was then started by mixing with a solution containing various concentrations of dATP in *RT buffer* supplemented with 10 mM magnesium acetate. The MDCC fluorophore on HIV-RT was excited at 425 nm and the fluorescence emission was measured as a function of time using a 475 nm single-band bandpass filter (Semrock).

6.3 RESULTS

Each of the labeling-site mutants of HIV-RT were expressed and purified in the same protocol that was described in Chapter 5, as described previously (146). In most cases the labeling efficiency was similar to that of the E36C labeling site that has been established as a good labeling site. Once the purified proteins were labeled with MDCC, the labeling site mutants were tested in steady state fluorimetric assays and stopped flow assays measuring nucleotide incorporation. None of the labeling-site mutants studied in

this chapter gave an appreciable signal for nucleotide incorporation that could be carried forward to future experiments.

In one of the better cases, the E300C labeling site showed a 10% decrease in fluorescence upon formation of the enzyme-DNA binary complex and a further 4% decrease in fluorescence upon formation of the ternary complex with enzyme-DNA-nucleotide (Figure 6.4). When incorporation of dATP was tested in the stopped flow experiment for this mutant, a small (%) change in signal was seen in a biphasic curve over a 2 second timescale (Figure 6.5).

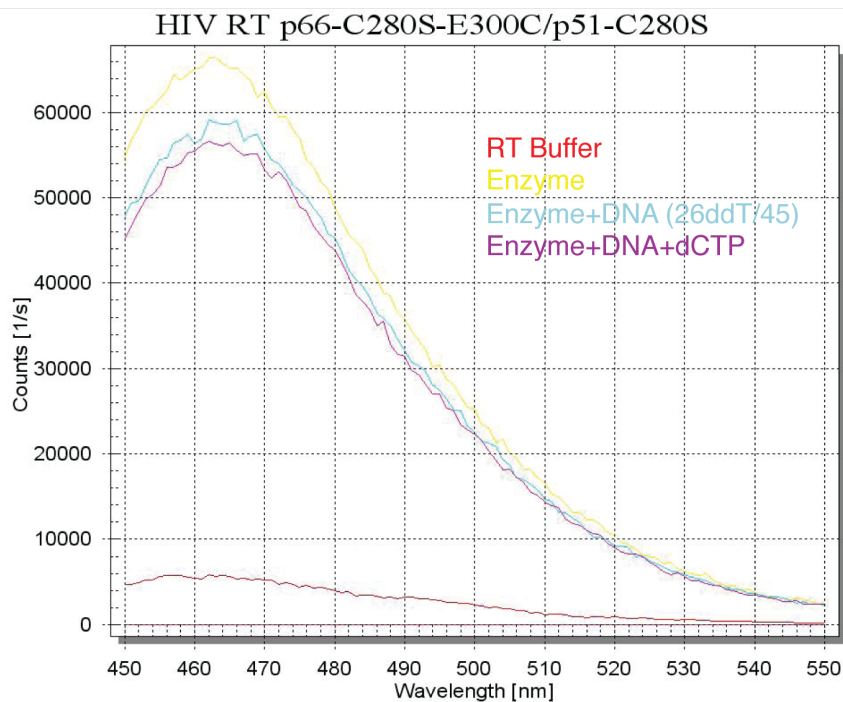


Figure 6.4. Emission spectra of HIV-RT p66-C280S-E300C-MDCC. Binding of DNA substrate to the MDCC-labeled enzyme at residue 300 produces a decrease in fluorescence emission (yellow to cyan) and the addition of the correct nucleotide dCTP produces a further decrease in fluorescence (cyan to magenta). The decrease upon binding nucleotide is only a 4% change in fluorescence emission. RT Buffer alone is shown as the red curve as a control.

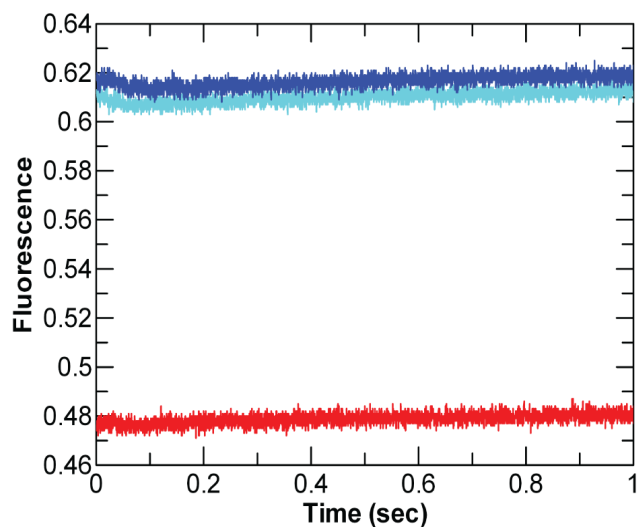


Figure 6.5. *Fluorescence Stopped-flow signal of HIV-RT p66-C280S-E300C-MDCC.* A preformed Enzyme-DNA complex with 200 nM HIV-RT p66-C280S-E300C and 300 nM 25/45mer DNA was rapidly mixed with increasing concentrations of dATP (2.5 (red), 30 (cyan) and 100 μ M (blue)). The MDCC-labeled protein was excited at 425 nm and emission was detected using a 475 nm single-band bandpass filter (Semrock).

Another of the better results was the Q334C small change in signal was seen in the stopped flow experiment due to the incorporation of dATP but due to the small amplitude of the signal, it was hard to interpret (Figure 6.6). It was noticed that for most of these mutants there was an increase in the starting point of the signal when dATP was mixed with enzyme-DNA compared to the no-dATP control. This led to the hypothesis that perhaps there was a rapid increase in fluorescence that was missed in the dead-time of the instrument (0.002 s). To explore this, the stopped flow experiment was repeated at 4°C and the results are shown in Figure 6.7. The results show that the signal amplitude was only 0.7% change in signal and therefore the labeling at this site would not be suitable for studies to measure a conformational change in the enzyme.

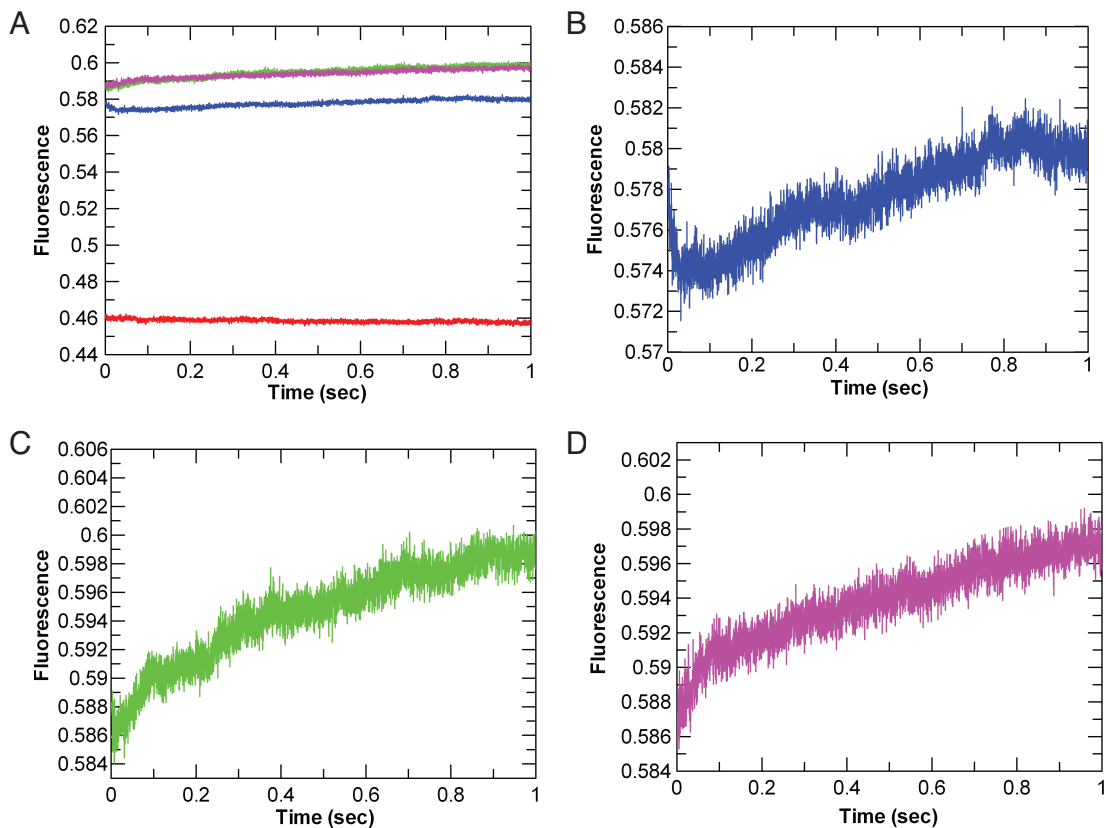


Figure 6.6. *Fluorescence Stopped-flow signal of HIV-RT p66-C280S-Q334C-MDCC.* (A) A preformed Enzyme-DNA complex with 200 nM HIV-RT p66-C280S-Q334C and 300 nM 25/45mer DNA was rapidly mixed with increasing concentrations of dATP (0 (red), 2.5 (blue), 30 (green) and 100 μM (magenta)). The MDCC-labeled protein was excited at 425 nm and emission was detected using a 475 nm single-band bandpass filter (Semrock). (B) The 2.5 μM dATP trace from A shown alone, was fit to a double exponential equation resulting in $k_1=49 \text{ s}^{-1}$ and $k_2=1.5 \text{ s}^{-1}$. (C) The 30 μM dATP trace from A shown alone, was fit to a double exponential equation resulting in $k_1=17.7 \text{ s}^{-1}$ and $k_2=1.2 \text{ s}^{-1}$. (D) The 100 μM dATP trace from A shown alone, was fit to a double exponential equation resulting in $k_1=51.5 \text{ s}^{-1}$ and $k_2=1.3 \text{ s}^{-1}$.

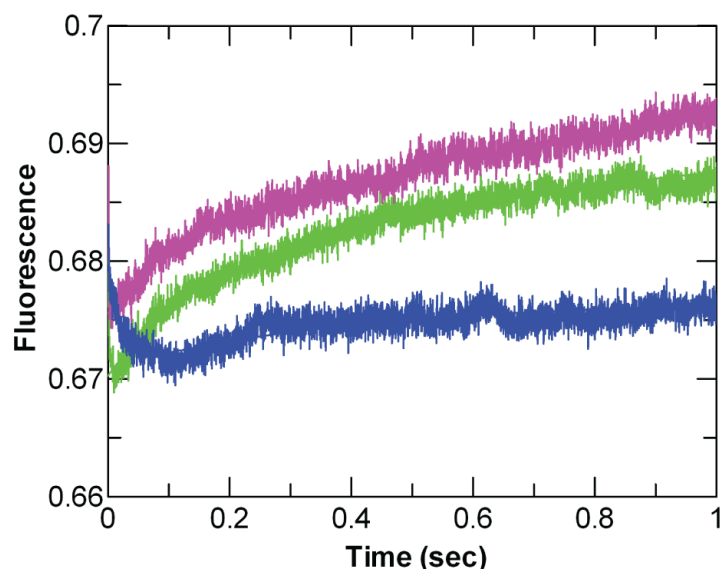


Figure 6.7. *Fluorescence Stopped-flow signal of HIV-RT p66-C280S-Q334C-MDCC at 4°C.* (A) A preformed Enzyme-DNA complex with 200 nM HIV-RT p66-C280S-Q334C and 300 nM 25/45mer DNA was rapidly mixed with increasing concentrations of dATP (2.5 (blue), 30 (green) and 100 μM (magenta)) at 4°C. The MDCC-labeled protein was excited at 425 nm and emission was detected using a 475 nm single-band bandpass filter (Semrock).

6.4 DISCUSSION

Somewhat surprisingly none of the eight sites for labeling with a fluorescent probe that were studied here provided a sufficient signal for measuring conformational changes in HIV-RT. An effective labeling position for monitoring conformational changes of the fingers subdomain of HIV-RT has been identified in previous work in our lab based on studies labeling the fingers of T7 DNA polymerase (146, 161). This labeling of residue 36 by mutation from a glutamic acid to a cysteine and reaction with the coumarin derivative MDCC fluorophore that can react with the thiol group of the cysteine to be covalently bound to the fingers subdomain. Stopped flow experiments

monitoring the change in fluorescence of the conformationally sensitive fluorophore lead to a 34% increase in fluorescence upon binding of DNA and upon binding of correct nucleotide a 30% decrease in fluorescence was observed. This large change in fluorescence represents the movement of the fingers subdomain during substrate binding that is estimated to be a 15Å conformational change upon nucleotide binding (168).

The goal of the work in this chapter was to utilize the methods previously employed to fluorescently label the fingers subdomain of RT to explore results from molecular dynamics simulation suggesting that residues distant from the active site were highly mobile during catalysis (167). The results presented above show that none of the residues when labeled with an MDCC fluorophore produced a signal that could be measured in the stopped flow. Each of the labeling sites tested was unable to produce a signal that was sufficient to accurately be measured in the stopped flow. As a standard, it is necessary that the signal change in stopped flow be significantly large enough to overcome the signal-to-noise ratio that is inherent in the stopped flow instrument. Realistically, a signal change of less than 2% is difficult to differentiate from the noise of the instrument and is not a good candidate for further studies with the stopped flow instrument. Beyond a reliable and measureable fluorescence signal for a particular labeling site on the enzyme, it is essential that this fluorescent label does not interfere with the enzymatic activity being measured. To control for this, a good candidate for a fluorescently labeled enzyme must be tested against the unlabeled enzyme for deficiencies in enzymatic activity. Once a site which produces a significant signal and does not interfere with the enzymatic activity is found, this can be used in further stopped-flow assays to delve into the rates of conformational changes of the enzyme. Unfortunately, the sites explored in this chapter did not produce a fluorescently labeled

protein that gave a large enough change in fluorescence signal upon nucleotide binding and incorporation to be used in our pre-steady state stopped-flow experiments.

The sites of labeling that were explored were hypothesized to be mobile based on molecular dynamics simulations. It is possible that the motions of the enzyme at these sites were too rapid to be measured on the time scale of our instrument. It is also possible that there is no significant movement of the labeled residues to be detected at all.

Appendix

Summary of clinical cases of *POLG* related diseases

Mutation	Disease	Genotype	Reference	Age of onset (years)	Average age of onset - All cases (years)	Average age of onset - Heterozygotes
H932Y	arPEO	compound heterozygous with G105IR	Mancuso 2004	n/a	33	33
	myopathy of upper limbs, mtDNA depletion	compound heterozygous with R386C	Giordano 2010	27		
	PEO	compound heterozygous with P587L and T251I	Tang 2011	31		
	peripheral neuropathy	compound heterozygous with P587L and T251I	Tang 2011	40		
R943H	adPEO	homozygous	Lamantea 2002	30	41	63
	adPEO	homozygous	Lamantea 2002	30		
	adPEO and premature ovarian failure	n/a	Blok 2009	n/a		
	adPEO	heterozygous	Brandon 2013	63		
R953C	adPEO	n/a	Luoma 2004	22	31	41
	PEO	compound heterozygous with W748S	Tang 2011	51		
	MNGIE-like	compound heterozygous with W748S	Tang 2011	50		
	arPEO	homozygous	Gurgel-Giannetti 2012	20		
A957S	arPEO	homozygous	Gurgel-Giannetti 2012	20	n/a	n/a
	arPEO	homozygous	Gurgel-Giannetti 2012	20		
	arPEO	homozygous	Gurgel-Giannetti 2012	20		
	mild adPEO	heterozygous	Lamantea 2002	n/a		
R1096C	mild adPEO	heterozygous	Lamantea 2002	n/a	18	25
	mild adPEO	heterozygous	Lamantea 2002	n/a		
	mild adPEO	heterozygous	Lamantea 2002	n/a		
	mild adPEO	heterozygous	Lamantea 2002	n/a		
	mild adPEO	heterozygous	Lamantea 2002	n/a		
	severe adPEO	heterozygous	Lamantea 2002	n/a		
	severe adPEO	homozygous	Lamantea 2002	n/a		
	sporadic or ar PEO	n/a	Agostino 2003	n/a		
	PEO	compound heterozygous with Q1236H	Horvath 2006	2		
	PEO	compound heterozygous with P648R	Horvath 2006	53		
	Alpers syndrome	compound heterozygous with Q1236H	Wong 2008	1		
	Alpers syndrome	compound heterozygous with T914P	Ashley 2008	1		
	PEO	compound heterozygous with R627Q	Schulte 2009	43		
	Encephalopathy	compound heterozygous with G848S	Tang 2011	2		
PEO	compound heterozygous with P648R	Kurt 2012	55			
SANDO	compound heterozygous with L591F	Kurt 2012	48			
PEO	compound heterozygous with A467T	Lax 2012	17			
PEO	compound heterozygous with W748S	Lax 2012	25			
Alpers syndrome	homozygous	Ashley 2008	0.42			
seizures	homozygous	Tang 2011	0.67			
seizures	homozygous	Tang 2011	1			
seizures	homozygous	Tang 2011	2			

References

1. Lee, H., Hanes, J., and Johnson, K. A. (2003) Toxicity of nucleoside analogues used to treat AIDS and the selectivity of the mitochondrial DNA polymerase, *Biochemistry* 42, 14711-14719.
2. Lewis, W., Day, B. J., and Copeland, W. C. (2003) Mitochondrial toxicity of NRTI antiviral drugs: An integrated cellular perspective, *Nature Reviews Drug Discovery* 2, 812-822.
3. Nunnari, J., and Suomalainen, A. (2012) Mitochondria: in sickness and in health, *Cell* 148, 1145-1159.
4. Copeland, W. C. (2008) Inherited mitochondrial diseases of DNA replication, *Annu Rev Med* 59, 131-146.
5. Stumpf, J. D., and Copeland, W. C. (2011) Mitochondrial DNA replication and disease: insights from DNA polymerase gamma mutations, *Cell Mol Life Sci* 68, 219-233.
6. Stumpf, J. D., Saneto, R. P., and Copeland, W. C. (2013) Clinical and molecular features of POLG-related mitochondrial disease, *Cold Spring Harb Perspect Biol* 5, a011395.
7. Lee, H. C., Chang, C. M., and Chi, C. W. (2010) Somatic mutations of mitochondrial DNA in aging and cancer progression, *Ageing Res Rev* 9 Suppl 1, S47-58.
8. Paradies, G., Petrosillo, G., Paradies, V., and Ruggiero, F. M. (2011) Mitochondrial dysfunction in brain aging: Role of oxidative stress and cardiolipin, *Neurochem Int* 58, 447-457.
9. Calvo, S. E., and Mootha, V. K. (2010) The mitochondrial proteome and human disease, *Annu Rev Genomics Hum Genet* 11, 25-44.
10. Anderson, S., Bankier, A. T., Barrell, B. G., de Bruijn, M. H., Coulson, A. R., Drouin, J., Eperon, I. C., Nierlich, D. P., Roe, B. A., Sanger, F., Schreier, P. H., Smith, A. J., Staden, R., and Young, I. G. (1981) Sequence and organization of the human mitochondrial genome, *Nature*. 290, 457-465.
11. Smeitink, J., van den Heuvel, L., and DiMauro, S. (2001) The genetics and pathology of oxidative phosphorylation, *Nat Rev Genet* 2, 342-352.
12. Wallace, D. C., Fan, W., and Procaccio, V. (2010) Mitochondrial energetics and therapeutics, *Annual review of pathology* 5, 297-348.
13. (2014) Human DNA Polymerase Gamma Mutation Database, NIEHS - NIH.
14. Suomalainen, A. (2011) Therapy for mitochondrial disorders: little proof, high research activity, some promise, *Semin Fetal Neonatal Med* 16, 236-240.
15. Trifunovic, A., Wredenberg, A., Falkenberg, M., Spelbrink, J. N., Rovio, A. T., Bruder, C. E., Bohlooly, Y., Gidlof, S., Oldfors, A., Wibom, R., Tornell, J., Jacobs, H. T., and Larsson, N. G. (2004) Premature ageing in mice expressing defective mitochondrial DNA polymerase, *Nature* 429, 417-423.
16. Kaguni, L. S. (2004) DNA polymerase gamma, the mitochondrial replicase, *Annu Rev Biochem* 73, 293-320.

17. Falkenberg, M., Larsson, N. G., and Gustafsson, C. M. (2007) DNA replication and transcription in Mammalian mitochondria, *Annu.Rev.Biochem.* 76:679-99., 679-699.
18. Ziebarth, T. D., Farr, C. L., and Kaguni, L. S. (2007) Modular architecture of the hexameric human mitochondrial DNA helicase, *J Mol Biol* 367, 1382-1391.
19. Wanrooij, S., and Falkenberg, M. (2010) The human mitochondrial replication fork in health and disease, *Biochim Biophys Acta* 1797, 1378-1388.
20. Wallace, D. C. (1999) Mitochondrial diseases in man and mouse, *Science* 283, 1482-1488.
21. Johnson, A. A., and Johnson, K. A. (2001) Fidelity of nucleotide incorporation by human mitochondrial DNA polymerase, *J.Biol.Chem.* 276, 38090-38096.
22. Johnson, A. A., and Johnson, K. A. (2001) Exonuclease proofreading by human mitochondrial DNA polymerase, *J.Biol.Chem.* 276, 38097-38107.
23. Longley, M. J., Prasad, R., Srivastava, D. K., Wilson, S. H., and Copeland, W. C. (1998) Identification of 5'-deoxyribose phosphate lyase activity in human DNA polymerase gamma and its role in mitochondrial base excision repair in vitro, *Proc.Natl.Acad.Sci.U.S.A* 95, 12244-12248.
24. Clayton, D. A., Doda, J. N., and Friedberg, E. C. (1975) Absence of a pyrimidine dimer repair mechanism for mitochondrial DNA in mouse and human cells, *Basic Life Sci* 5B, 589-591.
25. Pascucci, B., Versteegh, A., van Hoffen, A., van Zeeland, A. A., Mullenders, L. H., and Dogliotti, E. (1997) DNA repair of UV photoproducts and mutagenesis in human mitochondrial DNA, *Journal of Molecular Biology* 273, 417-427.
26. Croteau, D. L., Stierum, R. H., and Bohr, V. A. (1999) Mitochondrial DNA repair pathways, *Mutation research* 434, 137-148.
27. Mason, P. A., Matheson, E. C., Hall, A. G., and Lightowlers, R. N. (2003) Mismatch repair activity in mammalian mitochondria, *Nucleic Acids Research* 31, 1052-1058.
28. Cerritelli, S. M., Frolova, E. G., Feng, C., Grinberg, A., Love, P. E., and Crouch, R. J. (2003) Failure to produce mitochondrial DNA results in embryonic lethality in Rnaseh1 null mice, *Molecular Cell* 11, 807-815.
29. Van Goethem, G., Dermaut, B., Lofgren, A., Martin, J.J., Van Broeckhoven, C. (2001) Mutation of POLG is associated with progressive external ophthalmoplegia characterized by mtDNA deletions, *Nature genetics* 28, 2.
30. Suomalainen, A., Kaukonen, J., Amati, P., Timonen, R., Haltia, M., Weissenbach, J., Zeviani, M., Somer, H., and Peltonen, L. (1995) An autosomal locus predisposing to deletions of mitochondrial DNA, *Nature genetics* 9, 146-151.
31. Spelbrink, J. N., Li, F. Y., Tiranti, V., Nikali, K., Yuan, Q. P., Tariq, M., Wanrooij, S., Garrido, N., Comi, G., Morandi, L., Santoro, L., Toscano, A., Fabrizi, G. M., Somer, H., Croxen, R., Beeson, D., Poulton, J., Suomalainen, A., Jacobs, H. T., Zeviani, M., and Larsson, C. (2001) Human mitochondrial DNA deletions associated with mutations in the gene encoding Twinkle, a phage T7 gene 4-like protein localized in mitochondria, *Nat Genet* 28, 223-231.

32. Fadic, R., Russell, J. A., Vedanarayanan, V. V., Lehar, M., Kuncl, R. W., and Johns, D. R. (1997) Sensory ataxic neuropathy as the presenting feature of a novel mitochondrial disease, *Neurology* 49, 239-245.
33. Milone, M., Brunetti-Pierri, N., Tang, L. Y., Kumar, N., Mezei, M. M., Josephs, K., Powell, S., Simpson, E., and Wong, L. J. (2008) Sensory ataxic neuropathy with ophthalmoparesis caused by POLG mutations, *Neuromuscul Disord* 18, 626-632.
34. Blok, M. J., van den Bosch, B. J., Jongen, E., Hendrickx, A., de Die-Smulders, C. E., Hoogendijk, J. E., Brusse, E., de Visser, M., Poll-The, B. T., Bierau, J., de Coo, I. F., and Smeets, H. J. (2009) The unfolding clinical spectrum of POLG mutations, *Journal of medical genetics* 46, 776-785.
35. Luoma, P., Melberg, A., Rinne, J. O., Kaukonen, J. A., Nupponen, N. N., Chalmers, R. M., Oldfors, A., Rautakorpi, I., Peltonen, L., Majamaa, K., Somer, H., and Suomalainen, A. (2004) Parkinsonism, premature menopause, and mitochondrial DNA polymerase gamma mutations: clinical and molecular genetic study, *Lancet* 364, 875-882.
36. Saneto, R. P., Cohen, B. H., Copeland, W. C., and Naviaux, R. K. (2013) Alpers-Huttenlocher syndrome, *Pediatr Neurol* 48, 167-178.
37. Naviaux, R. K., and Nguyen, K. V. (2004) POLG mutations associated with Alpers' syndrome and mitochondrial DNA depletion, *Annals of neurology* 55, 706-712.
38. Ferrari, G., Lamantea, E., Donati, A., Filosto, M., Briem, E., Carrara, F., Parini, R., Simonati, A., Santer, R., and Zeviani, M. (2005) Infantile hepatocerebral syndromes associated with mutations in the mitochondrial DNA polymerase-gammaA, *Brain* 128, 723-731.
39. Okun, M. S., and Bhatti, M. T. (2004) SANDO: another presentation of mitochondrial disease, *Am J Ophthalmol* 137, 951-953.
40. Milone, M., and Massie, R. (2010) Polymerase gamma 1 mutations: clinical correlations, *Neurologist* 16, 84-91.
41. Holt, I. J., Lorimer, H. E., and Jacobs, H. T. (2000) Coupled leading- and lagging-strand synthesis of mammalian mitochondrial DNA, *Cell* 100, 515-524.
42. Yasukawa, T., Reyes, A., Cluett, T. J., Yang, M. Y., Bowmaker, M., Jacobs, H. T., and Holt, I. J. (2006) Replication of vertebrate mitochondrial DNA entails transient ribonucleotide incorporation throughout the lagging strand, *The EMBO journal* 25, 5358-5371.
43. Bowmaker, M., Yang, M. Y., Yasukawa, T., Reyes, A., Jacobs, H. T., Huberman, J. A., and Holt, I. J. (2003) Mammalian mitochondrial DNA replicates bidirectionally from an initiation zone, *J Biol Chem* 278, 50961-50969.
44. Yasukawa, T., Yang, M. Y., Jacobs, H. T., and Holt, I. J. (2005) A bidirectional origin of replication maps to the major noncoding region of human mitochondrial DNA, *Molecular Cell* 18, 651-662.

45. Lee, Y. S., Kennedy, W. D., and Yin, Y. W. (2009) Structural insight into processive human mitochondrial DNA synthesis and disease-related polymerase mutations, *Cell* 139, 312-324.
46. Steitz, T. A., Smerdon, S., Jager, J., Wang, J., Kohlstaedt, L. A., Friedman, J. M., Beese, L. S., and Rice, P. A. (1993) Two DNA polymerases: HIV reverse transcriptase and the Klenow fragment of Escherichia coli DNA polymerase I, *Cold Spring Harb Symp Quant Biol* 58, 495-504.
47. Doublet, S., Tabor, S., Long, A. M., Richardson, C. C., and Ellenberger, T. (1998) Crystal structure of a bacteriophage T7 DNA replication complex at 2.2 Å resolution, *Nature* 391, 251-258.
48. Graves, S. W., Johnson, A. A., and Johnson, K. A. (1998) Expression, purification, and initial kinetic characterization of the large subunit of the human mitochondrial DNA polymerase, *Biochemistry* 37, 6050-6058.
49. Johnson, A. A., Tsai, Y. C., Graves, S. W., and Johnson, K. A. (2000) Human mitochondrial DNA polymerase holoenzyme: Reconstitution and characterization, *Biochemistry* 39, 1702-1708.
50. Johnson, A. A., Ray, A. S., Hanes, J., Suo, Z. C., Colacino, J. M., Anderson, K. S., and Johnson, K. A. (2001) Toxicity of antiviral nucleoside analogs and the human mitochondrial DNA polymerase, *Journal of Biological Chemistry* 276, 40847-40857.
51. Johnson, A. A., Feng, J. Y., Anderson, K. S., and Johnson, K. A. (2001) Incorporation of nucleoside analogs by the human mitochondrial DNA polymerase correlates with drug toxicity, *Faseb Journal* 15, A520-A520.
52. Lee, H. R., and Johnson, K. A. (2003) Mismatch incorporation by human mitochondrial DNA polymerase gamma. Probing the fidelity of a DNA polymerase, *Biophysical Journal* 84, 359A-359A.
53. Lee, H. R., and Johnson, K. A. (2006) Fidelity of the human mitochondrial DNA polymerase, *J Biol Chem* 281, 36236-36240.
54. Hanes, J. W., Thal, D.M., Johnson, K.A. (2006) Incorporation and Replication of 8-oxo-deoxyguanosine by the Human Mitochondrial DNA Polymerase, *Journal of Biological Chemistry* 281, 7.
55. Batabyal, D., McKenzie, J. L., and Johnson, K. A. (2010) Role of histidine 932 of the human mitochondrial DNA polymerase in nucleotide discrimination and inherited disease, *J Biol Chem* 285, 34191-34201.
56. Lee, Y. S., Johnson, K. A., Molineux, I. J., and Yin, Y. W. (2010) A single mutation in human mitochondrial DNA polymerase Pol gammaA affects both polymerization and proofreading activities of only the holoenzyme, *J Biol Chem* 285, 28105-28116.
57. Estep, P. A., and Johnson, K. A. (2011) Effect of the Y955C mutation on mitochondrial DNA polymerase efficiency and fidelity, *Biochemistry submitted*.
58. Spinazzola, A., Invernizzi, F., Carrara, F., Lamantea, E., Donati, A., Dirocco, M., Giordano, I., Meznaric-Petrusa, M., Baruffini, E., Ferrero, I., and Zeviani, M.

- (2009) Clinical and molecular features of mitochondrial DNA depletion syndromes, *J Inherit Metab Dis* 32, 143-158.
59. Mancuso, M., Filosto, M., Bellan, M., Liguori, R., Montagna, P., Baruzzi, A., DiMauro, S., and Carelli, V. (2004) POLG mutations causing ophthalmoplegia, sensorimotor polyneuropathy, ataxia, and deafness, *Neurology* 62, 316-318.
 60. Giordano, C., Pichiorri, F., Blakely, E. L., Perli, E., Orlandi, M., Gallo, P., Taylor, R. W., Inghilleri, M., and d'Amati, G. (2010) Isolated distal myopathy of the upper limbs associated with mitochondrial DNA depletion and polymerase gamma mutations, *Arch Neurol* 67, 1144-1146.
 61. Tang, S., Wang, J., Lee, N. C., Milone, M., Halberg, M. C., Schmitt, E. S., Craigen, W. J., Zhang, W., and Wong, L. J. (2011) Mitochondrial DNA polymerase gamma mutations: an ever expanding molecular and clinical spectrum, *J Med Genet* 48, 669-681.
 62. Lamantea, E., Tiranti, V., Bordoni, A., Toscano, A., Bono, F., Servidei, S., Papadimitriou, A., Spelbrink, H., Silvestri, L., Casari, G., Comi, G. P., and Zeviani, M. (2002) Mutations of mitochondrial DNA polymerase gammaA are a frequent cause of autosomal dominant or recessive progressive external ophthalmoplegia, *Ann Neurol* 52, 211-219.
 63. Brandon, B. R., Diederich, N. J., Soni, M., Witte, K., Weinhold, M., Krause, M., and Jackson, S. (2013) Autosomal dominant mutations in POLG and C10orf2: association with late onset chronic progressive external ophthalmoplegia and Parkinsonism in two patients, *J Neurol* 260, 1931-1933.
 64. Baruffini, E., Horvath, R., Dallabona, C., Czermin, B., Lamantea, E., Bindoff, L., Invernizzi, F., Ferrero, I., Zeviani, M., and Lodi, T. (2011) Predicting the contribution of novel POLG mutations to human disease through analysis in yeast model, *Mitochondrion* 11, 182-190.
 65. Lim, S., Ponamarev, M.V., Longley, M.J., Copeland, W.C. (2003) Structural Determinants in Human Polymerase Gamma Account for Mitochondrial Toxicity from Nucleoside Analogs, *Journal of Molecular Biology* 329, 12.
 66. Gurgel-Giannetti, J., Camargos, S. T., Cardoso, F., Hirano, M., and DiMauro, S. (2012) POLG1 Arg953Cys mutation: expanded phenotype and recessive inheritance in a Brazilian family, *Muscle & nerve* 45, 453-454.
 67. Agostino, A., Valletta, L., Chinnery, P. F., Ferrari, G., Carrara, F., Taylor, R. W., Schaefer, A. M., Turnbull, D. M., Tiranti, V., and Zeviani, M. (2003) Mutations of ANT1, Twinkle, and POLG1 in sporadic progressive external ophthalmoplegia (PEO), *Neurology* 60, 1354-1356.
 68. Horvath, R., Hudson, G., Ferrari, G., Futterer, N., Ahola, S., Lamantea, E., Prokisch, H., Lochmuller, H., McFarland, R., Ramesh, V., Klopstock, T., Freisinger, P., Salvi, F., Mayr, J. A., Santer, R., Tesarova, M., Zeman, J., Udd, B., Taylor, R. W., Turnbull, D., Hanna, M., Fialho, D., Suomalainen, A., Zeviani, M., and Chinnery, P. F. (2006) Phenotypic spectrum associated with mutations of the mitochondrial polymerase gamma gene, *Brain*. 129, 1674-1684.

69. Wong, L. J., Naviaux, R. K., Brunetti-Pierri, N., Zhang, Q., Schmitt, E. S., Truong, C., Milone, M., Cohen, B. H., Wical, B., Ganesh, J., Basinger, A. A., Burton, B. K., Swoboda, K., Gilbert, D. L., Vanderver, A., Saneto, R. P., Maranda, B., Arnold, G., Abdenur, J. E., Waters, P. J., and Copeland, W. C. (2008) Molecular and clinical genetics of mitochondrial diseases due to POLG mutations, *Hum Mutat* 29, E150-172.
70. Ashley, N., O'Rourke, A., Smith, C., Adams, S., Gowda, V., Zeviani, M., Brown, G. K., Fratter, C., and Poulton, J. (2008) Depletion of mitochondrial DNA in fibroblast cultures from patients with POLG1 mutations is a consequence of catalytic mutations, *Human molecular genetics* 17, 2496-2506.
71. Schulte, C., Synofzik, M., Gasser, T., and Schols, L. (2009) Ataxia with ophthalmoplegia or sensory neuropathy is frequently caused by POLG mutations, *Neurology* 73, 898-900.
72. Kurt, B., Naini, A. B., Copeland, W. C., Lu, J., Dimauro, S., and Hirano, M. (2012) A novel gene mutation in a patient with SANDO, *J Exp Integr Med* 2.
73. Lax, N. Z., Whittaker, R. G., Hepplewhite, P. D., Reeve, A. K., Blakely, E. L., Jaros, E., Ince, P. G., Taylor, R. W., Fawcett, P. R., and Turnbull, D. M. (2012) Sensory neuronopathy in patients harbouring recessive polymerase gamma mutations, *Brain : a journal of neurology* 135, 62-71.
74. Shereda, R. D., Kozlov, A. G., Lohman, T. M., Cox, M. M., and Keck, J. L. (2008) SSB as an organizer/mobilizer of genome maintenance complexes, *Crit Rev Biochem Mol Biol* 43, 289-318.
75. Korhonen, J. A., Gaspari, M., and Falkenberg, M. (2003) TWINKLE Has 5' -> 3' DNA helicase activity and is specifically stimulated by mitochondrial single-stranded DNA-binding protein, *J.Biol.Chem.* 278, 48627-48632.
76. Farge, G., Holmlund, T., Khvorostova, J., Rofougaran, R., Hofer, A., and Falkenberg, M. (2008) The N-terminal domain of TWINKLE contributes to single-stranded DNA binding and DNA helicase activities, *Nucleic Acids Res* 36, 393-403.
77. Korhonen, J. A., Pham, X. H., Pellegrini, M., and Falkenberg, M. (2004) Reconstitution of a minimal mtDNA replisome in vitro, *EMBO J.* 23, 2423-2429.
78. Euro, L., Farnum, G. A., Palin, E., Suomalainen, A., and Kaguni, L. S. (2011) Clustering of Alpers disease mutations and catalytic defects in biochemical variants reveal new features of molecular mechanism of the human mitochondrial replicase, Pol gamma, *Nucleic Acids Res* 39, 9072-9084.
79. Chan, S. S., Santos, J. H., Meyer, J. N., Mandavilli, B. S., Cook, D. L., Jr., McCash, C. L., Kissling, G. E., Nyska, A., Foley, J. F., van Houten, B., Copeland, W. C., Walker, V. E., Witt, K. L., and Bishop, J. B. (2007) Mitochondrial toxicity in hearts of CD-1 mice following perinatal exposure to AZT, 3TC, or AZT/3TC in combination, *Environ Mol Mutagen* 48, 190-200.
80. Kerr, S. G., and Anderson, K. S. (1997) RNA dependent DNA replication fidelity of HIV-1 reverse transcriptase: Evidence of discrimination between DNA and RNA substrates, *Biochemistry* 36, 14056-14063.

81. Baltimore, D. (1970) RNA-dependent DNA polymerase in virions of RNA tumour viruses, *Nature* 226, 1209-1211.
82. Temin, H. M., and Mizutani, S. (1970) RNA-dependent DNA polymerase in virions of Rous sarcoma virus, *Nature* 226, 1211-1213.
83. Charneau, P., Mirambeau, G., Roux, P., Paulous, S., Buc, H., and Clavel, F. (1994) HIV-1 reverse transcription. A termination step at the center of the genome, *Journal of Molecular Biology* 241, 651-662.
84. Gotte, M., Rausch, J. W., Marchand, B., Sarafianos, S., and Le Grice, S. F. (2010) Reverse transcriptase in motion: conformational dynamics of enzyme-substrate interactions, *Biochim Biophys Acta* 1804, 1202-1212.
85. Sarafianos, S. G., Marchand, B., Das, K., Himmel, D., Parniak, M. A., Hughes, S. H., and Arnold, E. (2008) Structure and Function of HIV-1 Reverse Transcriptase: Molecular Mechanisms of Polymerization and Inhibition, *J Mol Biol*.
86. Huang, H. F., Chopra, R., Verdine, G. L., and Harrison, S. C. (1998) Structure of a covalently trapped catalytic complex of HIV-1 reverse transcriptase: Implications for drug resistance, *Science* 282, 1669-1675.
87. Deval, J., Courcambek, J., Selmi, B., Boretto, J., and Canard, B. (2004) Structural determinants and molecular mechanisms for the resistance of HIV-1 RT to nucleoside analogues, *Curr. Drug Metab.* 5, 305-316.
88. Broder, S. (2010) The development of antiretroviral therapy and its impact on the HIV-1/AIDS pandemic, *Antiviral research* 85, 1-18.
89. Broder, S. (1990) Clinical applications of 3'-azido-2',3'-dideoxythymidine (AZT) and related dideoxynucleosides, *Med Res Rev* 10, 419-439.
90. Spence, R. A., Kati, W. M., Anderson, K. S., and Johnson, K. A. (1995) Mechanism of inhibition of HIV-1 reverse transcriptase by nonnucleoside inhibitors, *Science* 267, 988-993.
91. Ren, J., and Stammers, D. K. (2008) Structural basis for drug resistance mechanisms for non-nucleoside inhibitors of HIV reverse transcriptase, *Virus Res* 134, 157-170.
92. Sarafianos, S. G., Das, K., Clark, A. D., Jr., Ding, J., Boyer, P. L., Hughes, S. H., and Arnold, E. (1999) Lamivudine (3TC) resistance in HIV-1 reverse transcriptase involves steric hindrance with beta-branched amino acids, *Proc.Natl.Acad.Sci.U.S.A.* 96, 10027-10032.
93. Das, K., Bandwar, R. P., White, K. L., Feng, J. Y., Sarafianos, S. G., Tuske, S., Tu, X., Clark, A. D., Jr., Boyer, P. L., Hou, X., Gaffney, B. L., Jones, R. A., Miller, M. D., Hughes, S. H., and Arnold, E. (2009) Structural basis for the role of the K65R mutation in HIV-1 reverse transcriptase polymerization, excision antagonism, and tenofovir resistance, *J Biol Chem* 284, 35092-35100.
94. Arion, D., Kaushik, N., McCormick, S., Borkow, G., and Parniak, M. A. (1998) Phenotypic mechanism of HIV-1 resistance to 3'-azido-3'-deoxythymidine (AZT): increased polymerization processivity and enhanced sensitivity to pyrophosphate of the mutant viral reverse transcriptase, *Biochemistry.* 37, 15908-15917.

95. Meyer, P. R., Matsuura, S. E., So, A. G., and Scott, W. A. (1998) Unblocking of chain-terminated primer by HIV-1 reverse transcriptase through a nucleotide-dependent mechanism, *Proc Natl Acad Sci U S A* 95, 13471-13476.
96. Meyer, P. R., Matsuura, S. E., Mian, A. M., So, A. G., and Scott, W. A. (1999) A mechanism of AZT resistance: an increase in nucleotide-dependent primer unblocking by mutant HIV-1 reverse transcriptase, *Mol.Cell.* 4, 35-43.
97. Boyer, P. L., Sarafianos, S. G., Arnold, E., and Hughes, S. H. (2001) Selective excision of AZTMP by drug-resistant human immunodeficiency virus reverse transcriptase, *J.Virol.* 75, 4832-4842.
98. Ray, A. S., Murakami, E., Basavapathruni, A., Vaccaro, J. A., Ulrich, D., Chu, C. K., Schinazi, R. F., and Anderson, K. S. (2003) Probing the molecular mechanisms of AZT drug resistance mediated by HIV-1 reverse transcriptase using a transient kinetic analysis, *Biochemistry* 42, 8831-8841.
99. Meyer, P. R., Matsuura, S. E., Schinazi, R. F., So, A. G., and Scott, W. A. (2000) Differential removal of thymidine nucleotide analogues from blocked DNA chains by human immunodeficiency virus reverse transcriptase in the presence of physiological concentrations of 2'-deoxynucleoside triphosphates, *Antimicrob.Agents Chemother.* 44, 3465-3472.
100. Tu, X., Das, K., Han, Q., Bauman, J. D., Clark, A. D., Jr., Hou, X., Frenkel, Y. V., Gaffney, B. L., Jones, R. A., Boyer, P. L., Hughes, S. H., Sarafianos, S. G., and Arnold, E. (2010) Structural basis of HIV-1 resistance to AZT by excision, *Nat Struct Mol Biol* 17, 1202-1209.
101. Roitberg, A. E., Okur, A., and Simmerling, C. (2007) Coupling of replica exchange simulations to a non-Boltzmann structure reservoir, *J Phys Chem B* 111, 2415-2418.
102. Farnum, G. A., Nurminen, A., and Kaguni, L. S. (2014) Mapping 136 pathogenic mutations into functional modules in human DNA polymerase gamma establishes predictive genotype-phenotype correlations for the complete spectrum of POLG syndromes, *Biochimica et biophysica acta* 1837, 1113-1121.
103. Graziewicz, M. A., Bienstock, R. J., and Copeland, W. C. (2007) The DNA polymerase gamma Y955C disease variant associated with PEO and parkinsonism mediates the incorporation and translesion synthesis opposite 7,8-dihydro-8-oxo-2'-deoxyguanosine, *Hum Mol Genet* 16, 2729-2739.
104. Stumpf, J. D., Bailey, C. M., Spell, D., Stillwagon, M., Anderson, K. S., and Copeland, W. C. (2010) mip1 Containing mutations associated with mitochondrial disease causes mutagenesis and depletion of mtDNA in *Saccharomyces cerevisiae*, *Hum Mol Genet* 19, 2123-2133.
105. Graziewicz, M. A., Longley, M. J., Bienstock, R. J., Zeviani, M., and Copeland, W. C. (2004) Structure-function defects of human mitochondrial DNA polymerase in autosomal dominant progressive external ophthalmoplegia, *Nature Structural & Molecular Biology* 11, 770-776.
106. Sohl, C. D., Kasiviswanathan, R., Copeland, W. C., and Anderson, K. S. (2013) Mutations in human DNA polymerase gamma confer unique mechanisms of

- catalytic deficiency that mirror the disease severity in mitochondrial disorder patients, *Human molecular genetics* 22, 1074-1085.
107. Longley, M. J., Ropp, P. A., Lim, S. E., and Copeland, W. C. (1998) Characterization of the native and recombinant catalytic subunit of human DNA polymerase gamma: identification of residues critical for exonuclease activity and dideoxynucleotide sensitivity, *Biochemistry* 37, 10529-10539.
 108. Yakubovskaya, E., Chen, Z., Carrodeguas, J. A., Kisker, C., and Bogenhagen, D. F. (2006) Functional human mitochondrial DNA polymerase gamma forms a heterotrimer, *J Biol Chem.* 281, 374-382.
 109. Carrodeguas, J. A., Theis, K., Bogenhagen, D. F., and Kisker, C. (2001) Crystal structure and deletion analysis show that the accessory subunit of mammalian DNA polymerase gamma, Pol gamma B, functions as a homodimer, *Mol.Cell* 7, 43-54.
 110. Patel, S. S., Wong, I., and Johnson, K. A. (1991) Pre-Steady-State Kinetic-Analysis of Processive Dna-Replication Including Complete Characterization of An Exonuclease-Deficient Mutant, *Biochemistry* 30, 511-525.
 111. Wong, I., Patel, S. S., and Johnson, K. A. (1991) An induced-fit kinetic mechanism for DNA replication fidelity: direct measurement by single-turnover kinetics, *Biochemistry* 30, 526-537.
 112. Johnson, K. A., Simpson, Z. B., and Blom, T. (2009) Global Kinetic Explorer: A new computer program for dynamic simulation and fitting of kinetic data, *Anal Biochem* 387, 20-29.
 113. Johnson, K. A., Simpson, Z. B., and Blom, T. (2009) FitSpace Explorer: An algorithm to evaluate multidimensional parameter space in fitting kinetic data, *Anal Biochem* 387, 30-41.
 114. Johnson, A. A., Tsai, Y.C., Graves, S.W., Johnson, K.A. (2000) Human Mitochondrial DNA Polymerase Holoenzyme: Reconstitution and Characterization, *Biochemistry* 39, 6.
 115. Johnson, K. A. (1993) Conformational coupling in DNA polymerase fidelity, *Annu. Rev. Biochem.* 62, 685-713.
 116. Batabyal, D., McKenzie, J. L., and Johnson, K. A. (2010) Role of histidine-932 of the human mitochondrial DNA polymerase in nucleotide discrimination and inherited disease, *J Biol Chem.*
 117. Lee, Y. S., Lee, S., Demeler, B., Molineux, I. J., Johnson, K. A., and Yin, Y. W. (2010) Each monomer of the dimeric accessory protein for human mitochondrial DNA polymerase has a distinct role in conferring processivity, *J Biol Chem* 285, 1490-1499.
 118. Hanes, J. W., Thal, D. M., and Johnson, K. A. (2006) Incorporation and replication of 8-oxo-deoxyguanosine by the human mitochondrial DNA polymerase, *J. Biol. Chem.* 281, 36241-36248.
 119. Hanes, J. W., and Johnson, K. A. (2007) A novel mechanism of selectivity against AZT by the human mitochondrial DNA polymerase, *Nucleic Acids Res.* 35, 6973-6983.

120. Shuster, R. C., Rubenstein, A. J., and Wallace, D. C. (1988) Mitochondrial DNA in anucleate human blood cells, *Biochemical and biophysical research communications* 155, 1360-1365.
121. Wiesner, R. J., Ruegg, J. C., and Morano, I. (1992) Counting target molecules by exponential polymerase chain reaction: copy number of mitochondrial DNA in rat tissues, *Biochemical and biophysical research communications* 183, 553-559.
122. Fernandez-Silva, P., Enriquez, J. A., and Montoya, J. (2003) Replication and transcription of mammalian mitochondrial DNA, *Exp Physiol* 88, 41-56.
123. Qian, Y., Kachroo, A. H., Yellman, C. M., Marcotte, E. M., and Johnson, K. A. (2014) Yeast cells expressing the human mitochondrial DNA polymerase reveal correlations between polymerase fidelity and human disease progression, *J Biol Chem* 289, 5970-5985.
124. Astatke, M., Ng, K., Grindley, N. D., and Joyce, C. M. (1998) A single side chain prevents Escherichia coli DNA polymerase I (Klenow fragment) from incorporating ribonucleotides, *Proc.Natl.Acad.Sci.U.S.A* 95, 3402-3407.
125. Tabor, S., and Richardson, C. C. (1995) A single residue in DNA polymerases of the Escherichia coli DNA polymerase I family is critical for distinguishing between deoxy- and dideoxyribonucleotides, *Proc.Natl.Acad.Sci.U.S.A* 92, 6339-6343.
126. Brune, M., Hunter, J. L., Corrie, J. E., and Webb, M. R. (1994) Direct, real-time measurement of rapid inorganic phosphate release using a novel fluorescent probe and its application to actomyosin subfragment 1 ATPase, *Biochemistry* 33, 8262-8271.
127. Hirshberg, M., Henrick, K., Haire, L. L., Vasisht, N., Brune, M., Corrie, J. E., and Webb, M. R. (1998) Crystal structure of phosphate binding protein labeled with a coumarin fluorophore, a probe for inorganic phosphate, *Biochemistry* 37, 10381-10385.
128. Kellinger, M. W., and Johnson, K. A. Nucleotide-dependent conformational change governs specificity and analog discrimination by HIV reverse transcriptase, *Proc Natl Acad Sci U S A* 107, 7734-7739.
129. Tsai, Y. C., and Johnson, K. A. (2006) A new paradigm for DNA polymerase specificity, *Biochemistry*. 45, 9675-9687.
130. Lim, S. E., Ponamarev, M. V., Longley, M. J., and Copeland, W. C. (2003) Structural determinants in human DNA polymerase gamma account for mitochondrial toxicity from nucleoside analogs, *J.Mol.Biol.* 329, 45-57.
131. Jemt, E., Farge, G., Backstrom, S., Holmlund, T., Gustafsson, C. M., and Falkenberg, M. (2011) The mitochondrial DNA helicase TWINKLE can assemble on a closed circular template and support initiation of DNA synthesis, *Nucleic Acids Res* 39, 9238-9249.
132. Briebe, L. G., Eichman, B. F., Kokoska, R. J., Doublié, S., Kunkel, T. A., and Ellenberger, T. (2004) Structural basis for the dual coding potential of 8-oxoguanosine by a high-fidelity DNA polymerase, *EMBO J* 23, 3452-3461.

133. Toth, E. A., Li, Y., Sawaya, M. R., Cheng, Y., and Ellenberger, T. (2003) The crystal structure of the bifunctional primase-helicase of bacteriophage T7, *Mol Cell* 12, 1113-1123.
134. Doublet, S., Tabor, S., Long, A. M., Richardson, C. C., and Ellenberger, T. (1998) Crystal structure of a bacteriophage T7 DNA replication complex at 2.2 Å resolution, *Nature* 391, 251-258.
135. Lee, J. Y., Finkelstein, I. J., Crozat, E., Sherratt, D. J., and Greene, E. C. (2012) Single-molecule imaging of DNA curtains reveals mechanisms of KOPS sequence targeting by the DNA translocase FtsK, *Proceedings of the National Academy of Sciences of the United States of America* 109, 6531-6536.
136. Crozat, E., Meglio, A., Allemand, J. F., Chivers, C. E., Howarth, M., Venien-Bryan, C., Grainge, I., and Sherratt, D. J. (2010) Separating speed and ability to displace roadblocks during DNA translocation by FtsK, *EMBO J* 29, 1423-1433.
137. Massey, T. H., Mercogliano, C. P., Yates, J., Sherratt, D. J., and Lowe, J. (2006) Double-stranded DNA translocation: structure and mechanism of hexameric FtsK, *Molecular Cell* 23, 457-469.
138. Chen, Z., Yang, H., and Pavletich, N. P. (2008) Mechanism of homologous recombination from the RecA-ssDNA/dsDNA structures, *Nature* 453, 489-484.
139. Martin, A., Baker, T. A., and Sauer, R. T. (2005) Rebuilt AAA + motors reveal operating principles for ATP-fuelled machines, *Nature* 437, 1115-1120.
140. Chang, D. D., and Clayton, D. A. (1985) Priming of human mitochondrial DNA replication occurs at the light-strand promoter, *Proc Natl Acad Sci U S A* 82, 351-355.
141. Chang, D. D., Hauswirth, W. W., and Clayton, D. A. (1985) Replication priming and transcription initiate from precisely the same site in mouse mitochondrial DNA, *EMBO J* 4, 1559-1567.
142. Longley, M. J., Humble, M. M., Sharief, F. S., and Copeland, W. C. (2010) Disease variants of the human mitochondrial DNA helicase encoded by C10orf2 differentially alter protein stability, nucleotide hydrolysis, and helicase activity, *J Biol Chem* 285, 29690-29702.
143. Estep, P. A., and Johnson, K. A. (2011) Effect of the Y955C mutation on mitochondrial DNA polymerase nucleotide incorporation efficiency and fidelity, *Biochemistry* 50, 6376-6386.
144. Kati, W. M., Johnson, K. A., Jerva, L. F., and Anderson, K. S. (1992) Mechanism and fidelity of HIV reverse transcriptase, *J.Biol.Chem.* 267, 25988-25997.
145. Spence, R. A., Anderson, K. S., and Johnson, K. A. (1996) HIV-1 reverse transcriptase resistance to nonnucleoside inhibitors, *Biochemistry* 35, 1054-1063.
146. Kellinger, M. W., and Johnson, K. A. (2010) Nucleotide-dependent conformational change governs specificity and analog discrimination by HIV reverse transcriptase, *Proc Natl Acad Sci U S A* 107, 7734-7739.
147. Ding, J., Das, K., Hsiou, Y., Sarafianos, S. G., Clark, A. D., Jr., Jacobo-Molina, A., Tantillo, C., Hughes, S. H., and Arnold, E. (1998) Structure and functional implications of the polymerase active site region in a complex of HIV-1 RT with

- a double-stranded DNA template-primer and an antibody Fab fragment at 2.8 Å resolution, *J Mol.Biol.* 284, 1095-1111.
148. Sarafianos, S. G., Das, K., Ding, J., Boyer, P. L., Hughes, S. H., and Arnold, E. (1999) Touching the heart of HIV-1 drug resistance: the fingers close down on the dNTP at the polymerase active site, *Chem Biol.* 6, R137-R146.
 149. Rhee, S. Y., Gonzales, M. J., Kantor, R., Betts, B. J., Ravela, J., and Shafer, R. W. (2003) Human immunodeficiency virus reverse transcriptase and protease sequence database, *Nucleic Acids Res* 31, 298-303.
 150. Kensch, O., Restle, T., Wohrl, B. M., Goody, R. S., and Steinhoff, H. J. (2000) Temperature-dependent equilibrium between the open and closed conformation of the p66 subunit of HIV-1 reverse transcriptase revealed by site-directed spin labelling, *J.Mol.Biol.* 301, 1029-1039.
 151. Mitsuya, H., Weinhold, K. J., Furman, P. A., St Clair, M. H., Lehrman, S. N., Gallo, R. C., Bolognesi, D., Barry, D. W., and Broder, S. (1985) 3'-Azido-3'-deoxythymidine (BW A509U): an antiviral agent that inhibits the infectivity and cytopathic effect of human T-lymphotropic virus type III/lymphadenopathy-associated virus in vitro, *Proc Natl Acad Sci U S A* 82, 7096-7100.
 152. Furman, P. A., Fyfe, J. A., St Clair, M. H., Weinhold, K., Rideout, J. L., Freeman, G. A., Lehrman, S. N., Bolognesi, D. P., Broder, S., and Mitsuya, H. (1986) Phosphorylation of 3'-azido-3'-deoxythymidine and selective interaction of the 5'-triphosphate with human immunodeficiency virus reverse transcriptase, *Proc.Natl.Acad.Sci.U.S.A* 83, 8333-8337.
 153. Lacey, S. F., Reardon, J. E., Furfine, E. S., Kunkel, T. A., Bebenek, K., Eckert, K. A., Kemp, S. D., and Larder, B. A. (1992) Biochemical studies on the reverse transcriptase and RNase H activities from human immunodeficiency virus strains resistant to 3'-azido-3'-deoxythymidine, *J Biol Chem* 267, 15789-15794.
 154. Gonzales, M. J., Wu, T. D., Taylor, J., Belitskaya, I., Kantor, R., Israelski, D., Chou, S., Zolopa, A. R., Fessel, W. J., and Shafer, R. W. (2003) Extended spectrum of HIV-1 reverse transcriptase mutations in patients receiving multiple nucleoside analog inhibitors, *AIDS* 17, 791-799.
 155. Jeeninga, R. E., Keulen, W., Boucher, C., Sanders, R. W., and Berkhout, B. (2001) Evolution of AZT resistance in HIV-1: the 41-70 intermediate that is not observed in vivo has a replication defect, *Virology* 283, 294-305.
 156. Larder, B. A., and Kemp, S. D. (1989) Multiple mutations in HIV-1 reverse transcriptase confer high-level resistance to zidovudine (AZT), *Science* 246, 1155-1158.
 157. Sarafianos, S. G., Clark, A. D., Jr., Das, K., Tuske, S., Birktoft, J. J., Ilankumaran, P., Ramesha, A. R., Sayer, J. M., Jerina, D. M., Boyer, P. L., Hughes, S. H., and Arnold, E. (2002) Structures of HIV-1 reverse transcriptase with pre- and post-translocation AZTMP-terminated DNA, *EMBO J.* 21, 6614-6624.
 158. Kerr, S. G., and Anderson, K. S. (1997) Pre-steady-state kinetic characterization of wild type and 3'-azido-3'-deoxythymidine (AZT) resistant human immunodeficiency virus type 1 reverse transcriptase: implication of RNA directed

- DNA polymerization in the mechanism of AZT resistance, *Biochemistry* 36, 14064-14070.
159. Kellinger, M. W., and Johnson, K. A. (2011) Role of induced fit in limiting discrimination against AZT by HIV reverse transcriptase, *Biochemistry* 50, 5008-5015.
 160. Schatz, O., Cromme, F. V., Gruninger-Leitch, F., and Le Grice, S. F. (1989) Point mutations in conserved amino acid residues within the C-terminal domain of HIV-1 reverse transcriptase specifically repress RNase H function, *FEBS letters* 257, 311-314.
 161. Tsai, Y. C., Jin, Z., and Johnson, K. A. (2009) Site-specific labeling of T7 DNA polymerase with a conformationally sensitive fluorophore and its use in detecting single-nucleotide polymorphisms, *Anal Biochem* 384, 136-144.
 162. Kruhoffer, M., Urbanke, C., and Grosse, F. (1993) Two step binding of HIV-1 reverse transcriptase to nucleic acid substrates, *Nucleic Acids Research* 21, 3943-3949.
 163. Divita, G., Muller, B., Immendorfer, U., Gautel, M., Rittinger, K., Restle, T., and Goody, R. S. (1993) Kinetics of interaction of HIV reverse transcriptase with primer/template, *Biochemistry* 32, 7966-7971.
 164. Sarafianos, S. G., Das, K., Tantillo, C., Clark, A. D., Jr., Ding, J., Whitcomb, J. M., Boyer, P. L., Hughes, S. H., and Arnold, E. (2001) Crystal structure of HIV-1 reverse transcriptase in complex with a polypurine tract RNA:DNA, *The EMBO journal* 20, 1449-1461.
 165. Lapkouski, M., Tian, L., Miller, J. T., Le Grice, S. F., and Yang, W. (2013) Complexes of HIV-1 RT, NNRTI and RNA/DNA hybrid reveal a structure compatible with RNA degradation, *Nature Structural & Molecular Biology* 20, 230-236.
 166. Johnson, K. A. (2008) Role of induced fit in enzyme specificity: a molecular forward/reverse switch, *J Biol Chem* 283, 26297-26301.
 167. Kirmizialtin, S., Nguyen, V., Johnson, K. A., and Elber, R. (2012) How conformational dynamics of DNA polymerase select correct substrates: experiments and simulations, *Structure* 20, 618-627.
 168. Rittinger, K., Divita, G., and Goody, R. S. (1995) Human immunodeficiency virus reverse transcriptase substrate-induced conformational changes and the mechanism of inhibition by nonnucleoside inhibitors, *Proc Natl Acad Sci U S A* 92, 8046-8049.

Vita

Jessica Lea Ziehr was born in Austin, Texas to father Mark McKenzie and mother Robin Anderson. She attended high school in Austin and began undergraduate studies at the University of Texas at Austin in 2005. As an undergraduate, Jessica worked in Dr. Kenneth Johnson's laboratory and developed a passion for enzyme kinetics. She received a Bachelor of Science degree in Biology in 2009, and decided to pursue a doctorate in cell and molecular biology from the Institute for Cellular and Molecular Biology at the University of Texas at Austin. As a first year graduate student, Jessica rotated in the labs of Dr. Rick Russell and Dr. Kevin Dalby, who both served as excellent mentors in the development of her knowledge of enzyme kinetics. In the summer of 2010, she joined the laboratory of Dr. Kenneth Johnson to study the kinetics of DNA polymerases. On August 7, 2010 she married her husband Nathan, and the two currently reside in Austin, Texas with their daughter Olivia.

Permanent address (or email): jessica.ziehr@gmail.com

This dissertation was typed by the author.